THÈSE DE DOCTORAT
DE L'UNIVERSITÉ PIERRE ET MARIE CURIE

Spécialité : Physique des plasmas

École doctorale n°564: Physique en Île-de-France

réalisée

au Laboratoire de Physique des Plasmas

sous la direction de Philippe SAVOINI & Dominique FONTAINE

présentée par

Clément MOISSARD

pour obtenir le grade de :

DOCTEUR DE L'UNIVERSITÉ PIERRE ET MARIE CURIE

Sujet de la thèse :

Interplanetary sheaths driven by magnetic clouds and their impact on Earth's magnetosheath

soutenue le 5 Février 2021

devant le jury composé de :

M^me^	Caterina RICONDA	Présidente
M.	Vincent GÉNOT	Rapporteur
M.	Francesco CALIFANO	Rapporteur
M^me^	Emilia KILPUA	Examinatrice
M.	Ronan MODOLO	Examinateur
M.	Philippe SAVOINI	Directeur de thèse
M^me^	Dominique FONTAINE	Directrice de thèse

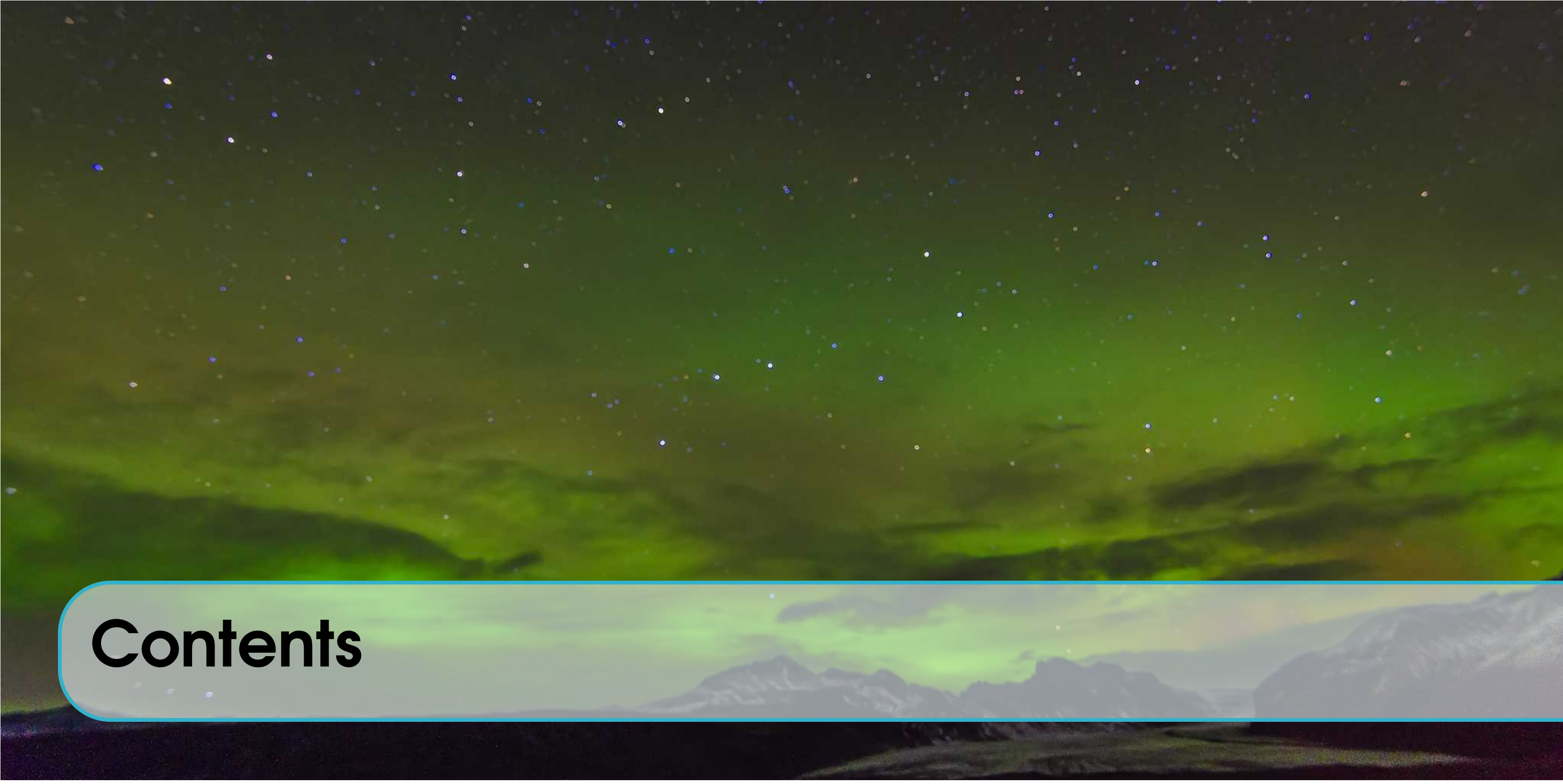

Contents

Acknowledgements

It takes a while to write a thesis. To do the research that goes into it, order the thoughts to make sense of what we find and what we do not. It takes a lot of thinking, obviously, and it also takes a lot of energy. It makes you go through a lot of different emotions, pleasure and frustration, excitement and disappointment, wonder and sometimes even anger. All of these do not always come from the PhD work itself, of course, but from juggling it with life, the first serious responsibilities and hardships of adulthood that tend to fall on us around the time we dive into this experience. Navigating all this can be tough, and exhilarating at the same time. But it would be impossible to grow through the toughness, or to find any beauty in it without the people around us. It is the people around us that make it all possible.

My first thoughts are for Philippe Savoini, who made me discover plasma physics seven years ago. I can still picture myself walking into his office, asking what he was doing. The excitement I felt listening to him explain his work in Space Physics set me on the path I am still on today. Thank you for this, and thank you for having been such a good PhD advisor: extremely available, and always willing to sit down and think or get your hands dirty to fix a problem; on top of being a life saviour when it comes to all things administrative.

Dominique Fontaine, also my PhD advisor, taught me a lot about physics, about the workplace, about patience, and about passion. The spark in her eyes is hard to miss when she explains the results of a study or another. I cannot thank you enough for all the discussions we had about my work and the rest of the solar system. Nor for helping me stick around for a few more months as a postdoc.

In the Laboratoire de Physique des Plasmas, there are so many other people to thank. Roland Grappin, for knocking on my door so often, just for the pleasure of talking about physics. Nicolas Aunai, for helping me compile my code the first time around after a couple months of despair, as well as for always asking the most annoying questions, and not letting me get away with half-baked answers. Nicolas Marsac and Alexis Jeandet for being the computer wizards we all need. Laurence Rezeau, for being so caring when things got tough in my personal life, as well as for proof reading my book and being so enthusiastic about it. Olivier Lecontel, for all the discussions about magnetic reconnection; we are not done. Pierre Morel, for the relaxed conversations that put things in perspective. Svetlana Starikovskaia, for helping me put together a convincing application to my postdoc. Gaëtan Gauthier and Vincent David, for getting me out of my office and helping me remember that being sociable is not necessarily ill-spent time. Gautier Nguyen, my office mate, for so many conversations about our works and for sharing really useful snippets of code. There are so many other people with whom I shared good conversations, moments, or even just a smile. You all count. Thank you so much.

Outside of the lab, but still at work: Ronan Modolo, my unofficial third PhD advisor. Well, you wrote the code, which gave you a semi-divine status as I kept calling you “the code father”. You were always available, encouraging, and really, really useful whenever I wanted to talk about it. Most of my work does not exist without you. Emilia Kilpua, you were always so cheerful and so, so efficient. Working with you was a pleasure, even if I managed to always get sick around the times you were in France. I hope I can make it up to you in the future. William Fox, you are the one that really taught me plasma physics, coding, conducting research, and to do it with panache; so long ago now. I cannot wait to resume our work together. Amitava Bhattacharjee and Hantao Ji, for cheering me up from the sidelines, whenever our paths crossed. I am so glad the plasma physics world is small enough that this can just “happen” on a semi-regular basis. Andrea Ciardi, for being so warm; we will have this beer, promess. Goodwin Gibbins, for teaching me with infinite patience about the thermodynamics of Earth; it is good to be able to really think about something other than my main topic. Caterina Riconda, for giving me the opportunity to teach plasma physics with you, for helping me find my next, next job, if all goes well; and for presiding at my PhD defence. Francesco Califano and Vincent Génot, who read my manuscript so thoroughly. Thank you for challenging me.

All the students I had in Jussieu. Sharing my love for physics with you is what makes it all worth it. I think especially about those who became more than students, and, dare I say, friends: Valentine Rehn and Keryan Borreca. This is not to say that I forget everyone else, obviously. The list is just so long.

Outside of work altogether, I want to thank Dr Clément Rieu, Dr Katia Verteletsky and Dr Quentin André for showing me how it’s done. And for being such close friends, of course. My parents, does it even make sense to say what for? Life? You are the best parents anyone could wish for. Emily, it is honestly hard to write about you without getting emotional, so I should keep it short. I love you. And finally, Élina, my newborn daughter. Your upcoming birth was the best motivation there was to write the final words to my thesis. And if you read these words in a few years, I love you too.

PS: A final note. Several dedicated people have patiently reread the following manuscript multiple times, Philippe, Dominique, Francesco, Vincent, another Vincent and Emily. Despite their best efforts to keep up, I kept adding small changes, rewriting things. Any error that is left in the manuscript – be it an error with the physics, a grammatical one, or something literary cringy – is my own.

Chapters head: Francisco Diez from Toronto, Canada: Aurora Borealis over Iceland - 2 Nov. 2013
CC BY 2.0 <https://creativecommons.org/licenses/by/2.0>

Summary / Résumé

The Sun often ejects large quantities of magnetic field embedded plasma called magnetic clouds. These can collide with the geomagnetic environment and sometimes perturb it to the point of causing dysfunctions in human technologies. When magnetic clouds travel fast enough, they can generate a shock, itself followed by a turbulent compressed stream named a sheath. Sheaths have recently been recognised as efficient drivers of geomagnetic activity. However, sheaths themselves and their interaction with the geomagnetic environment remain poorly known.

First, by making a statistical study on satellite data of 42 relatively well isolated sheaths, our work is the first to provide values of power and compressibility (which is an indication of the type of fluctuations) in sheaths. We also show the main parameters on which these two quantities depend.

Second, we perform the first ever 3D hybrid PIC simulation to include both an interplanetary shock/sheath self-consistently formed and a model of the geomagnetic environment. From this simulation, we show: the “rebound” of the bow shock’s motion after its interaction with the interplanetary shock (a known phenomenon) can be explained by a counter streaming flow of subalfvénic particles bouncing back on the magnetopause; the interplanetary shock can be accelerated on the flanks of the magnetopause in the plane perpendicular to the interplanetary magnetic field; an important velocity component perpendicular to the interplanetary magnetic field rises in the sheath, leading to a strong asymmetry in the magnetosheath’s compression.

We will conclude by discussing how our observational results could be used to guide efforts in future numerical simulations.

Des nuages magnétiques en provenance du soleil peuvent atteindre et perturber l'environnement géomagnétique et endommager certaines technologies. S'ils sont suffisamment rapides, ces nuages peuvent entraîner la formation d'un choc interplanétaire suivi d'une gaine turbulente de plasma compressé. Il a été montré récemment que ces gaines peuvent être très géoeffectives. Pourtant, les gaines, ainsi que leur interaction avec l'environment géomagnétique restent mal connus.

Nous fournissons pour la première fois, grâce à une étude statistique menée sur 42 gaines bien définies et isolées, des valeurs de la puissance des fluctuations magnétiques et de leur compressibilité (une indication sur le type des fluctuations). Les paramètres ayant une influence sur ces valeurs sont également mis en évidence.

Ensuite, nous présentons la première simulation PIC hybride 3D qui inclut à la fois un modèle de l'environnement géomagnétique et une gaine interplanétaire formée de manière auto-cohérente. Cette simulation permet la mise en évidence de plusieurs résultats nouveaux: le rebond du choc d'étrave suite à son interaction avec le choc interplanétaire (un phénomène connu) peut être expliqué par l'apparition d'un flux subalfvénique de particules ayant rebondies sur la magnétopause; le choc interplanétaire, d'abord freiné dans la magnétogaine, peut être accéléré sur les flancs de la magnétopause; enfin le plasma dans la gaine se propage avec une composante de vitesse perpendiculaire au champ magnétique interplanétaire, non présente en aval du choc, ce qui mène à une compression asymétrique de la magnétogaine.

Nous discuterons enfin des pistes que notre étude observationnelle nous donne pour développer plus avant nos simulations numériques.

Introduction

> **Note:** This short introduction is a simple primer on Space Weather, intended to give the reader some mental imagery of the context in which this thesis is set.

> *“With this a beautiful tint of pink finally mingled. The clouds of this color were most abundant to the northeast and northwest of the zenith [...]. There they shot across one another, intermingling and deepening until the sky was painfully lurid. There was no figure the imagination could not find portrayed by these instantaneous flashes.”* - New York Times, 1859

Sun and Earth’s supersonic, turbulent relationship

Imagine, if you will, that you are on a boat. An old boat mind you. The year is 1657. The exact year does not actually matter, I just would like you to see yourself as a XVII’s century sailor. Around you the only thing you can see is water. There is quite a bit of mist, which means that your only way to orientate your course is through a magnetic compass. Everything is well and you are following your route with confidence. But suddenly, you start noticing the compass’ needle shaking and moving a little bit to the west. Not much, just about a degree. After wondering if you should do anything about your direction, you decide to turn a bit more to the east so that the needle gets back to its initial position. A few hours pass before the mist dissipates, and the night falls. You can now check your position with the stars. Apparently, you got it slightly wrong, and you are now a few kilometres away from where you should be. It is not a big problem though, you adjust course and go back to reading your book to the light of a candle.

The year is now 1859. The date matters this time. On Thursday, September the 2nd, you arrive at your work at the Telegraph Office in Portland. Last Sunday, massive displays of aurora borealis were spotted in unusual places: many accounts have been made in France, England, and even Japan. This morning, you are receiving messages but everything seems a bit strange. Some still make sense but many do not and your system seems to go on overload, then disconnects, making it really hard to

do your job. Fortunately, a resourceful colleague from Boston surprises you with these few words, received through your telegraph:
“(Boston) Please cut off your battery entirely from the line for fifteen minutes.”
Since nothing is really working anyway, why not give it a go. You reply:
“(Portland) Will do so. It is now disconnected.”
You unplug your system. As you are turning away from your post to talk to a colleague about the fifteen minutes you just freed which you could probably use to get a coffee, you stare incredulously at your receptor: a message has arrived.
“(Boston) Mine is also disconnected, and we are working with the auroral current. How do you receive my writing?”
You sit down, intrigued. You start writing, hardly believing your own words:
"Better than with our batteries on. Current comes and goes gradually."
The reply comes fast:
“(Boston) [...] Suppose we work without batteries while we are affected by this trouble?"
“(Portland) Very well. Shall I go ahead with business?” [1]

1989, you are at home cooking pastas on the stove. Your kids are screaming behind you. They are just having fun watching cartoons on your new television set. Suddenly, the lights are out. You blame your stupid stove that takes too much power to function. You go to your circuit board and try to turn things back on. Nothing. That is unusual. You go outside and you find your street unusually dark. Other people are on the street as well. "You too?" you ask your neighbour. "Yes..." Going through your door again, you find that the kids are still screaming, only louder. You tell them that everything is okay, hoping that you are right[2]. That the power will be back any minute now. It is only after nine hours, a couple of candles and some tears, that your prediction becomes true.

The link between these three stories is the Sun. Or rather the supersonic, turbulent relationship between the Sun and Earth. Continuously, a plasma called the solar wind flows outwardly from the Sun. Most of the time, it is rather calm and does not cause any noticeable event on Earth, but between one and five times a day (Webb and Howard (2012)) the Sun sends out massive amounts of matter ($\sim 10^{13}$ – 10^{15} kg) and energy ($\sim 10^{23}$ J) (Emslie et al. (2004) and Webb and Howard (2012)) into space, called coronal mass ejections or CMEs. Roughly once a month (Kilpua et al. (2011) the interplanetary counterparts of these coronal mass ejections (CMEs), called interplanetary coronal mass ejections (ICMEs) encounter Earth. When they do, they may cause geomagnetic storms of more or less intensity. Before humanity started using magnetic stones as navigational aids in the middle ages, human technology had nothing to do with magnetic fields or currents. Geomagnetic storms prior to this did not have any effect on human life, other than making humans wonder in awe at the moving colours in the sky. As hinted by the progressively more inconvenient accounts in our three examples, it is the progress of human technology that makes the impact of geomagnetic storms become more and more potentially damaging (Baker et al. (2004), Eastwood et al. (2017)).

---

[1] I may have invented the context for literary purposes, but I did not invent the actual conversation, reported in the New York Times shortly after it took place (Anonymous (1859)). These events took place during the “Carrington event”, which is believed to be the strongest geomagnetic storm ever recorded. To learn more about the Carrington event, the reader is invited to look up the original article Carrington (1859), as well as a good review Muller (2014) and the references provided therein.

[2] Remember, 1989 is still the Cold War...

Earth generates its own magnetic field. And this is good news for life on our planet. It deviates the solar wind flow before it can have much effect on our atmosphere, which allows for at least two essential things: First, Earth gets to keep its atmosphere, which allows plants to breath and grow, and animals to breath and eat plants. Second, the upper layer of the atmosphere can act as a shield against energetic photons (Ratner and Walker (1972)) and particles (Juckett (2007)), a shield without which life as we know it would be severely handicapped.

On the contrary, other bodies such as Mars, Mercury, and our moon have such a weak magnetic field that the solar wind – especially during highly energetic events like encounters with interplanetary coronal mass ejections – can reach very low altitudes, or even touch the ground (constantly on the Moon, occasionally on Mercury). For example, it is believed that Mars' atmosphere is continuously swept away by the solar wind, leaving the planet with a thin atmosphere unfit to sustain life (Jakosky et al. (2018)).

Geomagnetic storms can disturb the field on Earth's surface, but these disturbances are not very large (a few dozen to a few hundred nanoteslas, compared to Earth's surface magnetic field which measures between $25 \cdot 10^3$ nT and $65 \cdot 10^3$ nT depending on location). However, with time passing, technological progress and the infrequency of strong geomagnetic storms, we have learned, unknowingly perhaps, to rely on Earth's magnetic field's stability. What happened in 1859, during the Carrington event, was that through Maxwell-Faraday's $\nabla \times E = -\frac{\partial B}{\partial t}$ disturbances to this magnetic field had unexpected effects on systems which used finely tuned electric fields and currents. At that time too, even if impressive, the geomagnetic storm (the biggest ever recorded) did not cause unruly damage, simply because it had not much to damage. As foreshadowed by the 1989 storm that left the whole region of Quebec without electricity for nine hours (Boteler (2019)), the picture is progressively changing owing to the fact that we increasingly rely on large scale technologies using electricity and that the systems on which society depends become evermore interdependent (Baker et al. (2004), Eastwood et al. (2017), Pulkkinen et al. (2017)). Nowadays, some governments (*e.g.* Progressive Management (2015), Jonas and McCarron (2016)) and agencies truly fear a new "Carrington event", because a large-scale power-cut would leave most usual operations stranded and difficult to get back in order. Imagine the impact of urban transports without electricity, and petrol pumps out of order.

Research efforts intended at understanding the whole chain of events from instabilities below the surface of the Sun to geomagnetic storms are increasing, as we try to predict the apparition of magnetic flux tubes at the surface of the Sun, whether or not they will lead to coronal mass ejections or even if coronal mass ejection can be formed another way, how interplanetary coronal mass ejections evolve during their journey through the interplanetary medium, and the impact they have on Earth's geomagnetic environment.

A laboratory for Astrophysics

Of course, not everything is doom and gloom, and heliophysicists (physicists who study the Sun, and its interaction with the contents of the heliosphere[3]) are not apocalypse announcers more than anyone else. These “pressing” questions of Space Weather are also rarely the reason they chose their field of study, apart from perhaps having the feeling that they are somehow working on “real-world” problems.

Most heliophysicists simply find a real beauty in the idea of “living with a star” (Schrijver and Schrijver (2015)), the poetic colouring of the auroras, and the scientific satisfaction that can be provided by the existence of satellite data. Indeed; heliophysics is the only branch of astrophysics that has access to *in-situ* data of its objects of study, while the rest of astrophysicists have to make do with only information transported by light and highly energetic particles. This is the main reason why the history of plasma physics is so tied to heliophysics even though plasmas can be found pretty much everywhere in the universe. Much of the interesting phenomena that could potentially explain signals from accreting flows around black holes in active nuclei galaxies, the physics of pulsar magnetospheres, the tantalising shapes of the crab nebula, and so many other fascinating astrophysical curiosities, are also present under one form or another in heliophysics. These phenomena range from collisionless plasma effects to turbulence, passing by magnetic reconnection and so many others. Although the regimes (namely the role played by radiation, relativistic or quantum effects) may differ greatly from one astrophysical scenario to the next (*e.g.* Uzdensky (2019)), the basic understanding and rigorous testing of plasma theories can more confidently be attained with heliophysical plasmas, as *in-situ* data strongly constrain the most imaginative theories (Fälthammar et al. (1978)).

---

[3] The heliosphere is the bubble carved out of the interstellar medium up to which the solar wind has an impact.

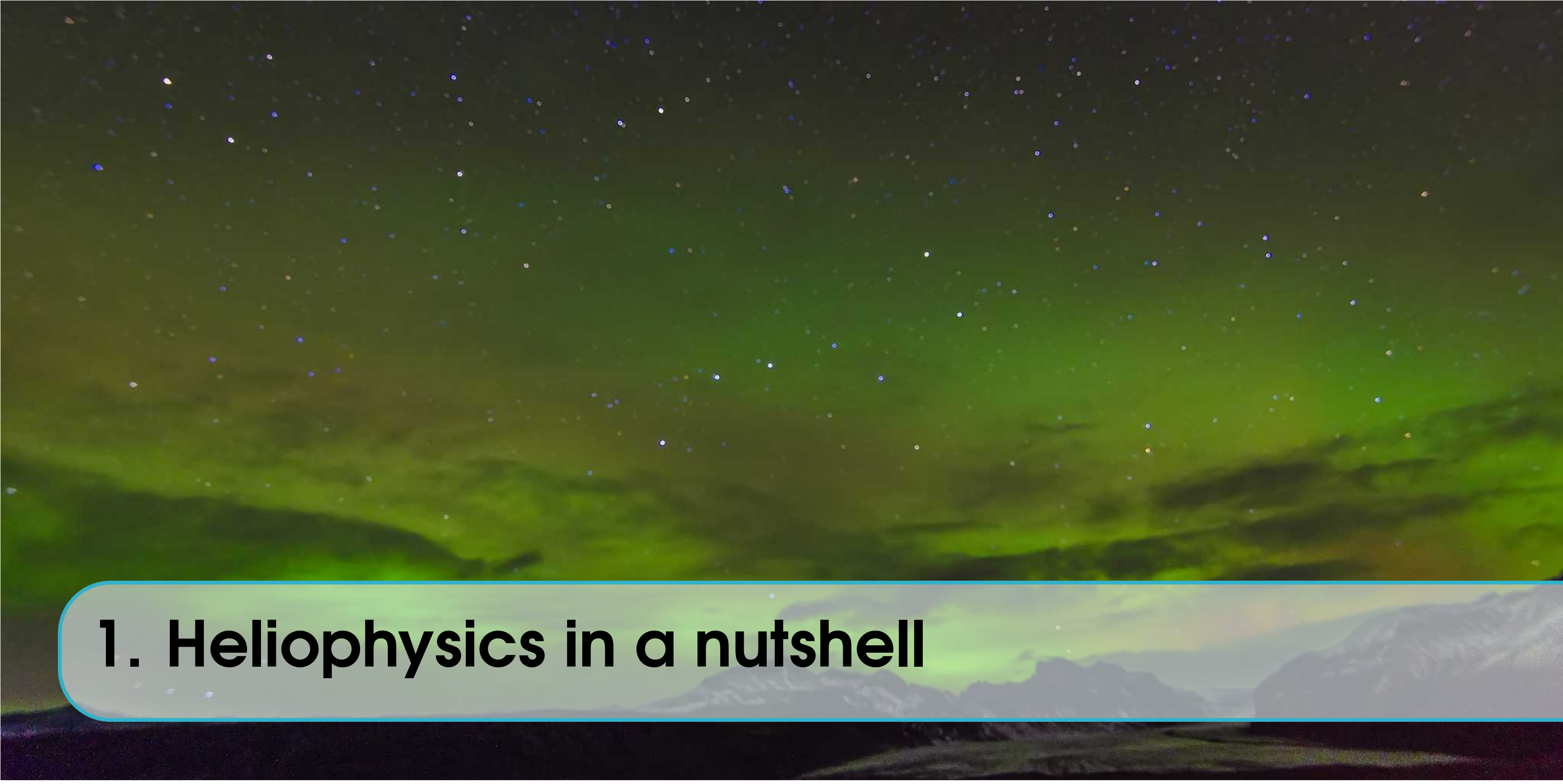

1. Heliophysics in a nutshell

> **Note:** This chapter introduces in thick strokes the essential vocabulary, concepts and equations that underlie the work presented in the rest of this thesis. The emphasis is put on building intuition and familiarity with these tools rather than on their rigorous derivation.

Contents

1.1 Introduction to the solar wind

First, let us define the solar wind, which is the medium constantly blown by the sun and in which all the planets of the solar system bathe. In subsection 1.1.1 we will explain, using a simple hydrodynamic model, how the solar wind is pushed away from the sun, and why it is necessarily supersonic. This last point will be, later on (subsection 1.3.1), shown to be central in this thesis because it is partly responsible for the structure of the geomagnetic environment. In subsection 1.1.2 we will show that, rather than using a simple hydrodynamic model, the solar wind is better described through plasma physics.

1.1.1 The supersonic solar wind: the Parker model

In 1951, Bierman (Biermann (1951)), observing comets, saw that they had two tails, one trailing the comet in the direction of motion, and the other radially pointing away from the sun. From this, he conjectured the possibility of a stream of particles constantly flowing out of the sun. This stream of particles is nowadays known as the solar wind. Parker (1958) then made the following calculations showing that not only the existence of the solar wind was understandable using relatively simple fluid mechanics, but also that it would necessarily be supersonic. Following Parker's steps, we will describe the solar wind as a neutral gas rather than a plasma; plasmas will be introduced in the next section subsection 1.1.2.

Parker's approach to describe the sun's atmosphere –the Heliosphere– makes use of the following hypotheses:

- The Heliosphere is treated as a neutral gas
- Steady-state, so nothing is time-dependent
- Spherical geometry, so every quantity depends only on r

We make use of the continuity equation, Euler's equation of motion for a neutral fluid and the law of perfect gases:

$$\begin{aligned} \text{Continuity equation:} \quad & \nabla \cdot (\rho \boldsymbol{u}) = 0 \\ \text{Equation of motion:} \quad & \rho(\boldsymbol{u} \cdot \boldsymbol{\nabla u})\boldsymbol{u} = -\mathscr{G}\frac{\rho M}{r^2}\boldsymbol{e_r} - \boldsymbol{\nabla} P \\ \text{Definition of the pressure:} \quad & P = \rho k_B T / \mu \end{aligned} \tag{1.1}$$

ρ and $\boldsymbol{u}$ are, respectively, the bulk flow's density and velocity. $\boldsymbol{e_r}$ is the radial direction pointing outward from the Sun. P is the thermal pressure, T the temperature and μ is the average mass of particles.

Using the spherical expressions of divergence ($\frac{1}{r^2}\nabla \cdot \boldsymbol{A} = \frac{\mathrm{d}r^2\boldsymbol{A}}{\mathrm{d}r}$) and gradient $\nabla f = \frac{\mathrm{d}f}{\mathrm{d}r}$, we obtain:

$$\begin{aligned} \text{Continuity equation:} \quad & \frac{\mathrm{d}(r^2 \rho u)}{\mathrm{d}r} = 0 \\ \text{Equation of motion:} \quad & \rho\left(u\frac{\mathrm{d}u}{\mathrm{d}r}\right) = -\mathscr{G}\frac{\rho M}{r^2} - \frac{1}{\mu}\frac{\mathrm{d}\rho k_B T}{\mathrm{d}r} \end{aligned} \tag{1.2}$$

We now make an important hypothesis: the temperature T is independent of the heliocentric distance r. This hypothesis was mathematically and observationally legitimated by Chapman and

Zirin (1957). Simply put, Chapman showed that due to thermal conduction, something as hot as the solar corona could not see its temperature drop too drastically with the heliocentric distance r, provided no brutal changes in density. The paper concludes with a temperature following roughly $T \propto r^{-2/7}$. Parker took the liberty to assume T constant because it simplifies the calculations vastly, and because the decrease in T is so much slower that the other quantities'. We can now write:

$$\begin{aligned} \text{Continuity equation:} \quad & 2r\rho u + r^2\rho\frac{\mathrm{d}u}{\mathrm{d}r} + r^2\frac{\mathrm{d}\rho}{\mathrm{d}r}u = 0 \\ \text{Equation of motion:} \quad & \rho\left(u\frac{\mathrm{d}u}{\mathrm{d}r}\right) = -\mathscr{G}\frac{\rho M}{r^2} - \frac{k_BT}{\mu}\frac{\mathrm{d}\rho}{\mathrm{d}r} \end{aligned} \tag{1.3}$$

This allows us to use the continuity equation to eliminate the density ρ from the equation of motion:

$$\begin{aligned} \text{Continuity equation:} \quad & \frac{1}{\rho}\frac{\mathrm{d}\rho}{\mathrm{d}r} = -\frac{2}{r} - \frac{1}{u}\frac{\mathrm{d}u}{\mathrm{d}r} \\ \text{Equation of motion:} \quad & u\frac{\mathrm{d}u}{\mathrm{d}r} = -\frac{\mathscr{G}M}{r^2} - \frac{k_BT}{\mu}\left\{-\frac{2}{r} - \frac{1}{u}\frac{\mathrm{d}u}{\mathrm{d}r}\right\} \end{aligned} \tag{1.4}$$

From which we obtain the famous equation controlling the velocity of the solar wind:

$$\boxed{\left\{u^2 - \frac{k_BT}{\mu}\right\}\frac{1}{u}\frac{\mathrm{d}u}{\mathrm{d}r} = -\frac{\mathscr{G}M}{r^2} + \frac{2k_BT}{\mu r}} \tag{1.5}$$

The right hand-side of this equation shows the competition between gravitation and thermal pressure in governing the motion of the fluid. From this equation emerges naturally a critical distance $r_c = \mathscr{G}M\mu/k_BT$, usually called the sonic point. With $M = 1.989 \cdot 10^{30}$ kg, $T \simeq 2 \cdot 10^6 K$, and $\mu \simeq m_p/2$ (with $m_p \simeq 1.67 \cdot 10^{-27} kg$) we find that r_c is about 6 solar radii.

The most interesting part of this equation stands on the left hand-side, with the term $\left\{u^2 - \frac{k_BT}{\mu}\right\}$ which shows the particular role played by the sound speed[1]: $C_S = \sqrt{\frac{k_BT}{\mu}}$. This equation mathematically allows for five classes of solutions. Figure 1.1 shows these five classes of solutions with: the fluid velocity normalised to the sound speed on the y-axis, and the radius normalised to the normalised to the critical radius r_c, which corresponds to the sonic point. Out of these solutions, we can quickly discard classes I and II, which are double-valued. Solution III asks for an already highly supersonic wind leaving directly from the sun's surface, which does not match any observation. Solution IV, called a solar breeze, poses a slightly subtler problem: without going into the detail of the proof, it comes from the fact that u tends to zero for large radii, which, through the equation of conservation and the relation between r and u, makes it so that ρ would tend toward a finite value at infinity, which is nonphysical, as it would mean that the solar wind expands in the entire universe. The right solution, then, is the quite peculiar solution V, which represents a slow solar wind starting from the surface of the sun, reaching the sonic speed at exactly the critical point r_c, and which then continues to accelerate and stays supersonic.

The historical importance of Parker's equation is to show that not only a solar wind would have to be supersonic – which has indeed been confirmed by Neugebauer and Snyder (1962) – but also that its existence and supersonic nature could be inferred from simple physical laws.

---

[1] In accordance with Parker's isothermal hypothesis, this is the isothermal sound speed.

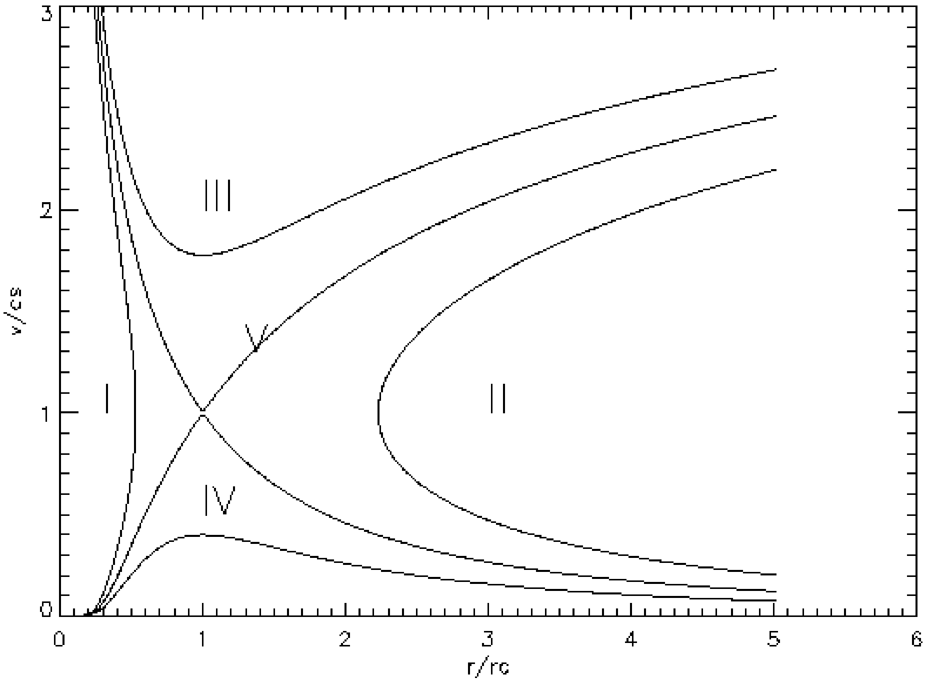

Figure 1.1: *Classes of solutions for the solar wind. y-axis: fluid velocity normalised to the sound speed c_s. x-axis: heliocentric distance, normalised to the critical radius r_c, which corresponds to the sonic point.*

1.1.2 The solar wind: a plasma

In the previous calculation, we ignored, for simplicity, the fact that the solar wind is a collection of charged particles. In reality, it is a *plasma* composed mostly of ionised hydrogen, and contains about 4% of Helium and trace amounts of heavier ions (Wurz (2005)).

An ensemble of particles is called a plasma when three (or sometimes four) criteria are fulfilled, which ensure that the particles exhibit collective behaviour. Let us define these three criteria, and test the solar wind against them.

Debye shielding, Debye sphere

The Debye length λ_D tells us how far the electric field of a charged particle can be felt by other particles. A positively charged ion, for example, tends to attract electrons. The temperature T, on the other hand, tends to pull the electrons away from specific locations, and in particular, from ions. The Debye length can be expressed as:

$$\lambda_D = \sqrt{\frac{\varepsilon_0 k_B T}{n_e e^2}} \tag{1.6}$$

The *first criterion* to define plasma is that the system considered should have a typical scale L larger than λ_D. Without this, the behaviour of particles would be dominated by the electrostatic field of the other particles:

$$\textit{First criterion:} \quad L \gg \lambda_D \tag{1.7}$$

In the solar wind at 1AU, with $n_e \sim 5 \cdot 10^6$ m^{-3} and $T \sim 1.2 \cdot 10^5$ K, we have $\lambda_D \sim 11$ m, therefore we can consider the solar wind as a plasma as long as we consider scales larger than roughly 11 m.

A *second criterion* demands that the number of electrons inside of a Debye sphere is large:

$$\textit{Second criterion:} \quad N_D = \frac{4}{3}\pi n_e \lambda_D^3 \gg 1 \tag{1.8}$$

For the solar wind, we have $N_D^{SW} \sim 2.5 \cdot 10^{10}$.

Plasma frequency

The *third criterion* is a comparison between the plasma frequency ω_p, and the typical time between collisions τ, which ensures that collisions do not interfere with the collective motion responsible for ensuring quasi-neutrality:

$$\textit{Third criterion:} \quad \omega_p \tau \gg 1 \tag{1.9}$$

The plasma frequency is the rate at which electrons oscillate around the ions when recovering from a disturbance to the charge neutrality and is expressed as:

$$\omega_p = \left(\frac{n_e e^2}{m_e \varepsilon_0} \right)^{1/2} \tag{1.10}$$

The electron/ion collision frequency can be roughly estimated (e.g. Rax (2005), where we used Rutherford diffusion, relevant for a fully ionised plasma and made the hypothesis of a Maxwellian distribution) as:

$$1/\tau = 1.2 \times 10^{-4} n_e T_e^{-3/2} \tag{1.11}$$

Qualitatively, we can understand this formula as: the faster an electron is, the less time it has to interact with an ion's electric field, and therefore, the less its motion can be modified by this interaction. The less dense the plasma is, the less likely collisions are to happen.

This leads to $\omega_p \tau \sim 10^{10}$.

Having $\omega_p \tau \gg 1$ insures that the collective motions of particles dominate over collisions.

A *fourth criterion*, sometimes omitted because it is somewhat a consequence of the previous ones, is that the plasma must be neutral at large scales. It is the criterion of quasi-neutrality: $n_e \simeq Z \cdot n_i$, where n_i is the ion density, and Z the atomic number (*e.g.* $Z = 1$ for a simple model of the solar wind, where we consider that it is composed only of protons and electrons).

Conclusion

The solar wind, with its high temperature and low density, is clearly a plasma. Debye spheres in the solar wind have roughly a 10 m radius, and contain several billions of charged particles. Collisions are extremely rare, on top of being rather inefficient, which ensures that the collective motions of particles in the solar wind are not disrupted by collisions.

For the sake of the argument, let us try and apply these criteria to Earth's atmosphere, by doing a thought experiment: Let us imagine that through some process (impossible of course), a part of the atmosphere gets ionised (say, one electron per molecule) without any change to the temperature or density. This would give us $n_e = 3 \cdot 10^{25}\mathrm{m}^{-3}$ and $T_e = 300\mathrm{K}$. Therefore, we would have $\lambda_D \sim 2\text{Å}$ (roughly the size of an atom), $N_D \sim 10^{-3}$ (this makes sense, since N_2 molecules are much bigger than a single atom). The Debye sphere would be smaller than the size of the ionised molecules and contain on average less than one electron. In other words, our atmosphere is much too dense and cold to be a plasma. It is impossible to compute the third criterion because at such a density and low temperature, the electrons and ions would already be "collided".

It is said that, as long as we ignore dark matter and dark energy, more than 99% of the Universe is made of plasma. Both the second and third (with Rutherford diffusion) aforementioned criteria ask for a large $\frac{T^{3/2}}{n_e^{1/2}}$. Most of the Universe being either extremely hot (ex: stars) or extremely rarefied (ex: stellar winds, interstellar medium), we now see why, most of it is indeed made of plasma.

1.2 Some phenomena in the solar wind: a first approach

We have just shown that the solar wind is a plasma, which therefore, by definition, exhibits collective behaviour. Let us then start this section by quoting one of the most revered textbooks on plasma physics, Chen (1974): “Because of collective behavior[2], a plasma does not tend to conform to external influences; rather, it often behaves as if it had a mind of its own”. We now have the opportunity to both provide a glimpse of how rich the physics of the solar wind can be, and to introduce essential concepts that will be used in the rest of this manuscript. To do so, we will introduce the simplest (yet vastly rich) description a plasma: Magnetohydrdynamics (subsection 1.2.1) and discuss its validity as well as some consequences. The rest of this section will be used to introduce the concept of turbulence (1.2.2) which we will reuse in chapters 3 and 4; some simple waves that can exist in a plasma (1.2.3) and in particular their speeds, which are extremely useful as a reference for comparing the velocity of flows as for example, in the case of shocks (1.2.5), which are one of the main topics of this manuscript.

There exist a few theoretical frameworks used to describe plasmas, which fundamentally all derive from the interplay between Newton’s second law applied to a large number of particles and Maxwell equations, where the source terms (charge density ρ_c, current density $\boldsymbol{j}$) come from the said particles.

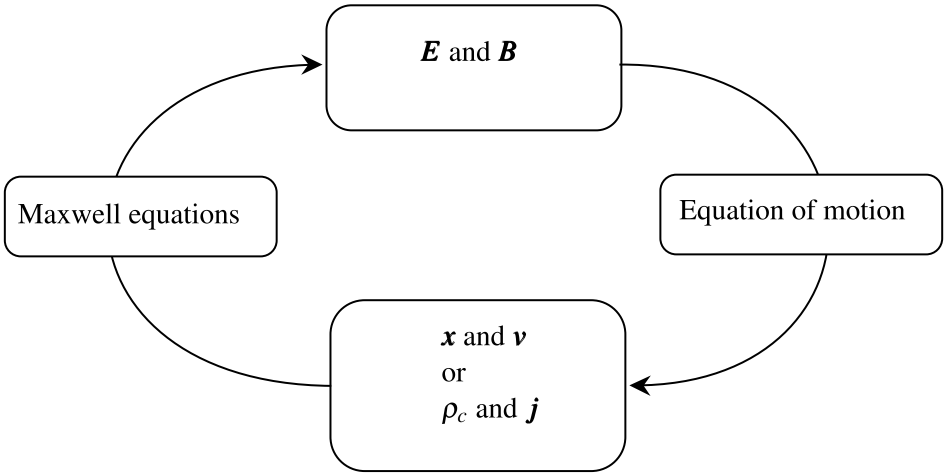

Indeed, at the most fundamental level, we can picture a plasma as a feedback loop between an ensemble of charged particles (each with a position $\boldsymbol{x}$ and velocity $\boldsymbol{v}$) obeying the laws of motion, evolving in an electromagnetic field (electric field $\boldsymbol{E}$ and magnetic field $\boldsymbol{B}$) which is itself dependant on the positions (volumic charges ρ) and speeds (currents $\boldsymbol{j}$) of the said particles through the Maxwell equations.

1.2.1 Ideal Magnetohydrodynamics

The most commonly used fluid description of a plasma is called magnetohydrodynamic, or MHD. From it, we can straightforwardly introduce important plasma behaviours and definitions. It is useful to think about the equations of MHD (although this is not the rigorous point of view adopted in most

---

[2] Francis Chen uses American English, I use British English.

introductory textbooks) as the equations one would use to describe a fluid: Continuity equation, Euler equation, plus a state equation, as well as a couple useful equations to describe the electromagnetic field (not all of the Maxwell arsenal is needed). The particularity here is that in Euler equation we find a force due to the presence of a magnetic field.

For the fluid part:

$$\begin{aligned} \text{Continuity equation:} \quad & \frac{\partial \rho}{\partial t} + \boldsymbol{\nabla} \cdot (\rho \boldsymbol{u}) = 0 \\ \text{Equation of motion:} \quad & \rho \left(\frac{\partial \boldsymbol{u}}{\partial t} + (\boldsymbol{u} \cdot \boldsymbol{\nabla} \boldsymbol{u}) \boldsymbol{u} \right) = -\boldsymbol{\nabla} P + \boldsymbol{j} \times \boldsymbol{B} \\ \text{Equation of energy:} \quad & \frac{\mathrm{d}}{\mathrm{d}t} \left(\frac{P}{\rho^{\gamma}} \right) = 0 \end{aligned} \tag{1.12}$$

ρ and $\boldsymbol{u}$ are, respectively, the bulk flow's density and velocity. P is the thermal pressure, $\boldsymbol{j}$ is the electric current and $\boldsymbol{B}$ the magnetic field. The $\boldsymbol{j} \times \boldsymbol{B}$ term is called the Lorentz force. γ is the polytropic index of the fluid.

For the magnetic field part:

$$\begin{aligned} \text{Induction equation (Or ideal Maxwell-Faraday):} \quad & \frac{\partial \boldsymbol{B}}{\partial t} = \boldsymbol{\nabla} \times (\boldsymbol{u} \times \boldsymbol{B}) \\ \text{Absence of magnetic monopoles:} \quad & \boldsymbol{\nabla} \cdot \boldsymbol{B} = 0 \\ \text{Maxwell-Ampère (non relativistic):} \quad & \boldsymbol{j} = \frac{\boldsymbol{\nabla} \times \boldsymbol{B}}{\mu_0} \end{aligned} \tag{1.13}$$

μ_0 is the magnetic permeability of free space.

Ohm's law and the induction equation

In order to obtain the equations of ideal magnetohydrodynamics, different routes can be taken: the fluid equations can for example be obtained as the first few moments of the Vlasov equation, which is an exact statistical description of a plasma to which we had a closure equation; or directly through a fluid approach, in a manner similar to the one commonly used to introduce the Navier-Stokes equation of fluid dynamics. No matter which route is taken to derive the equations of ideal magnetohydrodynamics, numerous approximations have to be made. These are beyond the scope of this thesis (see *e.g.* Boyd and Sanderson (2003)).

Here, we will limit ourselves to the discussion of Ohm's law, which will be used later in this manuscript, and which is used to write the induction equation in the previous paragraph.

Ohm's law derives from writing the expression of the equation of motion of the electron fluid:

$$m_e n_e \frac{\mathrm{D}\boldsymbol{u}_e}{\mathrm{D}t} = -e n_e (\boldsymbol{E} + \boldsymbol{u}_e \times \boldsymbol{B}) - \boldsymbol{\nabla} P_e - \frac{n_e m_e}{\tau} (\boldsymbol{u}_e - \boldsymbol{u}_i) \tag{1.14}$$

In this equation, the $\frac{\mathrm{D}}{\mathrm{D}t}$ notation represents the Lagragian time derivative, $-e n_e (\boldsymbol{E} + \boldsymbol{u}_e \times \boldsymbol{B})$ is the Lorentz force's effect on the electron fluid, $-\boldsymbol{\nabla} P_e$ the role of the electron pressure, and

$-\frac{n_e m_e}{\tau}(\boldsymbol{u}_e - \boldsymbol{u}_i)$ is one possible expression for the interaction between the ion/electron fluids, in this case representing a drag from the ions on the electrons.

In order to obtain the simplest possible form for Ohm's law which is used in ideal MHD, we make the following hypotheses:

- we neglect the inertia of electrons
- we suppose that the electrons follow the ions perfectly, therefore we can use the single bulk velocity of MHD $\boldsymbol{u}$ and write $\boldsymbol{u}_e = \boldsymbol{u}$
- we neglect the effect of electron pressure
- we neglect the ions drag

We can now write:

$$\boldsymbol{E} = -\boldsymbol{u} \times \boldsymbol{B} \tag{1.15}$$

This is sometimes summarised as stating that the electric field is simply the non-relativistic electric field in the frame of the fluid.

Once equation (1.15) is obtained, we can inject it in Maxwell-Faraday's equation $\frac{\partial \boldsymbol{B}}{\partial t} = -\boldsymbol{\nabla} \times \boldsymbol{E}$, and obtain the induction equation for ideal MHD:

$$\frac{\partial \boldsymbol{B}}{\partial t} = \boldsymbol{\nabla} \times (\boldsymbol{u} \times \boldsymbol{B}) \tag{1.16}$$

On the validity of using magnetohydrodynamics for studying the solar wind

The equations of MHD describe the motion of a fluid. In order to do so, we need to define a mesoscopic fluid element of volume $\delta\tau$ which will keep its identity; which in hydrodynamics is thanks to collisions. If we are to count on collisions, we would therefore need to have:

$$\lambda_c < (\delta\tau)^{1/3} \ll L \tag{1.17}$$

$\lambda_c = v_{th}\tau$ is the mean free path of particles. In the solar wind, with $T \sim 1.2 \cdot 10^5$ K, we have $v_{the} = \sqrt{3k_B T/m_e}$, and therefore $\lambda_c \sim 1$A.U.

This highlights one of the problems with MHD: a properly defined fluid element (in the sense of hydrodynamics) should be a sphere of diameter of the order of magnitude of the Sun-Earth distance.

This point of view might not be sufficient, however, for at least two reasons. The first is pragmatical: many MHD studies of the solar wind over the past decades have taught and continue to teach us a tremendous amount of relevant things about the physics of the solar wind. The second is physical: we do not necessarily need collisions so that the fluid elements keep their identity, as the magnetic field itself can act as a localising agent (see next paragraph).

This is one of the difficulties and beauties of plasma physics, some theories that are more correct are just too impractical, and the somewhat abusive use of simpler theories can be a great way of obtaining interesting results. Being aware of the limitations of our theoretical framework and tools is, however, good practice.

The “frozen-in” theorem

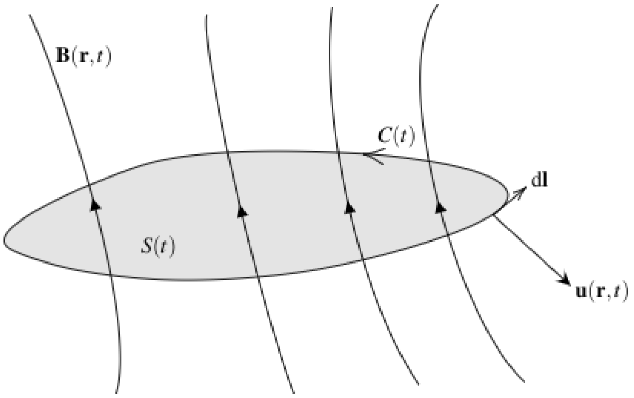

Figure 1.2: *Magnetic flux in motion*

Let us consider the temporal evolution of the magnetic flux through a surface $S(t)$ moving with the fluid: $\iint_{S(t)} \boldsymbol{B}(\boldsymbol{r},t) d\boldsymbol{S}$. This situation is represented on figure 1.2.

$$\frac{\mathrm{d}}{\mathrm{d}t} \iint_{S(t)} \boldsymbol{B}(\boldsymbol{r},t) d\boldsymbol{S} = \iint_S \frac{\partial \boldsymbol{B}}{\partial t} d\boldsymbol{S} + \oint_C \boldsymbol{B} \cdot \boldsymbol{u} \times d\boldsymbol{l} \tag{1.18}$$

The first term on the right hand-side represents the variation of the magnetic flux due to the change of $\boldsymbol{B}$ while the last term on the right hand-side represents the variation of the flux due to the change of $S(t)$ as it follows the fluid’s motion. Using the Stokes theorem, and some vector algebra, this becomes:

$$\frac{\mathrm{d}}{\mathrm{d}t} \iint_{S(t)} \boldsymbol{B}(\boldsymbol{r},t) d\boldsymbol{S} = \iint_S \left(\frac{\partial \boldsymbol{B}}{\partial t} - \boldsymbol{\nabla} \times (\boldsymbol{u} \times \boldsymbol{B}) \right) d\boldsymbol{S} \tag{1.19}$$

In the right hand-side of the equation, we recognise the terms from the induction equation (see equation (1.13)). The right hand-side of the equation is therefore zero, which allows us to conclude that the magnetic flux through a surface moving with the fluid is conserved. This is known as the frozen-in theorem. This theorem gives a physical reality to magnetic field lines by stating that the magnetic field can be treated as if “frozen” into the plasma; and conversely, the fluid is forced to follow the motions of the magnetic field lines.

1.2.2 Turbulence in the solar wind

When free energy is injected at large scales in a fluid where non-linear forces are dominant, the energy can cascade down to small scales. In the solar wind, this means that we can find waves at all frequencies. In the context of this manuscript, this matters because some of these frequencies are thought to have an influence on the coupling between the solar wind and Earth’s geomagnetic environment (*e.g.* Hynönen et al. (2020)). The study of turbulence is the study of the transfer of energy from scale to scale. It is often associated with the image of eddies (see figure 1.3).

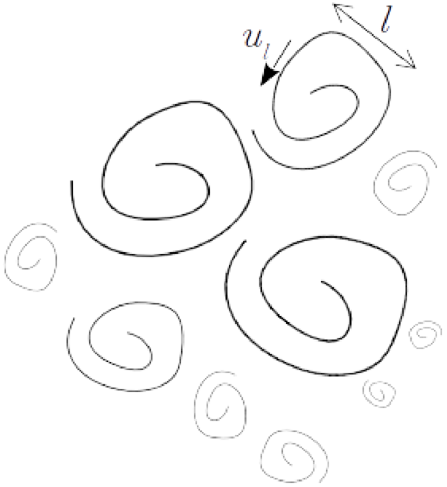

Figure 1.3: *Eddies: smaller and smaller patterns are generated as energy cascades down from the larger to the smaller scales*

Kolmogorov spectrum

Let us call ε the rate of transfer of energy from one scale to another. We make the assumption that ε is independent of the scale itself. A phenomenological approach to estimate ε is the following (see *e.g.* Galtier (2016)):

$$\varepsilon \sim \frac{u_l^2}{\tau_{tr}} \sim \frac{u_l^2}{l/u_l} \sim \frac{u_l^3}{l} \tag{1.20}$$

First, we assimilated the energy of an eddy of scale l as its kinetic energy u_l^2, with u_l the velocity of the fluid (for simplicity, we considered that the kinetic energy dominates, which is not always the case in the solar wind). Then we introduced a time of energy transfer τ_{tr}, that we estimated as the time it takes for the eddy to rotate on itself: $\tau_{tr} \sim l/u_l$.

Now, we want to look at the spectrum of energy in terms of the wave number $k = 2\pi/l$, $E(k)$. We can estimate that $E(k)k \sim u_l^2$, which, using the previous equation (1.20) leads to:

$$E(k)k \sim u_l^2 \sim (\varepsilon l)^{2/3} \sim \varepsilon^{2/3} k^{-2/3} \tag{1.21}$$

And we can conclude with the famous[3]:

$$E(k) \propto k^{-5/3} \tag{1.22}$$

Coupling between scales and non-linearity

In order to have coupling between different scales, we need non-linear terms in the equations that govern the evolution of the fluid. In the MHD equations above, one can find three non-linear terms

---

[3] This result can be rigorously demonstrated (*e.g.* Kolmogorov (1941); Galtier (2016)).

(five if we also think about ρ): $(\boldsymbol{u}\cdot\boldsymbol{\nabla})\boldsymbol{u}$ and $\boldsymbol{j}\times\boldsymbol{B}$ in the equation of motion, and $\boldsymbol{u}\times\boldsymbol{B}$ in the induction equation. It is pretty straightforward to see that these terms can allow for some energy transfer from one scale to another:

Let us imagine that the magnetic field and velocity field can both be expressed as monochromatic functions of space and time along the Sun-Earth axis x: $u = u_0\cos(\omega_1 t + k_1 x)$, and $B = B_0\cos(\omega_2 t + k_2 x + \phi)$, then a product between u and B will yield a term of higher frequencies, containing $\cos((\omega_1+\omega_2)t + (k_1+k_2)x)$. Through the motion and induction equations, these can elicit higher frequencies to appear in both u and B. These changes can themselves lead to ever higher frequencies.

Reynolds number in the solar wind

A simple approach to convince ourselves that the solar wind is indeed a likely place for turbulence to develop is to estimate the Reynolds number $R = UL/\nu$. Let us quite naively estimate U to be the average speed of the solar wind of $4\cdot10^2$ km/s, and L the Sun-Earth distance 1 AU $\sim 1.5\cdot10^8$ km. For ν we use an estimation of the viscosity due to Coulomb-scattering by Braginskii (Borovsky and Gary (2009)), $\nu_{Brag} = (3/10)r_L^2/\tau_{ii}$, where r_L is the ion gyroradius and τ_{ii} the ion-ion collision time. This yields $\nu_{Brag} = 3.8\cdot10^2\ \mathrm{m}^2/\mathrm{s}$. Finally, this leads to $R\sim10^{14}$. This shows that non-linear terms dominate in the solar wind, making the transition to turbulence possible.

> **Note:** This very high Reynolds number should not be taken at face value, and to know more about the "real" Reynolds number of the solar wind, we direct the interested reader towards the extremely clear and informative Borovsky and Gary (2009).

1.2.3 Characteristic speeds of MHD waves in the solar wind

The solar wind contains three main different types of MHD waves: Alfvén waves, and the fast and slow MHD waves (Bruno and Carbone (2013)). For the purpose of this introduction, we simply are interested in defining the characteristic velocities of the simplest MHD waves (we follow the approach of Bittencourt (2004)): the shear (transverse) Alfvén waves and two longitudinal magnetosonic waves: those propagating in the direction of the magnetic field, and those propagating in the direction perpendicular to it. Those are only limit cases; the description of the propagation of waves in any direction are beyond the scope of this thesis, and we refer the reader to introductory textbooks (*e.g.* Boyd and Sanderson (2003)).

> **Note:** By longitudinal, we mean that the fluid perturbation (*e.g.* the velocity perturbation) is parallel to the wave propagation. By transverse, we mean that the perturbation is perpendicular to the propagation.

Shear Alfvén waves propagating along the magnetic field lines

Shear Alfvén waves propagating along the magnetic field lines (sketched on figure 1.4) correspond to the propagation of shears of the magnetic field, due to the natural tendency of magnetic field lines to stay straight, and propagate at a velocity $V_A = \sqrt{\frac{B^2}{\rho\mu_0}}$ (called the Alfvén velocity); which correspond to the square root of the ratio between magnetic tension and plasma density. These waves are transverse: they correspond to variations of velocity and magnetic field that are transverse to the mean magnetic field.

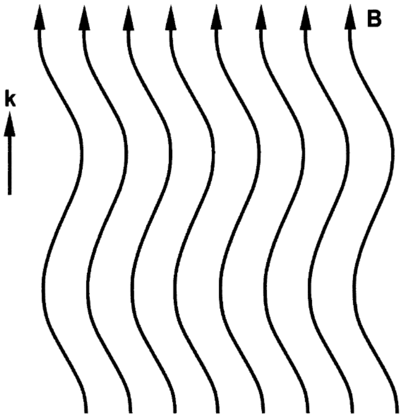

Figure 1.4: *Drawing of shear Alfvén waves,* ***from Bittencourt (2004)****. Shear Alfvén waves propagate along the magnetic field lines, and the fluctuations of the velocity and magnetic field are transverse to them.*

Longitudinal magnetosonic waves propagating along the magnetic field lines

Along the magnetic field line, there is no force due to the magnetic field, and therefore only the gas pressure term plays a role in the equation of motion. Therefore, longitudinal magnetosonic waves propagating along the magnetic field lines (sketched on figure 1.5) will behave just like sound waves in a non-magnetic fluid.

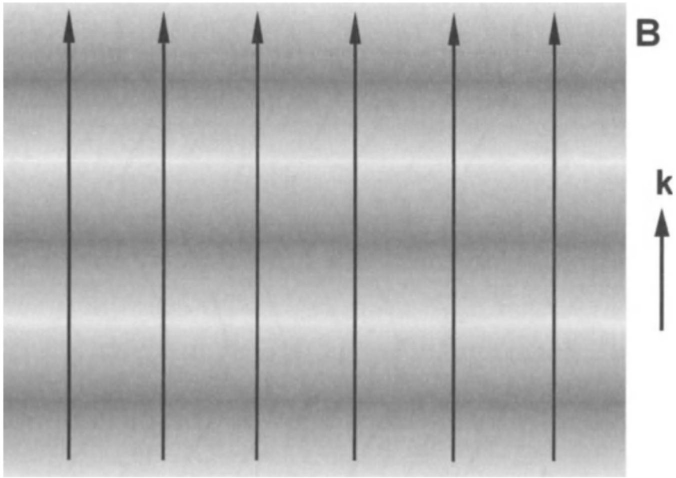

Figure 1.5: *Drawing of longitudinal sound waves,* ***from Bittencourt (2004)****. Longitudinal sound waves propagate along the magnetic field lines, and the fluctuations of velocity and density are also parallel to them.*

The sound speed is the name given to the ratio $\frac{\mathrm{d}p}{\mathrm{d}\rho}$:

$$\mathrm{d}p = C_S^2 \mathrm{d}\rho \tag{1.23}$$

In order to obtain the value of C_S, one can simply use a logarithmic derivation of the adiabatic equation used to “close” the system of MHD equations, given on page 13, $p\rho^{-\gamma} = Constant$:

$$\frac{\mathrm{d}p}{p} - \gamma \frac{\mathrm{d}\rho}{\rho} = 0 \tag{1.24}$$

Using the law of perfect gases $p = \frac{\rho k_B T}{m}$, one obtains the sound speed as:

$$C_S = \sqrt{\frac{\gamma k_B T}{m}} \tag{1.25}$$

Longitudinal magnetosonic waves propagating perpendicularly to the magnetic field lines

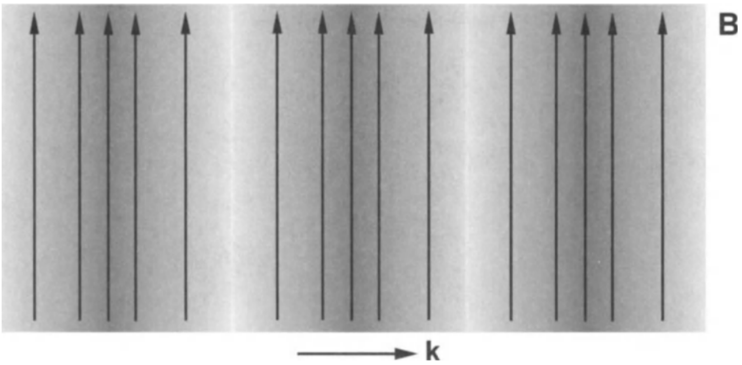

Figure 1.6: *Drawing of longitudinal magnetosonic waves, from Bittencourt (2004). Longitudinal magnetosonic waves propagate perpendicularly to the magnetic field lines, and the perturbations to the velocity, magnetic field and density are also perpendicular to them.*

V_{MS}, the speed of the magnetosonic waves that propagate perpendicularly to the mean magnetic field (see sketch on figure 1.6) can be obtained in much the same way as the sound speed; by taking into account the magnetic pressure on top of the thermal pressure:

$$\begin{aligned} &\mathrm{d}\left(p + \frac{B^2}{2\mu_0}\right) = V_{\mathrm{MS}}^2 \mathrm{d}\rho \\ &V_{\mathrm{MS}}^2 = \frac{\mathrm{d}p}{\mathrm{d}\rho} + \frac{\mathrm{d}}{\mathrm{d}\rho}\left(\frac{B^2}{2\mu_0}\right) \\ &V_{\mathrm{MS}}^2 = C_S^2 + \frac{\mathrm{d}}{\mathrm{d}\rho}\left(\frac{B^2}{2\mu_0}\right) \end{aligned} \tag{1.26}$$

Let us consider that the plasma is uniform along the magnetic field lines. The frozen-in theorem tells us that the magnetic flux through an elementary surface dS, BdS, is conserved if the said surface is tied in to the plasma. If we consider dS to follow the plasma, the mass per unit length, ρdS is also conserved. Using the subscript 0 to denote a state of equilibrium, we can write $B_0 dS_0 = BdS$, and $\rho_0 dS_0 = \rho dS$. By dividing the first equation by the second, we obtain: $B/\rho = B_0/\rho_0$.

This leads to:

$$V_{\mathrm{MS}}^2 = C_S^2 + \frac{\mathrm{d}}{\mathrm{d}\rho}\left(\frac{B_0^2\rho^2}{2\mu_0\rho_0^2}\right) \tag{1.27}$$

And finally:

$$V_{\mathrm{MS}}^2 = C_S^2 + V_A^2 \tag{1.28}$$

1.2.4 The Rankine-Hugoniot equations

Let us now derive a useful set of equations that will be convenient later on. From the MHD equations, if we make the hypothesis of a 1D geometry (*e.g.* along an arbitrary direction $\boldsymbol{e}_n$) as well as the hypothesis of stationarity, we can deduce conservation equations called the Rankine-Hugoniot equations.

Under these hypotheses we can, for example, project the continuity equation on $\boldsymbol{e}_n$ and it becomes: $\frac{\mathrm{d}\rho u_n}{\mathrm{d}n} = 0$.

This equation, which is now a general conservation equation that could be applied anywhere in the flow, becomes most helpful when we consider a planar discontinuity of which the direction $\boldsymbol{e}_n$ would be chosen to be the normal. If we assume that the values of the plasma parameters asymptotically tend towards some finite values on each side of the discontinuity that we can for example call “up” (for upstream) and “down” (for downstream), then we can integrate the previous equation, and write:

$$\rho^{\mathrm{up}} u_n^{\mathrm{up}} = \rho^{\mathrm{down}} u_n^{\mathrm{down}}$$

This is most conveniently written under the form:

$$[\rho u_n] = 0$$

, where it is understood that the brackets refer to a variation of the quantities from one side of the discontinuity to the other.

Applying the same method to the other MHD equations (and using the subscripts $t1$ and $t2$ for the tangential directions), one can obtain the full set of Rankine-Hugoniot equations, from which we left out the energy equation that requires a bit more thinking and that we will not use in this thesis:

$$\begin{aligned}
\text{Absence of magnetic monopoles:} &\quad [B_n] = 0 \\
\text{Continuity equation:} &\quad [\rho u_n] = 0 \\
\text{Maxwell-Faraday:} &\quad [u_n B_{t1} - u_{t1} B_n] = 0 \quad \& \quad [u_n B_{t2} - u_{t2} B_n] = 0 \\
\text{Equation of motion:} &\quad \left[\frac{1}{2}\rho u_n \boldsymbol{u} + (P_{\mathrm{th}} + \frac{B^2}{2\mu_0})\boldsymbol{e}_n - \frac{B_n \boldsymbol{B}}{\mu_0}\right] = 0
\end{aligned} \tag{1.29}$$

When considering a propagating discontinuity, we can place ourselves in a frame of reference in which the shock is immobile in order to recover the stationarity hypothesis. This frame is called the De Hoffmann-Teller frame (see De Hoffmann and Teller (1950), Treumann (2009)).

1.2.5 Shocks in the solar wind

There exist four types of discontinuities that are solutions to the Rankine-Hugoniot equations: the tangential discontinuities, the rotational discontinuities, the contact discontinuities, and the shocks (*e.g.* Belmont et al. (2018)). In this thesis, we are mostly interested in shocks, which are ubiquitous in the solar wind, and are a fundamental part of Space Weather, as interplanetary shocks are very geoeffective structures (*e.g.* Echer et al. (2004) and references therein), and the bow shock is the first frontier between the solar wind and Earth.

Shock waves are the class of solutions to the Rankine-Hugoniot equations for which the tangential component of the magnetic field keeps its direction; or in other terms, the magnetic fields upstream and downstream of the shock are in the same plane. They arise when a fast flow overtakes a slower one, or encounters a standing obstacle.

If the disturbance travels more slowly than the waves which can propagate in the medium, the upstream region can be “warned” by upstream propagating waves, and adiabatic changes can take place to make a smooth transition between, for example, the slower and the faster flows. Shocks, however, arise when the difference of speed between the two flows is higher than the characteristic velocities of the system, C_S, V_A or V_{MS}: the upstream medium cannot be “warned” and is “shocked” by the faster flow. Very roughly speaking, we can intuit by looking at figure 1.7, that if waves do not travel upstream of it, a gradient of velocity will tend to steepen (the velocity being greater at the top of the gradient than at the bottom) until this steepening is dampened by dissipative processes which are generally proportional to the gradient.

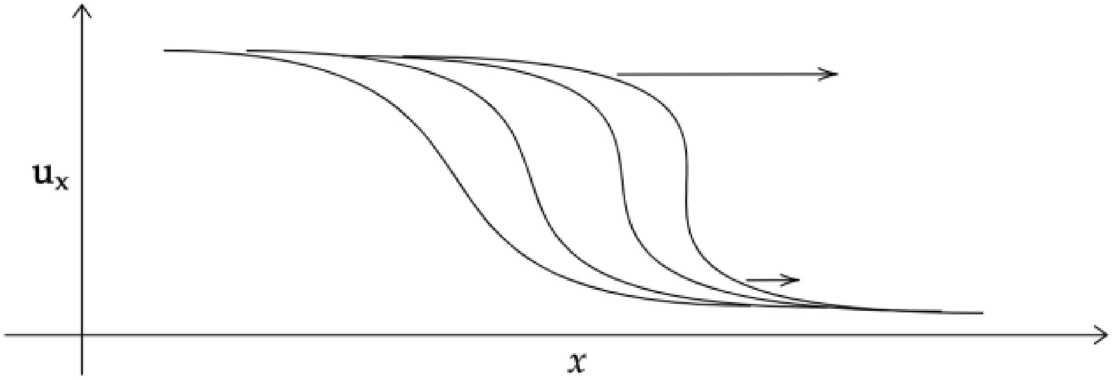

Figure 1.7: *Steepening of shock wave. y-axis: velocity u_x in the x direction.*

If we apply the Rankine-Hugoniot equations to such a shock, it should be easy to see that on the downstream side of the shock, both the magnetic field amplitude, the density and the temperature will have been increased, while the velocity will have decreased. The elevated temperature downstream is a sign that some dissipative phenomena must have taken place: the macroscopic free energy – for example the kinetic energy due to the difference of speed between upstream and downstream – has been converted into microscopic thermal motion. In a collisionless medium such as the solar wind, the exact processes through which this happens are usually called "anomalous dissipation" and their study is beyond the scope of this introduction (see *e.g.* Treumann (2009)).

The structure of shocks is governed by three main parameters: the Mach number, the plasma β upstream, and the angle between the upstream magnetic field and the shock normal (Treumann (2009)). The Mach number can be defined from any characteristic velocity of the system (see subsection 1.2.3): for example, it is common to encounter the Alfvén Mach number $M_A = \frac{v_{\text{shock}}}{V_A}$, the sonic Mach number $M_S = \frac{v_{\text{shock}}}{C_S}$, or the magnetosonic Mach number $M_{\text{MS}} = \frac{v_{\text{shock}}}{V_{\text{MS}}}$.

1.3 Earth as an obstacle in the way of the solar wind

1.3.1 The bow shock

As we saw earlier, the solar wind is supersonic close to the Sun, when it escapes its gravitational pull. As it flows away from the Sun, the solar wind barely slows down, while its density and temperature decrease. At 1 AU, the solar wind is generally supermagnetosonic. Fast magnetosonic waves are the fastest MHD waves propagating in the solar wind. If we use the average values for B, T_i, and n_i at 1 AU (Venzmer and Bothmer (2018)), and use $\gamma = 5/3$ we find:

$$V_{\mathrm{MS}} = 49 \text{ km/s} \tag{1.30}$$

With a velocity at 1 AU of about 400 km/s, it is easy to see that the solar wind is generally much faster than the MHD waves propagating in it. Any obstacle in its way should therefore lead to the creation of a standing shock wave, as the solar wind cannot be “warned” by waves propagating backwards from the obstacle (Axford (1962) and Kellogg (1962)). This shock indeed exists (*e.g.* Horbury et al. (2001)) and is called the bow shock.

Its position can be estimated (e.g. Dobrowolny and Formisano (1973), Petrinec (2002)) as:

$$R_{\mathrm{shock}} = 1 + 1.1 R_{\mathrm{M}} \frac{(\gamma - 1) M_{\mathrm{MS}}^2 + 2}{(\gamma + 1)(M_{\mathrm{MS}}^2 - 1)} \tag{1.31}$$

In this equation R_{shock} represents the distance between the bow shock and Earth on the Sun-Earth line, while R_{M} represents the distance between the magnetopause (see 1.3.2) and Earth in the Sun-Earth line. M_{MS} is the fast magnetosonic Mach number in the solar wind upstream of the bow shock.

This equation, which is semi-empirical, shows that the shock recedes to infinity as $M_{\mathrm{MS}}^2 \to 1$, *i.e.* when the solar wind is not faster that the fast magnetosonic waves.

1.3.2 The magnetopause and the magnetosphere

A second discontinuity can be found closer to Earth: the magnetopause, which marks the limit between a region where the magnetic field lines originate on Earth, and another where they are linked to the interplanetary space. This discontinuity can either be what we call a tangential discontinuity: the magnetic field is perpendicular to the normal of the discontinuity; or a rotational discontinuity: there is a change in direction of the magnetic field, but not of amplitude (*e.g.* Chou and Hau (2012)).

On one side of it is the relatively dense and highly turbulent plasma of the magnetosheath which ultimately comes from the solar wind and on the other side is the less dense and turbulent plasma of the magnetosphere. Magnetic field lines inside the magnetosphere resemble more the dipolar structure expected for the magnetic field generated by Earth’s hot metallic core. The frozen-in theorem (see 1.1) tells us that the plasma from the solar wind cannot, *in general*, cross the magnetopause and enter the magnetosphere, since the magnetic field lines found inside the magnetosphere are not connected to the magnetic field lines outside. It is in this relatively shielded environment that most human-made satellites evolve, and that Earth is seated.

The key words in the previous paragraph are “*in general*”: in some conditions the frozen-in theorem can be violated (as the hypotheses of MHD are not satisfied) and energy can flow from the solar wind to the magnetosphere. This is why the conditions at the magnetopause play such an important role in Space Weather.

The subsolar position of the magnetopause, r_{MP} can be estimated as the point of equilibrium between the dynamic pressure from the solar wind and the magnetic field pressure from Earth's magnetic dipole (Schield (1969)):

$$\rho u^2 = \left(\frac{M/r_{MP}^3}{2\mu_0} \right)^2 \tag{1.32}$$

1.3.3 The magnetosheath

On the Sun-Earth line, between the bow shock and the magnetopause, as we would expect it from what we learned about shocks in subsection 1.2.5, we find a region of compressed plasma with a strong magnetic field, a strong density, a low velocity, and strong levels of turbulence. This region, called the magnetosheath, extends on the flanks of the magnetopause, where the plasma is re-accelerated to supermagnetosonic speeds. It is very interesting for plasma physicists because its high levels of turbulence and proximity to Earth make it a fantastic laboratory for testing theories. The plasma of the magnetosheath is also in direct contact with the magnetopause, which is the last frontier before we reach the magnetic field lines attached to Earth: this gives the magnetosheath a fundamental role in Space Weather.

1.3.4 The ring current

At low latitudes, from the surface of Earth up to the magnetopause, the magnetic field generated by Earth's melted iron core is northward. Occasionally, when the interplanetary magnetic field is southward, some particles from the solar wind can penetrate inside the magnetosphere through a complex dance known as the Dungey cycle (see figure 1.9 in subsection 1.4.1). Once inside the magnetosphere, individual particles start gyrating along Earth's magnetic field lines, to form what are called the radiation belts. Depending on the history of their trajectories and energies, these particles might travel alternatively southward and northward, being reflected back and forth by the magnetic mirror force as they approach the pole's denser magnetic fields. Because of the curvature of the Earth's magnetic field lines they travel along, these particles undergo a drifting motion around Earth: westward for the ions, and eastward for the electrons. These drifts result in a net electric current circling Earth westward: the so-called ring current (Daglis et al. (1999), Egeland and Burke (2012)).

Electromagnetism's right hand rule shows immediately that a westward current circling Earth produces a southward magnetic field inside of the ring current. Under the scope of the Lenz law of induction, it should appear natural that the ring current tends to create a new magnetic field anti-parallel to Earth's magnetic field at low latitudes.

1.3.5 The Geocentric Solar Ecliptic (GSE) frame

In figure 1.8, we give a visual definition of the Geocentric Solar Ecliptic (GSE) frame, which is the frame most often used in the literature.

First, we define the origin as the centre of Earth. Then, we define the x axis as the Sun-Earth line. The z axis is then defined as the perpendicular to the ecliptic plane: the plane in which Earth

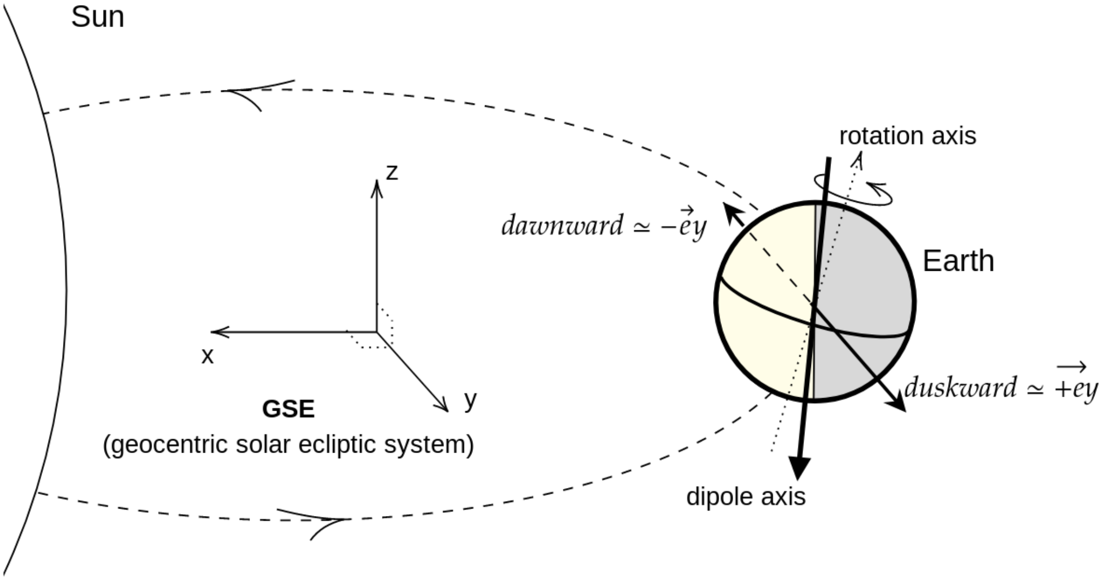

(xy) is the ecliptic plane, sometimes abusively called the equatorial plane

(xz) is sometimes called the noon-midnight meridian plane

Figure 1.8: *The GSE frame, and a few useful words*

rotates around the Sun. This z axis does not quite correspond to Earth's magnetic dipole nor to Earth's rotation on itself, but since the general orientation of these three axes is not too different, it is common to intuitively associate them, and this transpires in the terminology used in the literature:

For example, when authors discuss a "southward" magnetic field, or a negative B_z as a source of geomagnetic disturbances, it is because it has a large component opposed to Earth's magnetic dipole; even if in the GSE, the z direction is not strictly the direction of this dipole. Similarly, authors often mention the "duskward" direction as the direction of a geoeffective electric field. This comes from the ideal expression of Ohm's law (see (1.15) on page 14): A southward magnetic field, carried by a solar wind propagating roughly along the Sun-Earth line, gives rise to $\boldsymbol{E} = -\boldsymbol{u} \times \boldsymbol{B}$. With $\boldsymbol{B}||\boldsymbol{e}_z$ and $\boldsymbol{u}||\boldsymbol{e}_x$, we get $\boldsymbol{E}||\boldsymbol{e}_y$. While in the GSE, $\boldsymbol{e}_y$ is, rigorously, the component of the velocity of the Sun relative to the Earth that is perpendicular to the x axis; it is common to talk about the "duskward" direction, making a reference to Earth's rotation on itself.

1.4 Storms

As we close section 1.3, we now have an idea of what a relatively steady state picture of the Sun-Earth interaction looks like. It is now time to go back to the compass, telegraph and electrical power system of the introductory section, and ask ourselves: what went wrong?[4] In order to answer this question, we will first define geomagnetic storms and identify their most common drivers.

1.4.1 Geomagnetic storms

When the conditions upstream of the geomagnetic environment change, the geomagnetic environment reacts to it. Some of the swiftest changes occur when an interplanetary coronal mass ejection encounters Earth. When the geomagnetic activity following a swift change of solar wind condition is strong, we talk about a geomagnetic storm. The best driver of geomagnetic activity is the presence of a strong interplanetary southward magnetic field.

The Dungey cycle

Dungey (1961) explained the impact on the geomagnetic environment of driven southward interplanetary magnetic fields in the following way (see figure 1.9):

As a southward-oriented magnetic field line from the solar wind is pushed against the northward-oriented geomagnetic field, the two opposite magnetic fields are in a perfect situation to undergo magnetic reconnection (see 1 and 1’ on figure 1.9). Magnetic reconnection is the process through which magnetic field lines of opposite polarity can locally annihilate each other – thus transfering magnetic energy to particles (bulk flow velocity, temperature, or single particles acceleration) – and modify their topology (see Yamada et al. (2010) for a landmark review on magnetic reconnection). After reconnecting, magnetic field lines now have one foot on Earth, traverse the magnetosphere, and are open-ended on the other side, in the solar wind (2 and 2’). Some particles can travel along these magnetic field lines towards the poles but only the most energetic make it to the ionosphere. These particles, which represent a very small portion of all particles, can create the day-side auroras. Most particles, however, cannot reach the poles due to the strong mirror force created by the converging field lines. The newly formed half open-ended magnetic field lines, driven by the solar wind, are stretched (3, 3’, 4, 4’, 5, 5’). They are elongated behind Earth, in what is called the magnetospheric tail. Sometimes, the magnetic field lines of opposite polarity on opposite sides of the magnetospheric tail will be pushed against each other again, and can eventually undergo magnetic reconnection (6,

---

[4] The reader might find of interest to know that disturbances to the geomagnetic fields had been recognised from the very early work of W. Gilbert in 1600 (Chapman (1944)), and that the term “magnetic storm” was introduced in 1808 by A. van Humboldt (Malin and Barraclough (1991)). The idea that these disturbances may be due to the Sun’s activity started to clearly emerge in 1859 (Carrington (1859)), with the Carrington event briefly described in the introduction. Although Carrington himself was very prudent in his linking between his optical observations of a solar flare and the subsequent magnetic storms, stating “One swallow does not make a summer”; his observations are often regarded as the first clear demonstration of the Sun-Earth connection. The work of Birkeland (Egeland (2009)) in the early XXst century strongly suggested that charged particles travelling in the interplanetary medium could cause the auroras. And it was in 1919 that Lindemann (Lindemann (1919)), based on Earlier work by Chapman, first suggested that geomagnetic storms could be explained by neutral clouds of charged particles ejected by the Sun and encountering Earth. The interesting point of this very brief historical account is that all these ideas were formulated before the word “plasma” was coined by Langmuir in 1927, before the first theory of plasma physics was established by Alfvén in the 1940’s, and quite long before the solar wind was discovered (theoretically by Parker (1958) and observationally by Neugebauer and Snyder (1962).

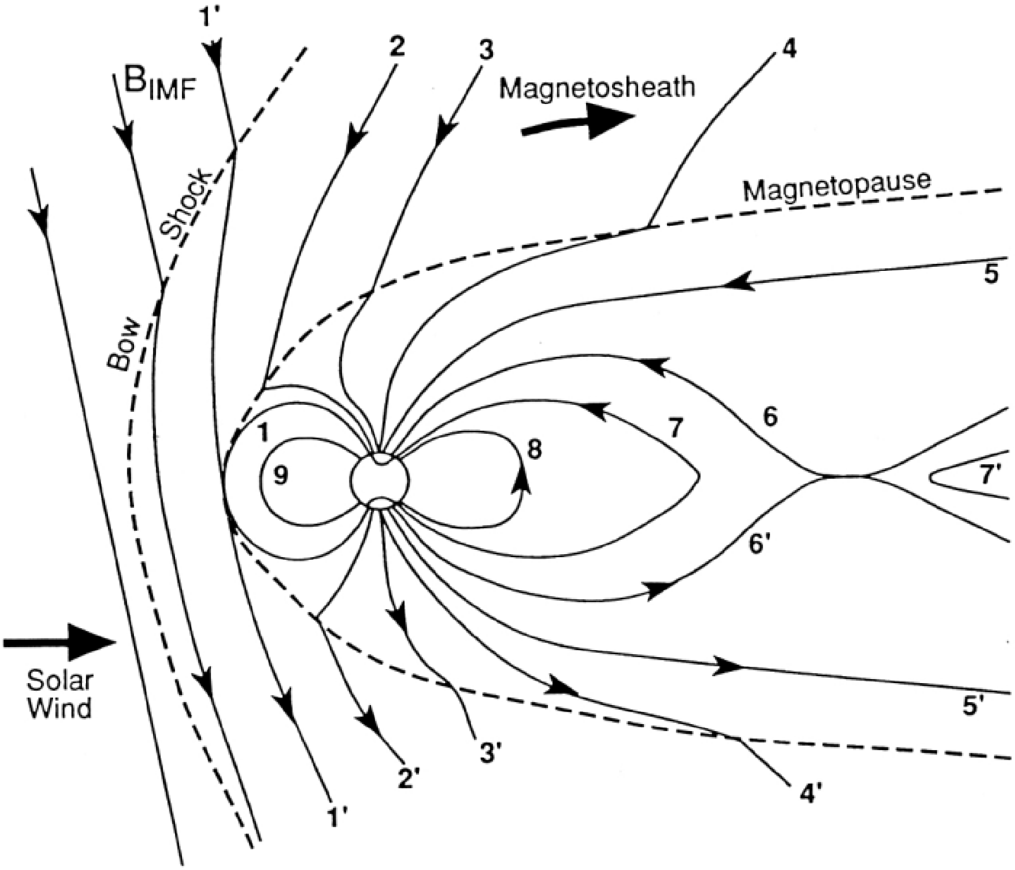

Figure 1.9: *The Dungey Cycle, from Yamada et al. (2010), adapted from Hughes (1995).*

6', 7, 7'). The figure here is not to scale, as the tail extends up to a few hundred Earth radii, and the reconnection layer is quite extended. The actual reconnection can happen anywhere along this long reconnection layer, and often needs some sort of trigger. Particles that did not penetrate at the poles on the dayside (most of them) are stored in the magnetospheric tail, and when reconnection happens, a large fraction of them are expelled towards the night side, attached to the newly reconnected magnetic field lines that now find themselves attached on both feet to Earth (7, 7', 8, 8'). Some of these particles will end up travelling to the poles and form the night-side auroras, while some others will become part of the radiation belts and reinforce the ring current.

The strength of a geomagnetic storm

The *Dst*, or disturbance storm time, is the most commonly used way of putting a number on geomagnetic activity[5]. The *Dst* was introduced by Sugiura (1964), and its value is based on measures of the magnetic field amplitude on the ground at four stations placed at low latitudes, slightly offset the magnetic equator. It is given in nT. Quiet states, with low geomagnetic activity, are used to define *Dst*'s origin at 0 nT. When the *Dst* takes on negative values, it means, in a way, that Earth's natural protection against the solar wind is weakened. Strong negative values of the *Dst* often correspond

---

[5] Since 1981, we also have access to the SYM-H index, which is essentially a better time-resolved version of the *Dst*.

to a strong southward interplanetary magnetic field leading a strengthening of the ring current[6] via the Dungey cycle. This picture has lead the Space Weather community to use the *Dst* to define the strength of magnetic storms: moderate storms are those events that lead to $Dst < -50$ nT, intense storm have $Dst < -100$ nT, and super-storms, $Dst < -250$ nT). This is an important etymological point: for example when writing "Major geomagnetic storms are caused by unusually intense solar wind southward magnetic fields that impinge upon the Earth's magnetosphere" in Tsurutani et al. (2020); what the author was really thinking is probably "Magnetic storms with unusually negative *Dst* are caused by [...]".

While the *Dst* index is the most common way of defining the intensity of geomagnetic storms, other geomagnetic indices exist and have been reported to correspond to different processes. A few examples are the Kp index; measuring ground variations of the horizontal component of the magnetic field mostly in the whole northern hemisphere and the *AE* (auroral electrojet); which roughly estimates the energy transferred from the magnetosphere to the ionosphere (Mayaud (1980)).

Consequences of geomagnetic storms

To return full circle to the events described in the *Introduction*, it is the variations thus induced in Earth's magnetic field that can cause movements of compasses' needles, inject energy into electric lines, and potentially cause technological damage (Baker et al. (2004), Progressive Management (2015), Eastwood et al. (2017)).

1.4.2 Interplanetary drivers of geomagnetic storms

Coronal mass ejections and their interplanetary counterparts

The Sun itself is a complex ball of plasma in which magnetic fields are generated and enhanced by the motions of the plasma (Charbonneau (2014)) in much the same way Earth's magnetic field is, only in a much more complicated fashion. In the convection zone of the Sun (roughly from one third of the radius to the surface), we can imagine complex flows of plasma in which are embedded a variety of magnetic flux tubes. Due to magnetic buoyency (Parker (1955)), these magnetic flux tubes will tend to rise to the surface, and from there, tend to further rise above it. At the surface of the Sun, the accumulation of new flux tubes cannot go on indefinitely and, periodically, the Sun will eject large quantities of matter and magnetic flux in space (*e.g.* Georgoulis et al. (2019)). This is called a coronal mass ejection.

We do not actually know much about how these coronal mass ejections evolve and propagate once they leave the solar surface. We do find echos of them in *in-situ* measurements from satellites in the solar wind, but it is not very clear how the coronal mass ejections observed through coronographs (cameras occulting the bright solar photosphere) relate to what we observe in satellites data. Since it is obvious that they are related, but that the evolution of coronal mass ejections in the interplanetary medium is not clear, it has been decided to call "interplanetary coronal mass ejections (or ICMEs)" the structures observed in *in-situ* measurements. Another reason this distinction is made is that surprisingly, there is a mismatch between the expected and the actual numbers of ICMEs: we "lose track" of quite a few CMEs, relatively more than would be expected from geometrical considerations alone (Kilpua et al. (2011)). Bridging the gap of knowledge between coronal mass ejections and

---

[6] The equivalence made here between the *Dst* and the ring current is an historical one (see Dessler and Parker (1959)) which is a simplification of reality (see for example Maltsev (2004)).

interplanetary coronal mass ejections is one of the main objectives of the Parker Solar Probe and the Solar Orbiter (see *e.g.* Tsurutani et al. (2020) and references therein).

Geomagnetic impact of interplanetary coronal mass ejections

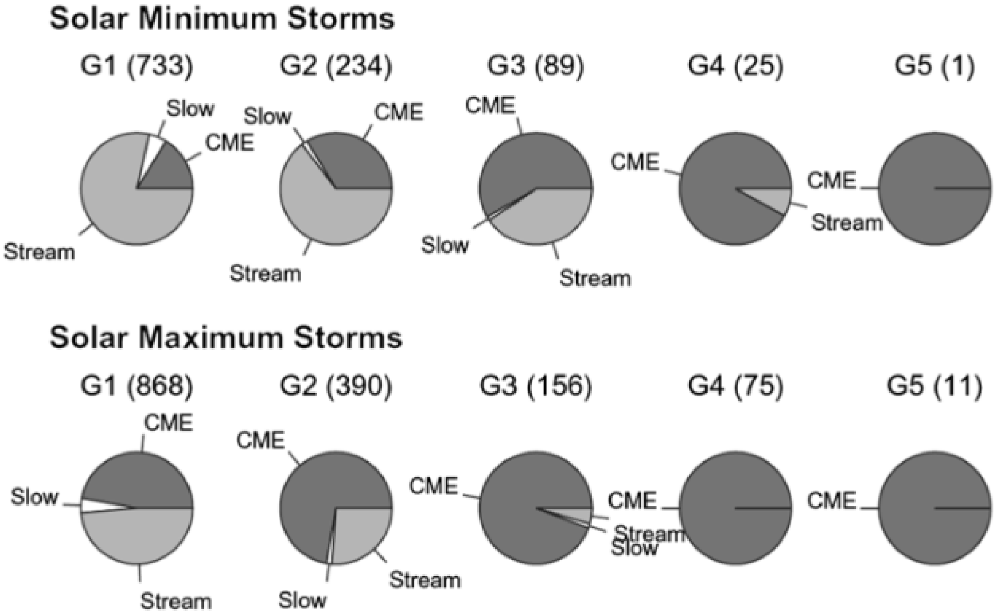

Figure 1.10: ***Figure from Richardson and Cane (2012).*** *Based on the NOAA G scale, these pie charts summarise the solar wind drivers of magnetic storms around solar minimum (top row) and solar maximum (bottom row of each pair) between years 1964 and 2011. Noted between parentheses are the number of storms included in each pie plot. "Unclear" events have been removed.*

Based on the NOAA G scale[7], which is itself based on the Kp index, figure 1.10 (from Richardson and Cane (2012)) shows that a vast amount of magnetic storms are due to interplanetary coronal mass ejections (Dark grey). A very significant part of storms are also caused by fast streams in the solar wind (light grey), and some rare storms can even be brought about by some intervals of slow solar wind (white). Generally, however, while minor and moderate storms can often be caused by streams (Echer et al. (2013)); the strong, severe and extreme storms are almost always caused by interplanetary mass ejections.

The term interplanetary mass ejections covers a range of structures. In some cases (like Richardson and Cane (2012), cited just above), the authors will use the term to mean generally: the interplanetary structures which are consequences of coronal mass ejections; this include the eventual shock driven by the structure, as well as the post-shock stream (often called sheath). This view is quite "solar", in the sense that it forgets that the consequences of coronal mass ejections do not only depend on the ejecta from the Sun, but also on the solar wind that the ejecta catches up with. Consequently, saying from figure 1.10 that coronal mass ejections are responsible for most intense

---

[7] `https://www.swpc.noaa.gov/noaa-scales-explanation`

geomagnetic storms does not teach us much about the physics of the storm generation. This is why many authors prefer to give different names to different interplanetary mass ejections, and to separate the core structure from its eventual shock and sheath.

The core structure of an interplanetary mass ejection is often named “magnetic cloud” or “non-magnetic cloud interplanetary mass ejection”. This speaks to the importance of the particular structure called a magnetic cloud.

1.4.3 Magnetic clouds

Definition

Let us now present the best known type of interplanetary coronal mass ejection: the magnetic cloud.

Most interplanetary coronal mass ejections are believed to be what we call a magnetic cloud. Indeed, our understanding of the ejection of coronal matter involves the destabilisation of a flux rope, and we therefore expect to find this flux rope further out of the Sun. "Magnetic cloud" is simply the name given to a structure containing a flux rope. A magnetic cloud should have very recognisable characteristics (Burlaga (1991), Lepping et al. (2003), Zurbuchen and Richardson (2005), Janvier et al. (2019)):

- It should contain a relatively strong interplanetary magnetic field (IMF) and an unusually low temperature: together, these means that magnetic clouds have very low plasma β.
- The field should rotate smoothly over approximately 0.25 AU, and its speed should be on average higher than the solar wind’s. Together these characteristics mean that the typical duration of an encounter with a magnetic cloud ranges from a few hours to couple days.
- It should be expanding at 1 AU, which can be seen in its speed profile: from high to lower velocity.
- It can contain suprathermal ($\geq$ 100 eV) electrons travelling in opposite directions along the axis of the cloud.

In-situ data

As we mentioned it in the introduction, Heliophysics occupies a very particular place in the broader field of Astrophysics because, since the nineteen-fifties and the beginning of the Space Age, we have material access to the objects studied: Satellites can monitor the solar wind from within and collect electromagnetic and plasma data, giving us direct access to all the relevant ingredients of the physics we want to study: the magnetic and electric fields, the plasma density, velocity and temperature, as well as the precise composition of the solar wind.

In the study of Space Weather, one particular location is particularly convenient: the Lagrange point L1. This point is situated on the Sun-Earth line exactly where the gravity of Earth slows down an object orbiting the Sun just enough that this object has the same orbital period as Earth (Lagrange, Joseph-Louis (1867)). This point is located at $1/100^{\text{th}}$ the distance between the Sun and Earth, or about 230 Earth Radii (R_E), from Earth. This is both really close to Earth – meaning that the solar wind conditions measured at L1 should almost not vary on the short distance they still have to travel to reach Earth’s magnetic environment – and far enough from Earth, so that the conditions at L1 are not influenced by the geomagnetic environment. Nowadays, quite a few satellites are in orbit around this Lagrange point L1: ACE[8] (Advanced Composition Explorer) (Stone et al. (1998)), Wind (Ogilvie and Desch (1997), Wilson (2017)), and SOHO (Domingo et al. (1995)) to cite only some of the most used satellites in the space physics community. The peculiar position of these satellites allows for a straightforward interpretation of the data collected by them: the plasma parameters measured at L1 are the conditions of the solar wind upstream of the geomagnetic environment.

Figure 1.11 is obtained from the *in-situ* data collected by the ACE spacecraft. From top to bottom are $|B|$ the amplitude of the magnetic field, $B_{x,y,z}$ its components, V the bulk flow velocity, N_p the proton density, T_p the proton temperature, and the plasma beta. Vertical purple bars mark the approximate beginning and end of the magnetic cloud. On this particularly beautiful magnetic cloud, we recover most of the characteristics listed on page 30. We can for example note a strong magnetic field rotating smoothly for approximately 15 hours, and a low plasma β. With an average (decreasing) speed of 700 km/s, we can estimate that this cloud has a size of about 0.26 AU, at 1 AU.

Due to the fact that when looking at real data we do not always recognise the characteristics expected of a magnetic cloud, it is common to use the general term interplanetary coronal mass ejection (ICME) – or the specific term non-magnetic cloud ICME – rather than the term magnetic cloud. There are a few explanations as to why a magnetic cloud ejected at the Sun could exhibit complex characteristics far from the textbook picture. Often, satellites encounter the flank of the magnetic cloud rather than the flux rope proper. Another possibility, which occurs especially around solar maxima[9] (Richardson and Cane (2004), Huttunen et al. (2005)), is that the cloud interacts with a complex solar wind, for example, it can be overtaken by fast flows or another interplanetary coronal mass ejection and be markedly deformed. Even if they may – in theory – be one and the same thing, the term "interplanetary coronal mass ejection (or ICME)" is used as a general encompassing term whereas the term "magnetic cloud (or MC)" is used only for these structures that clearly display the expected characteristics of a propagating flux rope.

The likelihood of finding southward magnetic fields in a magnetic cloud

Most identified magnetic clouds are the cause of geomagnetic storms (Zhang (2004)). The main reason behind this is that most magnetic clouds present long stretches of strong southward magnetic field.

Figure 1.12, inspired from Zurbuchen and Richardson (2005), is a simple sketch of a magnetic cloud. The magnetic cloud is represented with its feet still linked to the Sun, and its front is similar to a cylinder shape around which the magnetic field (black arrows) is wrapped in an helix. Using this sketch and simple geometrical considerations, we can convince ourselves that magnetic clouds are very likely to present strong southward magnetic fields for extended periods of time.

---

[8] DSCOVR, on top of being mostly used for monitoring climate change is progressively replacing ACE as the latter reaches the end of its life (see `https://www.nesdis.noaa.gov/content/dscovr-deep-space-climate-observatory`)

[9] The Sun has an eleven years long cycle corresponding to the progressive reversal of the Sun's dipole. Solar minimum is the name given to a situation where the magnetic configuration of the Sun resembles most a dipole: the Sun's magnetic field then constricts more efficiently matter close to the surface, and the number of coronal mass ejections, as well as the complexity of the solar wind are reduced. On the other hand, solar maximum is the name given to the transitory period during which the magnetic configuration of the Sun is at its most complex: sunspots form in large numbers, the solar wind's velocity changes rapidly and frequently, and we record a much larger number of coronal mass ejections (*e.g.* Meyer-Vernet (2007)).

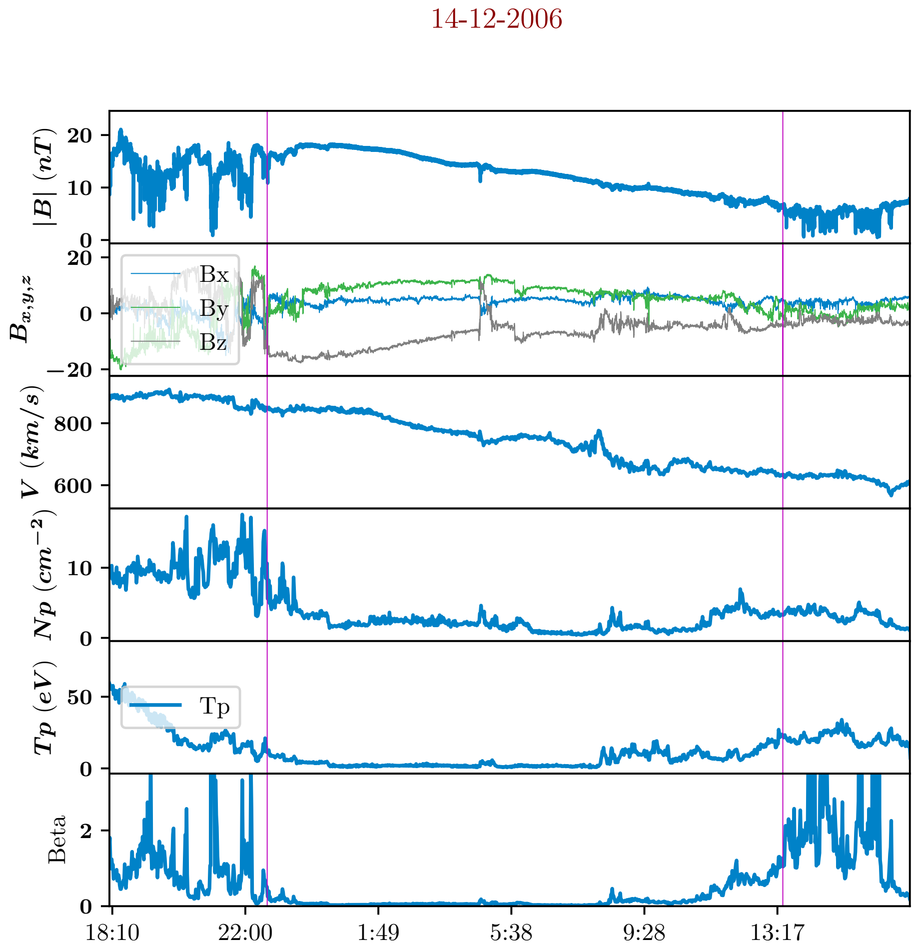

Figure 1.11: *Observation from ACE spacecraft of a typical magnetic cloud event, centred on the sheath. From top to bottom are* $|B|$ *the amplitude of the magnetic field,* $B_{x,y,z}$ *its components, V the bulk flow velocity,* N_p *the proton density,* T_p *the proton temperature, and the plasma Beta. This plot starts on 14 December 2006 18:06 UT to 15 December 2006 17:06 UT. Vertical purple bars mark the approximate beginning and end of the magnetic cloud.*

The first consideration (top panel of figure 1.12) is that when an interplanetary coronal mass ejection is crossed on one of its flanks, there is a high chance that even if it indeed possesses a flux rope structure, it might be impossible to recognise it (*e.g.* Wang et al. (2019) and references therein). Therefore, the structures that we actually call magnetic clouds are fairly often crossed close to their middle. As a consequence, the “cylindric” structure of recognisable magnetic clouds that we observe at 1 AU is most likely to have its axis contained in the (yz) plane, or close to it.

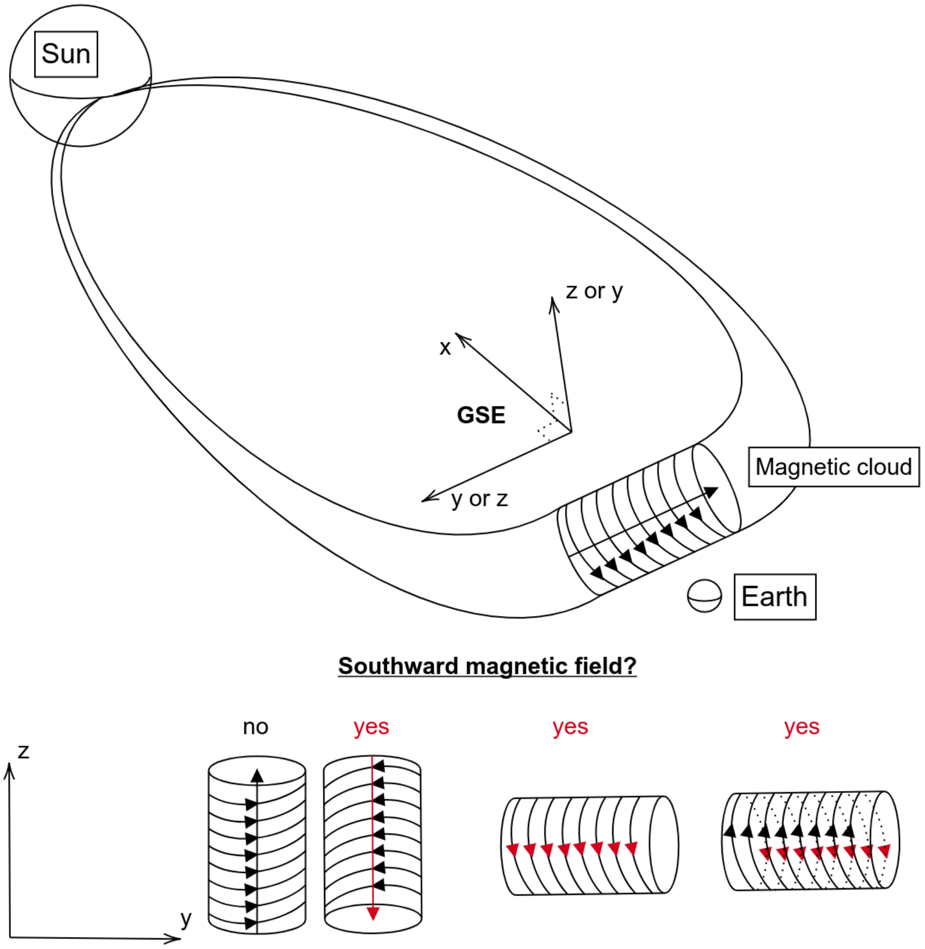

Figure 1.12: *Top: Diagram of a magnetic cloud in the GSE frame. The arrows represent the magnetic field. Bottom: geometrical considerations on the flux rope structure in the (yz) plane: Imagine crossing the flux rope from front to back. The red arrow(s) highlight(s) the presence of a southward magnetic field; if we would see a* $B_z < 0$, *we mark "yes", if not, we mark "no".*

The second consideration (bottom panel of figure 1.12) is based on the helicoidal structure, of a flux rope. We have marked in a red "yes" the configurations which would lead a satellite crossing the structure along the x axis to measure a southward magnetic (marked with a red arrow) for an extended period of time: either because the flux rope has its axis pointing towards the negative z, or because the flux rope has its axis along y, in which case the satellite would see a negative B_z either during the beginning of its crossing or toward the end.

Based on these very simple two hypotheses, we can estimate that a structure identified as a magnetic cloud has approximately a $3/4^{th}$ chance of presenting a long stretch of strong southward magnetic field.

Li et al. (2018) reports that indeed, out of 303 magnetic clouds observed with ACE and STEREO spacecrafts from 1995 to 2017, 85% presented a southward magnetic field of up to 50 nT.

Geomagnetic impact of magnetic clouds

The most important interplanetary parameter leading to geomagnetic activity is the southward B_z (Dungey (1961)), and most magnetic clouds present a southward B_z (Li et al. (2018)); therefore, it should follow that most magnetic clouds are geoeffective. This is exactly what a statistical study of 149 magnetic clouds found: Echer et al. (2005) showed that 77% of them led to at least a moderate geomagnetic storm ($Dst < -50$ nT).

1.4.4 Storms: beyond magnetic clouds and southward B_z

The fact that most magnetic clouds drive geomagnetic activity, however, does not mean that most geomagnetic activity is driven by magnetic clouds. In fact Gonzalez et al. (2011) have shown that, while magnetic clouds are the most common drivers of intense storms ($Dst <$ -100 nT) or even more intense storms, they were not, by any means, the sole drivers. As shown on figure 1.13, sheaths (green) come as a close second to magnetic clouds (blue) as drivers of intense geomagnetic activity.

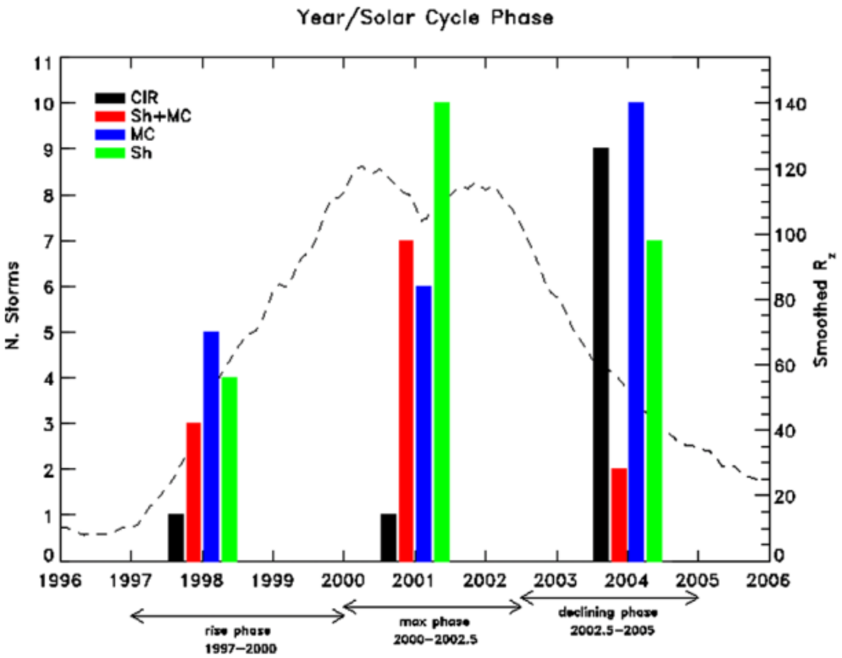

Figure 1.13: ***Figure from Gonzalez et al. (2011)***: *Distribution of the four main interplanetary structures causing intense magnetic storms according to the phase of the solar cycle 23*

Moreover, other drivers seem to be more effective at driving geomagnetic activity than magnetic clouds: using a definition of efficiency based on the effect of interplanetary B_z (or E_y) on a few geomagnetic indices, Yermolaev et al. (2010) showed that magnetic clouds were the least efficient drivers of geomagnetic activity, whereas sheaths were the most efficient.

Du et al. (2008a) studied a striking example of an intense magnetic storm ($Dst <$ -100 nT) which developed during northward interplanetary magnetic fields; further showing that the quest for a thorough understanding of the interplanetary causes of geomagnetic storms could not, despite many successes, stop at considering magnetic clouds and southward magnetic fields.

1.5 Selective summary

These ideas are some of the basic ideas of heliophysics. From them, we can dive in innumerable directions, most of which highly enthralling. For the purpose of this thesis, we will need to remember just a few of these ideas:

The hot star which we call Sun is constantly blowing a supersonic, turbulent wind in every direction (section 1.1), this solar wind interacts with Earth's magnetic field to create two frontiers: the bow shock, and a magnetopause. Between these two frontiers, one can find a highly turbulent region called the magnetosheath. Behind the magnetopause, we find the magnetosphere, a region of low-density plasma in which we live, on Earth (section 1.3). The complex magnetic field physics at the Sun leads to the intermittent propulsion of coronal mass ejections. Among these interplanetary coronal mass ejections, magnetic clouds are the most common drivers of geomagnetic activity, as they greatly modify the interactions between the solar wind and the magnetosheath (section 1.4). It seems, however, that magnetic clouds are not the only important drivers of magnetic storms, and that another interplanetary structure deserves more attention: the sheath.

2. Problem Statement

Note:
This chapter is intended to formally introduce the main object of study in this thesis: the magnetic cloud – driven sheath, and to point out its most striking characteristics. It then introduces the approach taken in this thesis to learn more about sheaths themselves and about their interaction with the geomagnetic environment.

Contents

A useful way to think about space physics is to regard the geomagnetic environment as a system which converts an input (the solar activity, and ultimately, the solar wind conditions upstream of Earth's geomagnetic environment) into an output (the geomagnetic activity). One of the goals of Space Weather is to be able to understand and predict the output based solely on measurements of the input. Being able to predict the geomagnetic activity would be useful to react early and take measures that would avert technological damages. The "problem" of Space Weather is a set of many smaller problems, and in this thesis, we shall direct our focus on a couple of aspects of one of these smaller problems: the wave content of sheaths driven by magnetic clouds and their role in geomagnetic activity beyond the eventual southward component of the magnetic field.

2.1 This thesis' object of study: sheaths driven by magnetic clouds

In the last few paragraphs, we have mentioned "sheaths" a few times, without presenting exactly what they are. This is the object of this section.

2.1.1 Interplanetary shocks and the formation of sheaths

More than half of magnetic clouds travel at a speed faster than the local speeds of waves in the solar wind (Chi et al. (2016)). Their propagation will lead to a pile-up of solar wind material and the creation of a shock wave. Figure 2.1 is probably the most famous sketch of a magnetic cloud. In front of the magnetic cloud, we find a shock and a turbulent sheath.

When a magnetic cloud interacts with the solar wind to form a shock wave, the shock wave is followed by a region called a sheath, placed between the shock and the magnetic cloud. The conditions of its formation explain its principal characteristics:

- The fast magnetic cloud overtaking the solar wind gives the sheath a high velocity.
- The high density and magnetic field amplitude found in sheaths can be explained in two ways: first, by invoking the Rankine-Hugoniot equations (see subsection 1.2.4); second, by the piling-up of solar wind material as the magnetic cloud sweeps through the interplanetary medium.
- The shock, which marks the beginning of the sheath, gives rise to a score of instabilities and waves that propagate mostly downstream[1]; this makes the sheath the host of enhanced plasma fluctuations and waves, and leads to its elevated temperature.

This characteristics are illustrated in figure 2.2, which shows an example of a typical magnetic cloud – driven sheath as observed in *in-situ* data from the ACE mission. From top to bottom, we represented the amplitude of the magnetic field $|B|$, its components $B_{x,y,z}$, the bulk flow velocity V, the proton density N_p, the proton temperature T_p, and the plasma Beta. From left to right, we see: a period of quiet solar wind, then the satellite encounters a shock which is easily identifiable by the simultaneous jumps of several quantities (*e.g.* the magnetic field, the velocity, density, and temperature) . The shock marks the beginning of the highly turbulent sheath with high magnetic

---

[1] This is because the shock is *a priori* faster than the local waves velocities. However, it does not have to be faster than all the waves to be formed, and upstream-propagating waves could exist, depending on the conditions. These very waves are actively studied (*e.g.* Tsurutani et al. (1983), Kajdič et al. (2012), Goncharov et al. (2014) or Borovsky (2020))

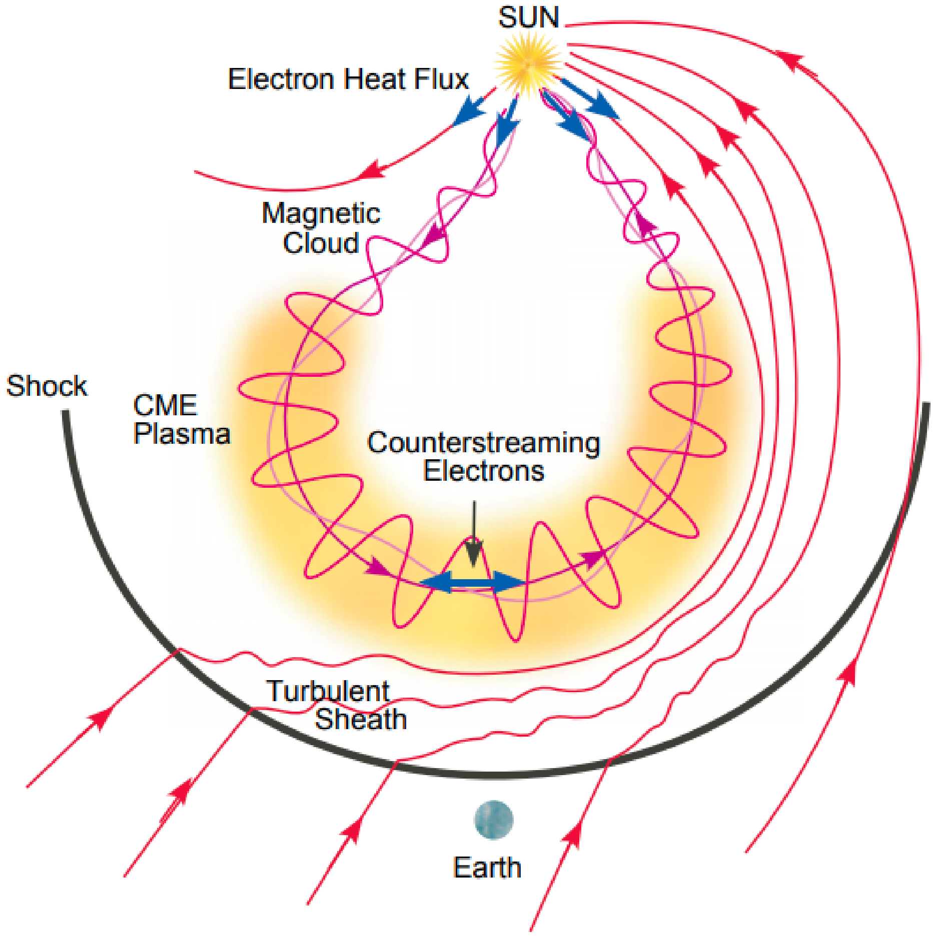

Figure 2.1: *From Zurbuchen and Richardson (2005). Schematics of three-dimensional structure of an ICME and upstream shock, along with its sheath.*

field amplitude, high velocity, high density and high temperature. The transition between the sheath and magnetic cloud is called the leading edge of the magnetic cloud. The time of the leading edge of the magnetic cloud is somewhat more difficult to define, and different people usually locate it slightly differently. To illustrate this difficulty, we have placed two different possible choices for the beginning of the magnetic cloud: the first one, marked with a continuous purple line, has been made based on the fact that the magnetic field components cease being turbulent and start rotating smoothly; the second choice has been made based on a simultaneous drop of proton density and temperature, followed by a relatively quiet stretch for these – and all other – quantities.

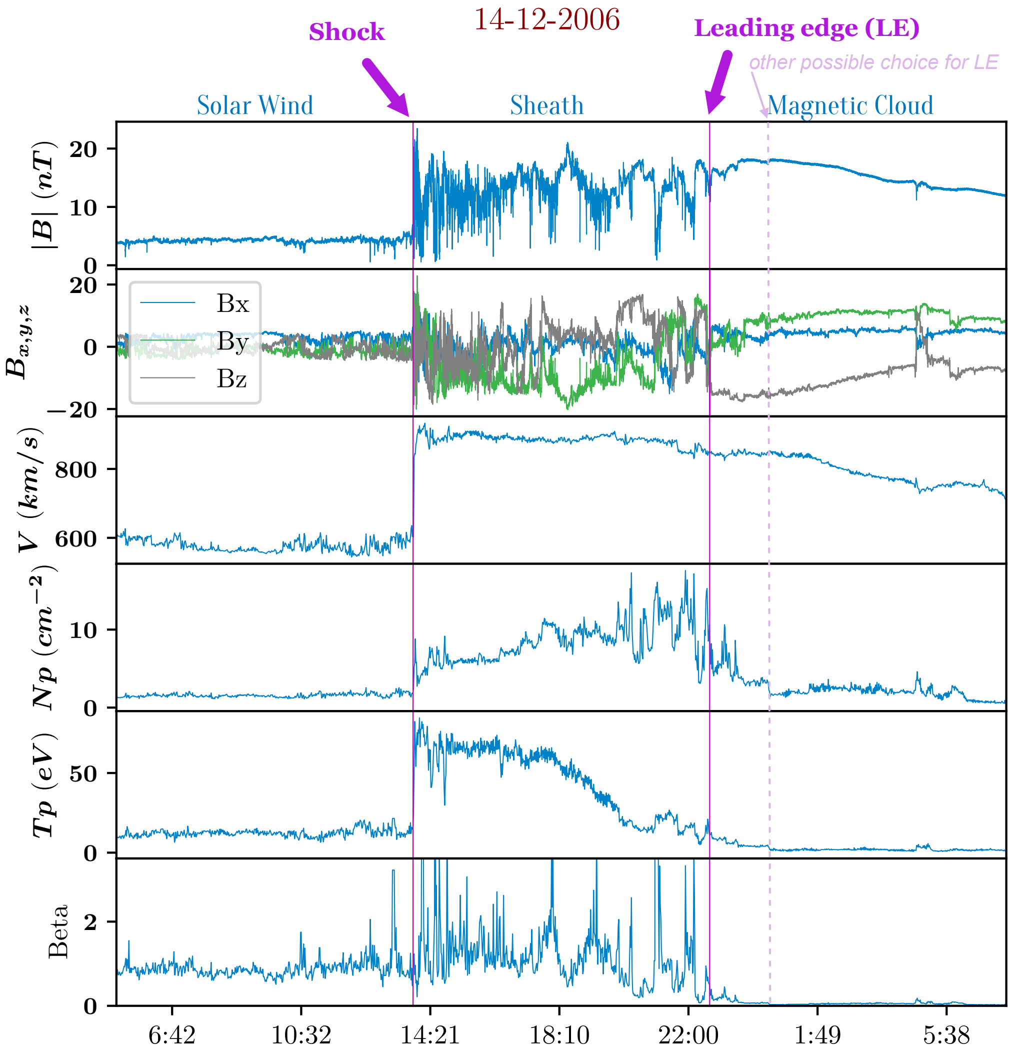

Figure 2.2: *Observation from ACE spacecraft of a typical magnetic cloud – driven sheath, centred on the sheath. From top to bottom are $|B|$ the amplitude of the magnetic field, $B_{x,y,z}$ its components, V the bulk flow velocity, N_p the proton density, T_p the proton temperature, and the plasma Beta. On this plot, and for all subsequent analysis of this event: the solar wind region spans from 14 December 2006 5:04 UT to 14 December 2006 14:14 UT, the sheath region spans from 14 December 2006 14:14 UT to 14 December 2006 22:52 UT and the magnetic cloud region spans from 14 December 2006 22:52 UT to 15 December 2006 7:25 UT. Vertical purple bars separate the three different regions of the event, from left to right: the solar wind, the sheath, and the magnetic cloud. The dashed vertical bar shows another possible choice for the leading edge.*

2.1.2 Sheaths' impact on geomagnetic activity

From Tsurutani et al. (1988), we know that sheaths (including their shock) can be geoeffective on their own. Huttunen and Koskinen (2004) (see figure 2.3) have for example shown that as much as 45% of intense geomagnetic storms ($Dst < -100$ nT) between 1997 and 2002 were caused by a shock/sheath. The percentage of storms caused by a shock/sheath seems to increase with the threshold chosen for the Dst.

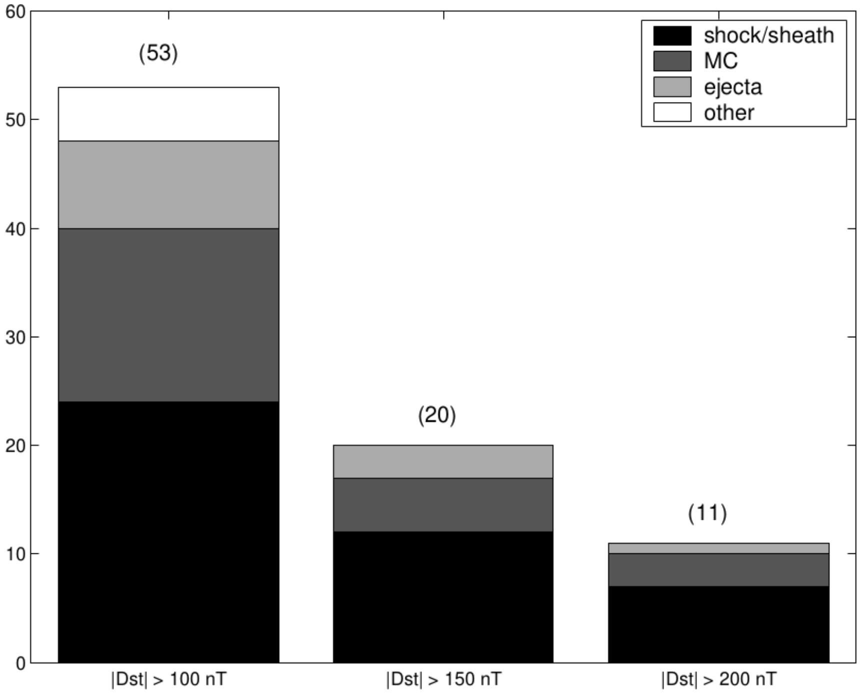

Figure 2.3: *From Huttunen and Koskinen (2004). Bars show the drivers of magnetic storms, during a 6-year interval (1997–2002), for three different level of the Dst depression. The numbers above each bar present the total number of storms in that category.*

One of the main lines of thinking to explain this high geoeffectiveness is that sheaths often contain strong southward magnetic fields (*e.g* Lugaz et al. (2016)). They can obtain these strong fields for example, by compressing pre-existing southward magnetic fields which can be found either in the solar wind or in a preceding interplanetary structure such as a magnetic cloud (Tsurutani et al. (1988), Meng et al. (2019)).

While sheaths have been given the spotlight because they can drive intense storms with a highly negative Dst; their impact on the Dst may not actually be the most interesting aspect of sheaths. Indeed, sheaths do not seem to cause the same type of geomagnetic storms as other drivers (*e.g.* Huttunen et al. (2002), Huttunen and Koskinen (2004)). For example, while magnetic clouds seem to have a strong impact on low latitude measurements of the magnetic field such as the Dst; sheaths seem to preferentially impact mid to high latitude processes, which are reflected on the Kp, or AE indices (see Kilpua et al. (2017a) and references therein).

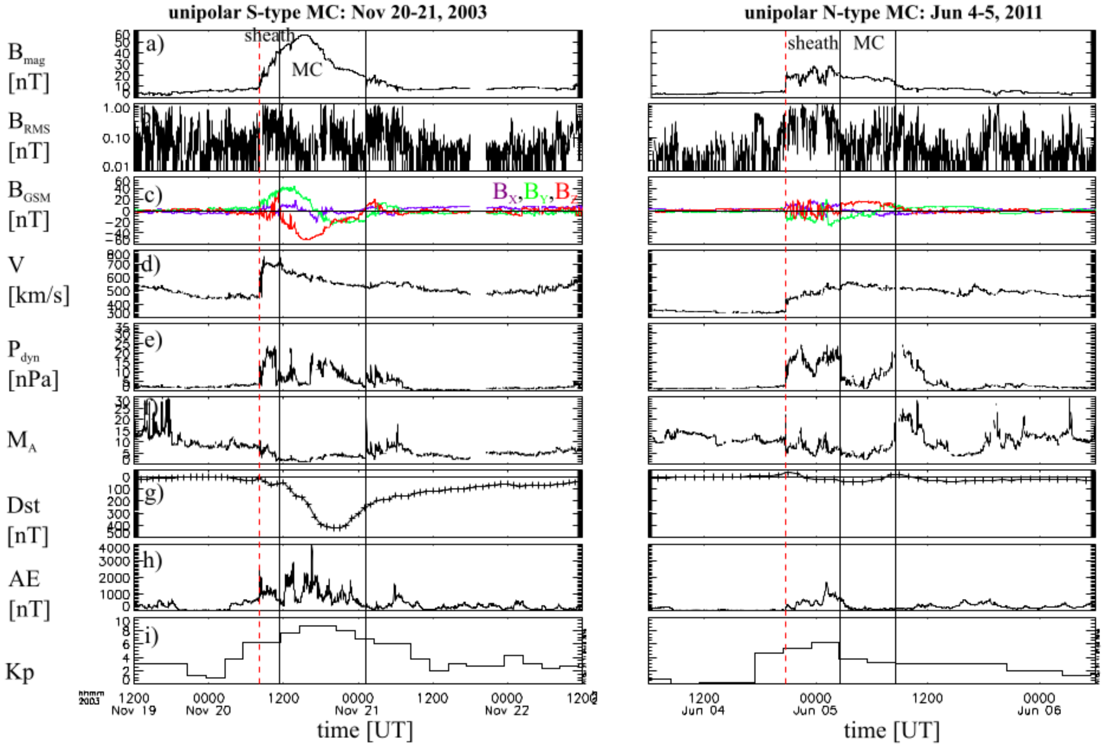

Figure 2.4: ***Figure from Kilpua et al. (2017a).*** *Comparison between two events: on the left hand-side, a magnetic cloud containting a strong southward Bz, and on the right hand-side, a magnetic cloud containing a strong northward Bz (therefore not expected to be geoeffective). The positions of the magnetic cloud and its preceding sheaths are marked using vertical lines on the figure. From top to bottom: amplitude of the magnetic field, Root-mean-square of the magnetic field, components of the magnetic field (Bz in red), bulk velocity of the plasma, dynamic pressure, Alfvén Mach number, Dst, AE, and Kp indices.*

As an example, let us examine figure 2.4. On the left hand-side, this figure shows the 19-20 November 2003 magnetic cloud which contains a strong southward Bz (red line on the third panel). As expected, it has a strong impact on diverse geomagnetic indexes (three last panels on left hand-side): the Dst (this cloud drove the largest Dst storm of Solar Cycle 23, with Dst reaching a minimum of -422 nT) , the AE, and the Kp. More interesting is the right hand-side showing the 4-5 June 2011 magnetic cloud containing a strong northward Bz: as expected, this magnetic cloud does not have any impact on the Dst, but the associated sheath does have an impact on AE and Kp (bottom two panels on the right hand-side).

This example shows that, because of their sheaths, even magnetic clouds that do not contain any southward Bz can be associated with geomagnetic activity (Kilpua et al. (2017a)). This activity might not always be adequately described by using the Dst index, but if using other geomagnetic indices, it is undeniable that it exists (see Borovsky and Shprits (2017) for a discussion on the pertinence of defining geomagnetic storms based solely on the *Dst* values).

2.1.3 What makes sheaths geoeffective?

Two aspects of sheaths have been credited for explaining their strong interaction with the geomagnetic environment:

1. Sheaths generally contain a lot of fluctuations of the interplanetary magnetic field, which could enhance viscous interactions at the magnetopause (*e.g.* Borovsky (2003), Osmane et al. (2015)), and affect the pressure balance at the magnetopause by modifying the magnetospheric currents (Bonde et al. (2018)).

2. Sheaths also display a high dynamic pressure, which should enhance compression of the bow shock and magnetopause (Schield (1969) Shue et al. (1997)); modify magnetopause currents and therefore the *Dst* in a different way than southward magnetic fields do (Burton et al. (1975)); enhance ionospheric Joule-Heating (Palmroth et al. (2004)); and inhibit polar cap potential saturation (Myllys et al. (2017)).

Together, an increase of dynamic pressure and magnetic field fluctuations have been reported to enhance the subsequent magnetic reconnection between a following southward *Bz* in the interplanetary magnetic field and the magnetospheric magnetic field; therefore increasing geomagnetic activity (Singh and Badruddin (2012)).

2.2 Research questions

Both the high fluctuations levels and high dynamic pressure found in magnetic cloud–driven sheaths are bound to hold some of the answers needed to explain the difference in geomagnetic impacts between sheaths and other types of interplanetary drivers. This is why, in this work, we want to know more about the fluctuations in sheaths themselves, as well as explore the global picture of the interaction between a sheath (with high dynamic pressure and high levels of fluctuations) and the geomagnetic environment.

2.2.1 Waves in sheaths

The study of waves in sheaths is a fairly recent undertaking of the space physics community. It is pushed by two complementary types of questioning: On one side, there are questions regarding their potential role in geomagnetic activity during the passage of a sheath; and on the other side sheaths are a formidable laboratory for collisionless turbulence. Indeed those two ways of questioning the solar wind are pretty much the bread and butter of most solar wind studies. The efforts that have been made in studying the fluctuations in sheaths have been both quite deep and scattered (*e.g.* Kilpua et al. (2017b); Ala-Lahti et al. (2018); Good et al. (2020); Kilpua et al. (2020)). We decided to undertake a more general and systematic approach to study these waves. Our simple but fundamental questions are:

- How much energy can we find in the waves in sheaths? What type of waves (*i.e.* compressible or incompressible) are they?
- Granted we know the answers to these questions, and can assign values to them on a significant number of sheaths, what do those values depend on?

These questions are a first step towards deciding how much of the geoeffectiveness of sheaths is indeed due to their high level of fluctuations.

2.2.2 Global simulations of the impact of a sheath

Observations of the geomagnetic response to sheaths give a few pointers on the processes at play during the encounter and are invaluable in constraining theories and models. However, be they ground-based or satellite-based, observations suffer from their lack of spatial resolution. Ground measurements, per nature, give information about the temporal evolution of a few specific parameters such as the geomagnetic indices, which represent the integration of a lot of different multi-scale processes in a set of single numbers; while satellites' data, despite being great at giving local details of the plasma parameters, electric and magnetic fields, give information which are fundamentally punctual. Researchers then have to make big leaps of imagination to construct a global view of the solar wind's interaction with the geomagnetic environment. A good complementary approach to observations are global simulations, that help build this global view, providing a support for intuition, and sometimes some ideas on where to look next for interesting observations.

Since the beginning of their usage during the Manhattan Project in the forties, numerical simulations have gained a central place in Physics. They are often thought of as the missing step between experiments (or observations) and theory. There are quite a few ways to think about numerical simulations and what they allow physicists to do. One, which may be the most natural, is to entrust a computer to do heavy calculations that a human could not possibly do even if she knows the theory. Another one is to chose which part of the physics they test by “turning on” or “turning off” some part(s) of the description. Again another is to give the possibility to run “inexpensive” virtual experiments, before running them in the real world, or, using the same philosophy, to vary parameters in virtual representations of systems we have no control over, such as the solar wind. In the case of space physics, all those aspects are present and make numerical simulations a pillar of this science.

For the work presented in this thesis, the main reason we run numerical simulations is to obtain a global picture of the interaction of a magnetic cloud – driven shock and sheath with the Earth’s bow shock and magnetosheath (*i.e.* we entrust a computer to run heavy calculations for us, so as to create a well-controlled virtual experiment where measurements are straightforward). The second part of the research presented in this thesis uses numerical simulations in order to explore broad questions:

- What happens to the interplanetary shock once it arrives at the bow shock, and further, when it travels inside the magnetosheath?
- What is the evolution of the main plasma parameters in the magnetosheath during its encounter with a magnetic cloud - driven sheath?
- How do the positions of the magnetopause and the bow shock vary?
- How are the fluctuations in the sheath transmitted through the bow shock?

3. Spectral analysis of space data: Method

Note: This chapter contains a few pointers on Fourier transforms and Morlet wavelets, and shows how they can be used to analyse data from satellites. The codes written for this chapter are available at `https://github.com/cmoissar/`.

Contents

3.1 Extracting the spectral characteristics of a temporal signal

In this chapter and the next, we will mostly be concerned with the power spectral density (*PSD*) of a temporal signal $x(t)$. The *PSD* is the representation of the average power per unit frequency found in a signal as a function of its frequency. It can be computed via different methods. For example, one can see it as the squares of the Fourier coefficients divided by the time over which the analysis is performed, but also as the average over time of a Morlet wavelet transform.

3.1.1 Parseval theorem and conventions

Let us call $x(t)$ a signal and $X(\omega)$ its transform, where ω is the pulsation, or 2π times the frequency. The Parseval theorem states that:

$$\int_{-\infty}^{+\infty} |x(t)|^2 dt = \int_{-\infty}^{+\infty} |X(\omega)|^2 d\omega \tag{3.1}$$

Reading this theorem as a physicist simply translates to the idea that both the left hand-side and the right hand-side terms represent the energy of the signal, and should therefore quite naturally be equal.

When we want to perform a spectral analysis of a temporal signal $x(t)$, whether it is through Fourier, Morlet, or any other transform, the most likely course of action will be to use a pre-defined library. The developers of this library will have chosen a convention regarding the transform (*i.e.* the value of λ in equation (3.3), or of A in (3.5)). It makes sense to take advantage of the Parseval theorem and to adjust the coefficient so that the transform conserves the energy of the signal. In practice, this means making sure that the integral of the square of the signal over a certain period of time, divided by that period of time is equal to the integral of the power spectral density (*PSD*) over the relevant frequencies. The following formula summarises this point of view:

$$\int_{\omega_{\text{min}}}^{\omega_{\text{max}}} PSD(x)(\omega) d\omega = \frac{1}{t_{\text{max}} - t_{\text{min}}} \int_{t_{\text{min}}}^{t_{\text{min}}} x^2(t) dt \tag{3.2}$$

This choice makes the interpretation of the *PSD* quite straightforward. As we can see, we just divided the expressions in the Parseval theorem (representing the energy) by the time on which we chose to analyse the signal, therefore defining the power of the signal. Note that for a signal whose spectral characteristics do not change over time, the *PSD* does not depend on the length of the window of integration $t_{\text{max}} - t_{\text{min}}$. This makes it the preferred choice for most studies in the solar wind since the length of the window of integration heavily varies from one study to the next.

3.1.2 Fourier Transform

A fairly good starting point when studying waves in any sort of quasi-static situation is to record a signal $x(t)$ and take its Fourier transform. Taking the Fourier transform of a temporal signal allows the user to get an idea of what type of waves or vibrations are present in the system. This is used widely in all sorts of domains, from the maintenance of machines (Renwick and Babson (1985)) to the study of space physics (Bruno and Carbone (2013)).

The Fourier transform can be defined as follows:

$$\tilde{x}(\omega) = \lambda \int_{t=t_0}^{t=t_0+T_{region}} x(t) e^{-i\omega t} dt \tag{3.3}$$

Where ω is the pulsation, T_{region} is the length of time on which we analyse the signal, and where λ can be chosen as 1, $\frac{1}{\sqrt{2\pi}}$, $\frac{1}{2\pi}$ or even $\frac{1}{2\pi \times T_{region}}$ depending on the convention.

To define the *PSD* from the Fourier transform, we just have to write:

$$PSD(f) = \tilde{x}^2(\omega) \tag{3.4}$$

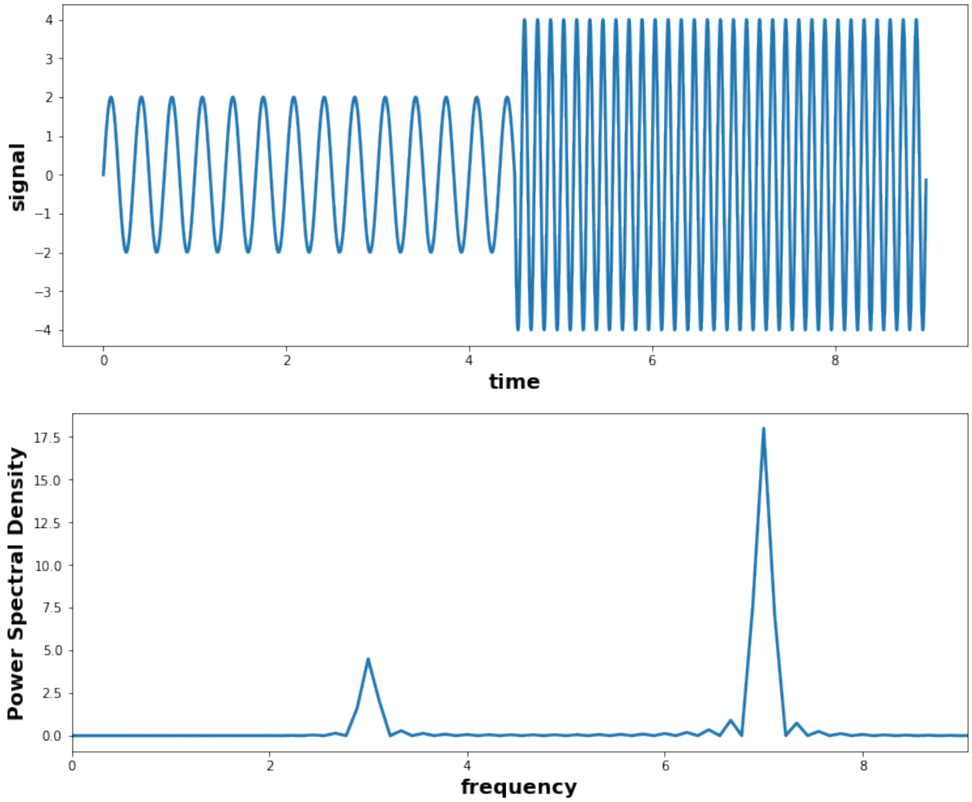

Figure 3.1: *Upper panel: a monochromatic signal changes frequency. Lower panel: its power spectral density calculated via a Fourier transform does not show the change.*

One of the main restrictions of the Fourier transform is that the resulting function does not depend on time. Figure 3.1 shows a periodic signal that sees its frequency change abruptly after a certain time (top panel), and its *PSD* computed from the Fourier transform (bottom panel). As this simple example shows, if the nature of the signal changes during the analysed sample, the result will not reflect this change.

3.1.3 Morlet wavelets

Morlet wavelets are a subset of a group of methods called time-frequency decomposition. As the name suggests, they have the ability to give the evolution of the spectrum in time; contrarily to Fourier transforms which gives a single fixed spectrum. This makes wavelets a very versatile and easy-to-use tool when we expect the signal to vary in time. This, too, can be invaluable in many different contexts, from medicine (Lin et al. (2001)) to space physics.

When doing a Fourier transform, what we were doing is using the family of the $e^{i\omega t}$ functions as a basis, and then making a projection of the signal on this basis. When doing a Wavelet transform, we are essentially doing the same thing, but we replace the $e^{i\omega t}$ by $e^{-\frac{t^2}{2\sigma_\omega^2}}e^{i\omega t}$, where $\sigma_\omega = \frac{n}{\omega}$, with n a parameter usually chosen between 2 and 15.

Similarly to the Fourier transform then, the Morlet transform of a signal x can be written as:

$$\mathscr{M}(x)(t,\omega) = A\int e^{-\frac{(t'-t)^2}{2\sigma_\omega^2}}e^{i\omega(t'-t)}x(t')dt' \tag{3.5}$$

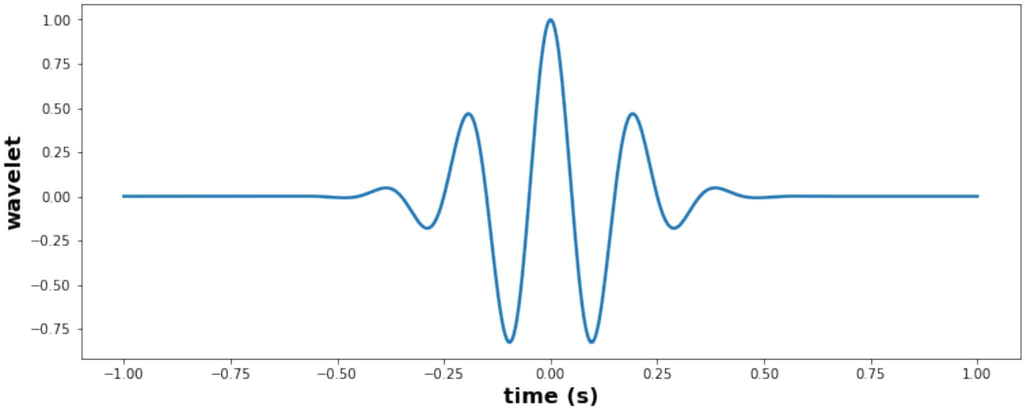

Figure 3.2: *One Wavelet, with $\omega = 2\pi f$, and $f = 5$ Hz. Here, the number of non-small peaks of the wavelet is $n = 5$.*

The function $e^{-\frac{t^2}{2\sigma_\omega^2}}e^{i\omega t}$ is a sine wave modulated by a Gaussian. Figure 3.2 shows the real part of a wavelet. Its shape depends on the parameter n which gives approximately the number of non-negligible peaks of the wave packet. This shape is very advantageous for a couple reasons:

First, its amplitude depends on time, which means that when there is no more, say ω_1 component of the signal, then it stops being reflected in the output of the wavelet transform. Going back to the example of the previous paragraph, one can see on figure 3.3 that the Morlet transform is well-adapted to the study of signals for which the spectral content varies over time.

Second advantage, the number of waves in a wave packet is constant (equal to n), which means that the size σ_ω of the wave packet automatically adapts to the frequency considered. Low frequency waves will therefore be analysed on longer times than high frequency waves. This means that there is less need to think about the window, as we would when we do a Fourier analysis (since $e^{-\frac{(t'-t)^2}{2\sigma_\omega^2}}$ is the window), and that all frequencies will be analysed with the same precision.

Wavelets are not necessarily meant as a replacement for the Fourier transform. Indeed, the output from a wavelet analysis is of a different nature than the one of a Fourier analysis. The information

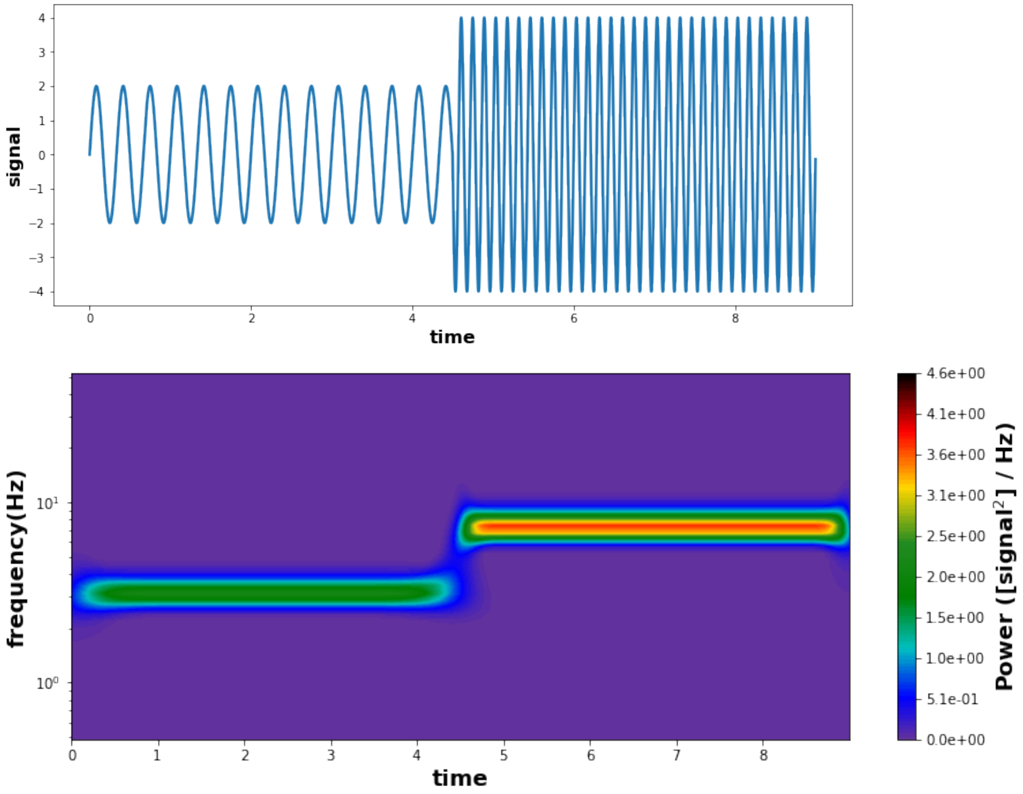

Figure 3.3: *Upper panel: a monochromatic signal changes frequency. Lower panel: its power spectral density calculated via a Morlet transform clearly shows the change.*

gained about the evolution over time also directly takes away from the precision in frequency. This makes wavelet analysis a great tool if we want to have a general idea of the spectral content of a signal, as well as its evolution in time. Fourier transforms, on the other hand, are far superior if the goal is to precisely isolate energy peaks at some frequencies.

3.2 Towards an application to space data

One of the most common way to study a magnetic cloud-driven sheath, is to look at the signal recorded by a satellite at the Lagrange point L1. The satellite can be seen as a static point, recording the passage of the solar wind and its changes in time. When it encounters a magnetic cloud–driven sheath, the satellite will therefore sequentially explore the quiet solar wind, then the sheath, then the magnetic cloud. Morlet wavelets allow us to see the changes in the wave content of these different regions at a glance.

3.2.1 Application 1: Wavelet analysis of Bz in the sheath of a magnetic cloud

In order to get a general idea of the types and amount of magnetic fluctuations in sheaths, let us start by using the very textbook-like event of December 14^{th} 2006 displayed on figure 2.2, on page 41. For the sake of simplicity, we just focus on the Morlet Wavelet analysis of the z component of the magnetic field.

Data selection

We use the data from the ACE mission (Stone et al. (1998)), in particular the ones from the Magnetic Field Experiment (MFE), which measures the magnetic field components with a 1-s resolution. Those data are available at `https://cdaweb.sci.gsfc.nasa.gov/index.html`.

Method

To obtain the figure 3.4, we simply apply the Morlet wavelets transform to B_z. In this figure, the y-axis does not represent the frequency but the period. The choice here was to put the large periods at the bottom of the graph and the small ones at the top, so that the graph reads naturally from small to high frequencies.

Result

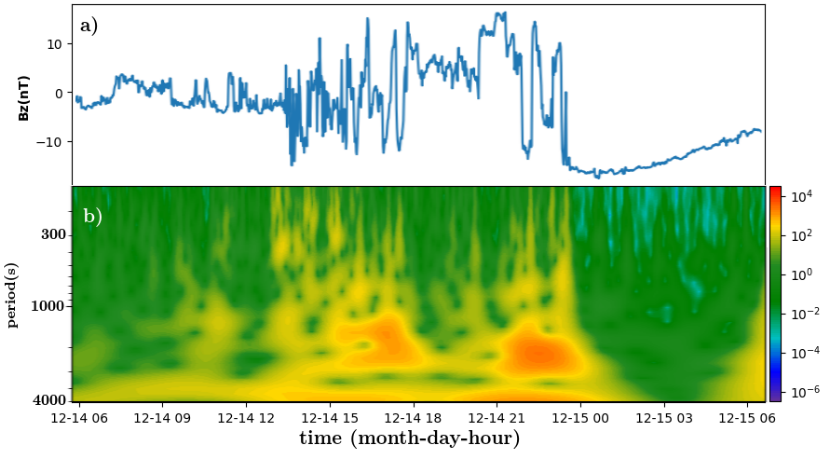

Figure 3.4: *Panel a) (top): Evolution of the z component of the magnetic field during the passage of a sheath. The sheath starts shortly before 15:00 on the December the* 14^{th} *2006. Panel b) Wavelet transform of the same signal.*

We see on figure 3.4 that the sheath contains more waves than the surrounding solar wind and shock. We also see that there are even more waves in the areas surrounding the shock and the leading edge of the magnetic cloud.

Comparison to the literature

The previous plot was intended to reproduce results from Kilpua et al. (2013) in order to validate our method and understanding. Indeed, figure 3.5, adapted from Kilpua et al. (2013) shows results from the same method applied to the same event: it is almost identical to figure 3.4.

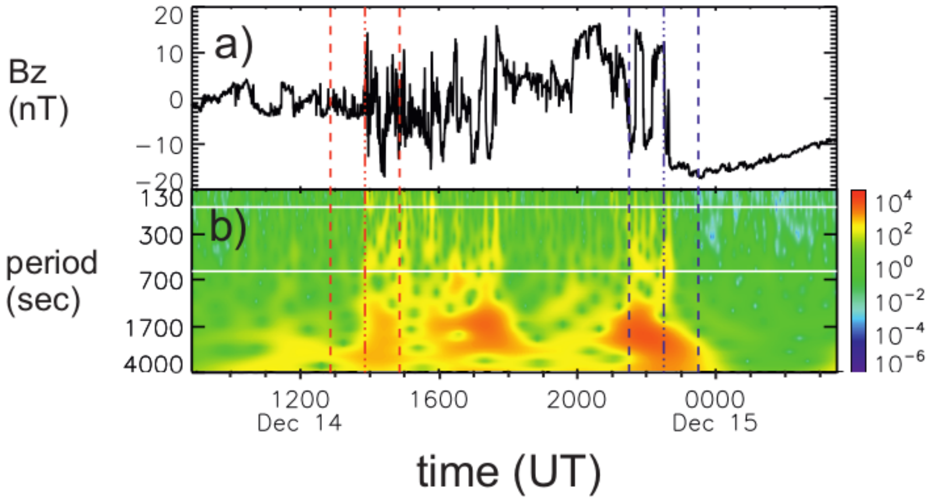

Figure 3.5: ***Adapted from Kilpua et al. (2013)***. *Example event on 14 December 2006. The panels show the following from top to bottom: (a) IMF Z component in GSM (B_z), (b) wavelet spectrogram for B_z. The red dash-dotted line marks the shock, and the blue dash-dotted line the leading edge. The 1 h regions adjacent to the shock and the leading edge are bounded by the pairs of dashed lines.*

3.3 Power spectral density from Morlet wavelets

As we mentioned earlier, one of the advantages of Morlet wavelets is that the size of the time window on which the analysed signal is integrated depends – by construction – on the frequency (see equation (3.5)). This means that when we define the *PSD* from a Morlet transform, the obtained spectrum is smooth, because it has the same resolution for all the frequencies.

3.3.1 Method

Here, we choose to use the Morlet method to get to the power spectral density (PSD) of the magnetic field in the solar wind. To obtain the *PSD*, one simply has to use the following formula to the signal $x(t)$:

$$PSD(x)(\omega) = \frac{1}{T_{region}} \int_{T_{region}} \mathscr{M}^2(x)(t,\omega)dt \tag{3.6}$$

, where $\mathscr{M}(x)(t,\omega)$ is defined from formula (3.5), and T_{region} is the time on which we analyse the signal. Once we have this definition, it is easy to adjust any coefficient required to make sure the Parseval theorem is verified for any signal. If we call u the unit of the analysed signal, the unit of the *PSD* is u^2/Hz.

If we want to have the *PSD* of a vector quantity such as the magnetic field, we have to add the *PSD*s of its components. As shown on equation (3.2), the *PSD* should be seen as a representation of the average energy carried by, for example, the magnetic field. As such, when we talk about the *PSD* of the magnetic field, we mean:

$$PSD(\boldsymbol{B}) = PSD(B_x) + PSD(B_y) + PSD(B_z) \tag{3.7}$$

This is different from $PSD(\boldsymbol{B}) = PSD(|B|)$. An easy way to be convinced of the difference is to think about $PSD(\sqrt{\cos^2(\omega t) + \sin^2(\omega t)}) = PSD(1) = 0$ *.versus.* $PSD(\cos(\omega t)) + PSD(\sin(\omega t)) = 1/2 + 1/2$.

> **Note:** In Moissard et al. (2019) and in the next chapter, we used the notation $\mathscr{W} = \mathscr{M}^2(f)$ which, for example, allowed us to directly sum the different components: $\mathscr{W}(\boldsymbol{B}) = \mathscr{W}(B_x) + \mathscr{W}(B_y) + \mathscr{W}(B_z)$.

3.3.2 Application 2: Power spectral density plots in the solar wind

Retrieving the average slope of the magnetic turbulence in the solar wind

Podesta et al. (2007) set out to establish a solid baseline for the exponent of turbulent cascades for both the magnetic field and the velocity in the solar wind. Their study provides the perfect anchor to test out the tools we developed. Here, we try to reproduce the magnetic energy spectra on figure 2 of the aforementioned paper. To do so, we use the same dataset as the authors: 81 days of solar wind data, from November the 15th at 00:00:00 in 2000 to February the 4th at 00:00:00. 81 days is a good length to have solid statistics, as it represents three solar rotations of 27 days each. The data are from the MFI (Magnetic Field Instrument) on-board the *Wind* spacecraft (Lepping et al. (1995)). They can be accessed at `https://cdaweb.gsfc.nasa.gov/`. We chose the 3 s averages of magnetic field data.

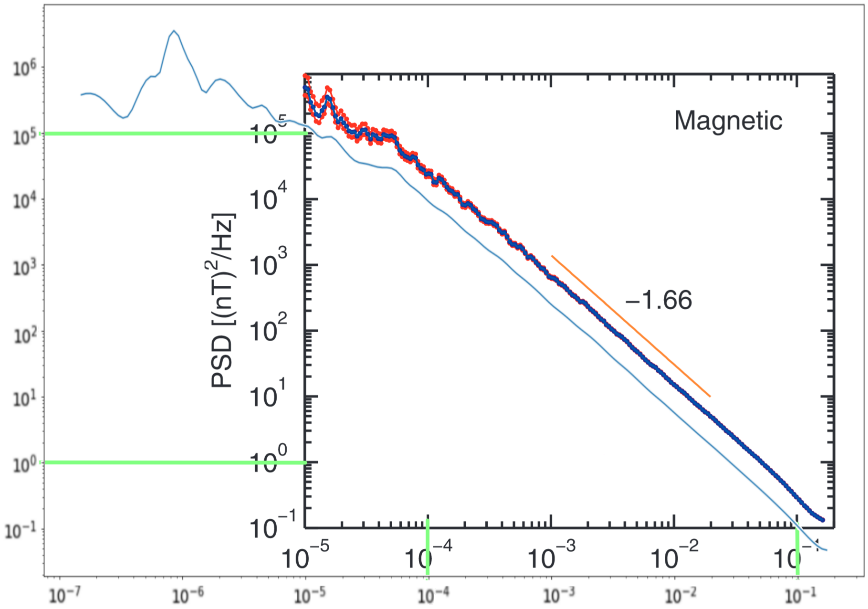

Figure 3.6: *The superposed blue and red lines, in the thick black graph is a* ***figure from Podesta et al. (2007)****. The authors plotted the power spectral density (PSD) of the magnetic field based on 81 days of solar wind data. The thin blue line is the PSD of the same data obtained with the method explained above. The green lines are just a way to ensure the axes are coherent between the two figures.*

Figure 3.6 displays our result (thin blue line) plotted over a figure from Podesta et al. (2007) (thick blue and red lines). We have adapted our axes so that they match the ones from Podesta et al. (2007). You can see on the figure that this is the type of analysis which shows that the $-5/3$ Kolmogorov exponent (Kolmogorov (1941)) is also verified in the solar wind. While the slope and shape of the spectrum correspond between the two plots, the amplitude differs slightly.

Retrieving the onset of the dissipation range

This next plot (figure 3.7) is another similar comparison between our method on an hour of data from 13:00 on January the 30th, 1995. We compare our plot against figure 1 in Leamon et al. (1998). In this particular paper, the authors used yet another method to obtain the *PSD*: the correlation matrix method of Blackman and Tukey (1958). This plot is interesting because it explores a different range of frequencies. Indeed, it is right around the change of slope associated with the onset of dissipation. In this plot, we see that the “knee” is located at a frequency $\nu_{\mathrm{bf}} = 0.44$ Hz which is above the proton cyclotron frequency of $\nu_{\mathrm{pc}} = \frac{e<B>}{2\pi m_p} = 0.099$ Hz, estimated from the average magnetic field $< B >= 6.5$ nT in the analysed interval.

We can notice on figure 3.7 that the black line is much more noisy than the thin blue line (our method). The use of the Morlet transform (our method) to obtain the power spectral density (PSD) creates results that are much less noisy than other methods (see *e.g* Bruno and Carbone (2013)). Indeed, with Morlet, every frequency is treated with the same amount of precision (or the same number of points), whereas for other methods (*e.g.* the Fourier transform), higher frequencies are analyzed on many more "periods" than lower frequencies, leading to more noise at high frequencies.

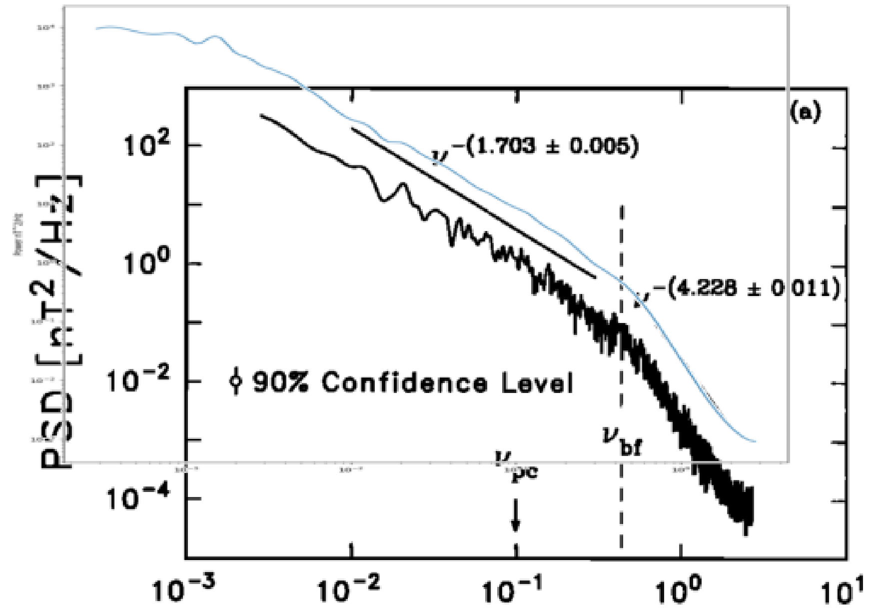

Figure 3.7: *The thick black line in the thick black graph is a* ***figure from Leamon et al. (1998)****. The authors plotted the power spectral density (PSD) of the magnetic field based on one hour of solar wind data. The thin blue line is the PSD of the same data obtained with our method.*

Of course, one could note that this noise is realistic and that it may actually be useful to know the amount of variation in the high frequency content during the analysed period of time. Quite often, however, the Fourier spectra is simply smoothed to get rid of the noise.

> **Note:** We can notice that in figure 3.6, and 3.7, the thin blue line representing the *PSD* obtained through the method described above, lies either above or below the corresponding *PSD* from the literature. This comes from the fact that, as mentioned at the beginning of this chapter, different authors adopt different conventions.

3.4 Why just the magnetic field?

This chapter and the next are an example of a common focus in space physics: the most studied fluctuations are magnetic fluctuations. There are two reasons for this: the first is that the magnetic field is a central quantity in plasma physics, which makes the mean magnetic field $\boldsymbol{B}_0$ a natural choice to frame the thinking. Once we define $\boldsymbol{B}_0$, it is natural to want to know more about the "rest" of the magnetic field $\delta\boldsymbol{B} = \boldsymbol{B} - \boldsymbol{B}_0$. The second reason is technological: the resolution of magnetic field measurements in space physics is much better than the resolution of particle measurements. Indeed, satellites designed for space physics deduce the magnetic field from the measurement of the current in three coils (*e.g.* Hospodarsky (2016)). The resolution of the signal is therefore essentially limited by the electrical system. Particle measurements are more difficult: a sufficient number of particles has to be collected by the instrument to compute satisfactorily their distribution function. Since the particles can only enter the detectors in the direction they are propagating towards, the measurements can only be updated after the satellite has rotated a few numbers of time to scan its environment (*e.g.* McComas et al. (1998)). These differences between the processes used to measure the said quantities explain why on ACE, for example, the magnetic field data is given with a resolution of 1 second, while the particle measurements are given with a resolution of 64 seconds. As far as we understand it, there is no fundamental reason why magnetic fluctuations should have more importance than other types of fluctuations such as velocity fluctuations. In theoretical works, both types of fluctuations are generally studied on an equal footing. In experimental works such as the one presented therein, pragmatical reasons make $\delta \boldsymbol{B}$ the favoured choice. Recent missions such as MMS vastly improved the resolution of particle measurements and, even if this type of study was always present, we should see more and more studies on the fluctuations of plasma quantities.

4. Spectral analysis of space data: Results

Note: This chapter can be read both as a guide and commentary to the article Moissard et al. (2019), which can be found in the annex. It will provide a how-to guide to reproduce the figures in the article, show some figures that were not included in the final manuscript and discuss some questions not addressed in the published work.

Its structure does not fit the usual "Method", "Result", "Discussion" template, because the method can only be correctly introduced as a step-by-step process based on the results from the previous step. We will, however, follow the "Method", "Result", "Discussion" for most steps of the process:

Section 4.1 analyses the fluctuations in a single, textbook-like sheath, as compared to the preceding quiet solar wind and the following magnetic cloud.
Section 4.2 explains how to condense the previous results in order to apply them to a large number of event and draw some general conclusions on the fluctuation content of sheaths.
Section 4.3 shows how to refine the previous analysis, and presents our final results on the general characteristics of fluctuations in sheaths.
Section 4.4 starts from the previous results and explains how we can reorder them to search for patterns that direct us towards a physical appreciation of the origin of the magnetic field fluctuations in sheaths.

Contents

4.1 What do the fluctuations in a textbook-like event look like?

We will study the December 14^{th} 2006 event, when the satellite ACE encountered a Magnectic Cloud (MC) preceded by a Sheath (Sh) that was formed between a magnetic cloud and the Solar Wind (SW) (see figure 2.2 on page 41). The sheath itself modestly caused the *Dst* to briefly fall down to -45 nT, which almost corresponds to a moderate geomagnetic storm (*Dst* < -50 nT, in the usual classification of storms). The following magnetic cloud, which contained a long lasting southward *Bz*, caused an intense storm, with the *Dst* reaching -162 nT. While in terms of *Dst*, the cloud was much more geoeffective than the sheath, the difference is much less marked if we look at the Kp and *AE* indexes. The sheath caused the Kp to make an excursion up to 7 (strong storm) and the *AE* to go up to 2000 nT; while the cloud caused the Kp to go up to 8 (severe storm) and the *AE* to also go up to 2000 nT. The December 14^{th} 2006 event is therefore a perfect example of a sheath which causes significant geomagnetic disturbances in a different manner from the one of a geomagnetic cloud.

The measurement of the magnetic field for the full event – with a transition from solar wind to sheath and then from sheath to magnetic cloud – is a signal containing a variety of frequencies evolving with time. This is why in this section, we apply the Morlet spectral analysis introduced in chapter 3 (both the full Morlet view and the *PSD*) to the fluctuations of the magnetic field, as defined in section 4.1.1.

4.1.1 Definition of the fluctuations

In this work, we define the fluctuations of the magnetic field as the variation around a mean magnetic field, defined as the magnetic field averaged on a sliding window (similarly to Tao et al. (2015)) of $T_W = 15$ min length. The duration of the window has been chosen to follow the slower variations of the magnetic field while not filtering the faster ones.

In mathematical terms, this is written as follows:

$$\begin{aligned} \langle B_{x,y,z} \rangle (t) &= \frac{1}{T_W} \int_{t-T_W/2}^{t+T_W/2} B_{x,y,z}(\tau) d\tau \\ \delta B_{x,y,z}(t) &= B_{x,y,z}(t) - \langle B_{x,y,z} \rangle (t) \end{aligned} \tag{4.1}$$

A good indicator of the nature of the fluctuations is the difference between the spectrum of $\delta \boldsymbol{B}_{||}$ (the component of $\boldsymbol{B}$ which is aligned with the average magnetic field $\boldsymbol{B}_0 =< \boldsymbol{B} >$) and the spectrum of $\delta \boldsymbol{B}_{\perp}$ (the components that are perpendicular to $\boldsymbol{B}_0$).

In order to define these two quantities we need a local orthonormal frame. We use the frame described in the following equations:

$$\begin{aligned} \boldsymbol{b}_0 &= \frac{\boldsymbol{B}_0}{|\boldsymbol{B}_0|} \\ \boldsymbol{b}_1 &= \frac{\boldsymbol{e}_j \times \boldsymbol{B}_0}{|\boldsymbol{e}_j \times \boldsymbol{B}_0|} \\ \boldsymbol{b}_2 &= \frac{\boldsymbol{B}_0 \times (\boldsymbol{e}_j \times \boldsymbol{B}_0)}{|\boldsymbol{B}_0 \times (\boldsymbol{e}_j \times \boldsymbol{B}_0)|} \end{aligned} \tag{4.2}$$

In equations (4.2), a natural choice for $\boldsymbol{e}_j$ could be $\boldsymbol{e}_x$. However, there is a risk that $\boldsymbol{B}_0$ also happens to be along the $\boldsymbol{e}_x$ direction. This would mean that $|\boldsymbol{e}_j \times \boldsymbol{B}_0|$ could potentially tend towards

0, which would result in a flawed definition of $\boldsymbol{b}_0$, $\boldsymbol{b}_1$, and $\boldsymbol{b}_2$. Building a frame from the knowledge of one vector is a well-known but still debated subject in applied mathematics (*e.g.* Duff et al. (2017)). In order to avoid this type of problem, we adopt the simple solution that follows: we select $\boldsymbol{e}_j$ for every region we want to analyse; $\boldsymbol{e}_j$ is automatically chosen as either $\boldsymbol{e}_x$, $\boldsymbol{e}_y$ or $\boldsymbol{e}_z$ in order to maximise the quantity $\|\boldsymbol{e}_j \times \boldsymbol{B}_0\|$.

This co-moving frame, represented on figure 4.1, allows us to define the parallel and perpendicular fluctuations by simple projections of $\delta\boldsymbol{B}$ on its axes:

$$\begin{aligned} \delta B_{||} &= (\boldsymbol{B} - \boldsymbol{B}_0) \cdot \boldsymbol{b}_0 \\ \delta B_{\perp 1} &= (\boldsymbol{B} - \boldsymbol{B}_0) \cdot \boldsymbol{b}_1 \\ \delta B_{\perp 2} &= (\boldsymbol{B} - \boldsymbol{B}_0) \cdot \boldsymbol{b}_2 \end{aligned} \tag{4.3}$$

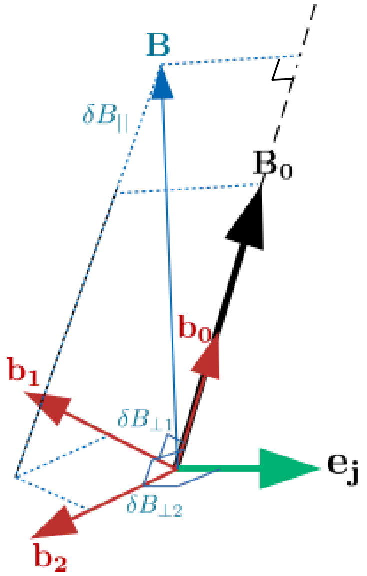

Figure 4.1: *A unit vector e_j (in green) is chosen from [e_x, e_y, e_z] to maximise the angle between $\boldsymbol{e}_j$ and the average magnetic field $\boldsymbol{B}_0$. An orthogonal frame ([$\boldsymbol{b}_0$, $\boldsymbol{b}_1$, $\boldsymbol{b}_2$] in red) is created from $\boldsymbol{B}_0$ and $\boldsymbol{e}_j$ for each point in time. This frame is used to compute $\delta B_{||}$ and $\delta B_{\perp}$*

4.1.2 Morlet wavelets

The Morlet transform is applied separately to $\delta B_{||}$, $\delta B_{\perp 1}$, and $\delta B_{\perp 2}$, and respectively noted $\mathscr{W}(\delta B_{||})$, $\mathscr{W}(\delta B_{\perp 1})$ and $\mathscr{W}(\delta B_{\perp 2})$. We then define $\mathscr{W}_{||} = \mathscr{W}(\delta B_{||})$, and $\mathscr{W}_{\perp} = \mathscr{W}(\delta B_{\perp 1}) + \mathscr{W}(\delta B_{\perp 2})$ as well as $\mathscr{W} = \mathscr{W}_{||} + \mathscr{W}_{\perp}$, which represents the total energy per unit volume and unit frequency of the fluctuations of $\boldsymbol{B}$.

Figure 4.2 represents the temporal evolution of $\mathscr{W}$ for the “14-12-2006” event: the horizontal axis represents the time, the vertical axis represents the frequency, and the colours represent the intensity $\mathscr{W}$ of the fluctuations, (in $nT^2.Hz^{-1}$).

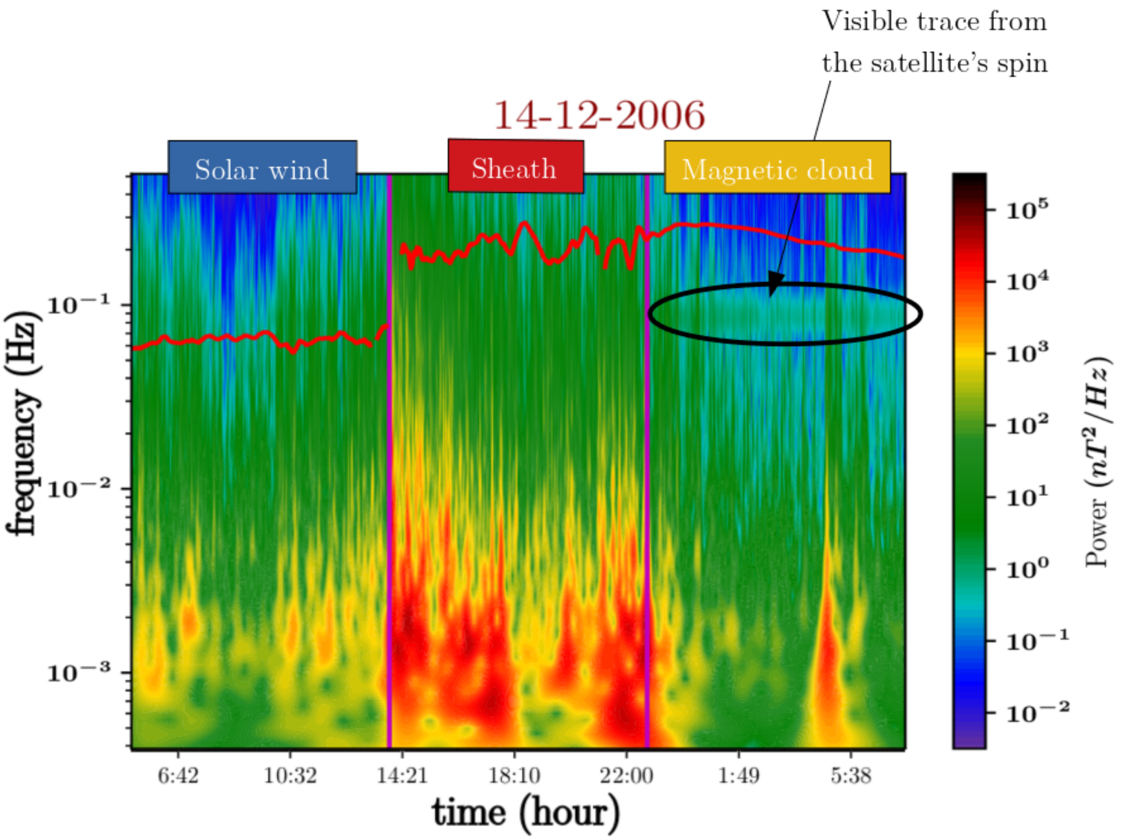

Figure 4.2: *Morlet wavelets of the 14-12-2006 event. The vertical axis represents the frequency of waves. The horizontal axis represents the time. The colour palette represents the amount of energy per unit volume and per unit frequency of the magnetic field: blue and green represent "low" energy content, while yellow and shades of red represent "high" energy content. The figure is divided in three regions by vertical purple bars: from left to right, these regions respectively correspond to the solar wind, the sheath, and the magnetic cloud. Towards the top of the figure, the red line represents the gyrofrequency of protons* $f_c = \omega_c/2\pi$ *based on the value of* $\boldsymbol{B}_0$.

If we focus on the left side of the figure, in the "solar wind" part, we observe that the lower part of the figure contains a lot more red than the upper part. This means that the magnetic field has more energy at low frequencies than at high frequencies, which is consistent with figures 3.6 and 3.7 as well as, of course, with the entirety of the literature on solar wind turbulence.
The same observation can be made in the sheath region. There, however, $\mathscr{W}$ is much higher than in the solar wind. This is expected, as the sheath is known to be a turbulent region.
In the magnetic cloud, the turbulence levels seem to resemble the solar wind's levels, or a bit less.

In the magnetic cloud, we can see a horizontal green band of waves around $10^{-1}Hz$. This is due to the satellite spin: ACE completes a rotation on itself every 12.8 seconds (Stone et al. (1998)). In general, we can see that the fluctuation spectra does not contain much power in the lowest frequencies, below $10^{-3}Hz$. This is because we averaged out the low frequencies through equation (4.1).

These two last remarks create two natural limits for the frequencies:

- A maximal limit to exclude the spin of the satellite $f_{max} = 5 \cdot 10^{-2}$ Hz $< f_{spin}$.
- And a lower limit which comes from the definition of the mean field $\mathbf{B_0}$: $f_{min} = 2/(15 \text{ min.}) = 3 \cdot 10^{-3}$ Hz $> 2/T_W$. As we have seen in chapter 3, below $1/T_W$, the spectra starts showing properties that are more linked to the mathematical definition of the mean magnetic field than they are to the actual spectral content of the physical magnetic field. Choosing $f_{min} = 2/T_W$ is a way to make sure the results focus on the physics we want to study.

These two limits will be seen as blue vertical bars in figure 4.3. Any following calculations made from the result of the Morlet transform $\mathscr{W}$ will exclude the data outside of these frequency limits.

4.1.3 Power Spectrum Density

Those limits also correspond to what is usually called the ULF (Ultra Low Frequency) bandwidth, which is relevant to interplanetary shocks (Kajdič et al. (2012)), to the study of sheaths (Kilpua et al. (2013)) and to the interaction of the solar wind with the terrestrial magnetosphere (Kepko et al. (2002); Osmane et al. (2015); Alimaganbetov and Streltsov (2018)).

We can then obtain figure 4.3 by integrating $\mathscr{W}(t,\omega)$ over the time T_{region} in each different region (solar wind, sheath, magnetic cloud), excluding the immediate surroundings of the shock and the leading edge. The result of this integration, as explained in section 3.3, represents the Power Spectrum Density (PSD) of the magnetic fluctuations and their components. We can separate the parallel fluctuations $PSD_{||}$ (in green in figure 4.3) from the perpendicular fluctuations $PSD_{\perp}$ (in grey) by making separate integration of $\mathscr{W}_{||}$ and $\mathscr{W}_{\perp}$. Their sum, $\mathscr{W} = \mathscr{W}_{||} + \mathscr{W}_{\perp}$, is displayed in blue.

$$PSD_{\perp,||}(\omega) = \frac{1}{T_{region}} \int_{T_{region}} \mathscr{W}_{\perp,||}(t,\omega)dt \tag{4.4}$$

In figure 4.3, we can see two clear trends. The first was already clear on figure 4.2: the fluctuations have much more power in the sheath than in the other regions investigated. We can also note that the fluctuations power in the solar wind preceding the sheath and in the following magnetic cloud have a similar order of magnitude, with a bit less power in the cloud than in the solar wind. Secondly, the gap between the green and the grey dotted lines is smaller in the middle panel than in the first one which suggests more isotropic (or compressible) fluctuations in the sheath. On the other hand the gap is very large in the right panel, the parallel power (green) being so low that the total power is almost equal to the perpendicular power: the fluctuations in the magnetic cloud are very anisotropic; or almost incompressible.

Summary

On these spectra, we observe two clear characteristics of sheaths: the power of the fluctuations is higher in the sheath than in the rest of the event (the blue line representing the total power in the magnetic fluctuations is higher in the sheath), and the fluctuations are more isotropic in the sheath than in the rest of the event, particularly more than in the magnetic cloud where the fluctuations are very anisotropic.

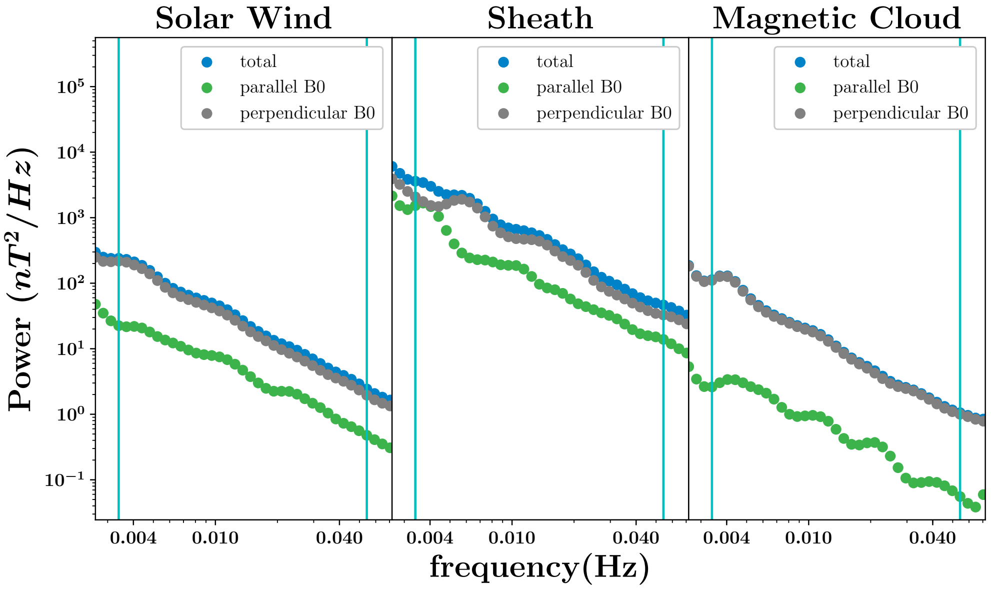

Figure 4.3: *Spectrum of the fluctuations of the magnetic field (or power spectrum density) on each region of the "14-12-2006" event. The vertical axis represents the energy per unit volume and per unit frequency, and the horizontal axis represents the frequency. In blue is the total energy PSD, in grey the energy of the fluctuations perpendicular to the mean magnetic field* $PSD_{\perp}$*, and in green is the energy of the fluctuations parallel to the mean magnetic field* $PSD_{||}$*. The cyan vertical bars mark the frequency limits inside of which the analysis was performed.*

4.2 Power and Anisotropy in a list of events (raw)

4.2.1 Method: Condensing the results

Morlet wavelets are a fantastic tool to build intuition and precise understanding on the inner workings of events. Their main advantage – namely the quantity of information packed in a wavelet plot – is also their main inconvenience. Too much information can make the recognition of a pattern very difficult. Indeed, if we are to check whether or not the characteristics we just discovered in a textbook-like sheath and its surroundings are a particularity of this event or could be found as a general pattern of sheaths; we need a way to compare the results obtained for the December 14^{th} 2006 event with those obtained for many other sheaths.

We condense the results obtained in section 4.1 by defining six numbers: P_{SW}, P_{Sh}, P_{MC} and A_{SW}, A_{Sh}, A_{MC}. The first three numbers – P_{SW}, P_{Sh}, and P_{MC} – represent the average power in the ULF fluctuations during the three different intervals: solar wind, sheath, magnetic cloud. A_{SW}, A_{Sh}, A_{MC} represent the anisotropy of the fluctuations in these same three intervals.

This can be done quite simply by using the following integrals over the time intervals (T_{region}) spanning the different regions; as well as over the frequency. The subscript *region* represents either the solar wind SW, the sheath Sh or the magnetic cloud MC:

$$P_{region\ (\perp,||)} = \frac{1}{T_{region}} \int_{T_{region}} \int_{f_{min}}^{f_{max}} \mathscr{W}_{(\perp,||)}(t,f)\, df\, dt \tag{4.5}$$

The anisotropy A compares the perpendicular power to the parallel power:

$$A_{region} = \frac{P_{region\perp}}{2 \cdot P_{region||}} \tag{4.6}$$

The factor 2 at the denominator allows $A = 1$ to represent the isotropic case, and $A > 1$ to represent stronger perpendicular fluctuations than parallel fluctuations (degree of anisotropy).

For the "14-12-2006" event, these numbers are given in Table 4.1.

P_{SW}	P_{Sh}	P_{MC}	
1.2	10.0	0.55	(nT^2)
A_{SW}	A_{Sh}	A_{MC}	
3	2	11	

Table 4.1: *Power and anisotropy of the different regions of the "14-12-2006" event*

The values of P_{SW}, P_{Sh}, P_{MC} and A_{SW}, A_{Sh}, A_{MC}, given in table 4.1 are a concise and quantitative way of representing the properties of the fluctuations in the "14-12-2006" event. The conclusions correspond to those given at the end of subsection 4.1.3: compared to the solar wind, there is an augmentation of the power in the sheath ($P_{Sh} > P_{SW}$) as well as a decrease of the anisotropy ($A_{Sh} < A_{SW}$). In the magnetic cloud, the fluctuations have an opposite behaviour to the fluctuations in the sheath: the power drops ($P_{MC} < P_{Sh}$) and the anisotropy increases ($A_{MC} > A_{Sh}, A_{SW}$).

This same method can be applied to obtain P_{SW}, P_{Sh}, P_{MC} and A_{SW}, A_{Sh}, A_{MC} for any event of the form: solar wind interval, sheath, magnetic cloud. A list of such events, relatively well isolated from other events (such as a stream interaction region, an interplanetary coronal mass ejection or some unidentified disturbances in the solar wind) is given in Masías-Meza et al. (2016).

4.2.2 Temporary result: Power and Anisotropy in 42 sheaths

P_{SW}, P_{Sh}, P_{MC} and A_{SW}, A_{Sh}, A_{MC} are computed for each event of Masías-Meza et al. (2016)'s list containing 42 sheaths[1].

In figure 4.4 we plot P_{SW} (blue squares), P_{Sh} (red diamonds), P_{MC} (yellow circles) and in figure 4.5, we plot A_{SW} (blue squares), A_{Sh} (red diamonds), A_{MC} (yellow circles).

In figures 4.4 and 4.5 we can see that the trends noticed in figure 4.3 and table 4.1 are followed by the majority of events in Masías-Meza et al. (2016)'s list: fluctuations in sheaths (red diamonds) have more power and are more isotropic than fluctuations in the quiet solar wind intervals (blue

---

[1] Remark: Masías-Meza et al. (2016) contains 44 sheaths, but for two of them, the magnetic data is missing on the ACE mission.

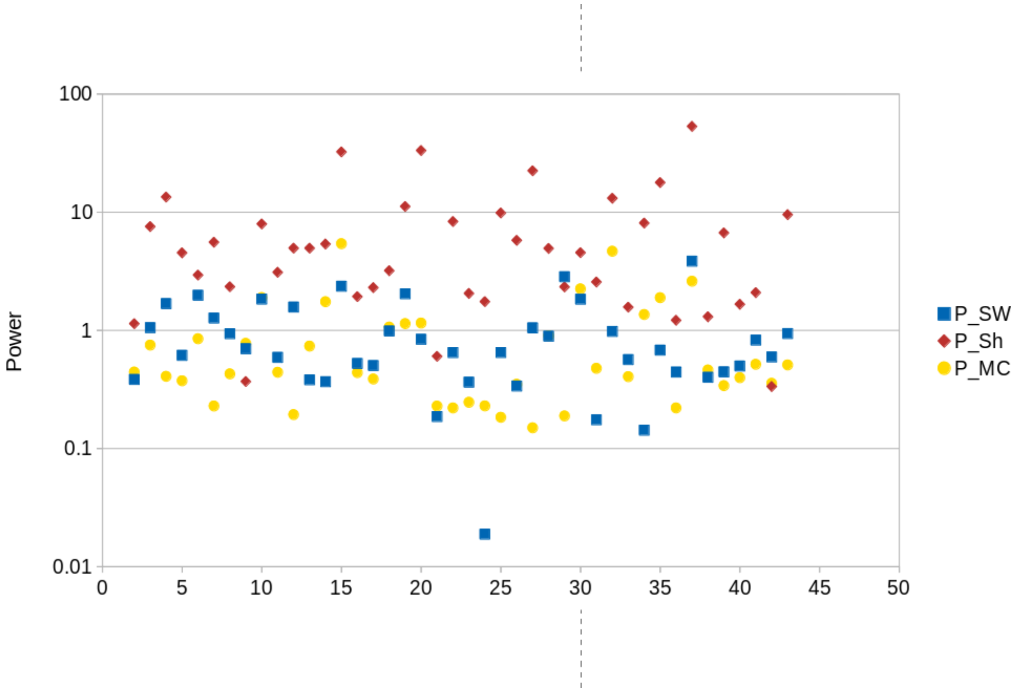

Figure 4.4: *Every event is labelled by a number from 1 to 42 represented on the horizontal axis. The vertical axis is the value of the Power P, which is the average quantity of energy per unit volume for a region of the event. The values of P vary between* 0.01 *and* 100 nT^2. *The power of the fluctuations* P_{SW} *in the solar wind preceding the sheath is represented in blue,* P_{Sh} *in the sheath in red and* P_{MC} *in the magnetic cloud in yellow.*

squares) preceding them. The fluctuations in the solar wind intervals, in turn, are more isotropic than those in magnetic clouds (yellow circles), and contain similar power. It can appear quite surprising that the fluctuations in magnetic clouds are almost as strong, in general, as the fluctuations in the quiet intervals of solar wind. We believe, however, that the initial intuition that magnetic clouds host only weak magnetic fluctuations comes from the fact that the eye tends to naturally compare the level of fluctuations to the mean value of the field. In other term, we are accustomed to think in terms of relative rather than absolute amplitude of the fluctuations. The values of P_{SW}, P_{Sh}, P_{MC} and A_{SW}, A_{Sh}, A_{MC} vary widely from one event to the other. While as a whole they seem to follow clear trends, every single event is quite unique.

P_{SW}	P_{Sh}	P_{MC}	
0.95 ± 0.79	7.9 ± 10.4	0.91 ± 1.1	(nT^2)
A_{SW}	A_{Sh}	A_{MC}	
6 ± 3	4 ± 3	14 ± 12	

Table 4.2: *Average power and anisotropy of the magnetic field fluctuations with their standard deviation in the different parts of the 42 events in* nT^2.

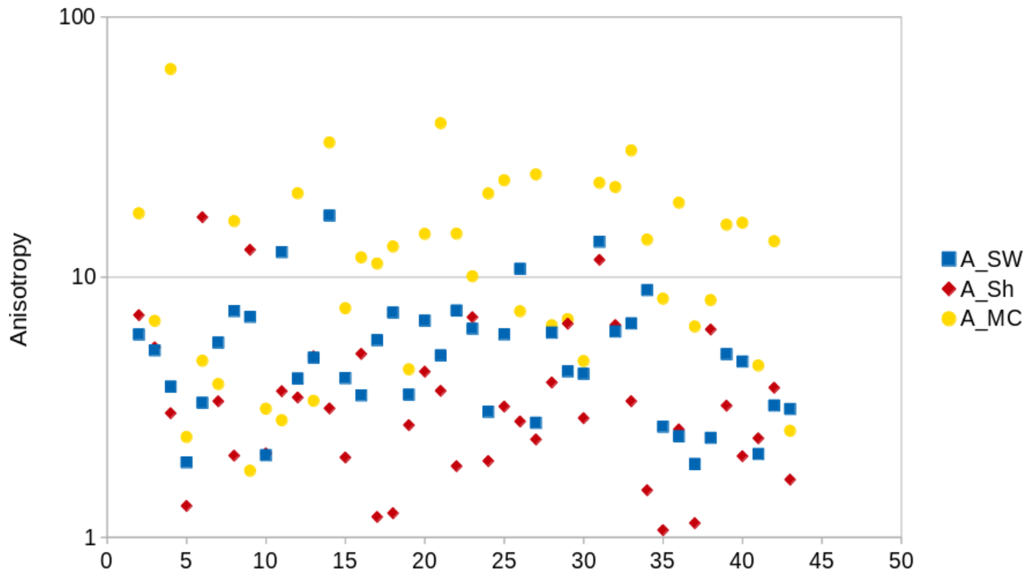

Figure 4.5: *Every event is labelled by a number from 1 to 42 represented on the horizontal axis. The vertical axis is the value of A, the anisotropy of the fluctuations of the magnetic field. In blue we represent A in the solar wind preceding the sheath, in red we represent the value of A in the sheath and in yellow we represent A in the magnetic cloud.*

Table 4.2 summarises the results displayed on figures 4.4 and 4.5. On average, the power of the fluctuations in the solar wind intervals are of 0.95 nT^2, which is almost equal to the power of the fluctuations in the magnetic clouds, of $P_{MC} = 0.91$ nT^2. The power in the sheaths is almost an order of magnitude higher, with $P_{Sh} = 7.9$ nT^2. The anisotropy is quite high in the magnetic clouds ($A_{MC} = 14$), and it is slightly lower in the sheaths than it is the solar wind intervals, with $A_{Sh} = 4$, and $A_{SW} = 6$. This makes sheaths the most compressible type of interval in our study.

4.3 Power and Anisotropy in a list of events (refined)

4.3.1 Discussion: On the complexity of sheaths

Going back to figure 4.2 on page 63, one can see that at the shock, slightly before 14:21, every frequency presents a heightened $\mathscr{W}$. The same thing can be seen around 5:38 when a small structure is encountered in the magnetic cloud.

Before going any further, we want to make sure that our results do not present artefacts from contingent physics. In the solar wind, and particularly around and inside sheaths regions, one can find many "events within the event", *i.e.* short regions which are present, but could as well not have been. There are two distinct reasons why these types of "events within the event", can be considered as "outliers" and are not welcome in an early analysis like ours.

The first reason is mathematical, and it is that a good part of these "outliers" involve quite sharp modifications of the magnetic field for which our analysis tools are misadapted. Indeed, as the field varies sharply and durably, the average magnetic field, as defined by equation (4.1), cannot follow its variations quickly enough, and mathematically, most of the field becomes then described as a fluctuation, which is nonphysical. Since the average magnetic field is mathematically ill-defined, the projections on it and the subsequent definitions of parallel and perpendicular fluctuations also do not make any sense. Moreover, Morlet wavelets see this kind of sharp and durable transition at all frequencies, and the spikes in power it produces are enormous, which completely skews the results for entire regions. We shall call these the "type I outliers". The shock, of course, is not contingent to the physics of the sheath; it has, however, to be removed from the analysis for the aforementioned reason, and is therefore included in the "type I outliers".

The second reason is that these "events within the event" can sometimes not really be representative of the regions in which they can be found, and their inclusion would blur the research of patterns in the sheaths and their surrounding regions. It is our intuition that they can have two types of origins: 1) They are not caused by the main structure of the event (*e.g.* by the dissipation of energy after the shock, or by the piling up of the solar wind), but are solitary waves or structures created outside of the magnetic cloud / sheath, and travelling through them, in which case we qualify them as contingent, rather than essential to the physics we are trying to uncover. 2) They are a result of the proximity of a frontier (shock or leading edge of the magnetic cloud); for example, the shock can reflect particles or generate upstream waves that propagate and heavily perturb the solar wind in close proximity to the sheath. Data containing these are also excluded from the analysis because they are not representative of the quiet solar wind, or magnetic cloud, with which the sheath interacts. Another point of view would be that these "events within the event" still do exist and are still very much part of the events. We fully acknowledge this, but prefer to leave it until more research is done on sheaths, and more data (*e.g.* lists of isolated sheaths) are available. We shall call these the "type II outliers".

4.3.2 Method: Definition of relevant zones

The way we decided to deal with these "outliers" is to use manually select *zones* on which we perform the analysis. This is as close as we can to follow the usual methods of solar wind studies. Indeed, in turbulence studies in the solar wind, it is usual to only do analyses on relatively homogeneous stretches of data. This is harder to do for data in and around sheaths. As we said previously, "events within the event" can come, broadly speaking, in two types of flavor. One (type I outliers) is a sharp change in the field, for which our tools are not adapted. We mostly avoid those when choosing the *zones*. Sometimes, we realised *a posteriori* that a *zone* contained a type I outlier and discarded it in the final analysis. The other type (type II outliers) are the stretches of data with a particularity that makes us suspect they found their origin outside of the region under study and are not really representative of the latter. These can be, for example, a small flux rope-like region in a sheath, or a very turbulent region in the solar wind. We analysed most of these stretches of data in their own particular zone, to deepen and test our understanding, but decided to discard them in final analysis.

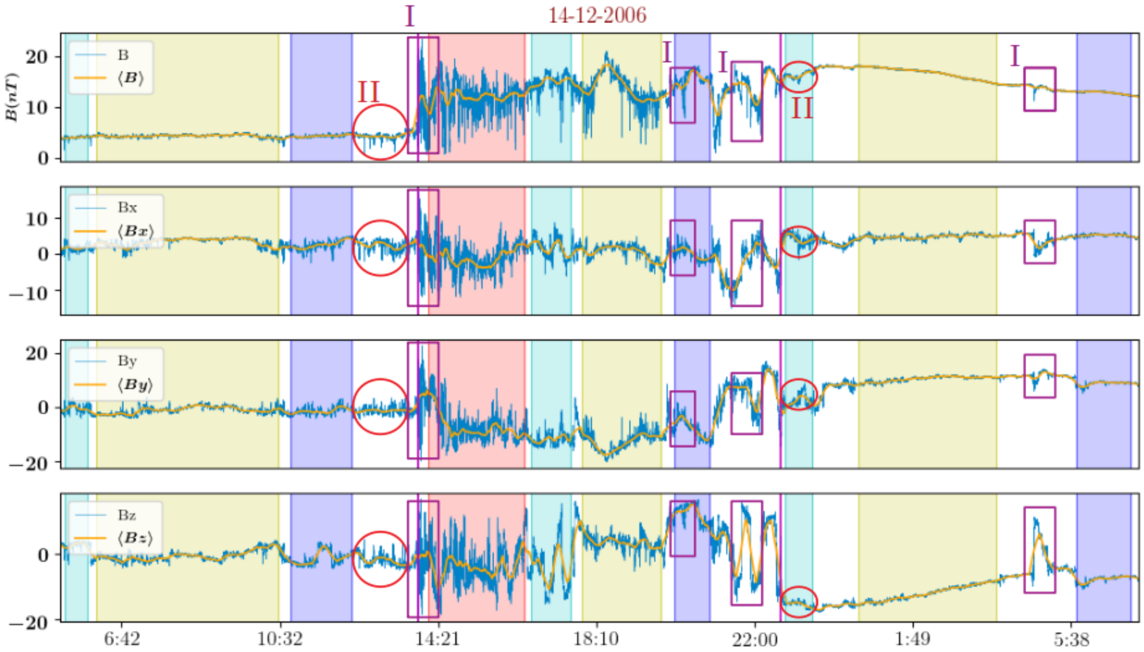

Figure 4.6: *Zones selection in the "14-12-2006" event. The sheath is delimited by the two purple vertical bars. From top to bottom we see the magnetic field amplitude, and its x, y, z components. Different zones are shown as coloured spans. The positions of type I outliers have been marked out by purple rectangles, and the type II outliers have been circled in red.*

Figure 4.6 shows the process of zones selection on the 14^{th} December 2006 event. Starting on the left side of the figure, in the solar wind interval preceding the sheath, we placed three zones: blue, yellow and purple spans. After the purple span, there is a type II outlier: a zone in the solar wind that contains a lot of fluctuations. It is probably due to its proximity to the shock wave. Because we want to know what the fluctuations in the solar wind look like before their interaction with the shock, we do not analyse the data on this stretch. Continuing from left to right, we encounter the shock, which is considered as a type I outlier: both our definition of fluctuations and the Morlet transform are not adapted to this kind of sharp change in the data. Then, there are a red, blue and yellow spans, which are analysed. The next purple zone contains a type I outlier and is discarded. There is then an area without any zone because it contains a few sharp changes in a row (type I outliers). The next blue span, when we enter the magnetic cloud is a type II outlier: it contains more fluctuations that the rest of the cloud, which is probably due to its proximity to the sheath. Since we placed a zone on it, we know the results, which are, for this zone called $MC1$: $P_{MC1} = 1.4$ nT^2, and $A_{MC1} = 10$; whereas in the rest of the magnetic cloud, we have $P_{MC} = 0.1$ nT^2 and $A_{MC} = 85$. This shows that this small stretch of data at the beginning of the cloud has characteristics between those of the sheath and those of the rest of the cloud. Slightly before 5:38, we see the type I outlier that caused the spike on the global wavelets analysis of figure 4.2, page 63. After this, there is a last purple span, which is analysed.

Once the "zones" are chosen, the Morlet analysis is applied on these separately. The results are then averaged to give the numbers P_{SW} and A_{SW}. The average is weighted proportionally to the time duration of the zones.

This "zone selection method" changes the previous results for the December 14^{th} 2006 event displayed in table 4.1 (page 66), to the results of table 4.3. These adjustments make the difference of power and anisotropy from one region to the next (solar wind, sheath, magnetic cloud) even clearer than it was in table 4.1: for example, the sheath has over ten times more power than the solar wind, and is much more isotropic that the magnetic cloud.

P_{SW}	P_{Sh}	P_{MC}	
0.7	11	0.1	(nT^2)
A_{SW}	A_{Sh}	A_{MC}	
5	2	85	

Table 4.3: *Power and anisotropy of the different regions of the "14-12-2006" event, with the "zone selection method".*

4.3.3 Definitive results: Anisotropy and power in sheaths

Using the “zone selection method” on every single event of the list gives the definitive results that were published in Moissard et al. (2019). They are reproduced here on the bottom panels of figure 4.7 (Power) and figure 4.8 (Anisotropy). The top panels of figures 4.7 and 4.8 display the “raw” results without the “zone selection method”: *i.e.* these are figures 4.4 and 4.5, reproduced here for comparison.

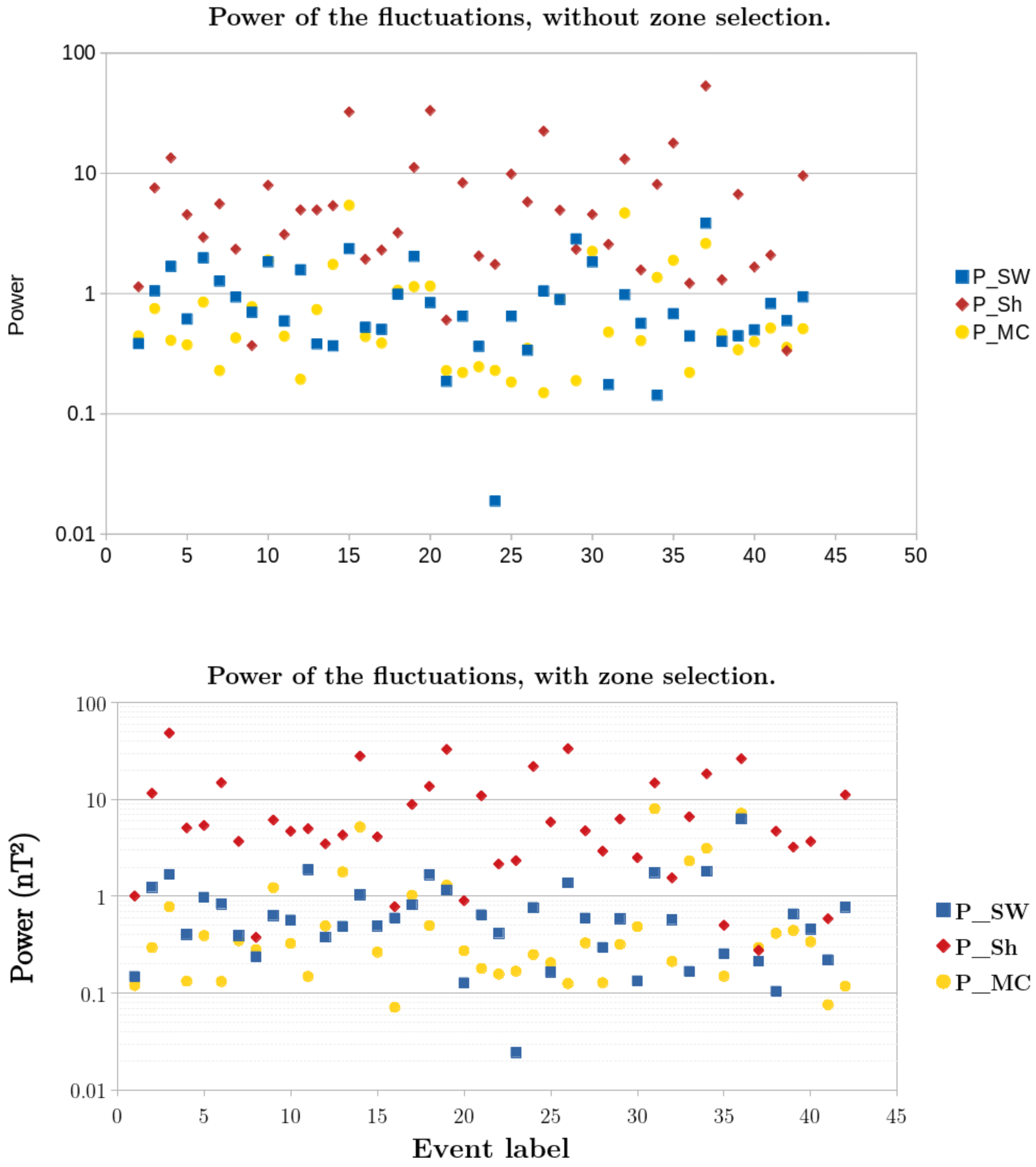

Figure 4.7: *Top: analysis without zones selection. Bottom: analysis with zone selection*

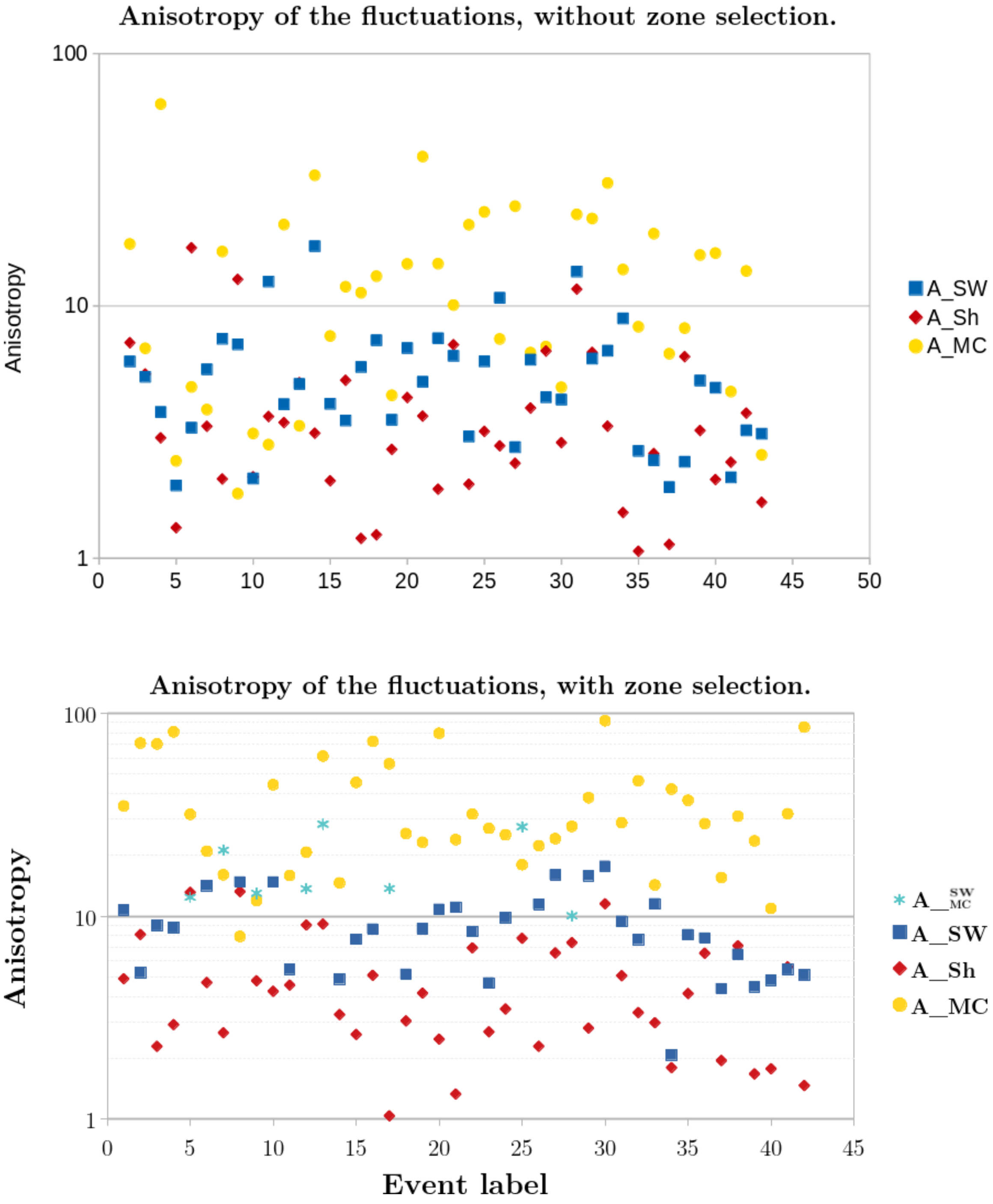

Figure 4.8: *Top: analysis without zones selection. Bottom: analysis with zone selection*

While the trends from the previous section 4.2 are conserved, the separation between the values obtained for the solar wind intervals, sheaths, and magnetic clouds, is much clearer in the bottom panels of figures 4.7 and 4.8. These "refined" results are summarised in table 4.4.

P_{SW}	P_{Sh}	P_{MC}	
0.8 ± 1.0	9.3 ± 10.8	1.0 ± 1.8	(nT^2)
A_{SW}	A_{Sh}	A_{MC}	
10 ± 6	5 ± 3	36 ± 23	
C_{SW}	C_{Sh}	C_{MC}	
0.07 ± 0.04	0.15 ± 0.08	0.02 ± 0.01	

Table 4.4: *Average power, anisotropy and compressibility of the magnetic field fluctuations and their standard deviation in the different parts of the 42 events; with the "zone selection method".*

Table 4.4 shows the power and anisotropy (compressibility) of fluctuations in sheaths, and allows to compare them to their values in the preceding stretches of solar wind and following magnetic clouds:
While in the solar wind the power of the fluctuations is relatively low ($P_{SW} \sim 0.8$ nT^2), it gains an order of magnitude in the sheaths, with $P_{Sh} \sim 9.3$ nT^2. The variability from sheath to sheath is large, with $\sigma P_{Sh} \sim 10.8$ nT^2. The power in the magnetic cloud is very similar to the power in the solar wind, with $P_{MC} \sim 1.0$ nT^2 (and $P_{SW} \sim 0.8$ nT^2).
The compressibility of sheaths is about twice what it is in the solar wind, with $C_{Sh} \sim 0.15$ (corresponding to $A_{Sh} \sim 5$) and $C_{SW} \sim 0.07$ (corresponding to $A_{SW} \sim 10$). In the magnetic clouds, the compressibility is very low, with $C_{MC} \sim 0.02$ (coresponding to a large anisotropy of $A_{MC} \sim 36$).

To our knowledge, these results are new in three ways: they give a statistical, quantitative estimation of the power and anisotropy of magnetic fluctuations in sheaths; they show that the power of the fluctuations in the solar wind and magnetic clouds are very similar, contrary to intuition; and they show that fluctuations in sheaths are much more compressible than in other environments.

> **Note:** The equivalence made in this chapter between anisotropy and incompressibility is specific to the solar wind, and comes down to the fact that most of the fluctuations' power is contained in the perpendicular fluctuations. Usually, compressibility is defined as $C = P_{||}/P$. The anisotropy is defined as $A = P_{\perp}/(2P_{||})$. If we allow ourselves to write $P = P_{\perp}$, then $C = P_{||}/P_{\perp} = 2/A$. Defining the incompressibiliy as the inverse of the compressibility, we see that, in the solar wind, where indeed $P \simeq P_{\perp}$, the incompressibility is directly proportional to the anisotropy as defined above.

4.3.4 Unpublished result: Studying the spectra's slopes

It has been reported in the literature that slow streams and fast streams do not have the same spectra slopes (*e.g.* Marsch (1991), Bruno et al. (2014)). However, to our knowledge, such an analysis has never been pursued specifically on sheaths.

We performed the same analysis as presented in the rest of this chapter on the slopes of the spectra: the results are given in figure 4.9, and table 4.5. On figure 4.9, the slopes tend to fall on each side of the expected Kolmogorov slope of -1.66. One could be tempted to conclude that the slopes are in general steeper in the sheaths than in the magnetic clouds, where they are in turn steeper that in the solar wind intervals. However, the large uncertainties and the fact that the three averages for solar wind intervals, sheaths and magnetic clouds fall slightly short of -1.66 (see table 4.5) made us wary of publishing these results before pushing the analysis further.

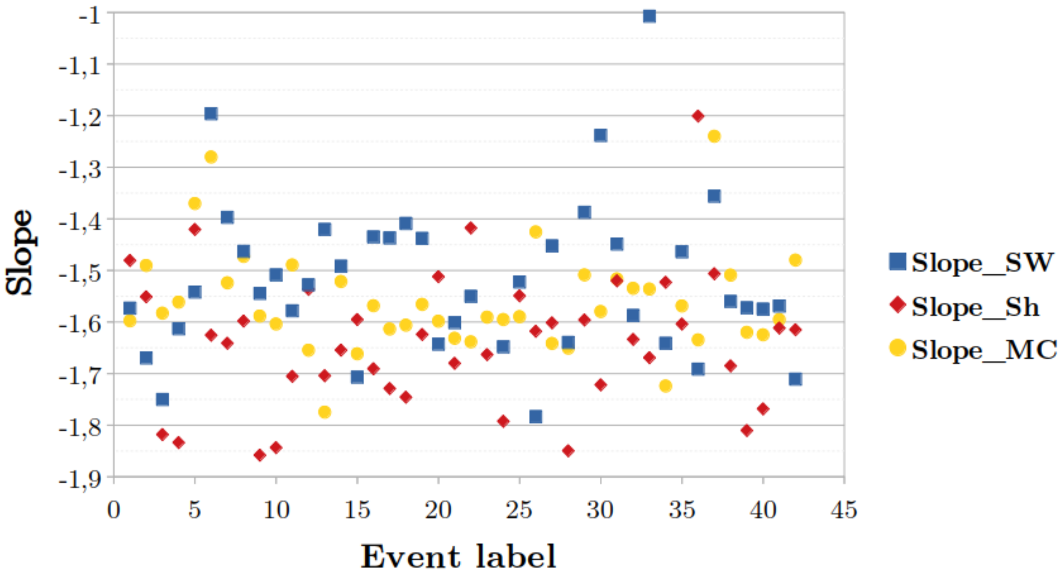

Figure 4.9: *The vertical axis is the value of the slope of the fluctuation spectrum in the solar wind intervals (blue), sheaths (red) and magnetic clouds (yellow).*

$Slope_{SW}$	$Slope_{Sh}$	$Slope_{MC}$
-1.49 ± 0.23	-1.64 ± 0.13	-1.56 ± 0.1

Table 4.5: *Average slopes of the spectrum of the magnetic field fluctuations and their standard deviation in the different parts of the 42 events; with the "zone selection method".*

4.4 Parameters influencing the magnetic fluctuations

The first part of this work showed that sheaths contain a lot of turbulent magnetic energy, and that the fluctuations of the magnetic field are relatively isotropic, or compressible. Now the question is: what are the parameters that influence these two characteristics? In other words, if we were to define a “good” sheath as a sheath with high power and low anisotropy, what would be the ingredients that make a “good” sheath?

To answer this question, we use the same data that were used to generate figures 4.7 and 4.8 and try and order them by another parameter. Indeed, in those figures, the order of the data points was quite arbitrarily chosen to be the order of apparition of the event in Masías-Meza et al. (2016)’s list, *i.e.* chronological. We can also order these data points with some more physical quantities such as the Mach number of the shock, the angle between the interplanetary magnetic field in the solar wind and the shock’s normal, *etc.*

A summary of the approach used in this section is this:

The power and anisotropy, as defined in section 4.2 and further refined with the method outlined in section 4.3 are seen as an output. We define some physically relevant parameters that we expect to have an influence on this output. These parameters are then seen as an input. We try to answer the question: which input parameters indeed have a visible impact on the output, and what kind of impact is it?

4.4.1 Computing the input parameters

The input parameters we focus on are some sort of macroscopic characteristics of the sheath. As a general concept, it is easy to form a vague idea of what "the velocity of a sheath" is, or "the amount of fluctuations in the preceding solar wind". Giving numbers corresponding to these ideas can be done in a lot of different ways. We chose to use the tried and true method described at `https://ipshocks.fi/documentation`, and adapted it to our particular needs.

As an example, let us give a definition for the Alfven Mach number of the sheath. The theoretical expression for this quantity is $M_A = \frac{|\boldsymbol{V}_{up} \cdot \hat{\boldsymbol{n}} - V_{shock}|}{V_{Aup}}$, so we need a definition of $\boldsymbol{V}_{up}$, the velocity of the solar wind upstream of the shock, of the shock’s normal $\hat{\boldsymbol{n}}$ and of the shock’s speed V_{shock}.

Following the `https://ipshocks.fi/documentation`’s method, we define $\boldsymbol{V}_{up}$ as the average bulk velocity of the plasma in a 15 min-long interval starting 30 min, and ending 15 min, ahead of the shock. The 15 min interval just upstream of the shock is ignored because the plasma in there is likely to have "seen" the shock due to fast particles moving upstream, fast waves (*e.g.* whistler waves) travelling upstream, or intricate phenomena such as shock reformation (*e.g.* Lembège and Savoini (2002); Lembège et al. (2009)).

The normal of the shock $\hat{\boldsymbol{n}}$ is a particularly tricky one to define when the only available measurements come from a single satellite. The following definition makes use of the equations of MHD (conservation of the transverse electric field $\boldsymbol{V} \times \boldsymbol{B}$ and of $\boldsymbol{B} \cdot \hat{\boldsymbol{n}}$) to define $\hat{\boldsymbol{n}}$:

$$\hat{\boldsymbol{n}} = \frac{(\boldsymbol{B}_{down} - \boldsymbol{B}_{up}) \times ((\boldsymbol{B}_{down} - \boldsymbol{B}_{up}) \times (\boldsymbol{V}_{down} - \boldsymbol{V}_{up}))}{|(\boldsymbol{B}_{down} - \boldsymbol{B}_{up}) \times ((\boldsymbol{B}_{down} - \boldsymbol{B}_{up}) \times (\boldsymbol{V}_{down} - \boldsymbol{V}_{up}))|} \tag{4.7}$$

If we imagine, for example, that the term $(\boldsymbol{V}_{down} - \boldsymbol{V}_{up})$ is parallel to $\hat{\boldsymbol{e}}_{\boldsymbol{x}}$ (shock propagating radially, anti-sunward), we can readily see that the previous formula gives us $\hat{\boldsymbol{n}}||\hat{\boldsymbol{e}}_{\boldsymbol{x}}$.

Defining the shock speed V_{shock} also makes use of MHD theory. Indeed V_{shock} is the velocity of the frame in which the equation of mass conservation $(N_{down}(\boldsymbol{V}_{down} - \boldsymbol{V}_{shock}) = N_{up}(\boldsymbol{V}_{up} - \boldsymbol{V}_{shock}))$ is verified:

$$V_{shock} = \left| \frac{N_{down}\boldsymbol{V}_{down} - N_{up}\boldsymbol{V}_{up}}{N_{down} - N_{up}} \cdot \hat{\boldsymbol{n}} \right| \tag{4.8}$$

In this equation, some parameters correspond to the downstream of the shock (down subscript), which are defined as the average of a quantity in a 15 min-long interval starting 15 min after the shock. Their definition mirrors the definition of the upstream (up subscript), which are defined as the average of a quantity in a 15 min-long interval starting 30 min before the shock.

4.4.2 Testing outputs against one input parameter

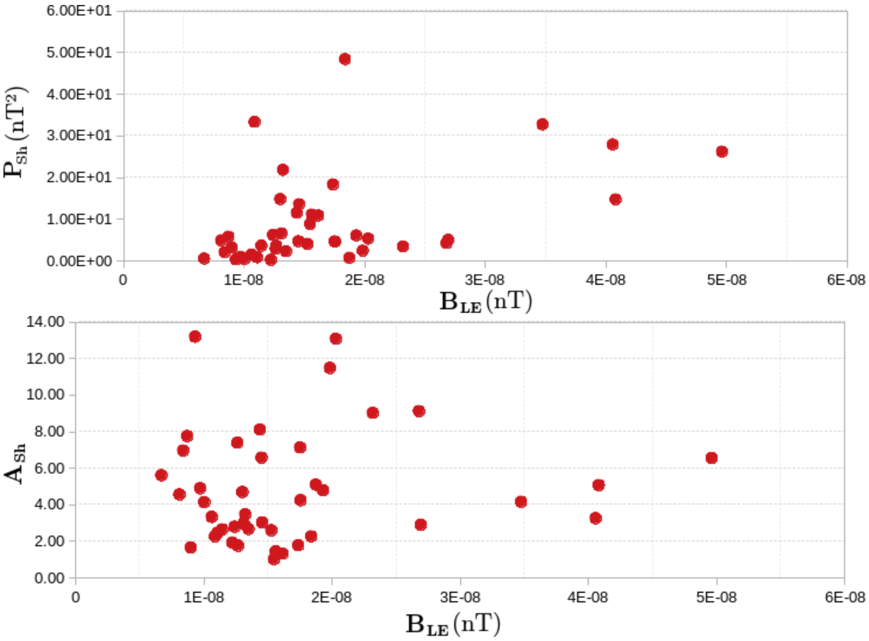

Figure 4.10: *For every event, a red dot is placed on the diagram shown above with, on the vertical axis the power or the anisotropy in the sheath (output parameter) and on the horizontal axis the amplitude of the magnetic field at the leading edge (LE) of the magnetic cloud (input parameter)*

In figure 4.10, a red dot is placed for every sheath in Masías-Meza et al. (2016)'s list. The y-axis corresponds to the power or the anisotropy in the sheath (output parameter) and the x-axis corresponds to the amplitude of the magnetic field at the leading edge (LE) of the magnetic cloud (input parameter). Figure 4.10 is exactly the same as figures 4.7 and figures 4.8 where we have kept only the red dots (sheaths), and ordered these in terms of the amplitude of the magnetic field in the beginning of the magnetic cloud. This particular figure, like many others that are not shown in this thesis, do not elicit much in terms of conclusions: it is hard to see any clear pattern. This is interesting in itself, as it tells us that the magnetic field's amplitude in the magnetic cloud does not seem to have any clear influence on the fluctuation content of the sheath preceding it.

The most interesting results, reproduced from Moissard et al. (2019) are figure 4.11 displaying the impact of the magnetic cloud's velocity V_{LE} on the sheaths' fluctuations; figure 4.12 which displays the role of the fluctuations already present in the solar wind (characterised by P_{SW} and A_{SW}); and figures 4.13, 4.14 and 4.15 which study the role played by the shock's parameters (Alfvén Mach number M_A, upstream plasma beta β_{up}, and shock angle θ_{Bn}).

The velocity of the magnetic cloud

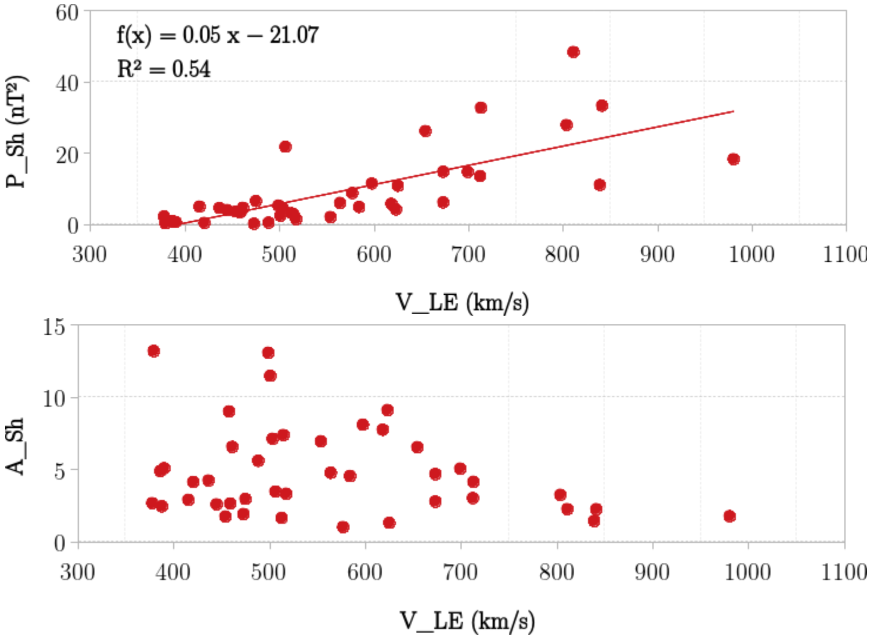

Figure 4.11: *y-axis: Power or Anisotropy in the sheath. x-axis: amplitude of the velocity at the leading edge (LE) of the magnetic cloud*

Figure 4.11 shows the dependency of the sheath fluctuations on the velocity V_{LE} of the beginning of the magnetic cloud (LE stands for leading edge). We can see a relatively clear pattern: as the velocity increases, P_{Sh} tends to increase, while A_{Sh} seems to be limited to smaller and smaller values. On the upper panel, we superimposed a linear fit on the scattered red dots: a coefficient of determination of $R^2 = 0.54$ corresponds to a correlation coefficient of $R = 0.73$ which is generally considered as a sign of a moderately high correlation (*e.g.* Mukaka (2012)). It is not surprising that R^2 is not higher, since we do not expect the velocity of the magnetic cloud do be the only important parameter for the fluctuations in the sheath.

The fluctuations in the upstream solar wind interval

Next, in figure 4.12 we compare the fluctuations in the sheaths with the fluctuations in the solar wind that precedes them. We do not find any correlation between the anisotropy in the sheath A_{Sh} and the fluctuations in the solar wind: indeed on panel a) and c) on the left side of the figure, we can see that both P_{SW} and A_{SW} can correspond to any value of the A_{Sh}. Panel b) (top right) shows that high values of P_{Sh} are not reached when A_{SW} is high but only for a hardly significant number of cases, whereas values of P_{Sh} span the whole range when A_{SW} is low: there is no visible correlation between P_{Sh} and A_{SW}. The power of the fluctuations in the solar wind P_{SW}, however, seems to moderately correlate with the power of the fluctuations in the sheath P_{Sh}. Indeed, in panel d), a linear fit indicates a link between P_{Sh} and P_{SW}, while also making clear that P_{SW} is not the only factor at play (Coefficient of determination $R^2 = 0.42$, or $R = 0.65$). This may indicate that the power of the fluctuations in the solar wind has an effect on the fluctuations in the sheath. However, it could also be that sheaths that are highly turbulent are also likely to emit strong upstream waves or reflect a quantity of particles

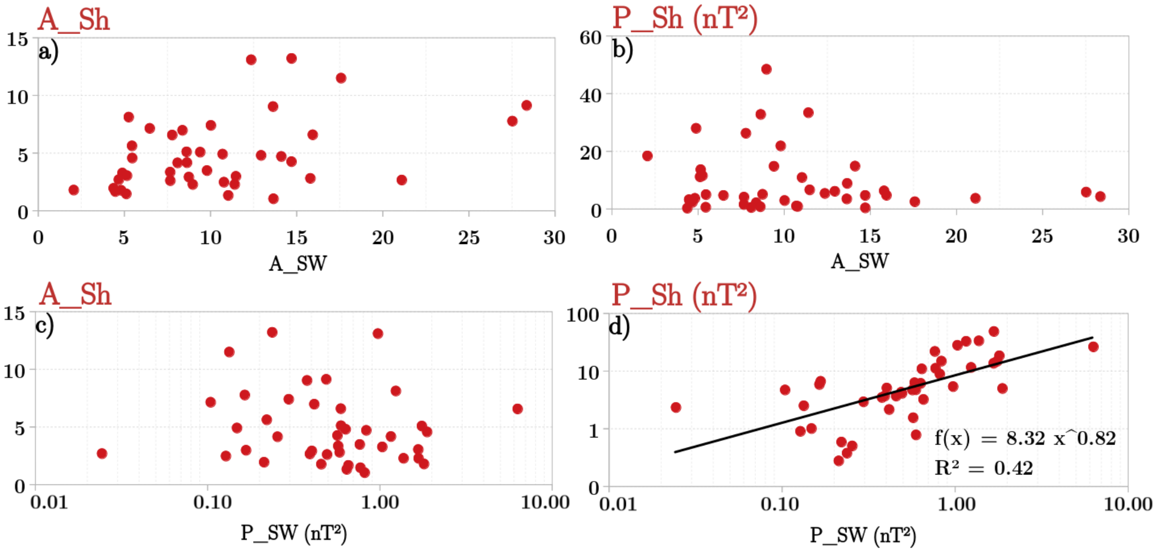

Figure 4.12: *y-axis: Power or Anisotropy in the sheath. x-axis: Power or Anisotropy in the preceding solar wind*

far upstream; in other words, P_{SW} and P_{Sh} could have a common origin. In any case, in the events studied in this analysis, highly turbulent sheaths are likely to be preceded by highly turbulent solar wind intervals.

The parameters of the shock

We now concentrate on the effect of the shock's parameters on the sheath's fluctuations. Indeed, the shock is *a priori* one of the main factors in the downstream structure of the sheath (Kataoka et al. (2005)). Figures 4.13, 4.14 and 4.15 show the sheath's anisotropy and power as functions of the shock's main parameters M_A, β_{up} and θ_{Bn}.

On the top panel of figure 4.13 we observe that for low values of the Alfvén Mach number ($M_A < 4$ or so) A_{Sh} can take on any value. The values of A_{Sh} seem to be more constrained at higher values of M_A. On the bottom panel, we see that for $M_A < 4$ or so, most P_{Sh} do not reach higher values than 10 nT^2. At higher values of M_A, the power tends to be high, and the anisotropy tends to be low. These two patterns are similar to the ones observed in figure 4.11 where we compared the fluctuations in the sheaths with the velocity of the magnetic cloud. This is not surprising: the velocity of the cloud and the Mach number of the shock should be intimately linked and can both serve as a proxy for the energy to be dissipated by the shock. We can see, though, that the regression coefficient of the linear fit on the bottom panel is - surprisingly - quite low, indicating that the shock's Mach number is a poorer predictor of the power of the fluctuations in the sheath than the velocity of the magnetic cloud. Rather, it seems that the value $M_A \sim 4$ serves as a threshold for the state of the fluctuations downstream of the shock.

On figure 4.14, one can see that values of $\beta_{up} > 1.1$ or so are associated with a smaller range of values for both A_{Sh} and P_{Sh}, whereas almost any type of fluctuations can be found at $\beta_{up} < 1.1$. A

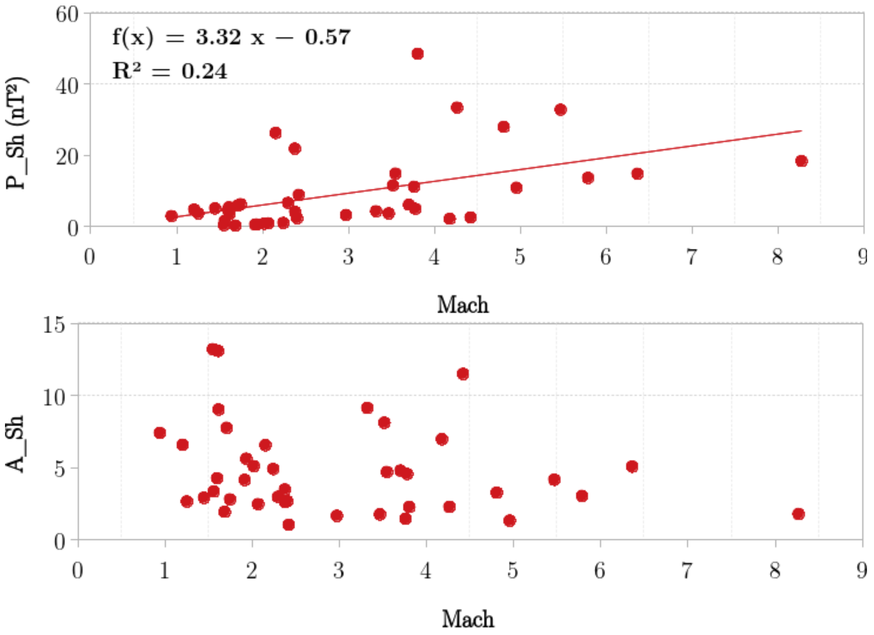

Figure 4.13: *y-axis: Power or Anisotropy in the sheath. x-axis: Alfvén Mach number of the shock*

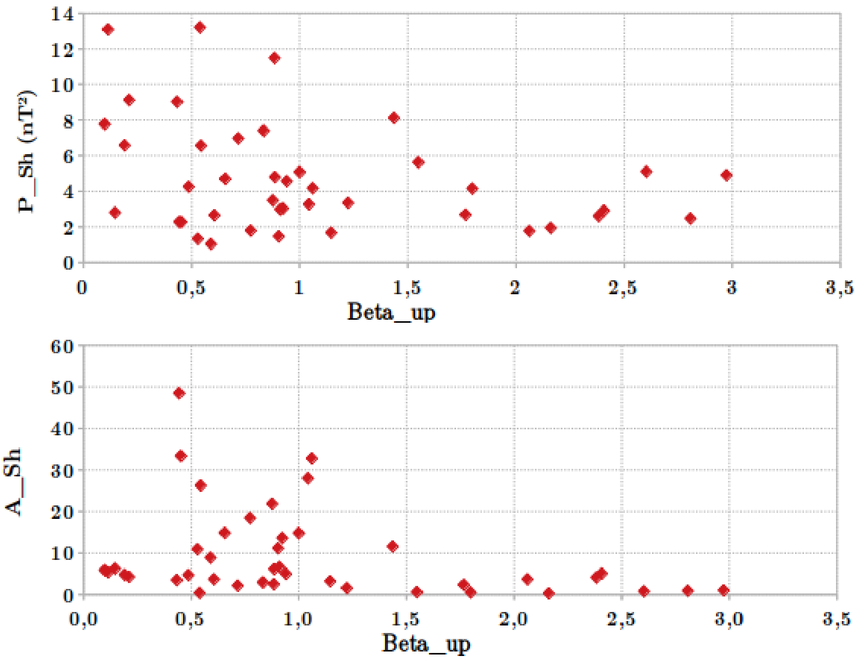

Figure 4.14: *y-axis: Power or Anisotropy in the sheath. x-axis: Plasma beta in the preceding solar wind*

possible interpretation is that high β_{up} events are dominated by the physics of thermal agitation. A large thermal agitation, if not constrained by a strong magnetic field, would lead to a low anisotropy. It would also lead to a small amount of fluctuations because there is not much magnetic field to compress. A low β_{up} would mean that the physics is dominated by a strong magnetic field, potentially leading to a high anisotropy, and fuelling the fluctuations.

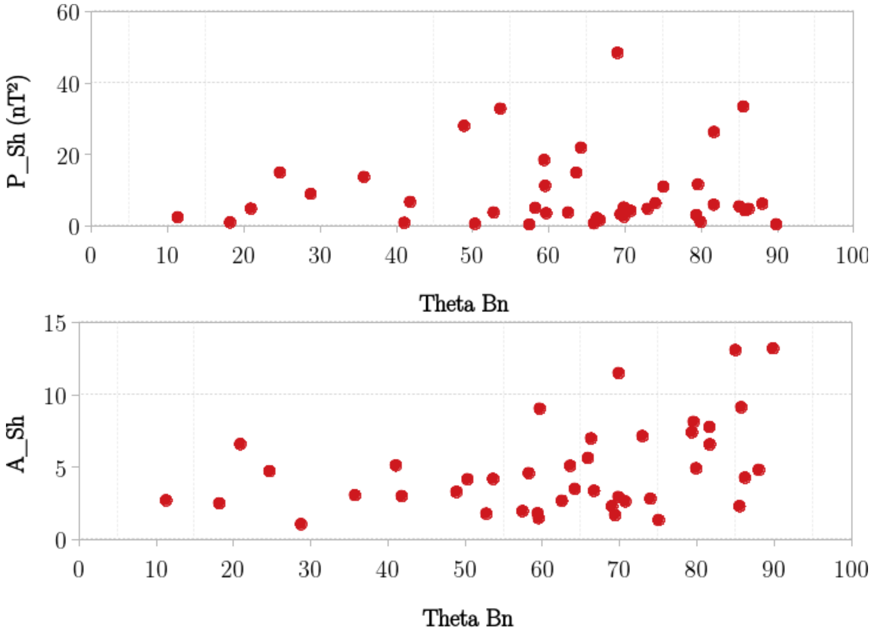

Figure 4.15: *y-axis: Power or Anisotropy in the sheath. x-axis: Angle between the interplanetary magnetic field and the shock's normal*

Similarly, we can see on figure 4.15 that the ranges of values accessible to A_{Sh} and P_{Sh} seem to be constrained by θ_{Bn}. For $\theta_{Bn} < 45°$ (indicative of quasi-parallel shocks) the trend shows that $A_{Sh} < 7$ and $P_{Sh} < 15$ nT^2. The fact that quasi-parallel shocks show a relatively low level of turbulence in the sheath is rather surprising as we generally expect the opposite behaviour (Treumann (2009)). A tentative explanation of this peculiar behaviour is that the low compression (characteristic of quasi-parallel shocks) by the shock of the fluctuations contained in the upstream solar wind could lead to only on low level of fluctuations inside the sheath. For small angles, there is only a limited number of events, so these conclusions should be taken with some reserve until the effect of the angle has been studied with more cases. For higher values of θ_{Bn} (indicative of quasi-perpendicular shocks), A_{Sh} and P_{Sh} explore the whole range of values.

4.4.3 Unpublished results: multiple input parameters

Figures 4.11 or 4.12, for example, gave us imperfect correlations between sheaths' fluctuations and single input parameters. It is then clear that the output parameters do not solely depend on a single input parameter. It is tempting then, to try and find a combination of input parameters that would, once woven into a formula, provide us with a good prediction for the output parameters.

An approach to find such a function is the multiple linear regression. We assume that the output parameter depends on a set of input parameters through a formula of the type:

$$\text{output} = a \times \text{input}_a^{\alpha} + b \times \text{input}_b^{\beta} + c \times \text{input}_c^{\gamma}... \quad (4.9)$$

Then we run this function through a multiple linear regression algorithm that gives us the parameters a, α, b, β, c, and γ together with a margin of certainty. This approach is used in an array of different circumstances, as for example the study of the impact of gender and age on salary (*e.g.* Billard (2017)).

It is more common, in physics, to use an expression based on multiples rather that sums of the input parameters:

$$\text{output} = C\text{input}_a^{\alpha}\text{input}_b^{\beta}\text{input}_c^{\gamma}... \quad (4.10)$$

C is a constant of proportionality. Using a logarithm on both sides of (4.10) gets us back to an expression of the form (4.9), which is the one most multiple linear regression algorithms are built to use.

When testing outputs against single input parameters (subsection 4.4.2), it appeared that the most important parameters to predict the behaviour of the fluctuations in the sheath seemed to be the power of the fluctuations in the solar wind P_{SW} the velocity of the leading edge of the magnetic cloud V_{LE}, the plasma Beta upstream of the shock β_{up} and the angle between the magnetic field upstream of the shock and the normal to the shock θ_{Bn}. The Alfvén Mach number and the velocity of the magnetic cloud are clearly dependent on each other, so we do not use M_A here. It thus seemed natural to hope to find a formula of the form:

$$\text{Power} = C \times P_{SW}^{\alpha} V_{LE}^{\beta} \beta_{up}^{\gamma} \theta_{Bn}^{\delta} \quad (4.11)$$

This is what we fed a multiple linear regression tool (we used the Python module '*statsmodels*'), using the logarithm method outlined above.

Figure 4.16 represents the power or the anisotropy in the sheath against the best fit based on equation (4.10). On the top panel, we can see for example that the best fit results in a squared correlation coefficient of $R^2 = 0.65$. This corresponds to a correlation coefficient of $R = 0.81$, which is just enough to be considered significant. It is also better than our best correlation with a single parameter: $R^2 = 0.54$ between P_{Sh} and V_{LE} on figure 4.11. The best fit found by the multiple linear regression method is:

$$P_{Sh} \simeq C \times P_{SW}^{0.34} V_{LE}^{3.1} \beta_{up}^{-0.086} \theta_{Bn}^{-0.34} \quad (4.12)$$

This equation is interesting because it seems to tell us that the power in the solar wind P_{SW} and the angle between the normal of the shock and the magnetic field in the solar wind θ_{Bn} have an approximately equal importance on the value of P_{Sh}. It also tells us that the most important parameter is the velocity of the magnetic cloud's leading edge. These are also the conclusions of Moissard et al. (2019). The role of the β_{up}, however, is completely masked by this approach. This makes sense, when looking at P_{Sh} versus β_{up} (see figure 9 in Moissard et al. (2019)), we did not find any correlations. We did find, however, that for $\beta_{up} > 1.1$, the power tended to drop drastically. This kind of threshold-based behaviour cannot be well represented by a linear fit.

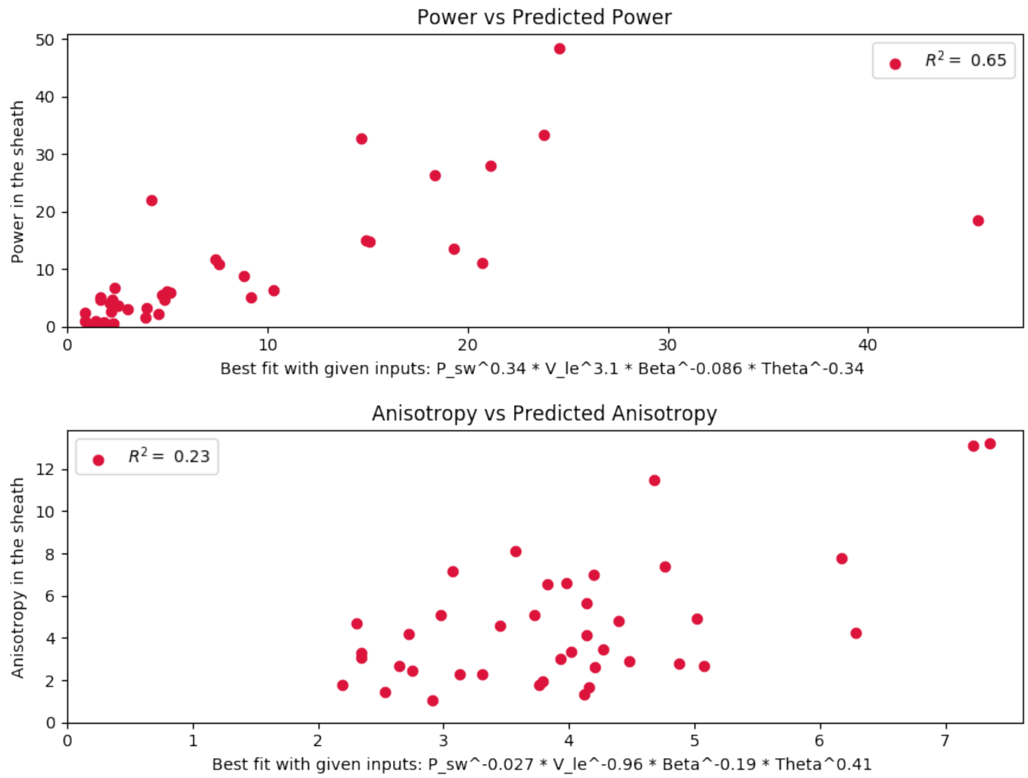

Figure 4.16: *For every event, a red dot is placed on the diagram shown above with, on the vertical axis the power or the anisotropy in the sheath (output parameter) and on the horizontal axis the best fit based on equation* (4.10).

The bottom panel of figure 4.16 shows a very poor correlation between A_{Sh} and its best fit based on equation (4.10). Because early results were underwhelming, we decided to move on. With more work, however, this approach might still prove to be fruitful.

4.5 Summary and conclusions

Analysing a single textbook-like event, we found that the fluctuations in the sheath were more powerful and isotropic than in the preceding solar wind interval and the following magnetic cloud (section 4.1).

In section 4.2, we then presented a simple process to condense the results of an analysis on a single sheath, which allowed us to perform the same analysis on a list of 42 relatively isolated sheaths (Masías-Meza et al. (2016)). We found that the fluctuation power in the sheaths (7.9 ± 10.4) was almost ten times higher than in the solar wind (0.95 ± 0.79) and magnetic clouds (0.91 ± 1.1). The anisotropy was slightly less in sheaths (4 ± 3) than in the solar wind (6 ± 3), and the magnetic clouds had an elevated anisotropy (14 ± 12).

In order to refine our analysis (section 4.3), we manually selected *zones* of homogeneous data in the solar wind intervals, sheaths, and magnetic clouds, on which the tools we used (averaging, Morlet transforms) could be applied confidently. This selection made more obvious the difference between the different regions (solar wind, sheath, magnetic cloud) while keeping the same trends: the fluctuation power in the sheaths (9.3 ± 10.8) was almost ten times higher than in the solar wind (0.8 ± 1.0) and magnetic clouds (1.0 ± 1.8). The anisotropy was slightly less in sheaths (5 ± 3) than in the solar wind (10 ± 6), and the magnetic clouds had a markedly elevated anisotropy (36 ± 23). We therefore find that sheaths contain fluctuations that are, generally, compressible. This is congruent with, for example Ala-Lahti et al. (2018) who found that sheaths were an excellent place for the formation of mirror-modes, which are a type of wave one can find in compressible media.

In order to get a better understanding of the physics leading to the fluctuations in sheaths (section 4.4), we used the results from this analysis (values for the power and anisotropy in sheaths) and looked for correlations between these and paramaters describing the sheaths' surroundings (solar wind, shock, magnetic cloud). We found that the parameters with the strongest influence on the power and anisotropy of the fluctuations in the sheaths of these events, are mainly:

(i) the speed of the magnetic cloud,
(ii) the Alfvén Mach number of the shock,

as these two parameters increase, the power and isotropy of the fluctuations in the sheath increase.

(iii) the pre-existing fluctuation power in the solar wind,

to which the power in the sheath is roughly proportional but not the anisotropy.

(iv) the angle between the shock's normal and the magnetic field upstream of the shock,
(v) the beta of the solar wind,

which have a somewhat more subtle role. $\beta \sim 1.1$ in the solar wind serves as a threshold above which both the power and the anisotropy of the fluctuations in sheaths drop significantly. Similarly, quasi-parallel shocks have both low power and anisotropy whereas any values of P_{Sh} and A_{Sh} can be found next to quasi-perpendicular shocks.

Figure 4.17 summarises these results.

Following are our interpretations for the roles of these different parameters:

Velocity of the magnetic cloud and shock Mach number

The enhanced kinetic energy carried by fast magnetic clouds is dissipated in the sheath, giving rise through turbulent processes to small-scale structures, such as powerful magnetic fluctuations.

Pre-existing fluctuation power in the solar wind

A high level of magnetic fluctuations pre-existing in the solar wind can be compressed by the shock and lead to high fluctuations power in the sheath. This explanation only, however, would primarily lead to the compression of perpendicular fluctuations and lead to a high anisotropy. Yet, we do not observe such a correlation. This points to the conclusion that, on top of the strengthening of upstream fluctuations, a significant amount of fluctuations are created by the shock/sheath.

The shock's angle

Downstream of a quasi-perpendicular shock ($\theta_{Bn} > 45°$), both the fluctuation power and anisotropy in the sheaths cover a wide range of values. Downstream of quasi-parallel shocks ($\theta_{Bn} < 45°$), there

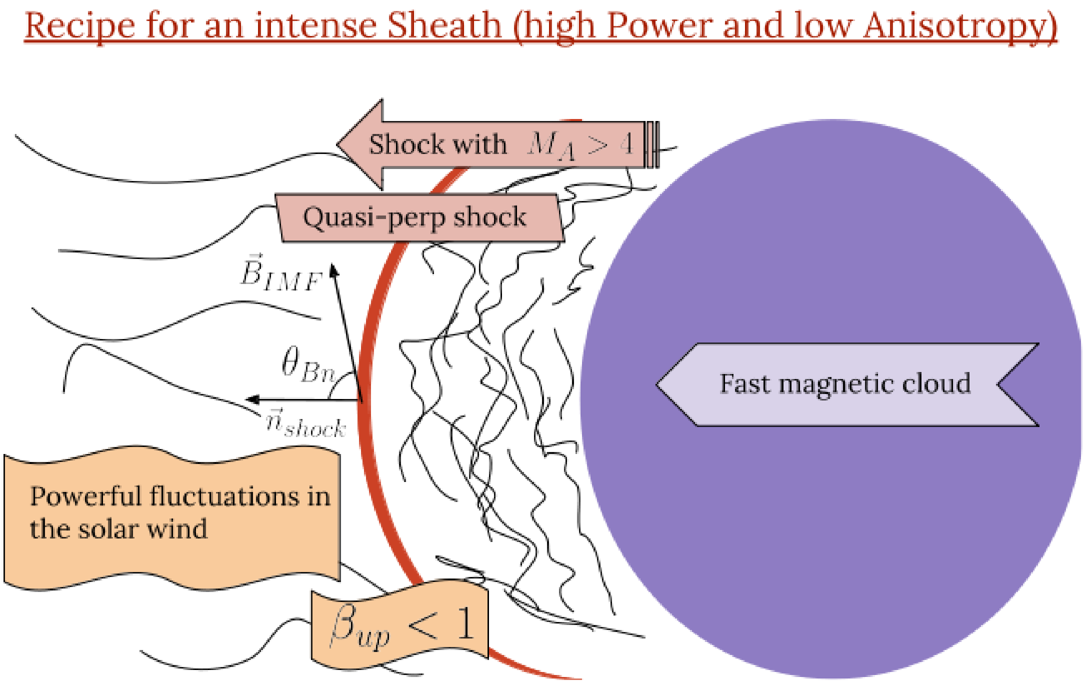

Figure 4.17: *Characterising the fluctuations in sheaths by two numbers (Power and Anisotropy), we find that, compared with the solar wind, sheaths have high power and low anisotropy. This is further enhanced when certain parameters are found in the magnetic cloud, shock and solar wind surrounding the sheaths. On the right side, the magnetic cloud is represented in purple. The shock is represented as a thick red line toward the center of the figure. Between the shock and the magnetic cloud, the sheath is drawn as a complex mix of twisted black lines in order to represent its high levels of fluctuations. The solar wind prior to the shock is represented as slightly twisted black lines to represent its lower levels of fluctuations compared with the sheath. The main "ingredients" for an "intense" sheath (high power and low anisotropy) are represented as flags directly on the figure.*

is a trend toward more isotropy, which is expected. However the fluctuation power goes down to low values, which is the opposite of what we find behind the terrestrial bow shock Blanco-Cano et al. (2006); Du et al. (2008b). The low number of quasi-parallel shocks in our set of data do not allow us to make any conclusion. The latter effect (low power) might be linked to a weaker compression of the interplanetary magnetic field in quasi-parallel than in quasi-perpendicular configurations, leading to weaker magnetic fields in the sheath and maybe to weaker fluctuations. Such an effect would require to be more deeply investigated.

Plasma beta

Below a threshold value of about 1.1, the fluctuation power and anisotropy in the sheath cover a wide range of values without any obvious correlation. Above this threshold value of 1.1, both the sheath power and anisotropy reduce to weak values. In this case, the thermal energy exceeds the magnetic energy and therefore the magnetic fluctuations might become a secondary effect, possibly less powerful and guided than in presence of a strong magnetic field.

In a few words

Sheaths have elevated levels of fluctuations ($P_{Sh} \simeq 9.3$ nT^2) compared to the solar wind ($P_{SW} \simeq 0.8$ nT^2) and magnetic clouds ($P_{MC} \simeq 1.0$ nT^2) . These fluctuations are also more compressible ($C_{Sh} \simeq 0.15$) than in the solar wind ($C_{SW} \simeq 0.07$) and magnetic clouds ($C_{MC} \simeq 0.02$).

The power and anisotropy of the fluctuations depend mostly on the speed of the magnetic cloud ($R^2 = 0.54$), the Alfvén Mach number of the shock (threshold at $M_A \sim 4$ under which the power is relatively low and the anisotropy can be high), the pre-existing fluctuation power in the solar wind ($R^2 = 0.42$), whether or not the shock is quasi-perpendicular or quasi-parallel, and the beta in the upstream the solar wind (threshold at $\beta \sim 1.1$ above which both the power and anisotropy are quite low).

5. Numerical simulations: Methods

Note: This chapter starts with section 5.1, describing the pre-existing code used in this work: LatHyS. It then describes in general terms the objective of the new developments made in LatHyS during this PhD (section 5.3.1). Section 5.2 describe the choices we made in the pre-existing LatHyS framework. Section 5.3 is where the work described changes from "user" to "developer" and shows how a magnetic cloud was introduced in the simulation, leading to the auto-consistent formation of an interplanetary sheath. Section 5.4 describes some adaptations made to the saving of data during LatHyS simulations. This chapter finishes with section 5.5, which describes the visualisation tools we created specifically for the analysis of the highly dynamic processes explored in this work.

Most of the codes presented in this section can be found at `https://github.com/cmoissar/`.

Note: In this chapter, the term "sheath" is used to refer to the sheath self-consistently created upstream of the magnetic cloud and downstream of the interplanetary shock. The term "magnetosheath" is used to refer to the sheath formed self-consistently upstream of the obstacle and downstream of the bow shock.

Note: The simulation described in this chapter ran on the CINES supercomputer Occigen. It used 7200 processors and ran for slightly over 37 hours, for a total of $\sim$ 270,000 computational hours.

Contents

5.1 The LatHyS Code

> **Note:** The LatHyS (LATMOS Hybrid Simulations) code is most completely described in Ronan Modolo's PhD thesis (Modolo (2004)), where the author describes the code he had been building from scratch for the past few years. We only made use of some of the possibilities of the code and will therefore only make a minimal presentation of it, based on the physics being represented rather than the intricacies of the computational model.

5.1.1 A code to study space physics

LatHyS (LATMOS Hybrid Simulations) is a 3D hybrid particle-in-cell code used to run global simulations of planetary environments. It is being used by different teams to study the physics (and chemistry) of the interaction of the solar wind with the Martian atmosphere, Mercury, Earth, Ganymede and Titan (*e.g.* Turc et al. (2015), Modolo et al. (2018) and references therein).

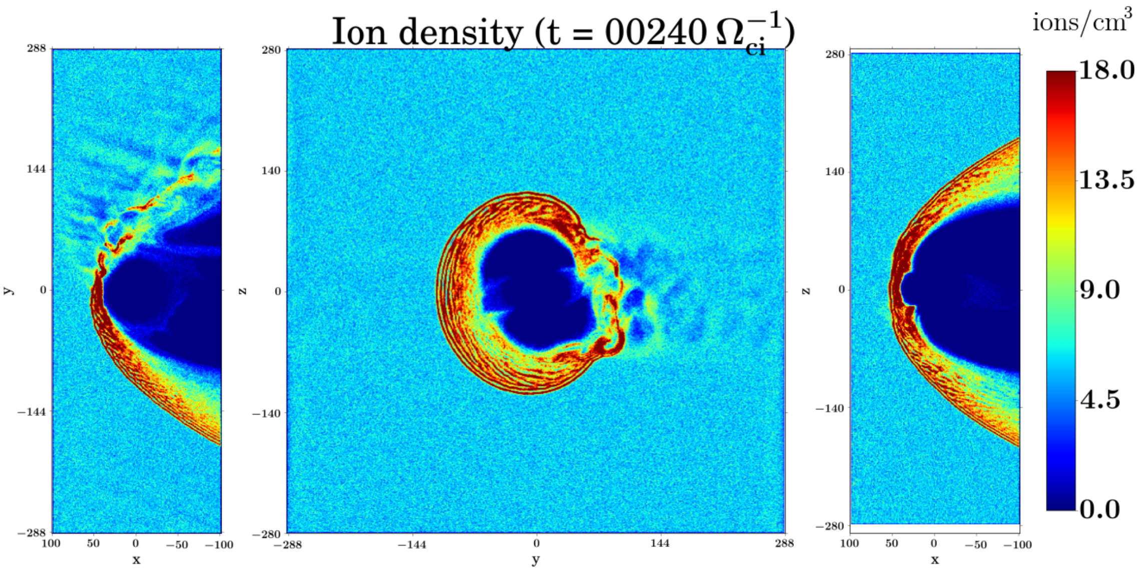

Figure 5.1: *Output from a LatHyS simulation: 2D cuts are made in the 3D density array. From left to right,* (xy) *plane for* $z = 0$*,* (yz) *plane for* $x = 0$ *and* (xz) *plane for* $y = 0$*. For x, y and z,* 0 *represents the center of the planet.*

Advantages of a 3D scheme

Planetary environments, their magnetosphere, magnetosheath, bow shock, *etc.* are intrinsically 3D systems where a lot cannot be grasped without having the 3D picture in mind. 2D simulations, for example, can cause an artificially strong compression of the interplanetary magnetic field onto the obstacle: The magnetic field lines which are in the simulation plane are constrained in that plane and cannot slide along the obstacle. This is something that we need to avoid, because the compression of the magnetosheath by the interplanetary shock and sheath is one the main ways that they influence the geomagnetic environment. The retro-action of the compressed magnetosheath on the shock would also be ill-represented if the field lines are not allowed to slip along the magnetopause.

Advantages of an hybrid scheme

The fact that ions are treated kinetically gives a few advantages over a MHD simulation.

One of the most obvious things is the added ability to describe fundamentally kinetic phenomena, such as Earth's foreshock. Earth's foreshock is created when some ions from the solar wind are reflected on the bow shock and travel sunward following interplanetary magnetic field lines (see *e.g.* Savoini et al. (2013)), against the bulk flow of the solar wind. Figure 5.1 is an example output from a LatHyS simulation: the density is displayed in three planes, from left to right: the ecliptic plane (xy), the (yz) plane, and the noon-midnight meridian plane (xz). The direction of the interplanetary magnetic field (IMF) was chosen at a 20° angle from the Sun-Earth direction (x), in the (xy) plane. This means that the duskward part of the bow shock is a parallel shock, which makes the foreshock quite prevalent.

Going further into modules that we did not use, the LatHyS kinetic framework can also be used to model chemical reactions (see Modolo (2004)).

Ideally, simulating electron's kinetic behaviour would represent the physics even better. This is, however, prohibitively costly in terms of computational hours with today's technology, for running global simulations. Both the bow shock and the interplanetary shock we want to simulate have a thickness of a few ion skin depth (d_i). As collisionless shocks, they involve kinetic processes, and this is why it matters to have kinetic ions in the simulation. The kinetic processes of the electrons, however, generally happen at much smaller scales. Not considering the kinetic effects of electrons does mean that some phenomena will not be correctly represented though, such as magnetic reconnection, acceleration of high energy electrons as *e.g.* the Van Allen belts (Lapenta (2012)). If we accept the loss of a correct decription of these, simulating electrons as a massless fluid a good compromise: it still allows for important effects linked to the decoupling between ions and electrons – such as the Hall effect for example – while giving hybrid particle-in-cell schemes a much lower computational cost than a full particle-in-cell code.

5.1.2 A 3D PIC-hybrid code

The most accurate way of simulating a plasma would be through the N-body problem: the motion of a particle would be calculated using the Newton equations where the force would be the Lorentz force calculated by summing the fields generated by all the other individual particles. The computing power required to run this type of code would scale as N^2 where N is the number of particles. This is technically impossible at any significant scale even with modern supercomputers.

LatHyS is a 3D PIC (particle-in-cell) hybrid code, which uses a statistical approach for the ions and a fluid approach for the electrons; this approach makes for a much more reasonable demand on computing power.

The particle-in-cell method "solves" the Vlasov equation, which models the dynamics of a collisionless plasma:

$$\frac{\partial f}{\partial t} + \boldsymbol{v}\frac{\partial f}{\partial \boldsymbol{r}} + q(\boldsymbol{E} + \boldsymbol{v} \times \boldsymbol{B})\frac{\partial f}{\partial \boldsymbol{v}} = 0 \tag{5.1}$$

where $f = f(\boldsymbol{r}, \boldsymbol{v}, t)$ is the distribution function of the ions (see *e.g.* Boyd and Sanderson (2003)).

In order to compute the evolution of f, the PIC method uses so-called macroparticles (noted f_p), which represent clouds of particles close to each other in the phase-space, or rather; distribution functions with a small volume in the phase space, that can move with time. The assumption is that the distribution function f can be given by the sum of many macroparticles, which also obey the Vlasov equation:

$$f(\boldsymbol{r},\boldsymbol{v},t) = \sum_p f_p(\boldsymbol{r},\boldsymbol{v},t) \tag{5.2}$$

It is usual to give these macroparticles a shape in both space ($\mathscr{S}_r$) and velocity space ($\mathscr{S}_v$), and two free parameters $\boldsymbol{r}_p$ and $\boldsymbol{v}_p$ which represent their centre in the phase space: $f_p(\boldsymbol{r},\boldsymbol{v},t) = N_p\mathscr{S}_r(\boldsymbol{r}-\boldsymbol{r}_p)\mathscr{S}_v(\boldsymbol{v}-\boldsymbol{v}_p)$, where N_p is the number of particles represented by the macroparticle in a statistical sense. It can be shown that for the macroparticles to follow the Vlasov equation, their centre ($\boldsymbol{r}_p$, $\boldsymbol{v}_p$) have to obey equations which turn out to look exactly like Newton's laws of motion:

$$\begin{aligned} \frac{\mathrm{d}\boldsymbol{r}_p}{\mathrm{d}t} &= \boldsymbol{v}_p \\ \frac{\mathrm{d}\boldsymbol{v}_p}{\mathrm{d}t} &= \frac{q_p}{m_p}(\boldsymbol{E}+\boldsymbol{v}_p\times\boldsymbol{B}) \end{aligned} \tag{5.3}$$

In the above equation, q_p and m_p are respectively the charge and mass of the macroparticle, and $\boldsymbol{E}$ and $\boldsymbol{B}$ are the electric and magnetic field electromagnetic field calculated on a grid.

Once the macroparticles have been "pushed" with the help of the above equations, their positions and velocities are used to compute the ion mean quantities such as the density n, the velocity $\boldsymbol{u}$ and the temperature T.

> **Note:** It is tempting to think about simulating the motion of macroparticles evolving in an electromagnetic field as solving a N-body problem, only with fewer particles than in reality; not least because this is what the equations describing the motion of their centre seem to tell us. This view, however, is not correct. The main physical reason for this is to consider how particles generate their electromagnetic field, with a $1/r^2$ dependence. This means that in a simulation box with only a few charged particles, collisions in the sense of strong deviations by Rutherford diffusion would be over-represented. As we have shown in the introduction (see equation (1.8)), a Debye sphere in the solar wind contains several billions of particles, and those screen each other's electric field so that the plasma can display collective behaviour at larger scales. In a code solving the N-body problem, you would need billions of particles simply to simulate the inside of a Debye sphere, which is not, by definition, a plasma: for example, the average electrostatic potential energy of a particle is stronger than its average kinetic (thermal) energy inside of the Debye sphere, and much lower outside. The choice of putting the electromagnetic field on a grid in a particle-in-cell code is not simply a matter of decreasing the computational cost (even though it certainly does), but a way of retrieving the smooth field of the Vlasov equation; which allows to retrieve the dominance of thermal energy over electric potential energy. Macroparticles, then, do not simply represent particles, but clouds of particles that are close to each other in phase space. It is assumed that the superposition of several macroparticles give the distribution function. Their position and shape in phase space is used to compute directly a smooth electromagnetic field which punctual charged particles would not allow.
>
> It can, indeed, be shown that in order to verify the first few moments of the Vlasov equation; the centre of macroparticles have to follow Newton's laws of motions in the mean electromagnetic field of the Vlasov equation. These are the equations actually solved by particle-in-cell codes, and is also the source of the confusion.

In LatHys, the electrons are treated as a massless fluid, essentially present to insure electroneutrality, therefore $n_e = n_i$. This excludes plasma oscillations from the phenomena that can be modelled by the code. The simulations are also limited to scales larger than the Debye length λ_D, and time resolutions larger than the plasma frequency ω_p.

In order to obtain $\boldsymbol{E}$, we write the fluid equation of motion of the electrons:

$$n_e m_e \frac{\mathrm{d}\boldsymbol{u}_e}{\mathrm{d}t} = -en_e\left(\boldsymbol{E} + \boldsymbol{u}_e \times \boldsymbol{B}\right) - \boldsymbol{\nabla} n_e k_B T_e = 0 \tag{5.4}$$

The hypothesis is made that the pressure is isotropic. The temperature is computed with the hypothesis that the electron fluid has a polytropic index of 2, which can be written $n_e/T_e = C$, with C a constant.

In order to compute the electric field from (5.4), we make use of the following hypotheses:

- The electrons are mass-less and their density is chosen to satisfy electro-neutrality.
- The plasma is non-relativistic, so the displacement current $\frac{1}{c^2}\frac{\partial E}{\partial t}$ can be omitted in Maxwell-Ampère

Using $\boldsymbol{u}_e = \boldsymbol{u}_i - \frac{\boldsymbol{J}}{en_e}$, we can compute the electric field with Ohm's law, which is an equation of state (it only depends on other quantities and does not evolve with a differential equation):

$$\boldsymbol{E} = \underbrace{-\boldsymbol{u}_i \times \boldsymbol{B}}_{\text{advection term}} + \overbrace{\frac{(\boldsymbol{\nabla} \times \boldsymbol{B}) \times \boldsymbol{B}}{en_e\mu_0}}^{\text{Hall term}} \underbrace{-\frac{\boldsymbol{\nabla} n_e k_B T_e}{en_e}}_{\text{electronic pressure term}} \tag{5.5}$$

For the evolution of the magnetic field, the code makes use Faraday equation:

$$\frac{\partial \boldsymbol{B}}{\partial t} = -\boldsymbol{\nabla} \times \boldsymbol{E} \tag{5.6}$$

For more details on PIC codes subtle points, see Lapenta (2015), from which the previous discussion is largely inspired, and Lapenta (2012) for more technical aspects.

5.1.3 General workflow - A

In this subsection, we briefly describe the functioning of LatHyS by matching the physics described in the previous subsection 5.1.2 to the names of the corresponding LatHyS files, which contain the subroutines applying these equations. Other useful files are briefly introduced. Figure 5.2 presents the general workflow of LatHyS:

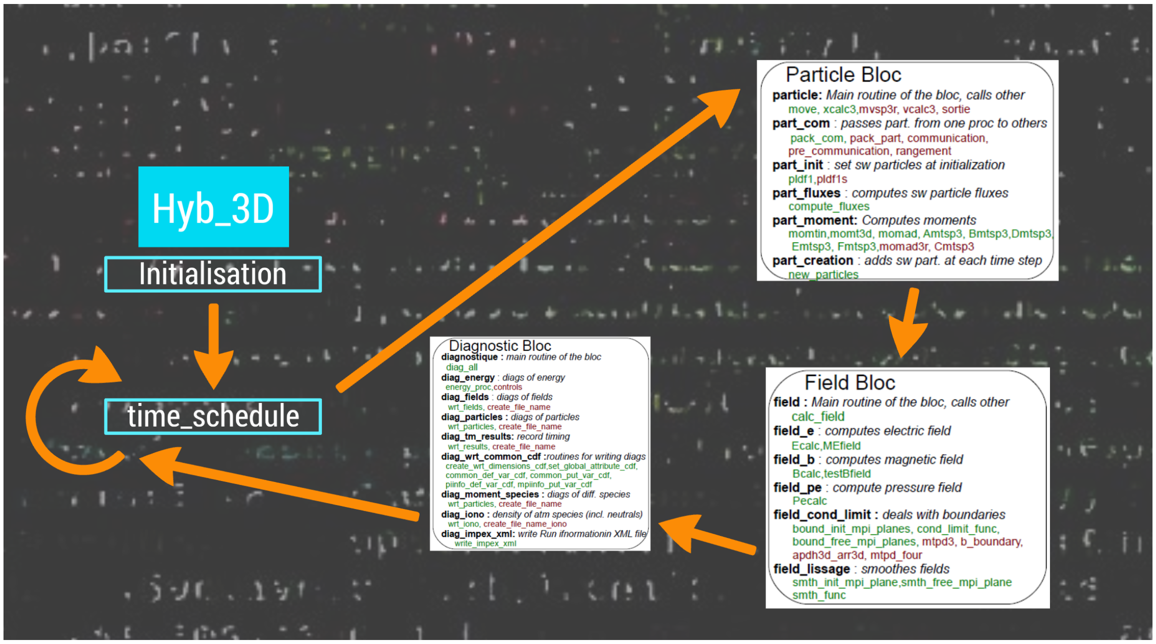

Figure 5.2: *General workflow of LatHyS*

First, the code starts with an "initialisation" phase in which Earth's dipole is created and the solar wind is placed (already in motion) in the simulation box. Then, the code enters the main loop, that will be repeated until the end of the simulation is reached. The main loop, or "time_schedule" goes through the following steps:

1. **Particle Bloc:**
    - Moves the macroparticles using Newton's laws of motion (5.3)
    - Computes moments of the distribution function (density, velocity, temperature)
    - Removes particles exiting the simulation box on the right side, and adds particles entering the box on the left side (a flux of ions is introduced with velocities chosen so that a Maxwellian distribution function of the solar wind is preserved)
2. **Field Bloc:**
    - Updates the electric field using Ohm's law (5.5)
    - Computes the magnetic field using the Maxwell-Faraday equation (5.6)
    - Every so often (not at each iteration), the magnetic field is smoothed to avoid numerical errors
3. **Diagnostic Bloc:**
    - Every so often (not at each iteration), the data is saved (*e.g.* the density, velocity, temperature, magnetic and electric field). We usually call these saves "time dumps" (see subsection 5.4.1)

5.2 Simulation setup and magnetosheath formation

> **Note:** We now present the choices made in the pre-existing code, in order to simulate the geomagnetic frontiers: the bow shock and the magnetopause, and the magnetosheath between them. This is the simulation setup in which we will later (section 5.3) introduce the interplanetary sheath.

5.2.1 General PIC-Hybrid setup

In our simulations, we only used protons to simulate the solar wind.

Choices of grid size and time step duration

The length of reference in our hybrid simulation is the ion skin depth $d_i = \frac{c}{\omega_{pi}}$, where $\omega_{pi} = \sqrt{\frac{e^2 N_{sw}}{\varepsilon_0 m_i}}$. Ideally, we would want a grid size lower than 1 d_i. This, however, is quite demanding in terms of computational power. We therefore chose to have $dx = dy = dz = 1 d_i$, which is an often used and relatively good compromise between feasibility and the physics being represented. Each grid cell is a cube of dimension $(1\ d_i)^3$. We will therefore talk about x, y and z interchangeably in terms of cell numbers or in terms of d_i.

The choice of the duration dt of a time step is linked to the equations involving a time derivation used in LatHyS: The Newton equations (5.3) used to push the macroparticles, and the combination of Maxwell-Faraday (5.6) and the Ohm's law (5.5). These equations help us estimate a few different pulsations that we will note $\{\omega_j\}$, corresponding to the phenomena they describe (see *e.g.* Matthews (1994)). The duration of the time step should be chosen so that it is lower than all the $2\pi/\omega_j$.

$$\begin{aligned}
&\omega_L \sim kv \\
&\omega_G \sim eB/m \\
&\omega_D \sim k^2 B/\mu_0 e n_e \\
&\omega_T \sim k^2 k_B T/eB
\end{aligned} \tag{5.7}$$

Here, ω_L is a "linear" pulsation, based on the maximum velocity v of the simulated particles, and k, a maximal wave number. ω_L is estimated from Newton's equation of motion (5.3). ω_G is the gyration pulsation of ions, estimated from injecting the advection term in Ohm's law (5.5) into the Maxwell-Faraday equation (5.6). ω_D is usually called the frequency of the dispersive effect in the magnetic field. ω_D is estimated from injecting the Hall term in equation (5.5) into the Maxwell-Faraday equation (5.6), and is a simplified version of both frequencies of the whistler waves and the Hall drift waves (see *e.g.* Huba (2003)). ω_T is estimated from injecting the electronic pressure term in equation (5.5) into the Maxwell-Faraday equation (5.6).

These estimations help us choose the simulation time step. For example, stating that we require the simulation step dt to be smaller than $(1/\omega_L)$ is usually called the CFL condition, which corresponds to the fact that numerical methods break down when particles travel through more than one cell during one time step.

In equations (5.7) we shall therefore look at some extreme values expected for the parameters: k represents $2\pi/\Delta x$ where Δx is the cell size of $1 d_i \simeq 92$ km. v is the fastest velocity encountered during the course of the simulation: 750 km/s. B has a maximum of 50 nT and a minimum of 10 nT. And en_e is $1.6 \cdot 10^{-19} \times 6 \cdot 10^6$ Coulomb.m^{-3}. These parameters give us:

$$\begin{aligned}
\omega_L &\sim 51 \text{ rad/s}\\
\omega_G &\sim 5 \text{ rad/s}\\
\omega_D &\sim 189 \text{ rad/s}\\
\omega_T &\sim 6 \text{ rad/s}
\end{aligned} \tag{5.8}$$

In LatHyS, times are normalised in terms of solar wind Ω_{ci}^{-1}. With $B_{sw} = 10$ nT, we have $\Omega_{\text{ci}}^{-1} \sim 1$ rad/s. Rewriting the above pulsations in terms of times thus gives us:

$$\begin{aligned}
t_L &\sim 0.02\ \Omega_{\text{ci}}^{-1}\\
t_G &\sim 0.2\ \Omega_{\text{ci}}^{-1}\\
t_D &\sim 0.005\ \Omega_{\text{ci}}^{-1}\\
t_T &\sim 0.2\ \Omega_{\text{ci}}^{-1}
\end{aligned} \tag{5.9}$$

Our final choice for dt was $dt = 0.005\ \Omega_{\text{ci}}^{-1}$. By choosing dt equal to the smallest time determined above, we can have confidence that the simulation properly resolves the Newton equation, Ohm's law and the Maxwell-Faraday equation.

Solar wind parameters

The solar wind is injected from the left side of the box as a superalfvénic flow ($u_0 = 400$ km/s, $V_A = 89.4$ km/s, $M_A = 4.47$) of protons neutralised by a massless electron fluid. The bulk flow velocity is in the x direction. The ions have a Maxwellian distribution of velocities chosen so that the plasma β of the solar wind is equal to 0.5. The electron temperature is also chosen so that $\beta_e = 0.5$. The density of the solar wind is $n_0 = 6$ ions/cm^3 and the interplanetary magnetic field amplitude is $B_0 = 10$ nT. All these parameters are chosen because they are average values found in the solar wind. The magnetic field is chosen to be quite strong (above the average of $B = 6$ nT at 1 A.U. (Venzmer and Bothmer (2018)) for empirical numerical stability reasons[1]. 10 nT is still a very common value to observe in the solar wind. These choices of solar wind parameters imply $d_i = 92.6$ km. These values will be summarised in a table at the end of section 5.3, on page 112.

Obstacle parameters

In the simulation, we define the obstacle as a surface of radius[2] $R_{obstacle} = 14\ d_i$ which removes the particles touching it from the box. From its centre to 0.75 $R_{obstacle}$ there is nothing: no particles, no magnetic field. Indeed, the resolution would be too low to model in any realistic manner the physics of the inner magnetosphere, ionosphere, *etc*. From 0.75 $R_{obstacle}$ onward, Earth's magnetic field is modelled by a simple magnetic dipole centred on the point $x = y = z = 0$ starting at the surface of the planet, and pointing in z direction:

$$\boldsymbol{B}_{\text{dipole}} = \left(\frac{3\boldsymbol{r}(\boldsymbol{r} \cdot \boldsymbol{M})}{r^2} - \boldsymbol{M} \right) / r^3 \tag{5.10}$$

---

[1] For some reason, when choosing an initial value of 6 nT for the magnetic field, the later introduction of a magnetic cloud/sheath led the simulations to crash. We are still unsure why.

[2] This is much less than the real value, which we discuss below.

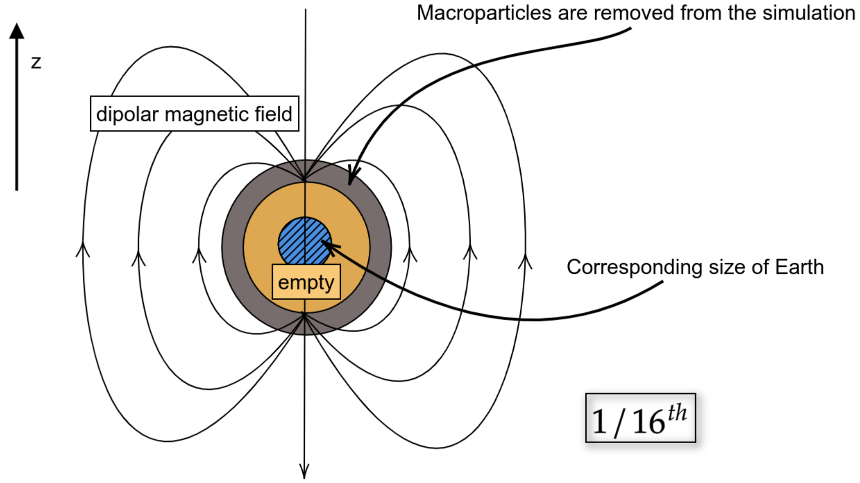

Figure 5.3: *Sketch of the obstacle in LatHyS. Magnetic field lines are represented with curved arrows, starting from just the outside of the yellow circle. The obstacle is represented in grey and yellow. The comparative size of Earth is represented in blue.*

, where $\boldsymbol{M}$ is the dipolar moment, given in Teslas.d_i^3. The value chosen for the simulations presented here is $900 \cdot 10^{-9} \times (14^3)$. This value is chosen so that the simulated geomagnetic environment is safely bigger (standoff distance of magnetopause $r_{MP} = 34\ d_i$) than the limit of validity estimated by Omidi et al. (2004) ($r_{MP} = 20\ d_i$) in order to correctly model Earth's magnetosphere (see formula below). In our simulation, since the dipole has no tilt from the z direction, the *GSE* and *GSM* reference frames are one and the same.

Using the pressure balance equation (1.32), we can write:

$$r_{MP} = \left(\frac{M^2}{2\mu_0 \times \rho_0 u_0^2}\right)^{1/6} = 34\ d_i \tag{5.11}$$

Since we kept realistic parameters for the solar wind flow, we can simply estimate the scale of the simulated geomagnetic environment, as compared to the real geomagnetic environment by using the dipole strength. With $M_{simu} = 900 \cdot 10^{-9} \times (14^3)[\text{Teslas} \cdot d_i^3]$, and $M_{real} = 7.9 \cdot 10^{25}$ Gauss.cm^3 (Bartels (1936), Olson and Amit (2006)), we can estimate the scaling ratio (using the magnetopause position) between our simulation and reality as:

$$\frac{r_{MP}^{\text{simu}}}{r_{MP}^{\text{real}}} = \left(\frac{M_{simu}}{M_{real}}\right)^{1/3} \simeq \frac{1}{16} \tag{5.12}$$

From this, we can also estimate what would be the size of Earth in our simulation (keeping in mind that the planet itself is not simulated). With our parameters and equation (5.11), $r_{MP}^{\text{real}} = 7.8\ \text{R}_\text{E}$, and $r_{MP}^{\text{simu}} = 34\ d_i$. Therefore $\text{R}_\text{E}^{\text{simu}} = 34/7.8 \simeq 4.4\ d_i$.

Figure 5.3 is a sketch of the obstacle that summarises its setup.

Choice of the box size

We used a setup similar to, albeit with a significantly larger box than Turc et al. (2015). The box dimensions are of 1500 cells in the X direction, 720 cells in the Y direction and 660 cells in the Z direction. There are two ways to think about how this translates to physical units. The first, and most natural one, is linked to the plasma: The length of the box in the X direction, L_x, is simply $L_x = 1500\ d_i$, $L_y = 720\ d_i$ and $L_z = 660\ d_i$. The second, which helps compare large-scale trajectories in the simulation to what they would mean for observations, is in terms of the planet radius. Then, we have $L_x = 344\ \mathrm{R_E}$, $L_y = 165\ \mathrm{R_E}$ and $L_z = 151\ \mathrm{R_E}$.This can be compared to the Earth-moon distance[3] of $\sim 60\ \mathrm{R_E}$.

The length of the box in the X direction has been chosen quite large to let enough room for the interplanetary shock to self-consistently develop, and propagate long enough that the sheath following it can expand. As we will see in the next chapter, by the time the shock reaches the magnetosheath, the sheath is about the same size as the magnetosheath itself (from the nose of the bow shock to the last plane on the right side of the simulation box). In the Y and Z directions the size box has been chosen to be large enough to accommodate the geomagnetic environment with room to spare (see next subsection). This is partly because the size of the geomagnetic environment will change during the simulation as it interacts with the shock/sheath/magnetic cloud and it is important that the plasma has enough space to flow around it, and partly to avoid unphysical things such as particles from the Earth's ionic foreshock leaving the box on one side and reentering on the other because of the periodic boundary conditions. could easily With this setup, a simulation took roughly 400.000 computational hours.

5.2.2 "Static" simulation of the geomagnetic environment

Magnetosphere and magnetosheath formation

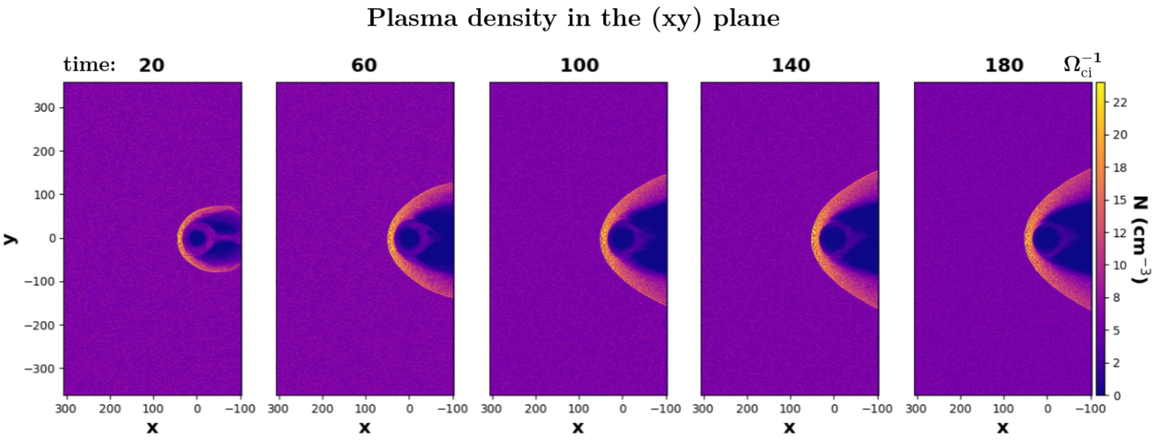

Figure 5.4: *From left to right, temporal evolution of the magnetosheath as it is self-consistently formed. The density in the ecliptic (xy) plane is used to show the magnetosheath's global structure.*

---

[3] We did not include the moon in our simulations, but it might be a relevant addition in a distant future, (*e.g.* Nishino et al. (2011)).

Figure 5.4 shows cuts of the plasma density in the ecliptic (xy) plane of the simulation box. At the beginning of the simulation, the solar wind is injected everywhere in the box and flows towards the right side. The interplanetary magnetic field is initially in the ecliptic (xy) plane, making an 85° angle with the x direction. Indeed, for quiet solar wind conditions the interplanetary magnetic field is most likely to be found in the ecliptic plane. We chose an angle of 85° for our simulation because it is the simplest case (quasi perpendicular shock). Other angles will be explored in the future (see the Conclusions of this manuscript). The obstacle is placed at $x = y = z = 0$ and the dipole is introduced. The magnetosphere, magnetopause and bow shock are self-consistently formed through the interaction between the solar wind and the obstacle (times 20 through 180, from left to right). By time 180 $\Omega_{\mathrm{ci}}^{-1}$ (last panel on the right), the simulated geomagnetic environment has reached a stationnary state and its shape does not visibly change.

Validity of the simulation: comparison with the literature

The magnetosheath simulated by LatHyS fits general macroscopic descriptions of the magnetosheath as described by theory and observed by satellites:

i. The nose of the magnetopause stands at 34 d_i (or 7.8 R_E) from the centre of the planet, which corresponds to formula (5.11). This is also above 20 d_i, which is the threshold found by Omidi et al. (2004) to allow a correct description of an Earth-like magnetosphere.

The "nose" of the magnetosheath is defined in this thesis as the area of the magnetosheath between the bow shock and the magnetopause along the Sun-Earth line. Any parameter A measured in our simulations in this region is denoted A^{nose}.

ii. The plasma velocity behind the bow shock, u^{nose}, should by definition be slower than the Alfvén speed (Lucek et al. (2005)). Let us name V_A the local Alfvén speed; and M_{A} the local Alfvén Mach number, equal to $M_{\mathrm{A}} = u/V_{\mathrm{A}}$, where u is the local flow velocity. In our simulations we see the bulk of the plasma slowing down from a superalfvénic speed of $u^{\mathrm{upstream}} = 400$ km/s($> V_{\mathrm{A}} = 99$ km/s, and $M_{\mathrm{A}} = 4$) to a subalfvénic speed of $u^{\mathrm{nose}} = 118$ km/s($< V_{\mathrm{A}} = 236$ km/s) and $M_A = 0.5$.

iii. From a quasi-radial velocity at ($u_x^{\mathrm{nose}} = -103$ km/s, $u_y^{\mathrm{nose}} = 0.08$ km/s, $u_z^{\mathrm{nose}} = -10.3$ km/s), the plasma deviates to flow around the magnetosphere (Lucek et al. (2005)). Indeed, in the equatorial (xy) plane, for $x = 0$ (the values of any parameters at $x = z = 0$ and $y > 0$ is referenced to by the notation A^{ydusk}) we observe a large velocity component along the y direction ($u_y^{\mathrm{ydusk}} = 89$ km/s) while the z component stays quite low ($u_z^{\mathrm{ydusk}} = 8$ km/s). The same thing is observed in the ecliptic plane (xz), with $V_z^{\mathrm{zup}} = 120$ km/s and $V_y^{\mathrm{zup}} = 4$ km/s (The notation A^{zup} represents the parameters at $x = y = 0$ and $z > 0$).

iv. From its subalfvénic velocity at the magnethosheath nose, the plasma is accelerated to super-alfvénic speeds on the flanks of the magnetosheath (Lucek et al. (2005)). ($u^{\mathrm{ydusk}} = 232$ km/s $>$ $V_{\mathrm{MC}} = 177$ km/s, and $M_{\mathrm{A}} = 1.3$).

    We can note, however, that this acceleration is not homogeneous, with, for example $u_{\mathrm{zdown}} = 302$ km/s $> V_{\mathrm{MC}} = 232$ km/s, and $M_{\mathrm{A}} = 1.3$. This makes sense: in the hereby reported simulation, most of the interplanetary magnetic field is along the y direction. When the magnetic field lines pile up against the magnetopause, they slip in the (xz) plane, and the plasma is accelerated by the release of the magnetic tension in slingshot-type effect (Lavraud et al. (2013), Turc et al. (2015)).

v. The plasma beta in the magnetosheath is usually of the order of unity (Lin et al. (1991)), which is retrieved in our simulations. Commonly observed total pressures of about 1 nPa (Lin et al. (1991)) are also reproduced in our simulation ($P_{\text{total}}^{\text{nose}} = 0.87$ nPa).

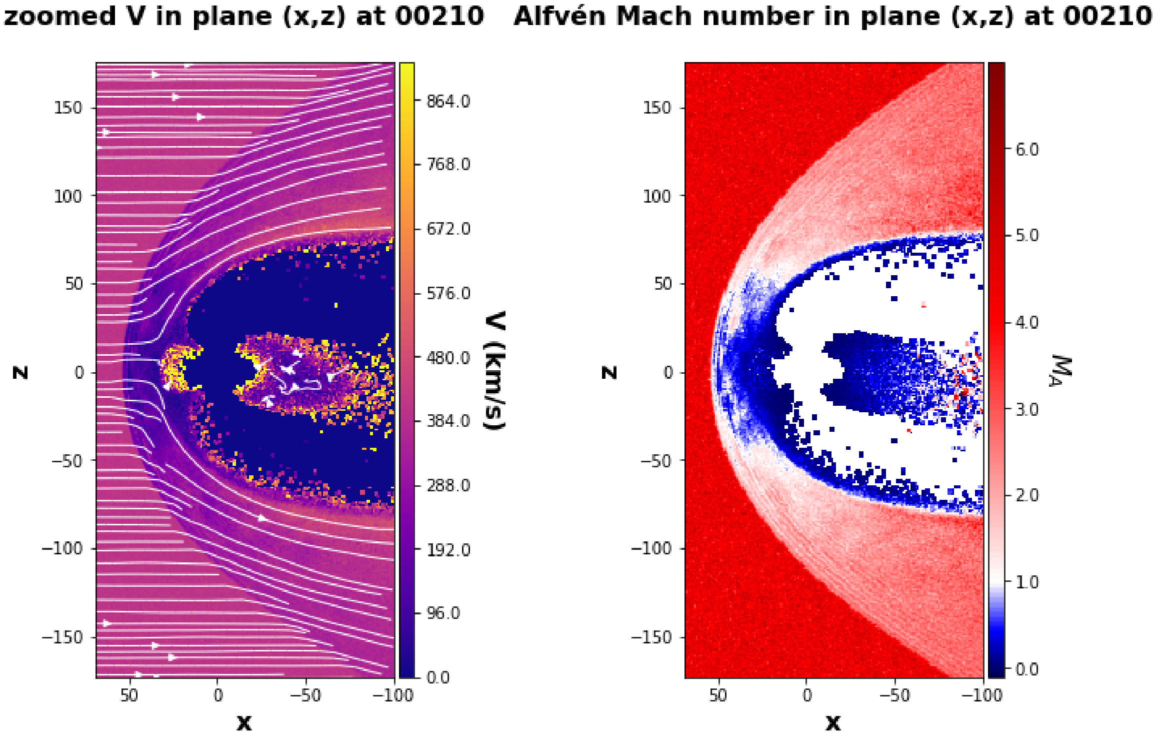
zoomed V in plane (x,z) at 00210

Alfvén Mach number in plane (x,z) at 00210

Figure 5.5: *Left panel: 2D map of the amplitude of the velocity in the noon-midnight meridian (xz) plane. Superimposed on it, in white, are the flow lines of the plasma. Right panel: 2D map of the local Alfvén Mach number. Blue corresponds to a subalfvénic flow and red to a superalfvénic flow.*

Figure 5.5 is a visual representation of points *ii*, *iii*, and *iv*. On the left panel, which is a 2D map of the velocity in the noon-midnight meridian plane (x,z), we drew the flow lines in white. We clearly see how they flow around the magnetopause. The right panel shows the local Alfvén Mach number M_A. If the flow is subalfvénic ($M_A < 1$), the area is coloured in blue, whereas if the flow is superalfvénic $M_A > 1$), the area is coloured in red.

5.3 Magnetic cloud-driven sheath

> **Note:** This section marks the change in the type of work present from user to developer, as we introduce the module developed in LatHyS during this doctoral work.

5.3.1 General simulation setup: Objective

This work aimed at getting a global picture of the interaction between a sheath and the magnetosheath. This required two structures: the magnetosheath, formed by the interaction between a quiet solar wind and a magnetic dipole representing Earth, and a magnetic-cloud driven sheath.

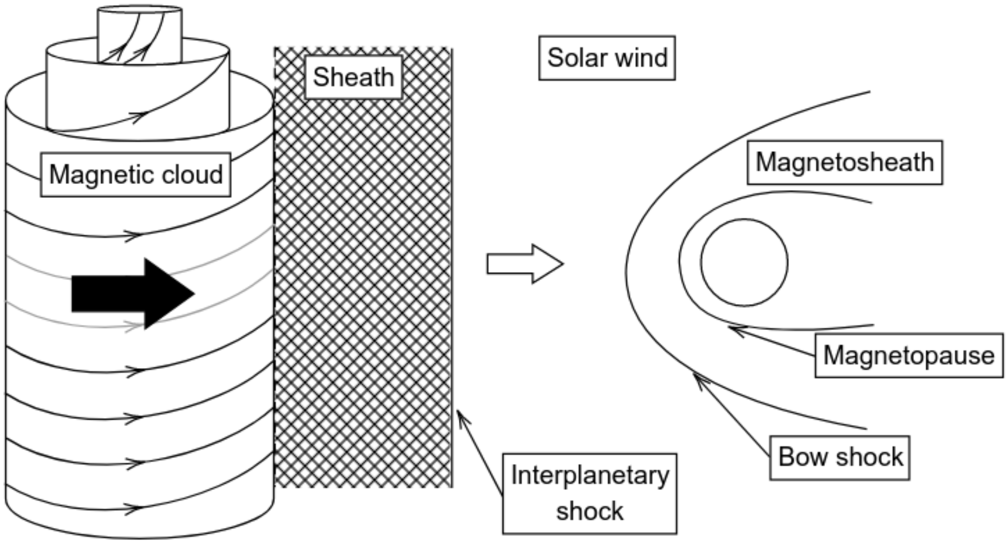

Figure 5.6: *Objective of this work, in terms of LatHyS setup*

The bow shock and magnetosheath have long been reproduced in numerical simulations: For example, in MHD simulations (*e.g.* Wang et al. (2020)), Vlasov simulations (*e.g.* Battarbee et al. (2020)), and Hybrid PIC simulations (*e.g.* Turc et al. (2015)). Simulations containing both a standing shock (*e.g.* the bow shock) and a propagating shock (*e.g.* the interplanetary shock) are much less common.

Spreiter and Stahara (1994) used a gasdynamic model to simulate the interaction of an interplanetary shock with the magnetopause. Koval et al. (2005), Samsonov et al. (2006, 2007) and Pallocchia et al. (2010) have used 3D MHD models to study the interaction of an interplanetary shock with the bow shock and magnetopause. The propagating shock in these simulations, however, was not simulated self-consistently but directly injected in the simulation following either a model (*e.g.* verifying Rankine-Hugoniot equations) or observational data. This forbade the inclusion of an interplanetary sheath. In Samsonov et al. (2006) and Pallocchia et al. (2010)'s code, while the bow shock is self-consistently simulated, the magnetopause motion is described by a model.

The challenge we undertake in this work is to have both a global 3D hybrid-PIC simulation of the geomagnetic environment (this was already made in LatHyS by Turc et al. (2015)) and a propagating interplanetary shock self-consistently created during the simulation by the interaction between a magnetic cloud (modelled) and a pristine solar wind. The self-consistent creation of the shock can then lead to the formation of a sheath. This, to our knowledge, has never been done before. Figure 5.6 summarises the objective we gave ourselves, in terms of numerical simulations.

5.3.2 General workflow - B

In order to introduce a magnetic cloud in the simulation box, we made use of a new module named "time_variation.F90" which is called at every iteration (see figure 5.7, similar to 5.2, with the addition of the "time_variation.F90" module). The idea was introduced in Lucile Turc's thesis (Turc (2014). At the beginning of the simulation (during the "initialisation") we create functions of the form "$quantity = f(t)$", where t is the simulation time. These functions will describe the evolution through time of the parameters of the solar wind injected at the entry plane the simulation box.

For example, if we want to describe a simple linear acceleration in time of the solar wind, we could define a function $u(t) = C \times t$ where C is a constant. At every time step, when new solar wind particles are injected in the simulation through the left side entry plane, their velocity will be informed by this function and the actual individual particle will have a velocity of $C \times t \pm p\sqrt{k_B T/m}$ where p is a random factor chosen so that the distribution of velocities is a Maxwellian.

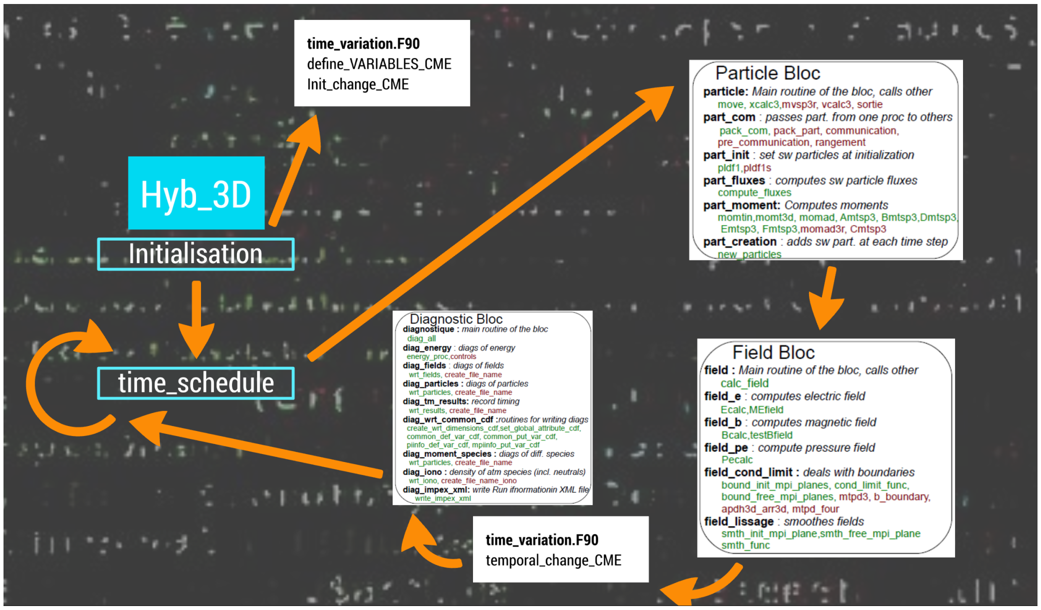

Figure 5.7: *General workflow of LatHyS updated to include variations in the injected solar wind.*

5.3.3 Description of the magnetic cloud

In order to create a shock and its sheath in the simulation box, we introduced a fast magnetic cloud at the entry plane and let it propagate along the solar wind in the box. The structure injected in the box was chosen to be without curvature. This choice is consistent with the massive size R_{MC} of magnetic clouds: with a typical size of $R_{\mathrm{MC}} \sim 1/3$ AU (Lepping et al. (2006)), their structure can be seen planar at the scale of the geomagnetic environment $R_{\mathrm{GE}} \sim 15R_E \sim 1/2000R_{\mathrm{MC}}$, where R_{GE} is the approximate size of the geomagnetic environment (including the bow shock), and R_E is Earth's radius.

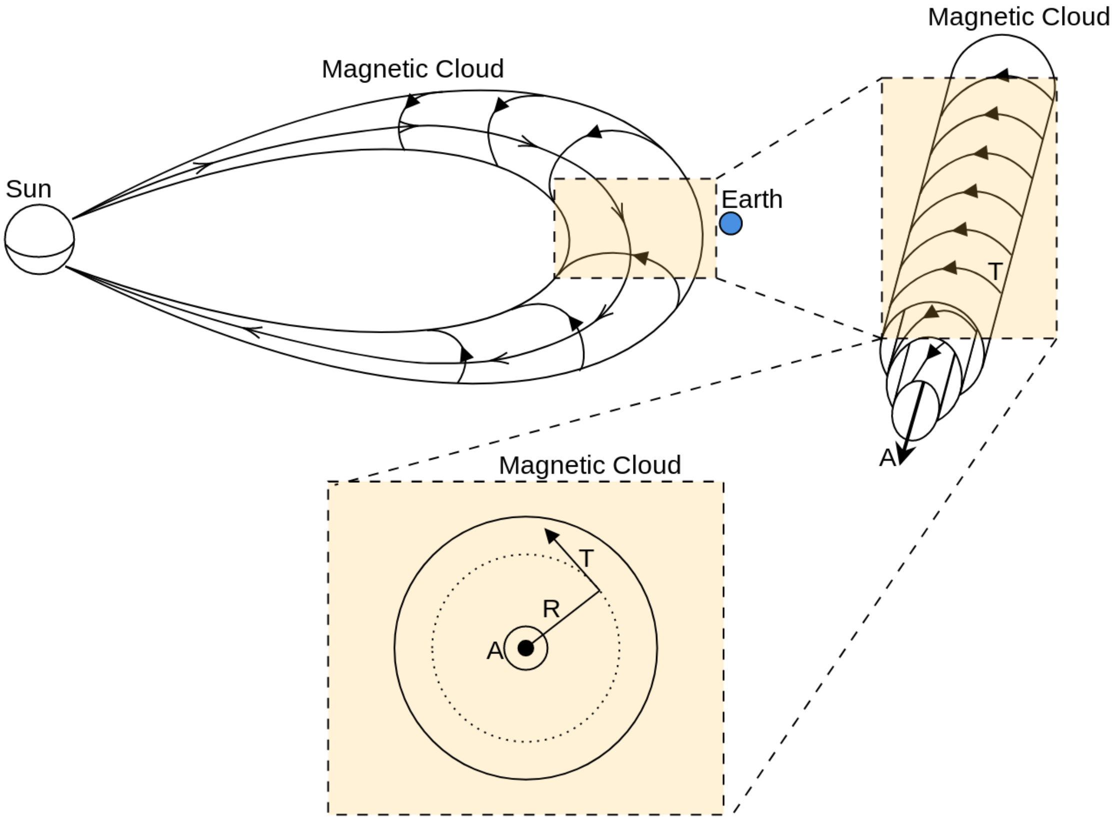

Figure 5.8: *Sketch of a simple mathematical model (flux rope) to describe the expected magnetic field measured when crossing head-on a radially expanding magnetic cloud. A, T and R stand respectively for the axial, tangential and radial directions.*

Figure 5.8 shows a progressively zoomed-in sketch of a magnetic cloud. Starting from the top left corner, we see a large structure with its feet on the sun (see section 1.4.3). By the time it reaches Earth (blue circle), the magnetic cloud as a size of roughly $1/3$ AU, which is vastly (about 2000 times) larger than the geomagnetic environment. In this sketch, as well as in our simulation, we decided that the magnetic cloud would cross Earth head-on, without any impact parameter (this specific condition is not needed by Burlaga (1988), presented thereafter). On the top right corner of the figure, we zoomed-into the magnetic cloud to introduce the flux rope structure. The flux rope is organised around an axial magnetic field (A denotes the axial direction), around which a tangential field is wrapped in an helix (T denotes the tangential direction). By cutting a plane through the flux rope magnetic cloud, we obtain the sketch on the bottom of figure 5.8, were we see again the axial (A) and tangential (T) directions, as well as the radial direction (R). There is no magnetic field in the radial direction.

For the magnetic field, we used the simple analytical model from Burlaga (1988), which is based on a similar geometry to figure 5.8. This model, which is the most common model used for magnetic clouds is derived from two hypotheses:

First, the structure is "force free", *i.e.* the magnetic field structure verifies $\boldsymbol{j} \times \boldsymbol{B} = \boldsymbol{0}$: the magnetic field arranges itself so the Lorentz force vanishes and no force is exerted on the particles. Another way to see it, less obvious at first sight, is that it corresponds to a situation in which the magnetic tension from the wrapping of the field lines compensates the magnetic pressure (Burlaga (1988)).

From this hypothesis, we can write the current as:

$$\boldsymbol{j} = \alpha \boldsymbol{B} \tag{5.13}$$

α in the above equation is a constant (that can take on any value). Injecting equation (5.13) into Maxwell-Ampere's equation leads to the following differential equation for $\boldsymbol{B}$:

$$\Delta \boldsymbol{B} = -(\mu_0 \alpha)^2 \boldsymbol{B} \tag{5.14}$$

Second, the geometry is cylindrical. This is simply a local approximation that corresponds to the observed structures of magnetic cloud and simplifies calculations.

The differential equation (5.14), under the cylindrical hypothesis, has for solutions the Bessel functions $J_0(r)$ and $J_1(r)$ as given in equation (5.15):

$$\begin{aligned} &\quad \text{Axial component} \\ &B_A = B_0 J_0(ar) \\ &\quad \text{Tangential component} \\ &B_T = B_0 H J_1(ar) \\ &\quad \text{Radial component} \\ &B_R = 0 \end{aligned} \tag{5.15}$$

In equations (5.15), B_A, B_T and B_R represent respectively the axial, tangential and radial magnetic field. a is a constant, and H is the handedness of the magnetic field ($H = \pm 1$). We chose $H = 1$ in this work.

These equations are solved for the radius r in a cylindrical geometry. However, in our simulations, the magnetic cloud has to be injected at the entrance plane, *i.e.* at a single location in space. Since the plasma injected at the entry plane has a velocity; we can simply vary the injected values of the magnetic field over time, and let the magnetic field get advected away. This allows us to recover a spatial structure which verifies the "force-free" equation (5.13).

In this work, we decided to make B_z the axial component, so $B_z = B_z(t)$, B_y the tangential component, so $B_y = B_y(t)$ and B_x the radial component so $B_x = Constant$. This conveniently solves a difficulty of the numerical scheme by keeping B_x constant. Indeed for simplicity, the velocity, temperature, magnetic field and density are chosen to be homogeneous on the whole entry plane, *i.e.* $\frac{\partial}{\partial y} = \frac{\partial}{\partial z} = 0$. Keeping B_x constant at the entry plane then straightforwardly insures that the introduced magnetic field verifies flux conservation through: $\frac{\partial Bx}{\partial x} = \frac{1}{V_{SW}}\frac{\partial Bx}{\partial t} = 0$, and then $\nabla \cdot B = 0$. The Maxwell-Faraday equation is built into the hybrid scheme and is therefore naturally verified throughout the simulation. It also insures that the magnetic flux conservation stays true in the whole box, since taking the divergence of the Maxwell-Faraday equation shows that $\boldsymbol{\nabla} \cdot \boldsymbol{B}$ is constant over time. This choice of keeping Bx constant, however, limits us to the study of a magnetic cloud crossed axially: $B_x = B_R = Constant$ means that the only variations are on B_y, and B_z, which corresponds to figure 5.8, of a magnetic cloud crossed axially.

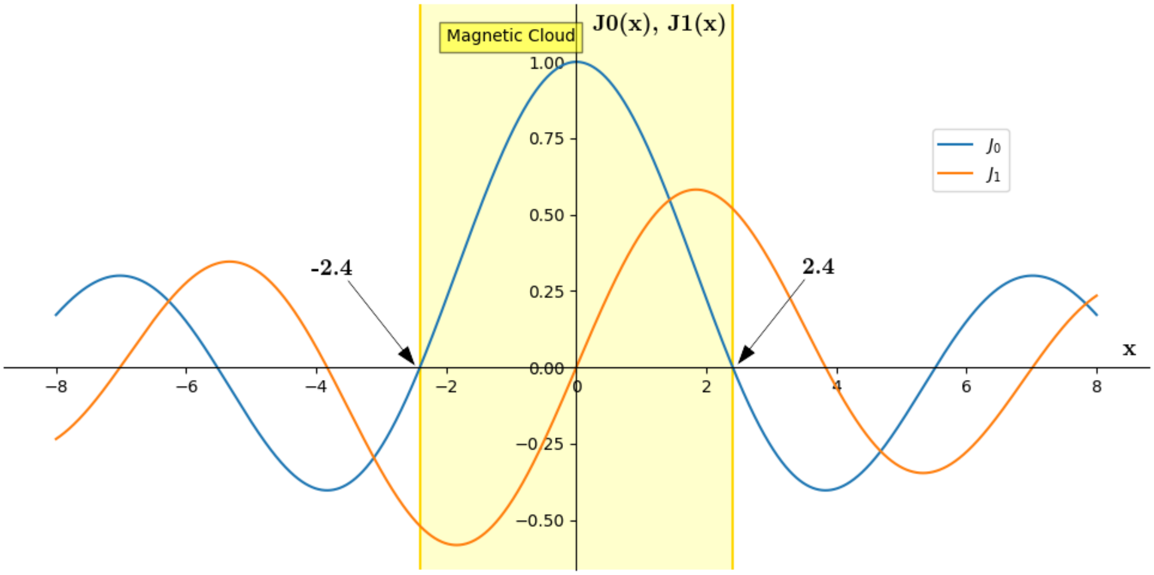

Figure 5.9: *Bessel functions J_0 and J_1*

Figure 5.9 represents the “generic” Bessel functions J_0 and J_1. When using these to describe the magnetic field, we need to understand how they can be linked to the solar wind. In Burlaga (1988)’s model, the magnetic cloud starts at $x = -2.4$ where $J_0(x) = 0$, *i.e.* when the axial magnetic field is null and starts to grow. It then ends at $x = 2.4$, where $J_0(x) = 0$ again. On figure 5.9, the pale yellow span indicates the part of the Bessel functions actually used to describe the magnetic cloud. This means that if we want our magnetic cloud to start being injected at a time t_0, we have to write:

$$\begin{aligned} B_x(t) &= Constant \\ B_z(t) &= B_0 J_0((a \cdot u_0)(t - t0) - 2.4) \\ B_y(t) &= B_0 J_1((a \cdot u_0)(t - t0) - 2.4) \end{aligned} \tag{5.16}$$

In the above equation, $(a \cdot u_0)(t - t0)$ is the radius r from equation (5.15), and the -2.4 as been added in the equation so that at $t = t_0$, $J_0 = 0$.

This also means, however, that – as is apparent on both figure 5.8 and figure 5.9 – J_1 starts at the non-zero value $J_1(2.4)$. This would cause numerical problems if not dealt with: the magnetic field would jump from one value in the solar wind to a completely different value in the magnetic cloud, and do so in single iteration. When this happens in a numerical simulation, the steep gradients often lead to some sort of numerical diffusion, or sometimes leads to the generation of unphysical waves; both of which are not desirable outcomes. This is true for both B_y, which would need to jump from its solar wind value to $B_0 J_1(-2.4)$ and B_z which would need to jump from its solar wind value to 0. We therefore included a soft transition with an hyperbolic tangent to go from the solar wind value to the magnetic cloud value of B_y and B_z:

$$\begin{aligned}
&B_x(t) = Constant \\
&B_y(t < t_0) = B_{ySW} + (B_{yMC} J_1(-2.4) - B_{ySW})\frac{1}{2}\left(1 + \tanh\left(\frac{t - t_0}{\tau_0}\right)\right) \\
&B_z(t < t_0) = B_{zSW} + (0 - B_{zSW})\frac{1}{2}\left(1 + \tanh\left(\frac{t - t_0}{\tau_0}\right)\right)
\end{aligned} \tag{5.17}$$

The subscript SW refers to the value of the subscripted quantity in the quiet solar wind, whereas the subscript MC refers to its value in the magnetic cloud, here used as a piston. t_0 is the time at which the piston starts, while τ_0 defines the sharpness of the transition from quiet solar wind conditions to magnetic cloud conditions. Once the smooth transition has been made, we can safely use the Bessel functions of Burlaga (1988)'s model.

The function $\frac{1}{2}\left(1 + \tanh\left(\frac{t-t_0}{\tau_0}\right)\right)$ smoothly goes from 0 to 1. The transition between these values happens around time t_0 and takes a few τ_0.

Following the common characteristics of magnetic clouds at 1 AU (see subsection 1.4.3 or a more recent, very complete superposed epoch analysis: Regnault et al. (2020)), we made our magnetic cloud model: faster than the solar wind, colder than the solar wind, and of the same density. To our knowledge, no model has been devised of the velocity and temperature in magnetic clouds, so we chose the simplest way to continuously go from one constant value to another: hyperbolic tangents. We actually summed two hyperbolic tangents with different transition times so that we could recover the pristine solar wind conditions after the passage of the magnetic cloud:

$$V(t) = V_{\mathrm{SW}} + (V_{\mathrm{MC}} - V_{\mathrm{SW}}) \times \left(\tanh\left(\frac{t - t_0}{\tau_0}\right) - \tanh\left(\frac{t - t_1}{\tau_1}\right)\right) \tag{5.18}$$

$$V^{\mathrm{th}}(t) = V^{\mathrm{th}}_{\mathrm{SW}} + (V^{\mathrm{th}}_{\mathrm{MC}} - V^{\mathrm{th}}_{\mathrm{SW}}) \times \left(\tanh\left(\frac{t - t_0}{\tau_0}\right) - \tanh\left(\frac{t - t_1}{\tau_1}\right)\right) \tag{5.19}$$

In the above equations, V and V^{th} are respectively the bulk and thermal velocities of the plasma. t_1 and τ_1 are used to define an end to the piston and play symmetric roles to t_0 and τ_0. τ_1 has been chosen longer than τ_0 to correspond to the trends in observations. The asymmetric shape of the piston's velocity is a simple consequence of the faster plasma piling-up as it travels through the solar wind; as such, this asymmetric shape could have developed on its own in the code. Choosing $\tau_0 < \tau_1$ economises computational hours.

The velocity of the introduced magnetic cloud was chosen so that its propagation self-consistently led to the formation of a shock and sheath. With $V_{\mathrm{MC}} - V_{\mathrm{SW}} = 750 - 400 = 350\mathrm{km\,/\,s} > V_{\mathrm{A}} = 89.4\mathrm{km\,/\,s}$, this gives us $M_A = 3.91$.

Figure 5.10 shows the model used for injecting the magnetic cloud by varying the solar wind conditions at the entrance of the simulation box. The values chosen for the magnetic field are quite high, going from 10nT in the solar wind to 50nT in the magnetic cloud. Albeit high, these values correspond to somewhat uncommon, but realistic clouds. This conveniently exacerbates the impact of the magnetic cloud on the magnetosheath, and helps avoid some numerical instabilities.

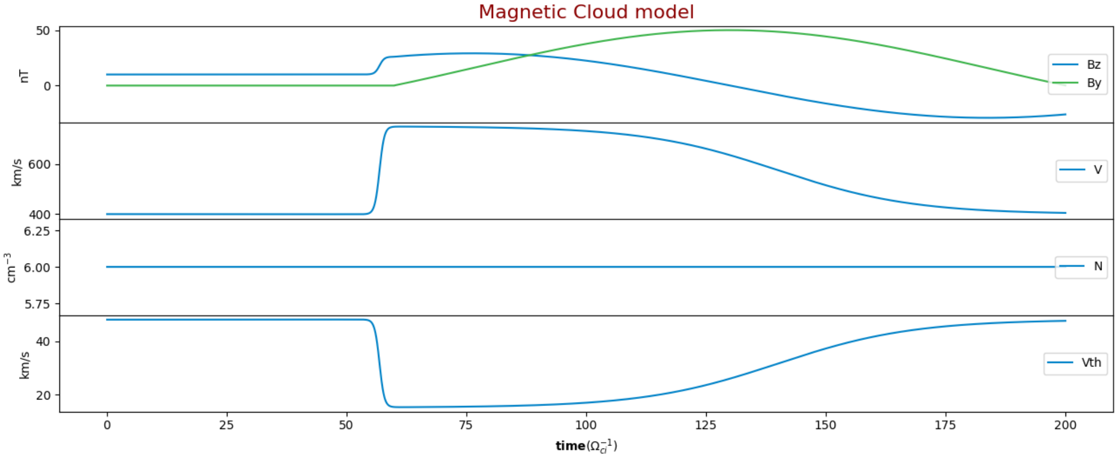

Figure 5.10: *Temporal profiles of the magnetic cloud model injected at the left boundary of the simulation. From top to bottom: y and z components of the magnetic field (B_x stays constant), bulk velocity, density, and thermal velocity.*

Unpublished work: a physical model?

It can be convenient, in numerical simulations, to avoid using too many free parameters if possible. Indeed, having to many free parameters can often hide a lack of knowledge and allow for nonphysical combinations of choices. When it comes to our model of magnetic cloud, we have quite a few: V_{MC}, V_{SW}, B_{yMC}, B_{ySW}, B_{zMC}, B_{zSW}, $V^{\mathrm{th}}_{\mathrm{MC}}$, $V^{\mathrm{th}}_{\mathrm{SW}}$, τ_0, τ_1 and N_{SW}.

While we limited their numbers by choosing to keep the density constant from the solar wind to the magnetic cloud, or by using the same transition times τ_0, τ_1 for the magnetic field, velocity and temperature; adding more physics to the model itself could decrease this number even more.

We started by making the hypothesis of a constant pressure (magnetic plus thermal) during the injection. Physically, it would correspond to a magnetic cloud which is in mechanical equilibrium with its surroundings. With this hypothesis, we could for example define the temperature variation automatically from the magnetic field variation. This hypothesis turns out to be impossible to verify in an interesting way. Let us, for example, fix $T_{\mathrm{SW}} = 240 \cdot 10^3$ K, $B_{\mathrm{SW}} = 10$ nT, $B_{\mathrm{MC}} = 50$ nT and $N_{\mathrm{MC}} = N_{\mathrm{SW}} = 6$ (ions/cm^{-3}). The temperature in the magnetic field needed to keep the pressure constant would then be:

$$T_{\mathrm{MC}} = T_{\mathrm{SW}} + \frac{B_{\mathrm{SW}}^2 - B_{\mathrm{MC}}}{2N_{\mathrm{SW}}k_B\mu_0} \simeq -11 \text{ MK} \tag{5.20}$$

This shows that, if we are to have a mechanical equilibrium between the magnetic cloud and its surrounding solar wind, the temperature in the magnetic cloud should be highly negative! In other words: there is no possible mechanical equilibrium between the magnetic cloud and the solar wind (given the parameters used here). This means that the hypothesis of constant pressure is not applicable and that the magnetic cloud is necessarily expanding. This, of course, is exactly what happens for most magnetic clouds in the interplanetary medium (Burlaga (1991), Lepping et al. (2003)). Even making wrong hypotheses can be interesting.

While we did not go further on this, the search for another physical hypothesis linking some plasma and electromagnetic parameters could prove fruitful since to our knowledge, no model exists for the velocity, density and temperature in magnetic clouds.

5.3.4 Formation of the shock and the sheath

We inject the magnetic cloud at time $t = 70\ \Omega_{\mathrm{ci}}^{-1}$ to let sufficient time for the bow shock, magnetopause and magnetosheath to be fully formed and to reach a stationary state, which happens around $t = 190\ \Omega_{\mathrm{ci}}^{-1}$. Indeed, with a propagation speed of $750\ \mathrm{km/s} \simeq 8.4\ V_A$ (V_A is estimated from the solar wind values $B = 10$ nT and $N = 6$ ion/ cm^3), the front of the injected structure should arrive[4] at the bow shock ($x \simeq 50 d_i$) at a time $t_{\mathrm{collision}} \simeq \frac{1350}{8.4} \simeq 230\ \Omega_{\mathrm{ci}}^{-1}$.

In practice, the high speed magnetic cloud injected through the left-hand side of the simulation box steepens and self-consistently forms a shock, which propagate slightly faster than the magnetic cloud. In the simulation, the interplanetary shock ends up reaching the bow shock at $t = 216.5\ \Omega_{\mathrm{ci}}^{-1}$, which is still sufficiently late for the magnetosheath to be stationary.

Between the magnetic cloud and the interplanetary shock, a sheath has self-consistently been formed. Figure 5.11 shows the spatial profile of the sheath, at $t = 210\ \Omega_{\mathrm{ci}}^{-1}$ (slightly before it would reach the bow shock). The figure is plotted along the x-axis, since the introduced event is planar. This particular figure was plotted using a cut through the simulation box at $y = z = 0$; however any other values of y and z would have yielded the same result (planar structure).

We recover (see figure 5.11) expected characteristics of observed sheaths (see *e.g.* Kilpua et al. (2017b)):

- The dynamic pressure is very large ($P_{dyn} \sim 5$ nPa).
- The magnetic field is significantly higher than in the solar wind ($B_{Sh} \sim 30\ \mathrm{nT} > B_{SW} = 10\ \mathrm{nT}$)
- There is an elevated level of fluctuations (visual for now, see section 7.3.2 in the Conclusions and Perspectives for more information)
- The plasma beta is quite high ($\beta \sim 1.5$)

---

[4] In the following calculation, we make use of the fact that $d_i \times \Omega_{\mathrm{ci}} = V_A$.

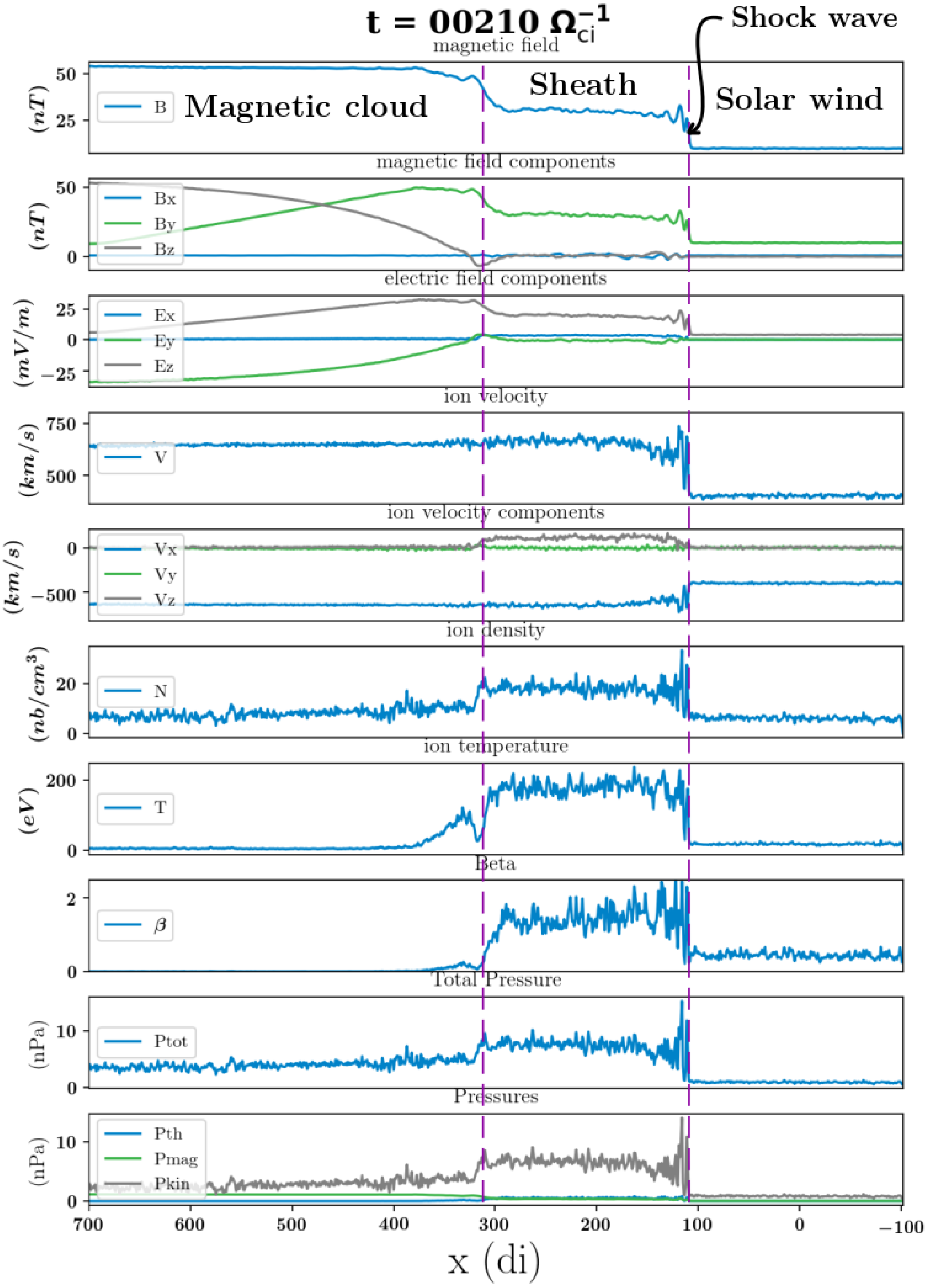

Figure 5.11: *Main parameters in the self-consistently created sheath at time* = 210 Ω_{ci}^{-1}, *shortly before its encounter with Earth. For clarity, Earth's geomagnetic environment has been removed from this plot. Earth's center would be located at* $x = 0$.

5.3.5 Summary of the simulation setup

dx, dy, dz	1 d_i
dt	0.005 $\Omega_{\mathrm{ci}}^{-1}$
tmax	300 $\Omega_{\mathrm{ci}}^{-1}$
Nx	1500
Ny	720
Nz	660
N procs	7200

Table 5.1: ***Simulation parameters***

	Solar wind	Magnetic cloud
B (nT)	10	50
B orientation	$B_x = B\cos(85^\circ) \mid B_y = B\sin(85^\circ) \mid B_z = 0$	variable
V (km/s)	400	750
N (ions/cm^{-3})	6	6
T (K)	240k	24k

Table 5.2: ***Macroscopic parameters***

In terms of parameters actually used in the simulation, the temperature in the solar wind is defined by the choice $\beta = 0.5$ (typical value in the solar wind); whereas the temperature in the magnetic cloud is chosen to be 10 times smaller than in the solar wind (what we see in the 14-12-2006 event).

	Start injection	Transition time	Start decreasing	Decrease time	Collision shock/shock
$\Omega_{\mathrm{ci}}^{-1}$	60	5	70	140	216.5

Table 5.3: ***Simulation timeline***

5.4 Developing new diagnostics in LatHyS

5.4.1 Unevenly separated time dumps

In LatHyS, as in most particle-in-cell codes, there is much more data being processed than data being saved. The reason is that in order to run and to simulate properly the physics, LatHyS has to keep track of the position and velocity of billions of particles, as well as the value of the electromagnetic field on hundreds of millions of grid-cells. It would be an extremely bad idea to try and save all this information at every iteration of the code: it would make simulations extremely slow, and thousands upon thousands of terabytes of data would need to find a home. Instead, what the code does is to create information, then use it for the next iteration before destroying it, thus constantly using the same memory space.

The choice of what to save is the responsibility of the user. Most of the figures included in the next few chapters of this manuscript have been generated using the most common way to save data on particle-in-cells codes: every few dozen or hundreds of iterations, the average of particle moments are saved along with the values of the electric and magnetic fields on each grid cell. Since each of these “time dumps” takes time during the simulation, and is costly in terms of memory, we usually save only the data at times of particular interest. In our case we decided to save at irregularly spaced times, in order to have a good resolution on the critical parts of the simulation: we monitor the formation of the magnetosheath with just a few time dumps, then we make them much closer to each other during the sheath/magnetosheath interaction, before spacing them more during the magnetic cloud/magnetosheath interaction which had already been studied by Turc et al. (2015).

The exact saving times are summarised in the table at the bottom of figure 5.12, along with a timeline of the simulation (arrows and boxes). The propagation of the sheath inside of the magnetosheath is monitored by saving the data every $\Omega_{\mathrm{ci}}^{-1}$.

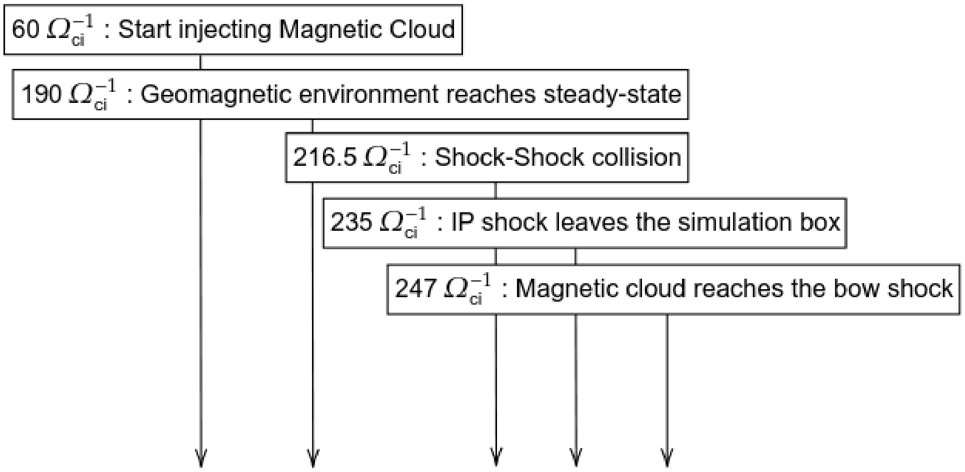

time (Ω_{ci}^{-1})	0	190	210	245	270	300
Save every	20	5	1	5	10	

Figure 5.12: *Arrows and frames above the table: “events” in the simulation. First row: time at which the frequency of saving changes. Second row: frequency of saving data from LatHyS.*

5.4.2 Virtual satellites

We also found it interesting to save additional data with a period of 1 Ω_{ci}^{-1} during the whole simulation, but only at a few fixed locations. To do so, we placed some "virtual satellites" in the simulation, recording the magnetic field, plasma density and bulk velocities. Having this fleet of satellites recording data in the simulation did not seem to slow it down. The satellites were placed according to the following rules (see figure 5.13):

- If the satellite is less than 120 d_i away from the obstacle's centre, we place one satellite every 10 d_i in the x, and every 25 d_i in the y and z directions.
- One satellite every 100 d_i in the y and z and at $x = 0$, and $x = 750$ otherwise.

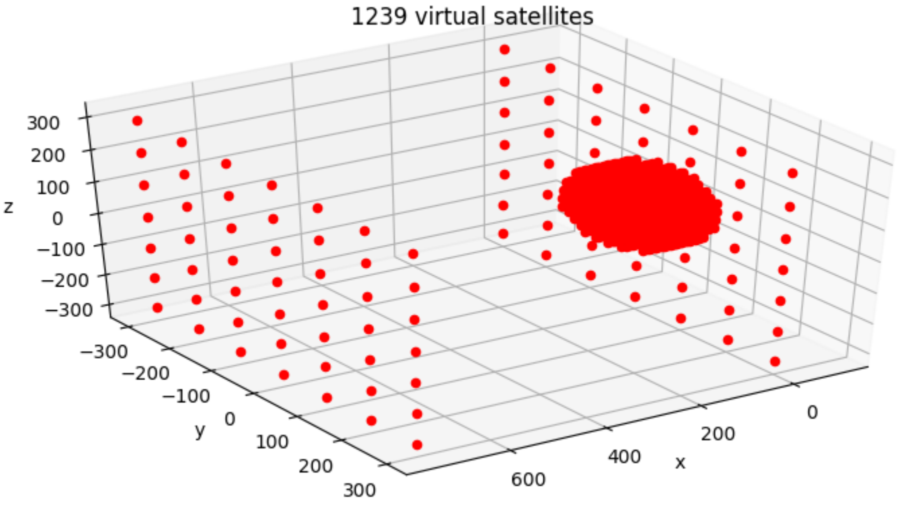

Figure 5.13: *Positions of the complete fleet of virtual satellites.*

From this fleet, we selected, *a posteriori*, a few virtual satellites that were placed at critical locations (see figure 5.14):

- Three satellites on the Sun-Earth line: one upstream of the bow shock in the solar wind, one just downstream of the bow shock, and likely to cross it at the slightest perturbation, and a second one downstream of the bow shock, deep inside the magnetosheath (roughly at mid-distance between the bow shock and the magnetopause).
- Two satellites on the x=z=0 line, in the equatorial plane, one on each side of Earth, roughly in the middle of the magnetosheath.
- Two satellites on the x=y=0 line, in the noon-midnight meridian plane, one on each side of Earth, roughly in the middle of the magnetosheath.
- One satellite far away from the magnetosheath (x=z=0, y=300), which will be used for reference, as it will measure the unperturbed planar event (magnetic cloud, sheath and shock).

We have written "roughly" in the middle because as we will explore in subsection 6.4, the magnetosheath changes its shape during the simulation, therefore it is impossible for a fixed point to actually stay in the middle of the magnetosheath.

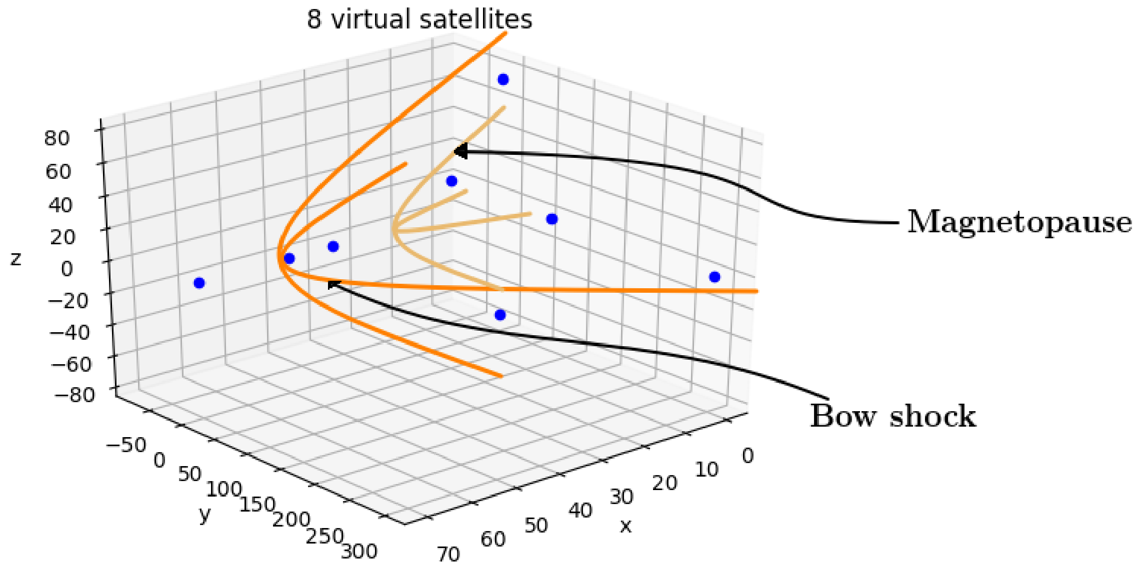

Figure 5.14: *Positions of a few virtual satellites placed at critical positions.*

5.5 From 3D data to numbers: boundary detection and boxes

> **Note:** This section describes codes written in python for the analysis of data from LatHyS. These codes address two major issues.
> The first one is memory: even when saving data at only relevant time dumps, the amount of data generated by our simulations is still very large: the simulation described in chapter 6 produced 4 files per time dump. The average size of these file is 11 Go, and there were 55 time dumps. This leads to roughly 2 To of data. These need to be processed. The second issue is that the interaction between two shocks, and between the magnetosheath and the interplanetary sheath, are very dynamic phenomena, in which the very geometry of our objects of study change over time. In order to follow the changes happening inside the magnetosheath, we need sophisticated automatic detection tools that can track the evolution of its geometry, and do so in 3D.

5.5.1 Boundary detection

In order to track the evolution of the magnetosheath, we need a method to locate the position of the bow shock and magnetopause. While this could be done systematically to automatically detect the whole surfaces defined by the bow shock and magnetopause, for our purposes, knowing their location along the x direction at $y = z = 0$ (Sun-Earth line), along the y direction at $x = z = 0$ (line orthogonal to the Sun-Earth direction, in the ecliptic plane, and passing through the planet) and along the z direction at $x = y = 0$ (line orthogonal to the Sun-Earth direction, in the noon-midnight meridian plane, and passing through the planet) is enough.

The detection method is devised around 1D slices of the simulation domain. Along any line, we average the data on a 10 by 10 square of neighbouring grid cells. This allows the data to be relatively smooth by averaging out the noise. More than 10 by 10, however, would be too large and we would loose in precision. For example, in order to get a 1D representation of the density along Sun-Earth line, we consider a long box going through the whole domain in the x direction, from $y = -5$ to $y = 5$ and from $z = -5$ to $z = 5$, and we average the data along the y and z directions.

The bow shock

On such a slice – scanned from outside of the magnetosheath towards the center of the planet – the bow shock's location is defined as the first local maximum of current where the following tests are verified:

- The current is significantly larger than in the rest of the box (empirically set at 1.7× the average of the current in the rest of the box).
- The coordinate is not next to the box's limits.
- The gradient of the magnetic field points towards earth. This last condition is only necessary along the x direction, in order to discriminate between the bow shock and the interplanetary shock.

Figure 5.15 shows this selection process on data from the simulation:

The upper panel (panel a)) shows the magnetic field magnitude (blue line) for a cut along Sun-Earth line, for x between -100 d_i and 200 d_i. Made at time $t = 210\ \Omega_{\mathrm{ci}}^{-1}$, this figure describes the situation a few time dumps before the shock / shock collision. From left to right, we can recognise the sheath (the fluctuations are barely visible because of the scale) and the interplanetary shock wave, located at $x \simeq 100\ d_i$. There is then an interval of solar wind, before we encounter the bow shock, at $x \simeq 50\ d_i$. We then see the magnetosheath, and the planet's dipole, where the magnetic field amplitude becomes large enough to go out of the scale. The planet centre is located at $x = 0\ d_i$, where the magnetic field is smaller. We then see the other side of the dipole. We will come back to panel a) after describing the other panels.

Panel b) displays the electric current (blue line) as well as its local maxima (blue dots), detected algorithmically. Panel c) represents the results of the tests (non-zero is True and 0 is False) corresponding to the conditions listed above: "j large" (orange) is True if $j > 1.7 \times < j >$; "close to planet" (green) excludes the few coordinate close to the edges of the simulation box, "b grad up" (red) tests for the direction of the magnetic field's gradient). An added test is "coord up" (purple), which simply tests that $x > 0$. Finally, "test up" is True if all the other tests are True and False otherwise. On this figure, since it shows a zoom on the simulation domain, the "close to planet" test (green) is always True.

We can now go back to panel a), where we also displayed the results of "test up" (orange), and the final position of the bow shock (red vertical bar). The final position of the bow shock is defined as the first local maximum of current where"test up" is true.

Along the y and z directions at $x = 0$, the bow shock detection is made the same way as along the x direction, with the exception of the "b grad up" test, which is omitted because we scan a part of the simulation box which does not contain the interplanetary shock, and there is therefore no need to discriminate between the interplanetary shock and the bow shock. Along the y and z directions, however, two bow shock positions need to be defined, one for positive coordinates, and one for negative coordinates.

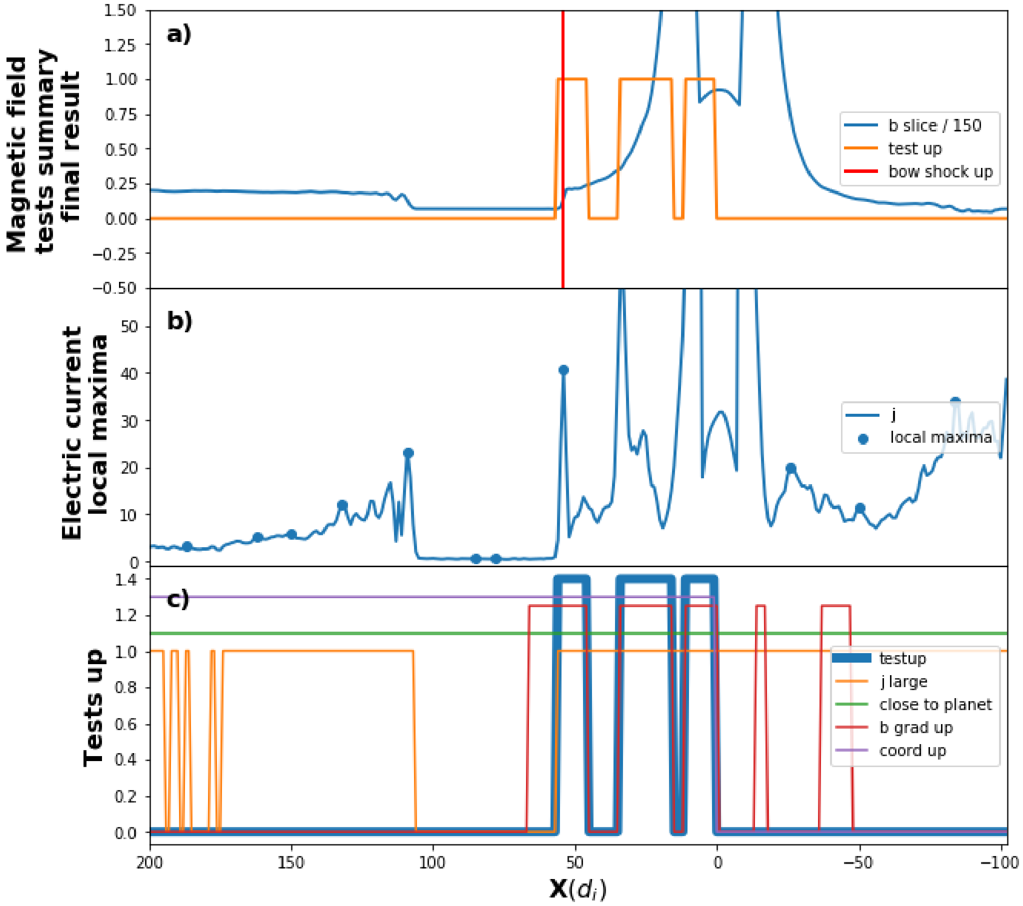

Figure 5.15: *From top to bottom: a) A "slice" of the magnetic field, along with the result of the tests (1 is True and 0 is False), and the final position of the bow shock. You can see that the algorithm found a shock downstream of Earth, which in the x direction does not have any meaning and is discarded. b) A slice of the electric current along with its automatically detected local maxima. c) The different tests ("j large" is True if* $j > 1.7\times < j >$*; "close to planet" excludes the few coordinate close to the edges of the simulation box, "b grad up" tests for the direction of the magnetic field's gradient) and their summary, "test up" is True if all the other tests are True.*

The magnetopause

For slices along the x and z directions, the magnetopause is defined as a local maximum of the current density where the coordinate is comprised between 15 and 80 d_i from the centre of the planet.

The top panel of figure 5.16 represents the density along the x direction, at $y = z = 0$, for x between -100 and 150. This figure is also made at time $t = 210\ \Omega_{\mathrm{ci}}^{-1}$, a few time dumps before the shock / shock collision. On the left side, we can recognise the turbulent interplanetary sheath. There is then a stretch of quiet solar wind, before we see the bow shock, the turbulent magnetosheath, and finally the location of the planet, where the density falls to zero in the code. In this case, the magnetopause is defined as the maximum of current density for $15d_i < |x| < 80d_i$. The test on the

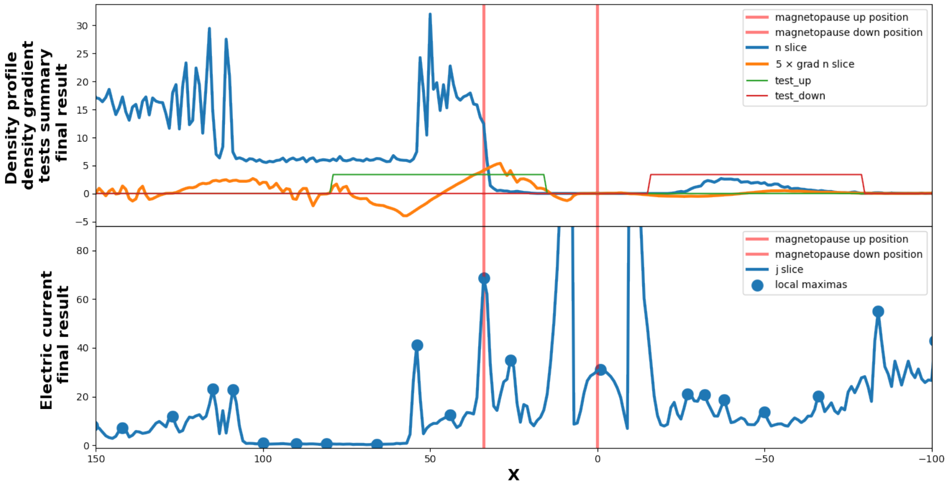

Figure 5.16: *From top to bottom: A "slice" of the density (blue) and its gradient (orange), along with the result of the tests (1 is True and 0 is False; in green if $x > 0$ and red if $x < 0$), and the final positions of the magnetopause (red vertical bar). On this slice along the x direction, the "bottom" position of the magnetopause is given the value 0, to be discarded. A slice of the electric current density along with its automatically detected local maxima. Here the magnetopause position corresponds to a local maximum of current density located between 15 and 80 d_i.*

coordinate (in green and red) is made in order to avoid the very strong currents that exist where the magnetic dipole is created. The final location of the magnetopause is marked with a red vertical bar. You can notice that there is a result at $x = 0$, this is a value chosen to then be discarded by the rest of the algorithm: indeed, in the x direction, the magnetopause is upstream of the planet and there is no magnetopause downstream.

Figure 5.17 is similar to 5.16 and the magnetopause along the z direction (at $x = y = 0$) is defined in the exact same way as along the x direction: as the location of the maximum electric current for $15d_i < |z| < 80d_i$.

Figure 5.18 shows the difference between the current structures in the (xy) and (xz) planes: while the magnetopause corresponds to a well defined current layer in the (xz) plane (left hand-side figure), the more complex current structures in the (xy) plane (right hand-side figures) do not allow such a clear identification of the magnetopause. This makes the peak current method impractical. Therefore we use a different approach in this plane (see figure 5.19), which is to define the magnetopause as the middle of the strong gradients of density, empirically defined as larger than 10% of the maximum density gradients in the box. On the top panel of figure 5.19, the gradient of density is represented with an orange line. The threshold test ($\partial n/\partial y > 0.1 \times max(\partial n/\partial y)$ is represented in green for $y > 0$ and red for $y < 0$. The final result (red vertical bar) is located at the middle of the longest stretch of this test being true.

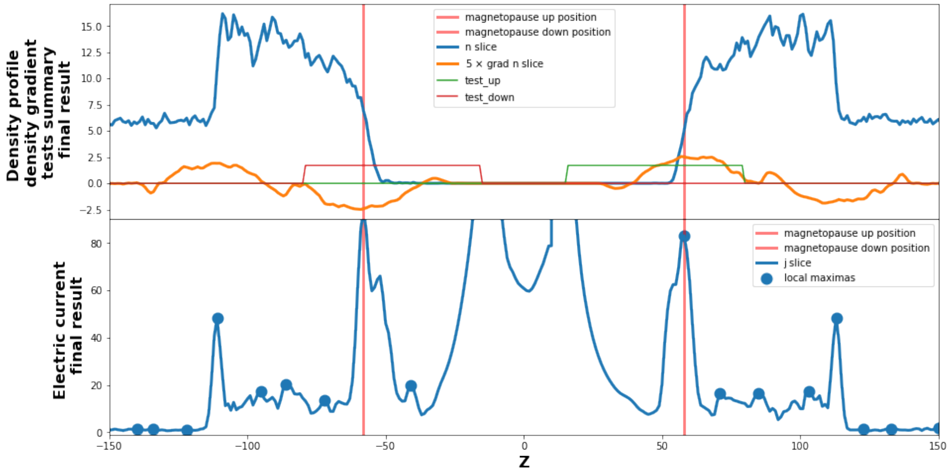

Figure 5.17: *From top to bottom: A "slice" of the density (blue) and its gradient (orange), along with the result of the tests (1 is True and 0 is False; in green if* $z > 0$ *and red if* $z < 0$*), and the final positions of the magnetopause (red vertical bar). A slice of the electric current density along with its automatically detected local maxima. Here the magnetopause position corresponds to a local maximum of current density located between* 15 *and* 80 d_i.

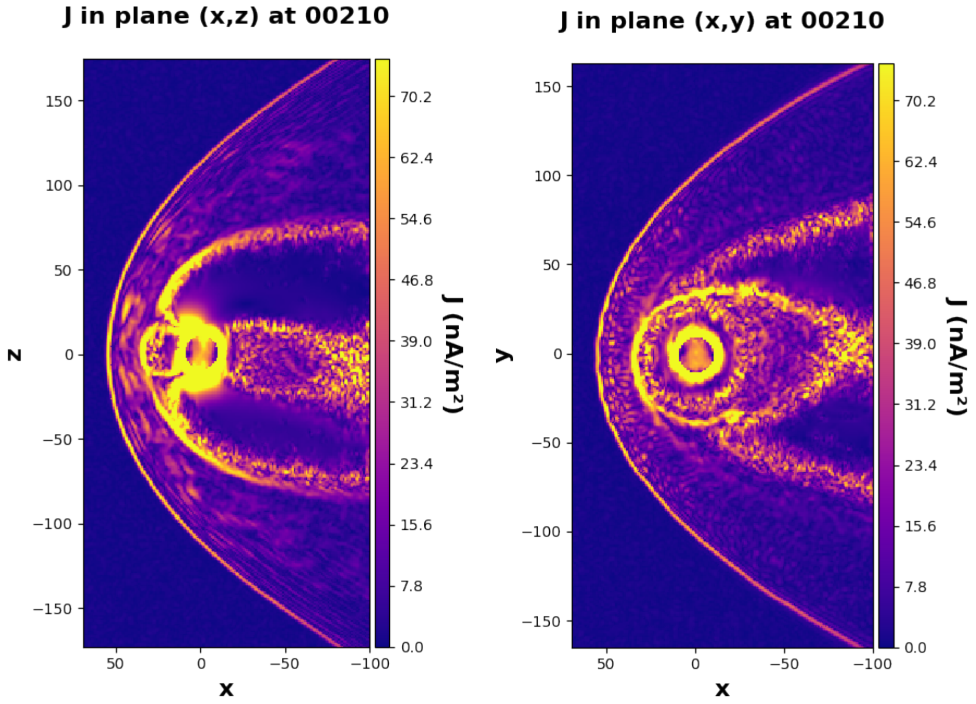

Figure 5.18: *Current density at time* $t = 210\ \Omega_{ci}^{-1}$ *(soon before the shock/shock collision). Two planes are shown: the equatorial plane (xy) and the noon-midnight meridian plane (xz).*

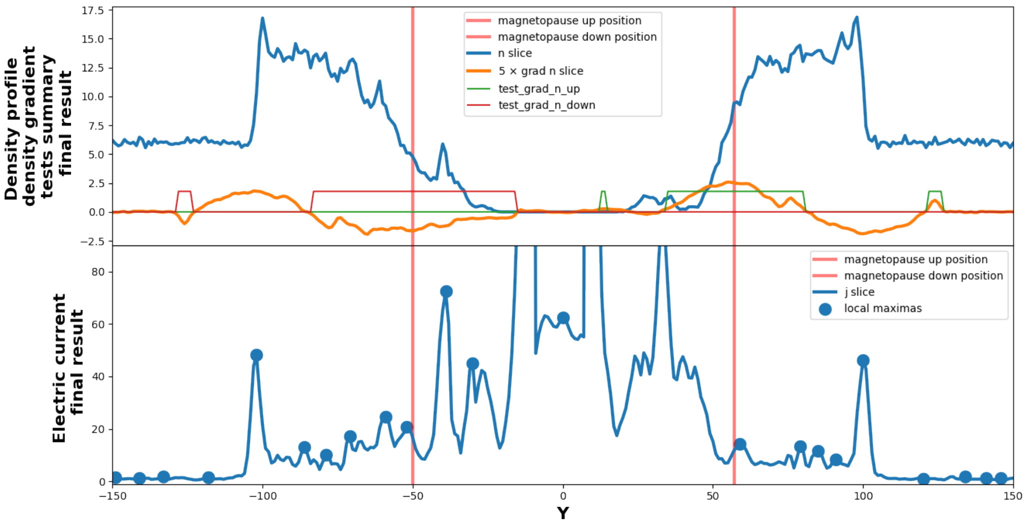

Figure 5.19: *From top to bottom: A "slice" of the density (blue) and its gradient (orange), along with the result of the tests (1 is True and 0 is False; in green if* $y > 0$ *and red if* $y < 0$*), and the final positions of the magnetopause (red vertical bar). A slice of the electric current density along with its automatically detected local maxima. Here the magnetopause position corresponds to the middle of a strong density gradient; the current structures being too complex in this plane to be used with coherent results.*

The interplanetary shock

The interplanetary shock is straightforwardly defined as the location of the largest velocity gradient in the box. On 5.20, we can see the velocity (top panel) and its gradient (bottom panel) along the x direction. This detection is made at the very edge of the simulation box ($y = max(y) - 2$, $z = max(z) - 2$). This allows us to simplify the test greatly by excluding the planet's geomagnetic environment from the cut along the x direction. The physical structures are the sheath, from $x \simeq 100$ to $x \simeq 300$ and the magnetic cloud, from $x \simeq 300$ to $x \simeq 800$.

The leading edge of the magnetic cloud

Similarly to the previous interplanetary shock's detection, the cut used for the detection of the magnetic cloud leading edge is taken at the very edge of the simulation box ($y = max(y) - 2$, $z = max(z) - 2$). The leading edge of the magnetic cloud, is defined as a local maximum of current density where the following conditions are met (see figure 5.21):

- There is a strong negative gradient of density (magnetic clouds are less dense than sheaths)
- There is a strong gradient of magnetic field (in our simulations, the magnetic field in the cloud is larger than in the sheath, this is not systematically true in observations)

Figure 5.21 shows, from top to bottom: the density, the magnetic field, the current, the density gradient $\partial n/\partial x$, the threshold test on the density gradient (true if $\partial n/\partial x$ is larger than its average value), the magnetic field's amplitude gradient $\partial|\boldsymbol{B}|/\partial x$ and the threshold test on its gradient (true if $\partial|\boldsymbol{B}|/\partial x$ is larger than its average value). Finally, the location of the magnetic cloud's leading edge

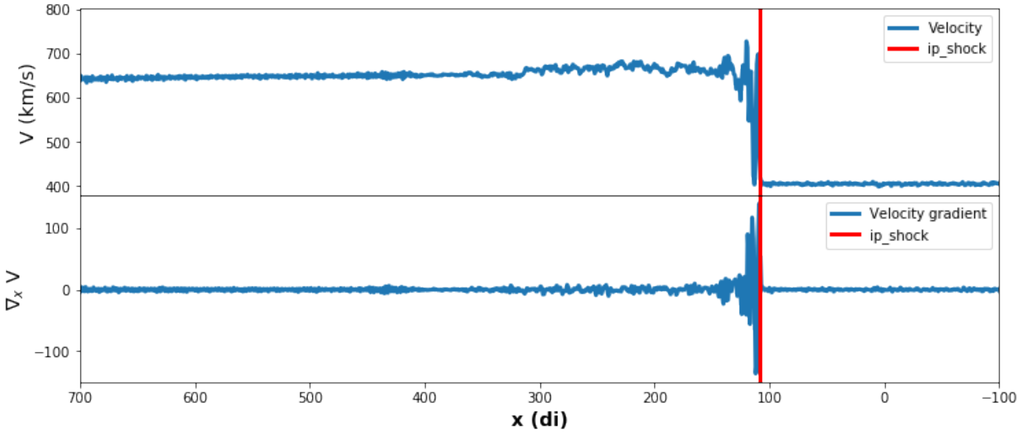

Figure 5.20: *From top to bottom, a slice of the plasma velocity and its gradient. The vertical red line shows the position of the interplanetary shock.*

is marked with a vertical red line.

It is still a matter of debate what type of discontinuity is the leading edge of a magnetic cloud. In our simulation, we could satisfy ourselves with an empirical definition based on a local maximum of current density, but it is much more complicated to agree on a specific definition with observational data (see figure 2.2 on page 41).

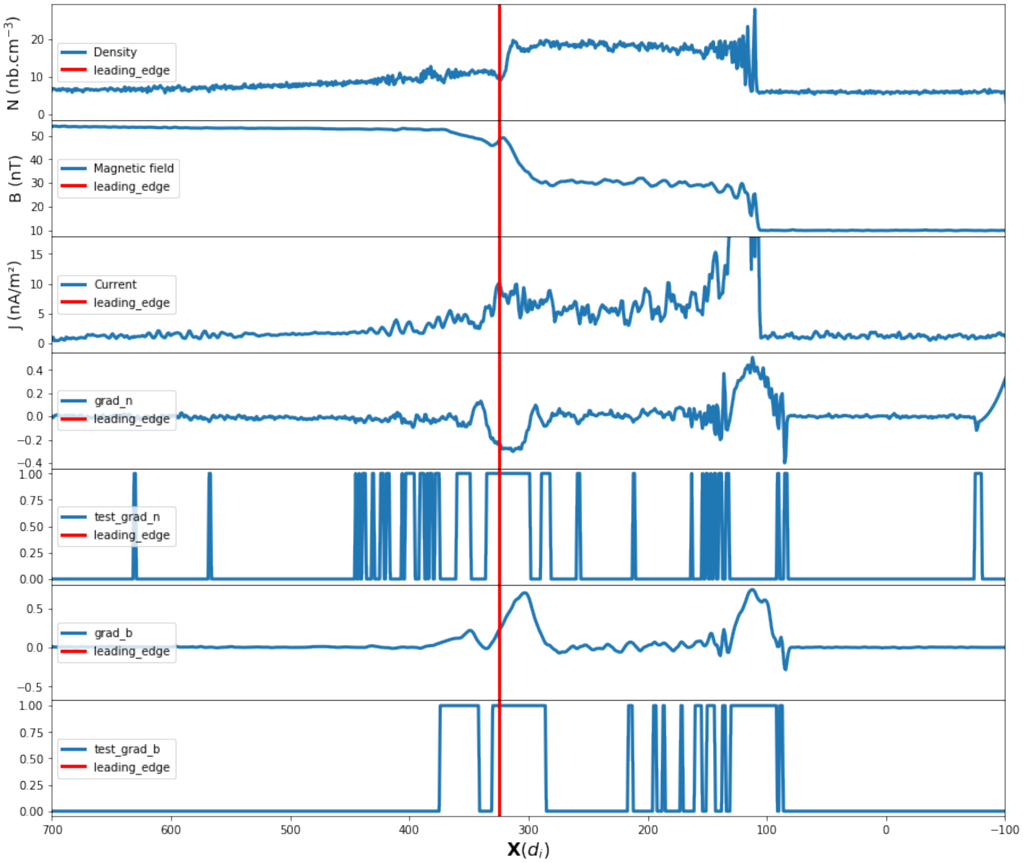

Figure 5.21: *From top to bottom: a slice of the density, a slice of the magnetic field amplitude, a slice of the electric current density, the gradient of the density, a threshold test for a negative density gradient, the gradient of the magnetic field, a threshold test for a strong positive gradient of magnetic field. The vertical red bar shows the position of the leading edge.*

One last test

An additional test has been made in order to make the process of boundaries detection robust. For each time dump, the boundary selection is first made according to the steps described above. Then, the newly found boundary positions are compared to the ones found for the previous time dump: if the position is too far away from the previous one, then its location is declared wrong, and the above tests are made once more, excluding the absurd location. Most time dumps do not need this last verification, which is the reason it is useful: it efficiently detects an odd result from a series of good ones.

Summary

Figure 5.22 shows the density in the noon-midnight meridian plane (xz). All the different boundaries, as detected by the algorithms described above are displayed as markers: red dots for the bow shock and magnetopause, cyan crosses for the interplanetary shock and magnetic cloud leading edge. The magnetosheath and interplanetary sheath are clearly recognisable.

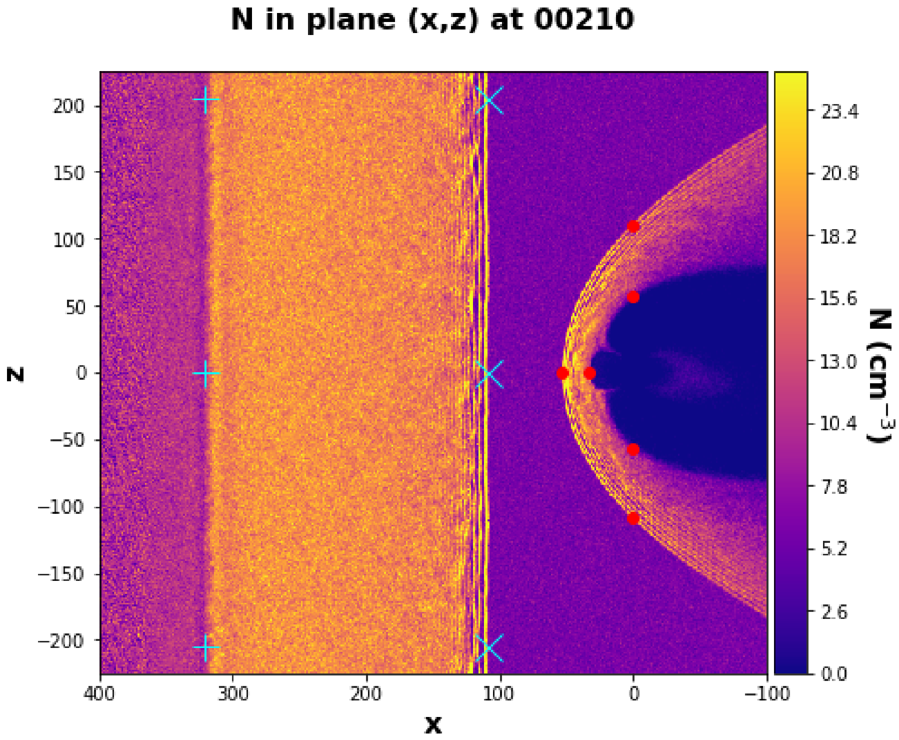

Figure 5.22: *Density at time* $t = 210\ \Omega_{ci}^{-1}$ *(soon before the shock/shock collision), in the noon-midnight meridian plane (xz). Red dots mark the positions of the bow shock and magnetopause as detected by the algorithms described in this section. Cyan diagonal crosses mark the position of the interplanetary shock, and the cyan "+" mark the position of the leading edge.*

5.5.2 Simple tracking: the "boxes method"

In order to probe the evolution of the magnetosheath during its interaction with the sheath, we focused on six regions, that we will from now on denote "*boxes*". To construct their positions, we made use of the boundaries that were detected as explained in subsection 5.5.1. This allows us to think about them as representing different regions of the magnetosheath, which a fixed location in the simulation could not do, owing to the movements of the magnetosheath itself. As we will see in section 7.3.2, measures at fixed locations can sometimes be confusing because they do not always represent the same region.

The first box is constructed so that its centre is along the Sun-Earth line, midway through the magnetosheath. The size of its edges is a few grid cells shorter than the thickness of the magnetosheath, so that the bow shock and magnetopause are safely excluded from the box. This box will be referred to as "nose". The four other boxes also have their centres midway through the magnetosheath on the lines starting from Earth's centre and going respectively along the y direction towards the positive or negative values of y, and along the z direction towards the positive or negative values of z. They are respectively called "ydusk", "ydawn", "zup" and "zdown". Finally, a box called "upstream" is placed upstream of the bow shock on the Sun-Earth line. Figure 5.23 shows the position of theses boxes in relation to each other and to the geomagnetic frontiers.

In the following chapter we will make use of these boxes to display the evolution of physical quantities inside of the magnetosheath. For example, if we wish to investigate the evolution of the density, we average the plasma density in each of the boxes, and display the evolution of the six numbers thus obtained against time (*e.g.* see figure 6.10 on page 139).

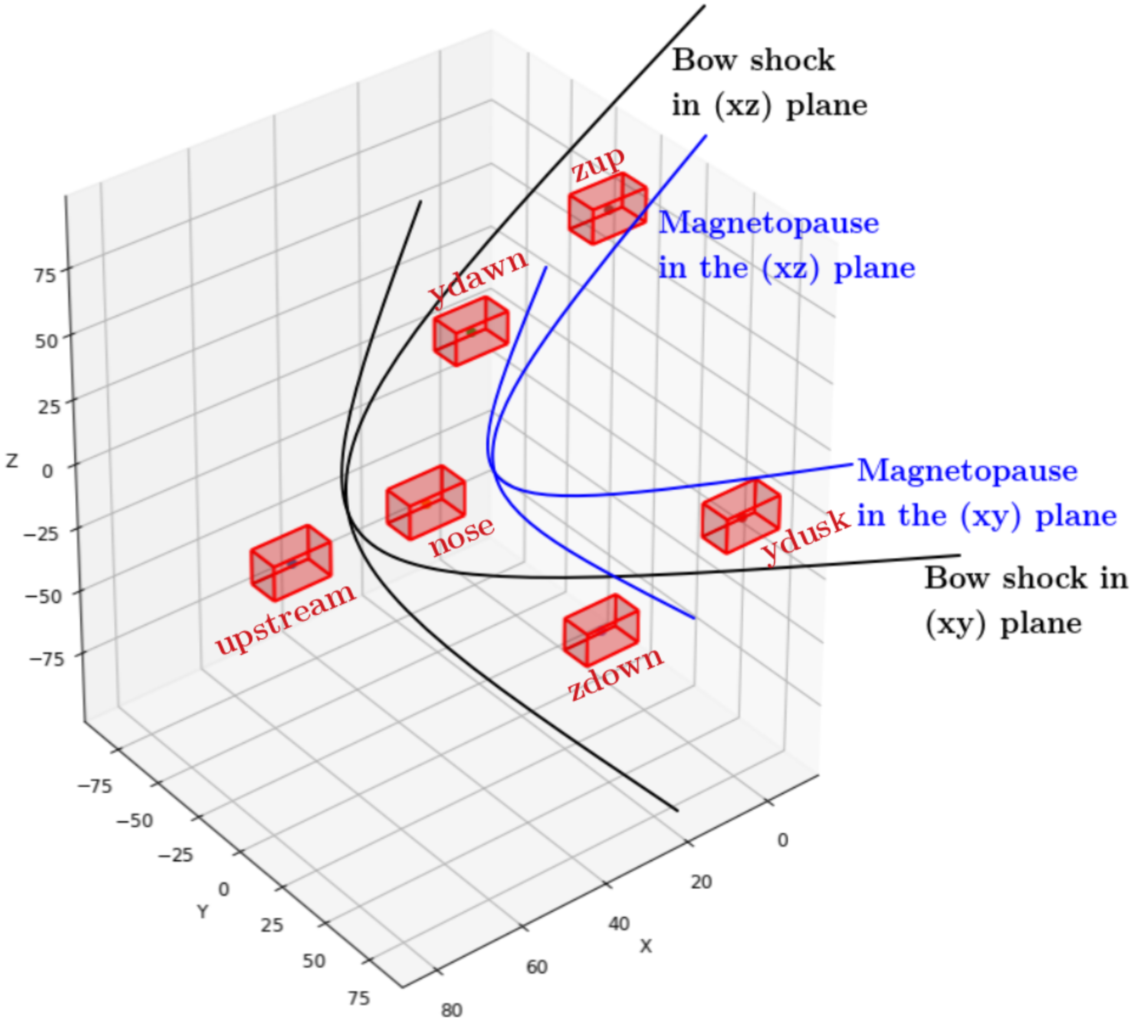

Figure 5.23: *Position of the boxes at time* $t = 210\ \Omega_{ci}^{-1}$*. Note: the boxes are actual cubes, but on this figure the axes do not all have the same scaling. Approximate positions of the bow shock and magnetopause have been drawn (black and blue lines) on top of the figure to guide the eye.*

6. Numerical Simulations: Results & discussions

Note: In this chapter, we present and discuss the results obtained from our LatHyS simulations of the interaction between the magnetosheath and the interplanetary sheath. First we analyse how the interplanetary shock changes as it traverses the bow shock and propagates in the magnetosheath (section 6.2). We then analyse how the magnetosheath evolves under the new upstream conditions imposed to it by the arrival of the interplanetary shock and sheath (section 6.3). Next, we see how the position of the geomagnetic frontiers – the bow shock and the magnetopause – react to the passage of the sheath (section 6.4). Finally, we explain a strong and peculiar asymmetry in the plane perpendicular to the interplanetary magnetic field (section 6.5).

Contents

6.1 Introduction and strategy

As described in chapter 5, we set up the planet's magnetic environment (magnetosphere/magnetopause/bow shock with an Alfvén Mach number of $M_A^{\text{bow shock}} = 4.5$) on one side of the 3D PIC-hybrid simulation box and the magnetic cloud/sheath/shock on the other side (the magnetic cloud – driven shock has $M_A^{\text{IP shock}} = 3.1$). Both shocks having a similar strength leads to them having a strong influence on each other. We can now observe the collision between the two collisionless shocks, and the interaction of the sheath with the magnetosheath.

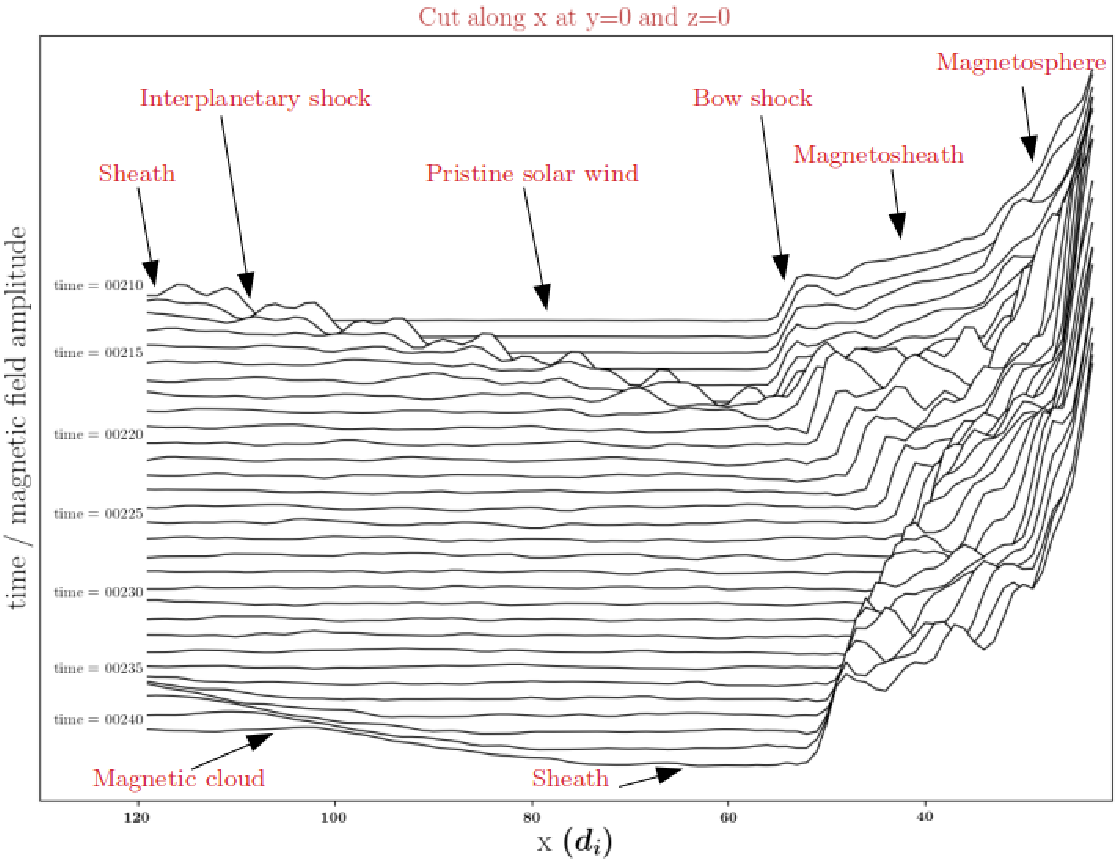

Figure 6.1: *Evolution of the magnetic field's amplitude in a cut taken along the X direction. The Y axis represents both the amplitude of the field, and the time, each new line from top to bottom representing a later state of the magnetic field.*

Figure 6.1 represents, on the y axis, both the amplitude of the magnetic field and its evolution in time. Because both are on the same axis, it is useful for gaining a qualitative intuition of the unfolding of the simulation, but unpractical if we wish to obtain quantitative information from it. Let us start by explaining the line at the top of the figure: it represents, at time $t = 210\ \Omega_{\text{ci}}^{-1}$, the amplitude of the magnetic field along the x direction, for a slice taken at $y = z = 0$ (on the Sun-Earth line). On this top line, we can recognise, from left to right: a small part of the turbulent sheath, the interplanetary shock, a stretch of quiet solar wind, the bow shock, the magnetosheath, and the beginning of the terrestrial dipole. On this figure, the location of the magnetopause can be guessed visually as the place at which the gradient of the magnetic field changes abruptly towards the right side of the box, at $x \sim 34\ d_i$. The line directly under this top line represents the magnetic field's amplitude at time $t = 211\ \Omega_{\rm ci}^{-1}$, the next line is the magnetic field's amplitude at time $t = 212\ \Omega_{\rm ci}^{-1}$ and so on as the rest of the figure is constructed in the same manner.

We can see the evolution of the simulation at a glance by looking from the top to the bottom of the figure: the interplanetary shock propagates through the pristine solar wind until it collides with the bow shock between times $t = 216\ \Omega_{\rm ci}^{-1}$ and $t = 217\ \Omega_{\rm ci}^{-1}$. From that time of collision, the position of the bow shock clearly recedes Earthward until $t = 228\ \Omega_{\rm ci}^{-1}$, when it reverses its direction of motion and expands sunward. In the latest times displayed (lower part of the figure), the magnetic cloud starts appearing on the left side.

A careful reading of figure 6.1 thus gives us a preview of the consequences of the magnetosheath-sheath interaction. After the two shocks collide around $216.5\ \Omega_{\rm ci}^{-1}$, we can see the following interesting phenomena:

- The propagation of the interplanetary shock through the magnetosheath does not appear to be as straightforward than in the solar wind prior to the collision: the planet's magnetic environment seems to have an influence on the interplanetary shock.
- The interplanetary shock, in turn, seems to heavily influence the planet's magnetic environment:
  - Both the bow shock and the magnetopause first recede, pushed back by the increased pressure in the sheath. Then, before the leading edge of the magnetic cloud reaches the magnetosphere, the bow shock expands again, and the magnetopause position seems to reach a minimum stable value.
  - The magnetic field amplitude in the magnetosheath becomes larger than it was in both the magnetosheath and the sheath.
  - The level of magnetic fluctuations in the magnetosheath is significantly enhanced during the passage of the sheath.

The three next sections will detail the first three points raised from figure 6.1.
In section 6.2 we analyse the propagation of the interplanetary shock inside the magnetosheath and answer the following questions: is it slowed down? does it keep its shape?
After having looked at how the magnetosheath changes the interplanetary shock, we explore the impact of the interplanetary shock and the following sheath on the magnetosheath:
In section 6.3, we discuss the response of the magnetosheath to the passage of the sheath in terms of the changes of the plasma and electromagnetic parameters inside of it.
In section 6.4, we look at the evolution of the positions of the bow shock and magnetopause after they encounter the interplanetary sheath.
Finally, a fourth section 6.5 will treat something that a 1D view could not catch: a strong asymmetry in the (xz) plane during the passage of the sheath.

6.2 Propagation of the IP shock in the magnetosheath

6.2.1 From the bow shock to the magnetopause

Figure 6.2 shows the position of the interplanetary (IP) shock (red line) as it crosses the bow shock (purple vertical dashed line) and propagates in the magnetosheath along the Sun-Earth line. The position of the interplanetary shock outside of the magnetosheath has been given for reference (blue line). On this plot, the positions and times are given respectively in $d_i = 93$ km and $\Omega_{\text{ci}}^{-1} = 1.0$ s (pristine solar wind values).

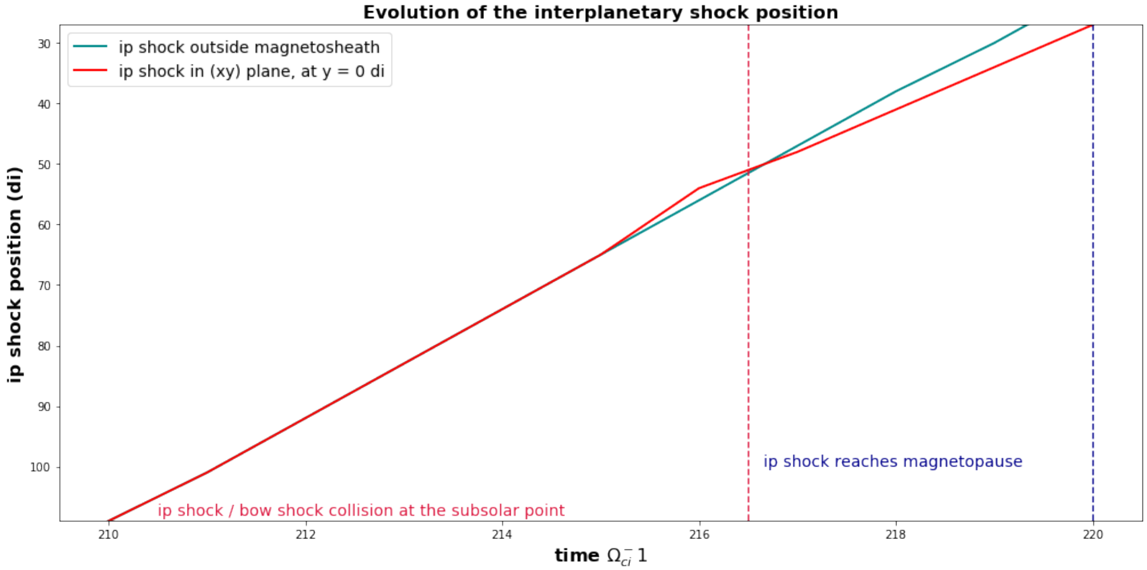

Figure 6.2: *Blue line: position of the unperturbed interplanetary shock, as followed outside of the magnetosheath. Red line: position of the interplanetary shock as followed along the Sun-Earth line* ($y = z = 0$) *until it reaches the magnetopause at* $t = 220\ \Omega_{ci}^{-1}$. *The two dashed vertical lines indicate the arrival of the interplanetary shock at the nose of the bow shock (red) and, later, at the nose of the magnetosheath (blue).*

At time $t = 216\ \Omega_{\text{ci}}^{-1}$, the IP shock's position is in advance as compared to the reference. This is not a physical effect, but an inaccuracy of the detection method. This is easily explained with figure 6.3: as the IP shock gets very close to the bow shock, the two shocks become almost a single discontinuity, and the position of the IP shock, defined as a local maximum of the velocity gradient becomes ill-defined.

Figure 6.2 indicates that the IP shock slows down as soon as it penetrates inside the magnetosheath, and then does not seem to slow down any more: the slope changes once and for all at $t = 216.5\ \Omega_{\text{ci}}^{-1}$. This result is consistent with observations from Koval et al. (2005), Koval et al. (2006a), Pallocchia et al. (2010) and simulations from Koval et al. (2005), Koval et al. (2006b), Samsonov et al. (2006) and Pallocchia et al. (2010). We can estimate the velocity of the interplanetary shock $v_{\text{prior}}^{\text{IS}}$ prior to the interaction with the magnetosheath:

$$v_{\text{prior}}^{IS} = 8.8\ d_i/\Omega_{\text{ci}}^{-1} = 7.9 \cdot 10^2 \text{ km/s} \tag{6.1}$$

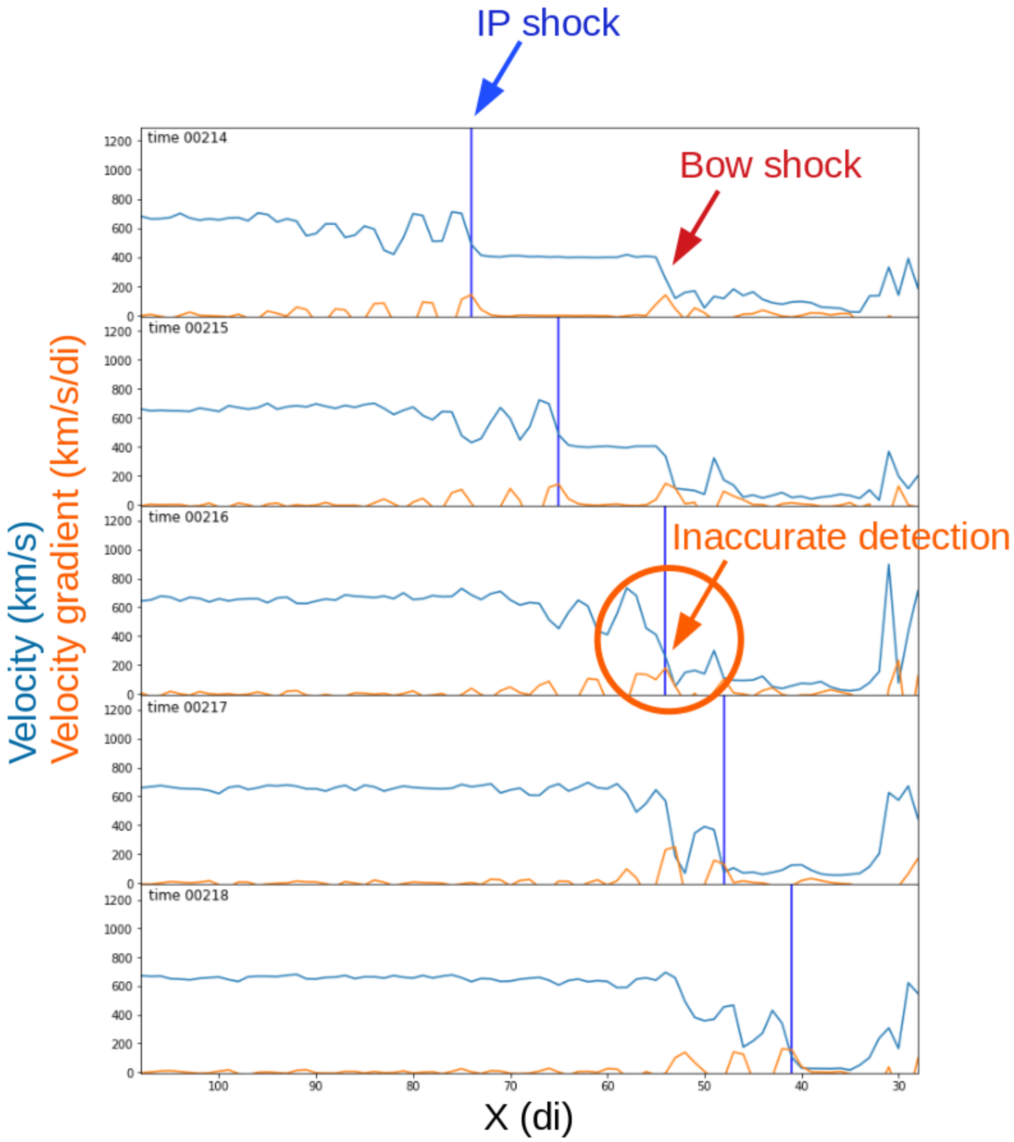

Figure 6.3: *Propagation of the interplanetary (IP) shock along the Sun-Earth line. The blue line represents the velocity and the orange line represents its gradient. The IP shock position, which is defined as a local maximum of the velocity gradient, is represented with a deep blue vertical bar. From top to bottom, the different plots are cuts at different simulation times. At* $t = 216\ \Omega_{ci}^{-1}$*, we can see that the detection of the IP shock, based on a local maximum of velocity gradient, is inaccurate because the IP shock and the bow shock are almost on top of each other.*

We can also estimate the velocity of the interplanetary shock v_{msh}^{IS} once it is propagating inside the magnetosheath:

$$v_{\mathrm{msh}}^{IS} = 7.0\ d_i/\Omega_{\mathrm{ci}}^{-1} = 6.3 \cdot 10^2\ \mathrm{km/s} \tag{6.2}$$

From this we can deduce two things:

- The ratio between the velocity of the interplanetary shock outside of the magnetosheath and inside of the magnetosheath is of $v^{IS}_{\text{msh}}/v^{IS}_{\text{prior}} = 0.8$. This is coherent with Koval et al. (2006a), which reported that the new speed of the interplanetary shock in the magnetosheath is 0.73 to 0.97 of its value in the solar wind.
- It takes, in our simulation, 3.5 Ω_{ci}^{-1} for the interplanetary shock to go from the bow shock to the magnetopause and there is a ratio of $1/16^{th}$ between the simulation and the reality. Therefore, in reality, it should take roughly 56 seconds for an interplanetary shock (under the conditions simulated here) to cross the magnetosheath. This is quite a short time (for example, Villante et al. (2004) assumes a transit time of 1-2 minutes) because our shock is quite a strong shock ($M_A = 3.1$).

From this deceleration of the interplanetary shock inside the magnetosheath, we can make the simple following logical conclusion: If the interplanetary shock slows down as soon as it crosses the bow shock and enters the magnetosheath, since the bow shock is curved, a natural consequence should be a resulting curvature of the interplanetary shock. Indeed, while the part of the interplanetary shock that already crossed the bow shock at its nose is travelling at a slower velocity; the rest of the interplanetary shock that has not yet crossed the bow shock still travels at full speed. This phenomenon can be seen at a glance by comparing figure 6.4 (before the collision) and figure 6.5 (after the collision).

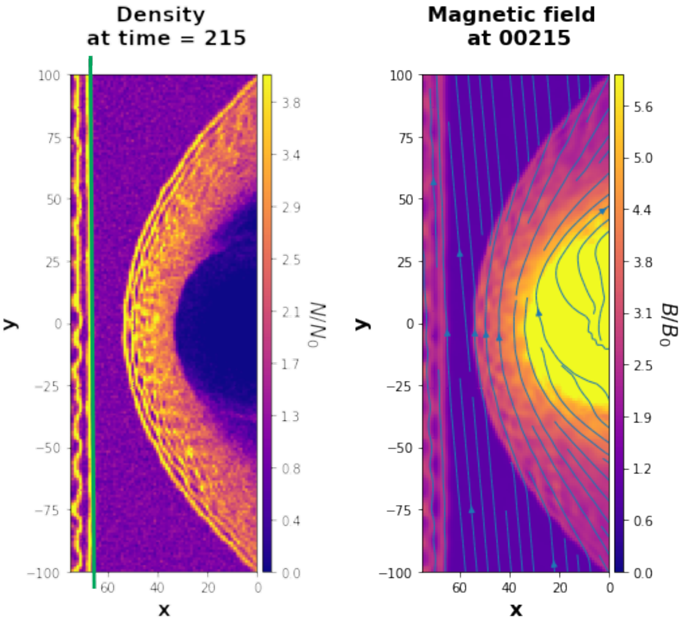

Figure 6.4: *Density and Magnetic field (with magnetic field lines) in the equatorial (xy) plane, soon before the shock/shock collision. On the left hand-side plot, a vertical green line marks the position of the interplanetary shock outside of the magnetosheath.*

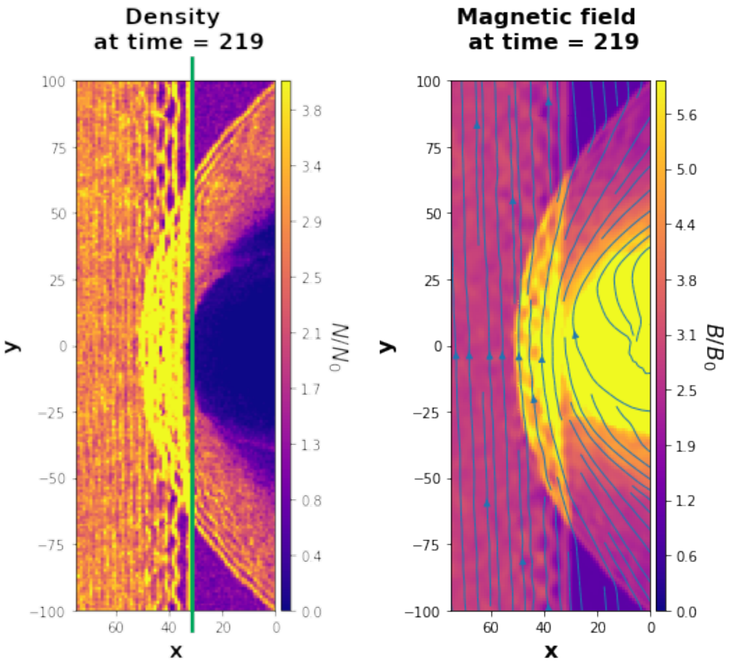

Figure 6.5: *Idem, soon after the shock/shock collision. The vertical green line makes the curvature of the interplanetary shock inside of the magnetosheath obvious.*

Figure 6.4 is a zoom on the magnetosheath which shows the density and the magnetic field in the (xy) plane just before the shock-shock collision. On the left side of the plots, at $x \simeq 65\ d_i$, we recognise the interplanetary shock. A green vertical straight line has been drawn on the shock front on the density plot. We can see that the shock is planar.

Figure 6.5 shows the density and the magnetic field in the (xy) plane just after the shock-shock collision. By drawing the straight green line again from the interplanetary shock's position outside of the magnetosheath, we can see the shock is slightly curved: the closer to $y = 0$ the shock is, the more its position is lagging behind the rest of the interplanetary shock's. This figure is very similar to figure 5 in Spreiter and Stahara (1994), which stated that the interplanetary shock was nearly planar in the magnetosheath, and to figure 5 in Koval et al. (2005), which emphasised the apparition of a curvature of the interplanetary shock inside the magnetosheath. While the two authors reported very similar results, they worded them very differently. We think that they did so because their expectations were different: while Spreiter and Stahara (1994) probably expected a markedly curved shock, Koval et al. (2005) noted a strong difference between their results and the arguments of Szabo et al. (2003) and Szabo (2004) which stated that the front of interplanetary shock waves travelling through the magnetosheath were most likely unperturbed.

6.2.2 On the flanks of the magnetopause

Following the same method, we now direct our attention to the propagation of the interplanetary shock on the flanks of the magnetosheath. Figure 6.6 is constructed in the same way as figure 6.2 (the red and blue lines are the same) but looks at later times. Two lines have been added to represent the propagation of the interplanetary shock along the flanks of the magnetopause: an orange line, which marks the interplanetary shock's position in the equatorial plane, at $z = 0$ and $y = 90\ d_i$; and a green line, which marks the interplanetary shock's position at $y = 0$ and $z = 80\ d_i$: above the northern pole. These locations have been chosen to cross the magnetosheath close to the magnetopause without crossing the latter. In figure 6.6 it clearly appears that in the (xy) plane the interplanetary shock (orange line) slows down compared to the unperturbed shock (blue line): the orange line passes durably under the blue line. In the (xz) plane (green line), on the other hand, the shock first slightly slows down (the green line passes under the blue line), before accelerating (the green line passes under the blue line).

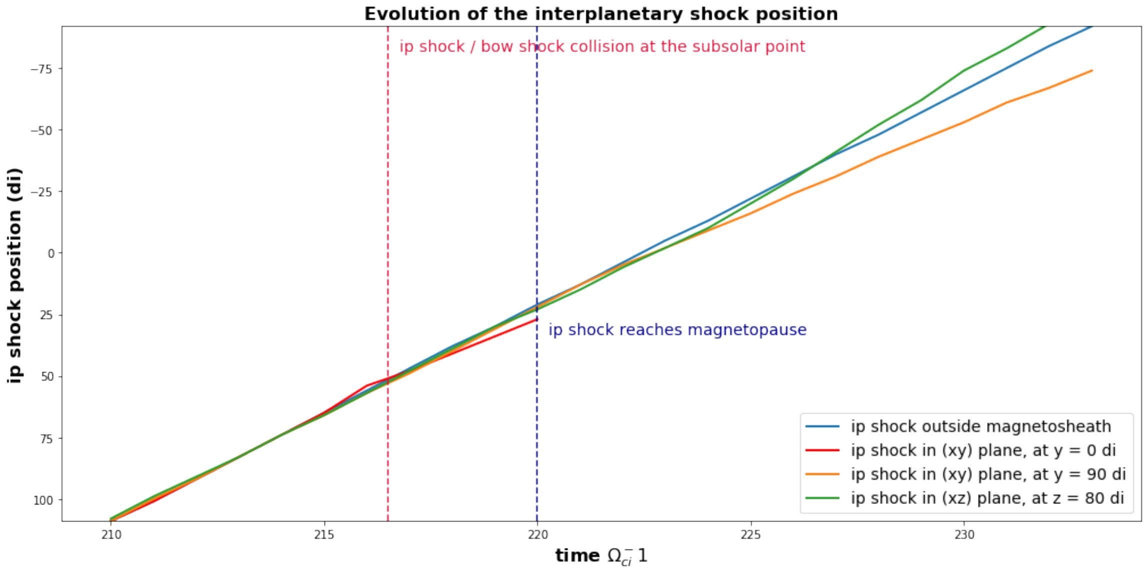

Figure 6.6: *Blue line: position of the unperturbed interplanetary shock, as followed outside of the magnetosheath. Red line: position of the interplanetary shock as followed along the Sun-Earth line ($y = z = 0$) until it reaches the magnetopause at $t = 220\ \Omega_{ci}^{-1}$. Green line: position of the interplanetary shock in the noon-midnight meridian plane along the line $y = 0$, $z = 80$. Orange line: position of the interplanetary shock in the equatorial plane along the line $y = 90$, $z = 0$. The two dashed vertical lines indicate the arrival of the interplanetary shock at the nose of the bow shock (red) and, later, at the nose of the magnetosheath (blue)*

Figure 6.7 shows the macroscopic result of this asymmetric acceleration of the interplanetary magnetic shock in the magnetosheath: both in the (xy) and (xz) plane the interplanetary shock front is curved. In the plane which contains most of the interplanetary magnetic field (in this case, the equatorial (xy) plane), the shock slows down near the magnetopause and becomes concave. In the plane perpendicular to the interplanetary magnetic field (in this case, the noon-midnight meridian (xz) plane), the shock accelerates slightly and becomes convex.

Our simulation points toward the same conclusion as Koval et al. (2005, 2006b), in which observations coupled with MHD modelling suggest that the interplanetary shock front is curved.

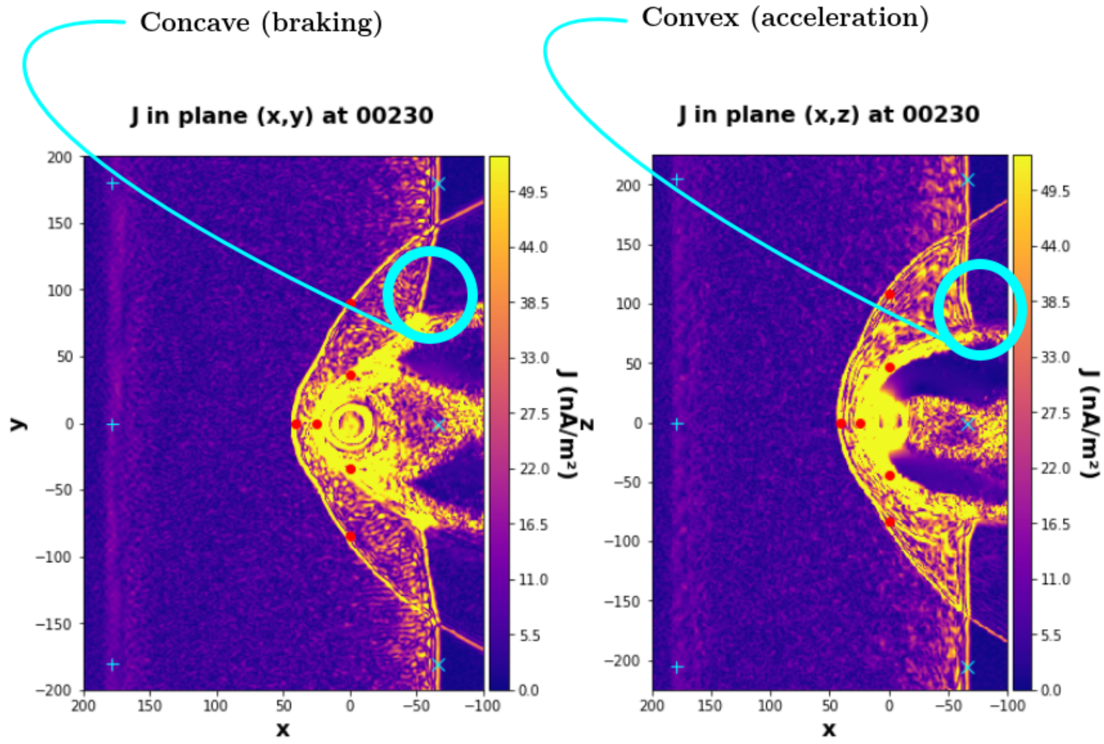

Figure 6.7: *Left panel: Current density in the equatorial (xy) plane. Right panel: Current density in the noon-midnight meridian (xz) plane. These slices are taken at time* $t = 230\Omega_{ci}$*, as the sheath has penetrated quite deeply into the magnetosheath.*

While the concave shape we observe in the interplanetary magnetic field's plane – resulting from a deceleration of the shock at the nose of the magnetosheath – has been noted by Koval et al. (2005), there exist, to our knowledge, no mention of a convex shape in the plane perpendicular to the interplanetary magnetic field.

We offer the following qualitative explanation, of which figure 6.8 is an illustration: In our simulations, most of the magnetic field in the solar wind are along the y direction. The field lines, pushed by the solar wind onto the geomagnetic dipole will be compressed at the center of the magnetopause and stretched on the wings of the magnetopause in the (xy) plane. Magnetic tension builds up in the thus stretched magnetic field lines, until they slip around the magnetopause. The magnetic tension is released and accelerate particles in the (xz) plane. As already mentioned on page 101 in subsection 5.2.2, this explanation is classically used to explain the faster plasmas velocities found in the magnetosheath's wings in the plane perpendicular to the mean IMF, as compared to the velocities in the plane containing the mean IMF (Chen et al. (1993); Lavraud et al. (2013), Turc et al. (2015)). Our simulations suggest that the very same explanation leads to a non-trivial curvature of the bow shock: concave in the plane containing the IMF, convex in the plane perpendicular to the IMF and a continuum in between.

Using figure 6.6, we can make a rough estimate of the expected delay/advance of the detection of the interplanetary shock by a satellite that would be placed at $17R_E$ downstream of Earth (corre-

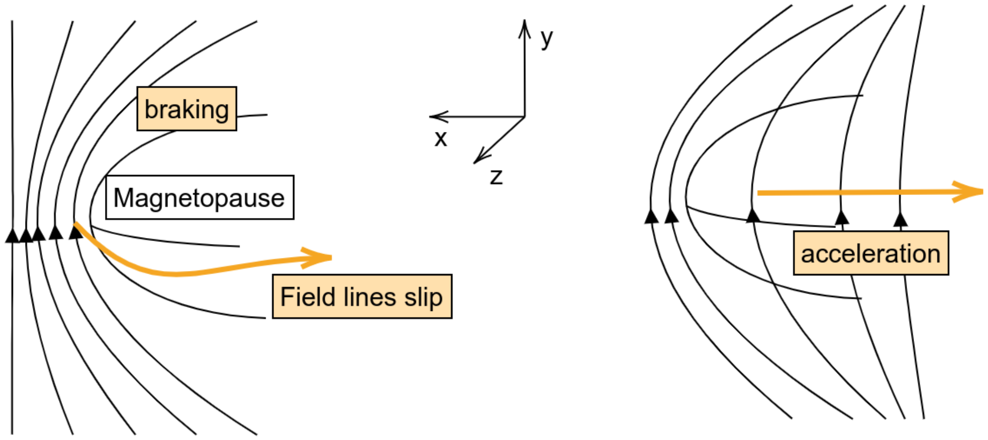

Figure 6.8: *Left side: magnetic field lines piling up on the magnetopause in the (xy) plane. This piling up leads to a braking of the plasma on the flanks in the (xy) plane. Some field lines can slip around the magnetopause and slid along the magnetopause at non-zero values of z. Releasing their magnetic tension, these end up accelerating the plasma in the (xz) plane.*

sponding to $-75\ d_i$ in our simulation), near the magnetopause in the magnetosheath:

- If the satellite is in the same plane as the interplanetary magnetic field (ecliptic plane (xy) in our simulation), we would expect the interplanetary shock to be decelerated, resulting in a delay of 32 seconds (the simulated delay is 2 $\Omega_{\mathrm{ci}}^{-1}$, times the scaling factor 16) compared to a constant-velocity interplanetary shock.
- If the satellite is in the plane perpendicular to the interplanetary magnetic field (noon-midnight meridian plane (xz) in our simulation), we would expect the interplanetary shock to be accelerated, resulting in an advance of 16 seconds (the simulated advance is 1 $\Omega_{\mathrm{ci}}^{-1}$, times the scaling factor 16) compared to a constant-velocity interplanetary shock.

6.3 Evolution of the magnetosheath's characteristics

In this section, we use the "boxes method" outlined in section 5.5.2. We discuss only a few of the many plots that can be obtained through this method. We first present a few of them that can be readily understood, then move on to more complex ones which suggest interesting physics.

6.3.1 The "boxes method": a reminder

The quantities represented are the average values of the physical parameters found at different locations inside the magnetosheath. The averaging is made on all of the cells inside the boxes: "upstream", "nose", "ydusk", "ydawn", "zup", "zdown" as the simulation unfolds. Figure 6.9 is a redrawing of figure 5.23 (page 125) on which we have coloured the different boxes using the same colour code used in the remainder of this section: "upstream" in fuchsia, "nose" in blue, "ydawn" in orange, "ydusk" in red, "zup" in dark green and "zdown" in light green.

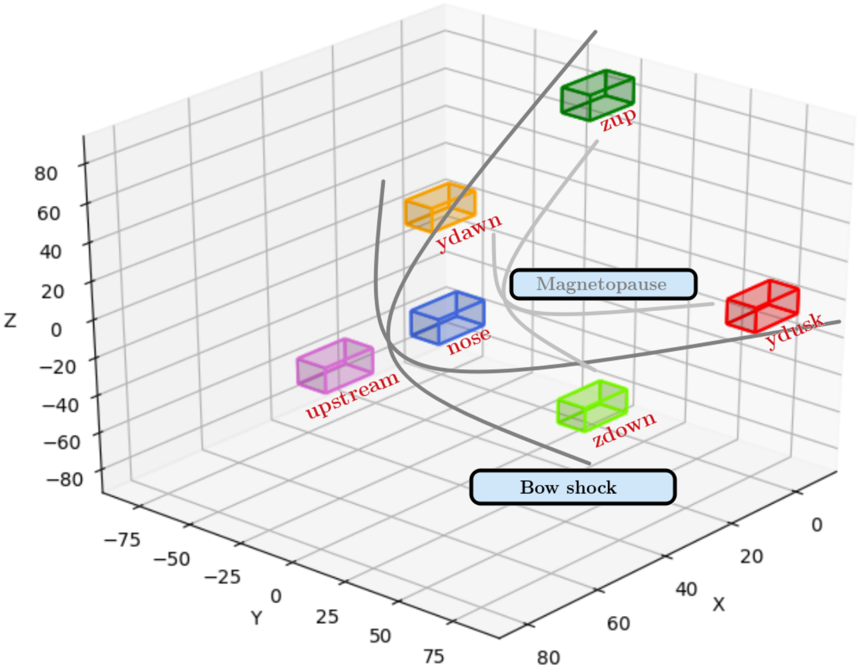

Figure 6.9: *Position of the boxes at time* $t = 210\ \Omega_{ci}^{-1}$, *the different locations have been given a colour which will be used in the remainder of this chapter: "upstream" in fuchsia, "nose" in blue, "ydawn" in orange, "ydusk" in red, "zup" in dark green and "zdown" in light green.*

6.3.2 Magnetosheath compression and construction of the plots

Because figure 6.10 is quite easy to understand, we use it here to explain the construction of the plots using the "boxes method". This figure is also interesting in its own right.

Figure 6.10 displays the evolution of the density. Dots of different colours represent the density as measured in different boxes. The evolution of the density at these different locations is shown as the upstream conditions change. The background colour of the plot is used to represent the upstream

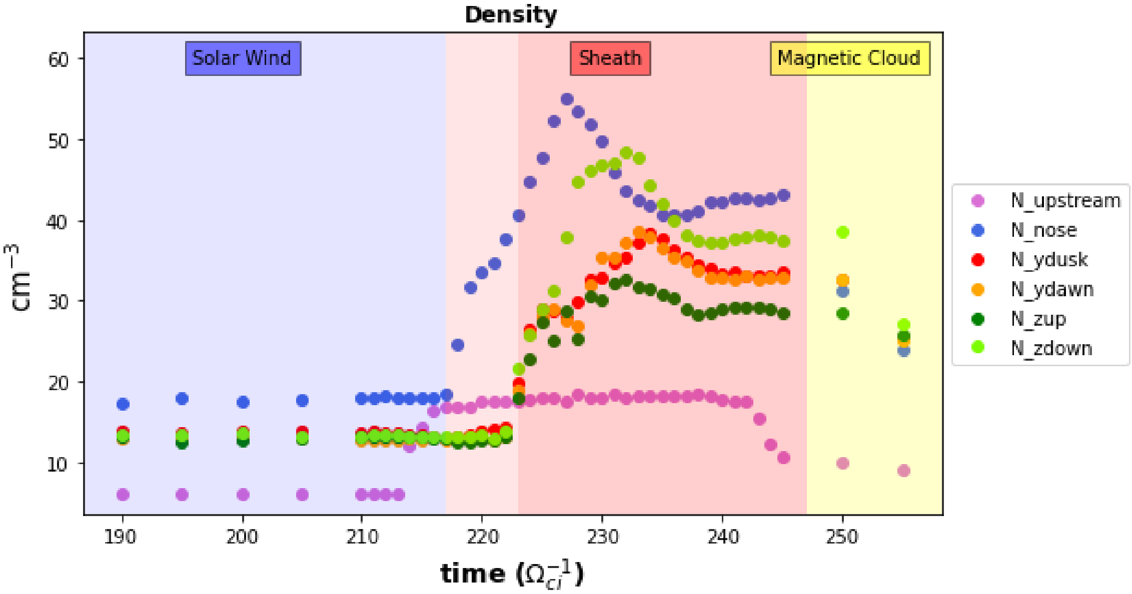

Figure 6.10: *Evolution of the density in the magnetosheath: during pristine solar wind conditions (blue span), then sheath (red span), then magnetic cloud (yellow span). The different coloured dots represent the density as measured at different places. "upstream" is upstream of the bow shock; "nose" is in the middle of the magnetosheath along the Sun-Earth line; "ydusk/ydawn" are measures taken on each side of the planet in the equatorial plane, in the middle of the magnetosheath along the y direction, around $x = z = 0$, "zup/zdown" are measures taken on each side of the planet in the noon-midnight meridian plane, in the middle of the magnetosheath along the z direction, around $x = y = 0$.*

conditions: pristine solar wind conditions (blue span), then sheath (red span), then magnetic cloud (yellow span). The passage of the sheath has been divided into two different colours to represent its progressive crossing of the magnetosheath. The first transition (from blue to pale red) represents the arrival of the interplanetary shock at the nose of the bow shock. The second transition (from pale red to red) represents the arrival of the interplanetary shock at the terminator plane (plane (xy), at $x = 0$). Not only $x = 0$ corresponds to the position of the planet's centre, it is also the position along x of the "ydusk/ydawn" and "zup/zdown" boxes. This is why the corresponding curves (orange, red, pale green and dark green) start changing at the transition from pale red to red.

First, let us look at the density in various places of the magnetosheath during upstream conditions corresponding to the pristine solar wind (blue span): as expected from the Rankine-Hugoniot equations (see 1.2.4), the density is higher in the magnetosheath ("nose", "ydusk", "ydawn", "zup" and "zdown") than in the solar wind ("upstream", represented in fuchsia). Then, when the interplanetary shock collides with the bow shock (transition from the blue to the red span), and afterwards when the sheath crosses the magnetosheath, the behaviour is again not surprising as we see the density rising inside the sheath with a slight delay from the upstream conditions, corresponding to the time the plasma takes to travel from upstream to downstream of the bow shock. The behaviour gets a bit more surprising around 228 Ω_{ci}^{-1} for the nose and between 230 and 235 Ω_{ci}^{-1} for the flanks: while the upstream conditions are quasi-stationary (the fuchsia dots line up horizontally), the density in the magnetosheath starts decreasing. This, as we will see in figure 6.1 of the next section, correlates with the expansion of the bow shock after a first phase of contraction.

A remark on this type of plots: because the size of the boxes on which the average is made is non-zero, it takes a few points for structures like the interplanetary shock to cross them. For example, if the size of the box is 12 d_i, with a shock speed of 8.4 V_A, it should take two to three points for the shock to cross the box, and therefore, two to three points for the quantity averaged in the box to go from the conditions prior to the shock's arrival to the conditions after the shock's arrival. See figure 6.11 for a visual aid. For example, this behaviour is quite recognisable on the fuchsia line (upstream box) in figure 6.10, between times $t = 214\ \Omega_{\mathrm{ci}}^{-1}$ and $t = 216\ \Omega_{\mathrm{ci}}^{-1}$.

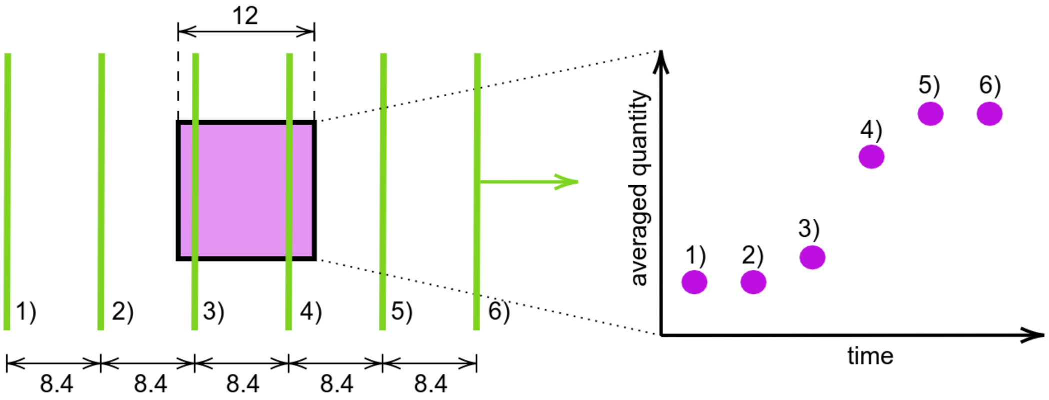

Figure 6.11: *Left side: the propagating interplanetary shock is drawn in green at 6 different time dumps. The box on which a parameter are averaged is drawn in purple. Right side: The corresponding value of the averaged parameter is displayed against time for the six different time dumps.*

A last comment on figure 6.10: While the behaviour of the magnetosheath's density is almost symmetrical in the equatorial plane (the orange "N_ydusk" and red "N_ydawn" curves are very similar), there is a striking difference between the dark green ("zup") and pale green ("zdown") curves. It seems that the southern part of the magnetosheath gets much more compressed than the northern part during the sheath/magnetosheath interaction. We will come back on this in section 6.5.

6.3.3 Energy transfers

The energy is distributed between the electromagnetic field $(\boldsymbol{E}, \boldsymbol{B})$ and the particles. Particles essentially have three types of energies, all of them kinetic, which are usually classified in terms of collective/random/individual motions. They correspond to bulk flow motion, thermal motion and individual accelerated particles. In this subsection, we try to gain some insight into the transfers of energy between these different parts of the plasma.

Average work of the electric field

The term $\boldsymbol{j} \cdot \boldsymbol{E}$, often called Joule-heating, is the work per unit volume and per unit time performed by the Lorentz force on the particles. Indeed, if we call $\dot{w}$ this quantity, we have:

$$\begin{aligned} \dot{w} &= \sum_{i=1}^{N} \boldsymbol{f}_L \boldsymbol{v}_i = \sum_{i=1}^{N} q_i (\boldsymbol{v}_i \times \boldsymbol{B} + \boldsymbol{E}) \cdot \boldsymbol{v}_i \\ &= \sum_{i=1}^{N} q_i \boldsymbol{E} \cdot \boldsymbol{v}_i = \left(\sum_{i=1}^{N} q_i \boldsymbol{v}_i \right) \cdot \boldsymbol{E} \\ \dot{w} &= \boldsymbol{j} \cdot \boldsymbol{E} \end{aligned} \tag{6.3}$$

In the previous equations, i represents an individual particle and N the total number of particles.

A positive $\boldsymbol{j} \cdot \boldsymbol{E}$ means that some energy is transferred from the fields to the particles, while a negative $\boldsymbol{j} \cdot \boldsymbol{E}$ means that the fields extract energy from the particles. There is, unfortunately, no easy way to know which type of particle motion (bulk flow, thermal, individual) is concerned by the energy exchange, because of the difficulty of disentangling transport (*e.g.* advection) and creation (*e.g.* transfer of energy from field to particles). Looking at the amplitude and sign of this quantity can still give us some precious information. The next three figures: 6.12, 6.13 and 6.14 represent the quantity $\boldsymbol{j} \cdot \boldsymbol{E}$, or the amount of energy transferred from the electric field to the particles per unit volume and per unit time.

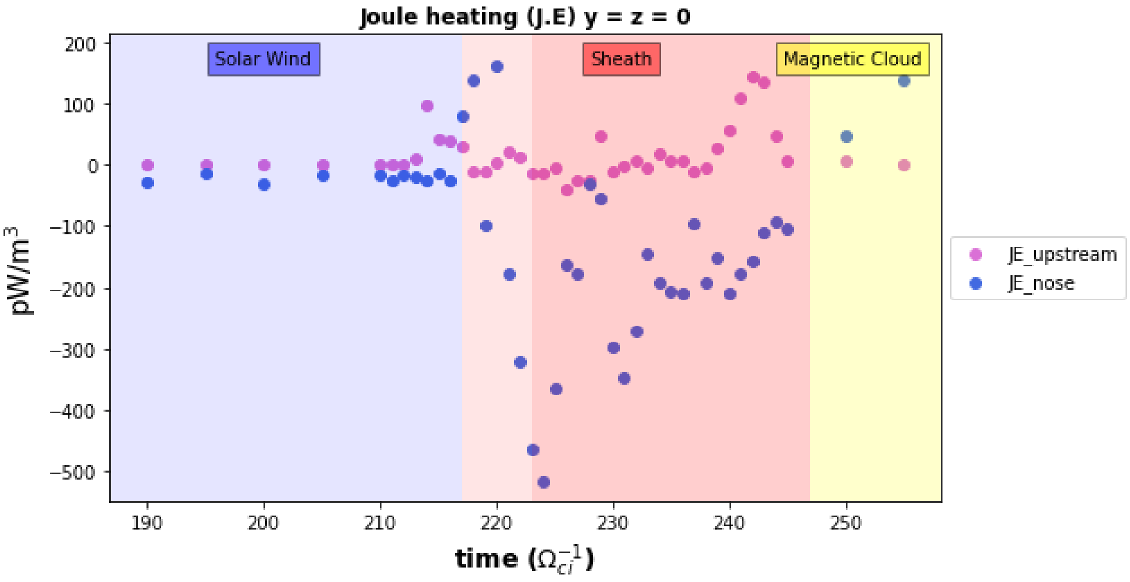

Figure 6.12: *Field-particles energy exchange at different locations of the magnetosheath before, during, and after the passage of a magnetic cloud-driven sheath.*

Let us first focus on the energy exchanges between fields and particles at the "nose" of the magnetosheath (figure 6.12). During the solar wind conditions (blue span), $\boldsymbol{j} \cdot \boldsymbol{E} \sim -20$ pW/m^3. The work performed by the Lorentz force on the particles is negative, which means that energy is transferred from the particles to the field. When the interplanetary shock arrives at the nose of the magnetosheath (times 217, 218 and 219 in the pale red span) it seems that the energy first goes mostly from fields to particles $\boldsymbol{j} \cdot \boldsymbol{E} > 0$ up to almost 200 $\mathrm{pW/m^3}$. Afterwards (after time 220), the energy goes from particles to fields $\boldsymbol{j} \cdot \boldsymbol{E} < 0$ down to an average of -200 $\mathrm{pW/m^3}$ in the rest of the pale red span and red span.

The initial transfer from particles to fields during the solar wind conditions ($\boldsymbol{j} \cdot \boldsymbol{E} < 0$ in the blue span) is a sign of the braking of the macroparticles arriving from the solar wind by the fields in the magnetosheath, *i.e.* part of their kinetic energy is transferred to the electromagnetic field. Later on, during the passage of the sheath (red span), the story is the same, but the flow has more kinetic energy (denser medium and faster macroparticles) and fields are more intense (because the magnetosheath is more compressed) therefore the values of $\boldsymbol{j} \cdot \boldsymbol{E}$ are accordingly greater. Just after the shock-shock collision (beginning of the pale red span), however, the energy is transferred from fields to particles. This could correspond to the arrival of the interplanetary shock: particles that were at a relatively low speed in the magnetosheath may be suddenly accelerated and heated as they encounter the interplanetary shock. The energy gained by the particles can only come from the electromagnetic field as the medium is collisionless.

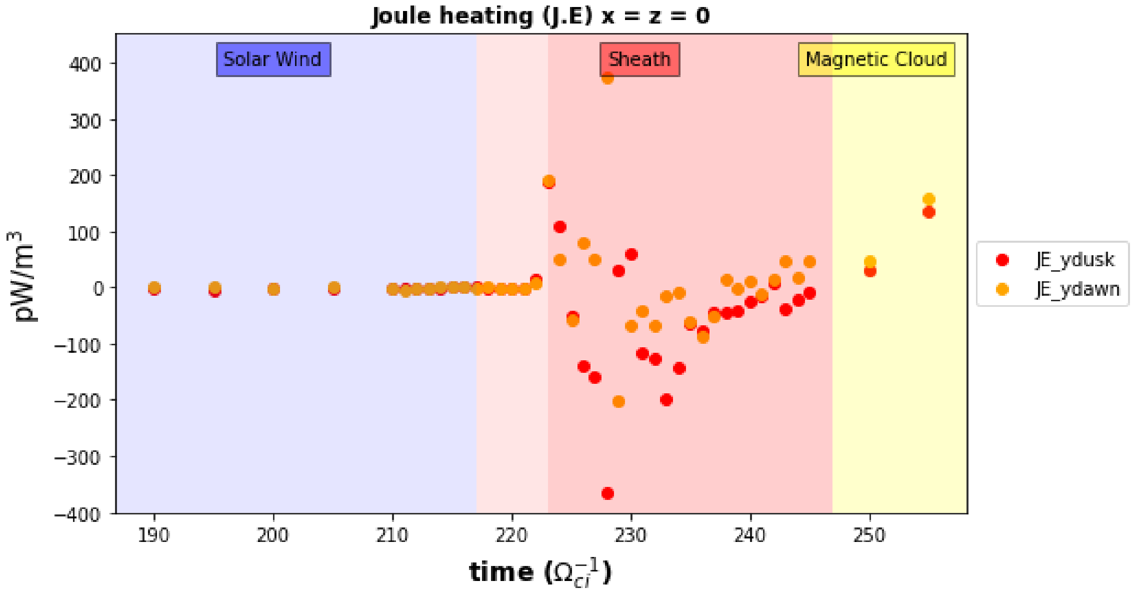

Figure 6.13: *Field-particles energy exchange at different locations of the magnetosheath before, during, and after the passage of a magnetic cloud-driven sheath.*

Figures 6.13 and 6.14, which represent the transfers of energy in the flanks, give us another point of view of the "slingshot" effect noticed in section 6.2 (particles are accelerated in the plane perpendicular to the interplanetary magnetic field (xz) and decelerated in the plane of the interplanetary magnetic field (xy)). In the (xy) plane, particles seem to lose energy to the electromagnetic field (during the sheath (red span) $\langle \boldsymbol{j} \cdot \boldsymbol{E} \rangle^{(xy)} \sim -24$ $\mathrm{pW/m^3} < 0$), whereas in the (xz) plane particles seem to gain energy from the field (during the sheath (red span) $\langle \boldsymbol{j} \cdot \boldsymbol{E} \rangle^{(xz)} \sim 71$ $\mathrm{pW/m^3} > 0$). This,

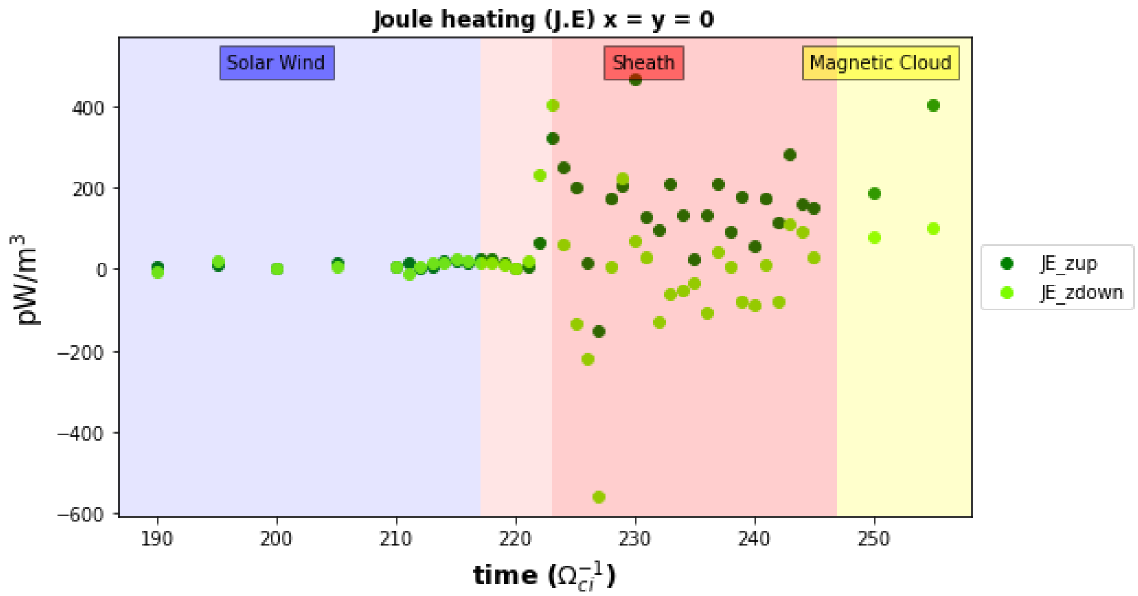

Figure 6.14: *Field-particles energy exchange at different locations of the magnetosheath before, during, and after the passage of a magnetic cloud-driven sheath.*

however, does not seem to work very well for the “z_down” part. The asymmetry between $z > 0$ and $z < 0$ that we noticed earlier is still present: particles seem to gain energy from the field for $z > 0$ (coherent with the “slingshot” effect), but for $z < 0$, particles sometimes gain and sometimes lose energy to the field, as if in this region, there was a mix between the “slingshot” effect and some braking of the particles.

> **Note:** The reason $\boldsymbol{j} \cdot \boldsymbol{E}$ is called the Joule-heating is because of an underlying assumption that the final state of energy is thermal. In a quasi-static scenario such as the passage of electrical current in a wire, this makes sense: as the current goes through the wire, an amount $\boldsymbol{j} \cdot \boldsymbol{E}$ of power is transferred to the electrons as they are accelerated by the electric field, they almost immediately collide with other electrons, or with the atoms of the wire, and this power is quickly dissipated as heat. In a collisionless medium such as the one forming the magnetosheath, it is much less obvious what the energy becomes once it is transferred from the field to the particles, and calling $\boldsymbol{j} \cdot \boldsymbol{E}$ the Joule-heating is more about tradition than about physics.

Temperature

The previous figures showed $\boldsymbol{j} \cdot \boldsymbol{E}$ as it was averaged in the "boxes". This is a macroscopic view that does not directly tell us how much energy is transmitted to smaller and smaller scales until it becomes thermal energy. Figure 6.15 is a representation of the evolution of temperature in the "boxes". The part of this figure that we found the most interesting is the time of the "peak" of temperature in the "nose": $t = 234\ \Omega_{\text{ci}}^{-1}$. It does not correspond to a peak of $\boldsymbol{j} \cdot \boldsymbol{E}$ in figure 6.12, nor to the time of maximum compression of the magnetosheath (figure 6.10). Instead, it seems that the plasma of the magnetosheath continues to be heated during the dilatation of the magnetosheath.

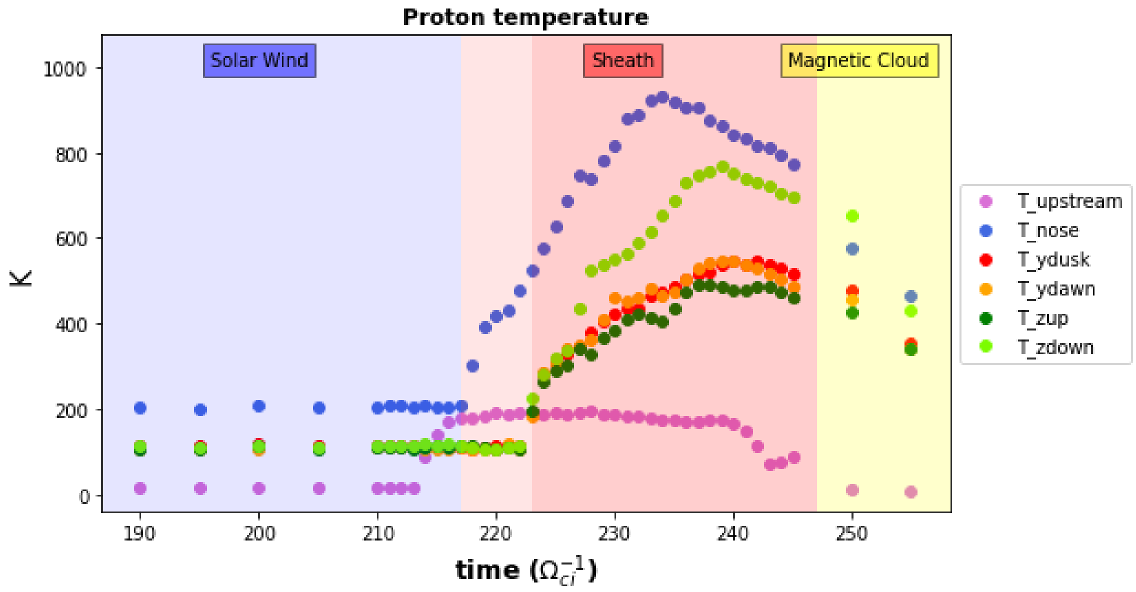

Figure 6.15: *Evolution of the protons' temperature at different locations.*

6.4 Evolution of the magnetosheath's shape

6.4.1 Sub-solar frontiers: numerical result and first interpretation

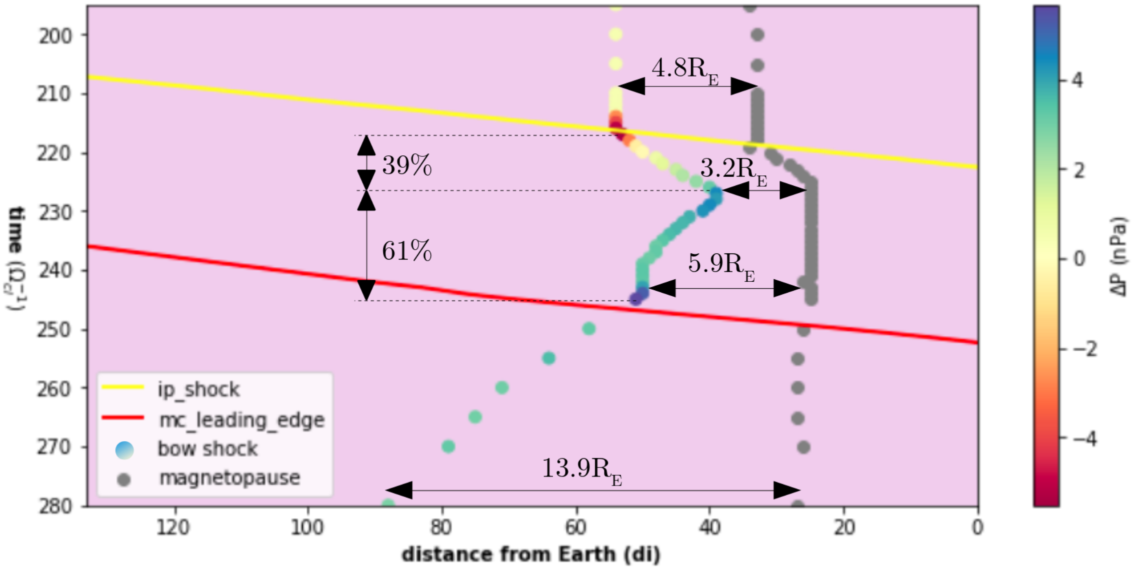

Figure 6.16: *Temporal evolution of the positions along the Sun-Earth line of the bow shock (multicolored dots) and magnetopause (grey dots). Unperturbed (as if the geomagnetic environment was absent) positions of the interplanetary shock (gold line) and magnetic cloud's leading edge (red line). The multicolored dots and the colorbar represent the difference between the total pressure in the inside of the magnetosheath and the total pressure upstream of the bow shock.*

Figure 6.16 represents the evolution of the bow shock and magnetopause positions in time, as they are crossed by the interplanetary shock and the leading edge of the magnetic cloud. The positions of the interplanetary shock (gold line) and the leading edge of the magnetic cloud (red line) are not actually tracked inside the magnetosheath and magnetosphere but far away from the geomagnetic environment: they serve here as a reference. The y-axis represents the time: earlier times are at the top of the axis, and later times are at the bottom. The x-axis represents the positions along the Sun-Earth line. The multicoloured points (from blue to yellow) represent the position of the bow shock. The grey points represent the position of the magnetopause.

When stable under the initial pristine solar wind conditions, the magnetosheath has a size of 21 d_i (or $4.8R_E$). This is slightly larger than the average of $3.4R_E$ reported by Farris et al. (1991), which is normal, since our Mach number ($M_A = 4.1$) is slightly lower than the average $M_A = 5.4$ in Farris et al. (1991). The magnetosheath then shrinks in size as it collides with the interplanetary shock, at time $t = 216.5\ \Omega_{\mathrm{ci}}^{-1}$. The compression phase that ensues lasts for 39% of the length of the sheath, and the magnetosheath reaches a minimum thickness of 14 d_i (or $3.2R_E$). Then, before any change in the upstream conditions occur, the bow shock starts expanding at time $t = 228\ \Omega_{\mathrm{ci}}^{-1}$; the leading edge of the magnetic cloud only arrives at the bow shock around $t = 245\ \Omega_{\mathrm{ci}}^{-1}$. This expansion phase lasts for 61% of the duration of the sheath, and the magnetosheath reaches a maximum thickness of

26 d_i (or $5.9R_E$); which is higher than under pristine solar wind conditions. Later on, when we stop the simulation at time $t = 280\ \Omega_{\text{ci}}^{-1}$, the magnetosheath is deep inside the magnetic cloud and has a thickness of $61d_i$ (or $13.9R_E$).

We have built into the figure a possible explanation for this dynamic reaction. On the solar wind side, the dynamic, thermal and magnetic pressures are pushing against the bow shock. On the other side of the bow shock, the thermal and magnetic pressures are pushing back. It appears that the difference between these pressures, $\Delta P =$ (pressure inside of the magnetosheath − pressure upstream of the bow shock), is roughly null during the first part of the simulation, before the interplanetary shock's arrival. It is therefore natural that the bow shock's position would be stable during quiet solar wind conditions. When the interplanetary shock arrives, however, this balance is thrown off, and the pressure outside of the bow shock is much stronger than the pressure inside. Two things happen then: the magnetosheath is compressed and heated, naturally adapting to the new outside conditions and progressively "trying" to regain the balance of forces on both sides of the bow shock. At the same time, the sheath, which is already made of a hot and dense plasma advecting a strongly compressed magnetic field, penetrates into the magnetosheah, reinforcing the thermal and magnetic pressures in the magnetosheath. Because of the mounting pressure inside of the magnetosheath, at some point the bow shock is pushed back and expands sunward, even though there are no changes in the upstream conditions. At the magnetopause, however, the plasma does not penetrate inside the magnetosphere, so only the build-up of pressure due to compression and heating can be responsible for its pushing back. The magnetopause therefore adapts to the upstream conditions, and then keeps a stable position. The bow shock seems to find a new position of equilibrium towards the end of the sheath. Then, as the interplanetary sheath gives way to the magnetic cloud, the pressure upstream of the magnetosheath suddenly drops and the bow shock resumes its sunward expansion.

6.4.2 Bow shock double-crossing : what a satellite would measure

This back and forth motion of the bow shock has been clearly observed experimentally in Alfsen et al. (1984); Šafránková et al. (2007) and Pallocchia et al. (2010): a satellite is in the magnetosheath close to the bow shock when an interplanetary shock collides with the bow shock. A few seconds after the impact, the satellite crosses the bow shock – as the latter travels Earthward – and finds itself in the solar wind. Only a few minutes later, and without any change in the upstream solar wind conditions, the satellite finds itself in the magnetosheath again after crossing the bow shock a second time – as the latter travels Sunward.

Figure 6.17 represents what a satellite placed next to the bow shock could observe on such an occasion. Using a virtual satellite in the simulation (see section 5.4.2 on page 114) placed at $x = 50\ d_i$ (just behind the bow shock when the magnetosheath has reached a stable position under pristine solar wind conditions), we observe a double crossing of the bow shock. The chain of events leading to the measurements taken by the virtual satellite would not be straightforward to understand if it were data from a real satellite.

On figure 6.17 we represented, from top to bottom: the magnetic field components, the plasma velocity components, and the plasma density. Between times $t \sim 180\ \Omega_{\text{ci}}^{-1}$ and $t \sim 216\ \Omega_{\text{ci}}^{-1}$, the virtual satellite is placed in the magnetosheath, where the velocity is very low and the density very high. Shortly after $216.5\ \Omega_{\text{ci}}^{-1}$ (time of the shock/shock collision), we observe a sudden peak of the

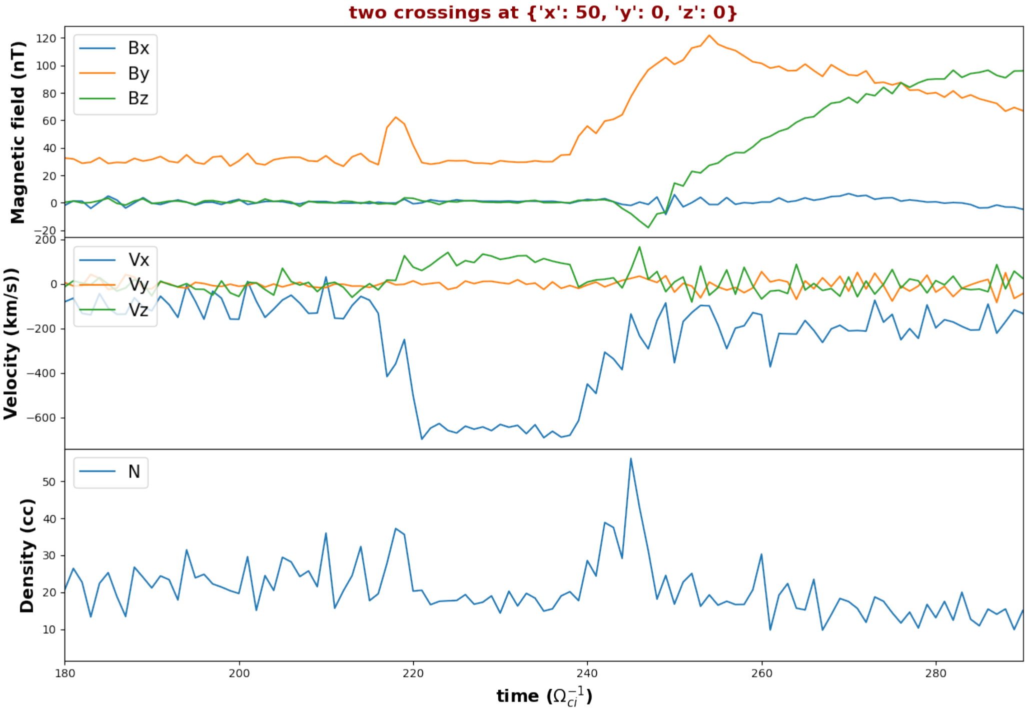

Figure 6.17: *Measurements made by a virtual satellite placed at* $x = 50\ d_i$, $y = z = 0$. *From top to bottom: Magnetic field components, velocity components, density.*

magnetic field amplitude. The magnetic field at this particular position is very strong because it is compressed by both shocks at once. As the bow shock recoils under the impact, the virtual satellite finds itself in the interplanetary medium for a brief period of time (from time $t \sim 220\ \Omega_{\text{ci}}^{-1}$ to time $t \sim 240\ \Omega_{\text{ci}}^{-1}$. At this time, the interplanetary medium in which the satellite finds itself is actually the interplanetary sheath, that we recognise easily with its large velocity. At time $t \sim 245\ \Omega_{\text{ci}}^{-1}$, the satellite crosses the bow shock once more, as the latter expands. As the satellite again finds itself inside the magnetosheath, it quickly starts measuring the high magnetic field and low density characteristic of the magnetic cloud, as it propagates through the magnetosheath.

6.4.3 The expansion of the bow shock: another interpretation

Another possible explanation for the back and forth motion of the bow shock, found in Samsonov et al. (2006) and Pallocchia et al. (2010) is that the interplanetary shock is partly reflected at the magnetopause. When the reflected interplanetary shock reaches the bow shock again from the Earth side, it causes the latter to expand. Samsonov et al. (2007) explains both the sunward motion of the shock as well as the end of the magnetopause's recession from the reflection of the interplanetary fast shock further inside the magnetosphere, on the plasmapause or even on the dayside ionosphere. As we will see, our simulation partly agrees with Samsonov et al. (2006) and Pallocchia et al. (2010), but contradicts Samsonov et al. (2007).

So far we offered two different explanations for the reversal of the bow shock's motion: a build-up of magnetic and thermal pressures inside of the magnetosheath until they eventually become large enough to overcome the upstream dynamic pressure (the explanation from subsection 6.4.1); or a reverse shock that would bounce back on the magnetopause (the explanation from Samsonov et al. (2006) and Pallocchia et al. (2010)). Using our "boxes method" to track the evolution of the pressures inside the magnetosheath actually gives us arguments to back up both interpretations:

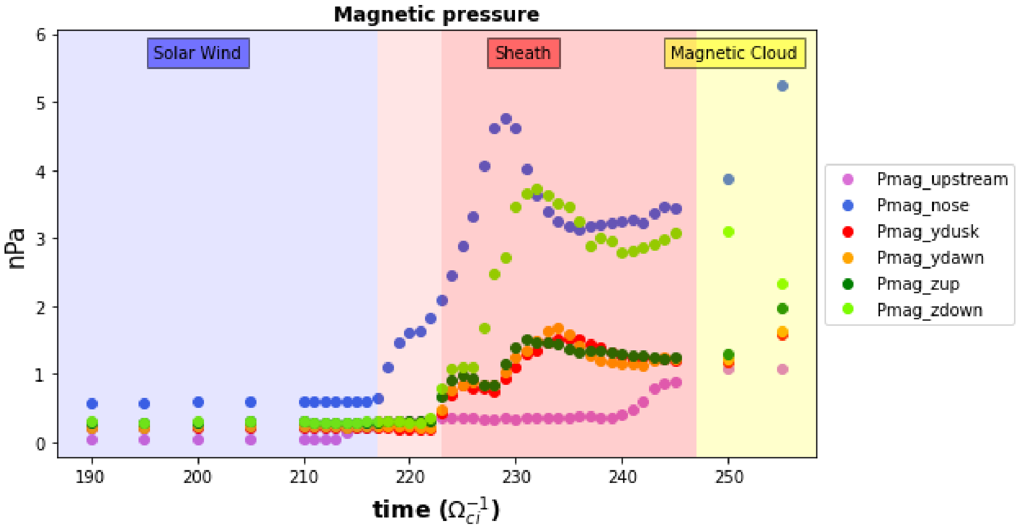

Figure 6.18: *Evolution of the magnetic pressure at different locations in the magnetosheath.*

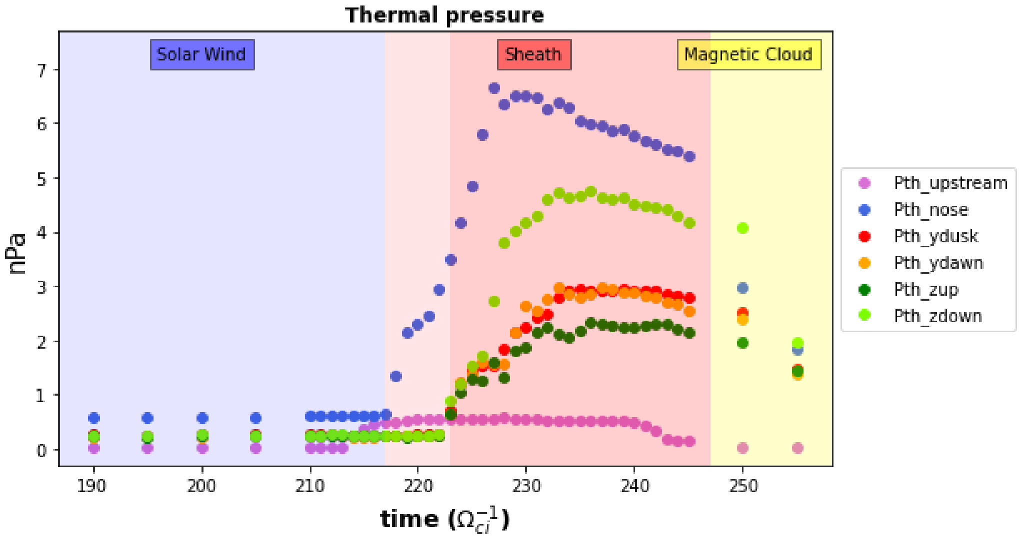

Figure 6.19: *Evolution of the thermal pressure at different locations in the magnetosheath.*

On the one hand, (looking at the blue dots representing the evolution of parameters in the "nose" of the magnetosheath) figures 6.18 and 6.19 show a very clear build-up of the magnetic and thermal pressures inside of the magnetosheath. They both rise quickly after the arrival of the sheath. It looks like the plasma of the interplanetary sheath, itself hot and carrying a large magnetic field,

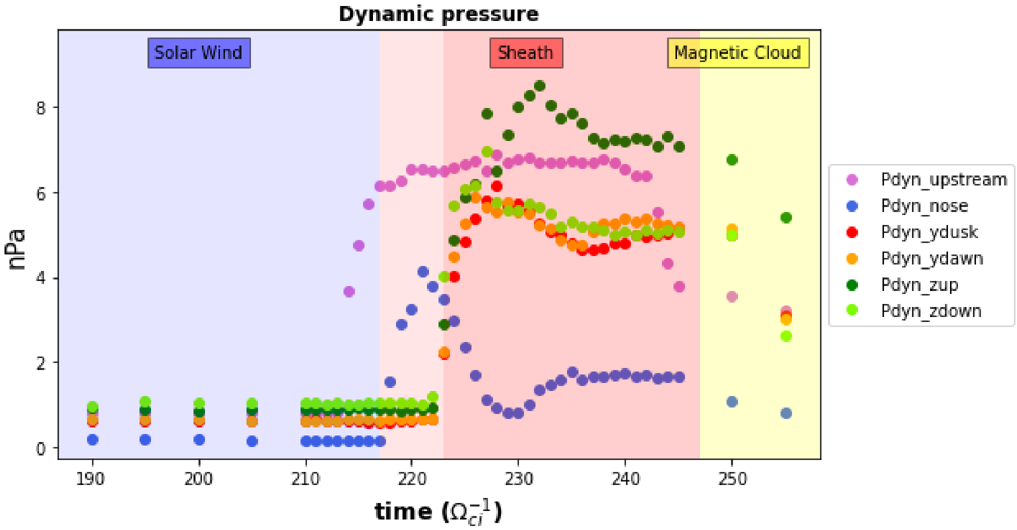

Figure 6.20: *Evolution of the dynamic pressure at different locations in the magnetosheath.*

penetrates inside the magnetosheath, which is rapidly seen in the "box" measurements. Then the magnetosheath progressively adapts to the new upstream conditions, until the build-up of pressure reaches a maximum around $t = 228\ \Omega_{\mathrm{ci}}^{-1}$. At this time, the bow shock stops moving Earthward and starts moving Sunward (see 6.16). As the shock expands again after $t = 228\ \Omega_{\mathrm{ci}}^{-1}$, the magnetic pressure falls rapidly as the magnetosheath is less compressed. Surprisingly the thermal pressure (Nk_BT) falls much slower. Since the density (N) does fall rapidly during the expansion of the magnetosheath (see figure 6.10), this indicates that the magnetosheath is still being heated (and T rises) after the reversal of the bow shock's motion (see section 6.3.3).

On the other hand, figure 6.20 indicates a sharp drop of dynamic pressure inside the "nose" of the magnetosheath, without any change in their upstream counterparts. This happens before the bow shock's expansion, which is marked by a small partial recovery of the dynamic pressure. This sharp drop could easily be explained by the apparition of a reflected shock wave at the magnetopause: if a substantial amount of particles starts travelling sunward, while a large amount is still travelling Earthward, the average of their velocities should indeed drop, also leading to a drop in dynamic pressure.

Since we do not see this reflected shock wave on any 2D cut, we offer a softer explanation: the drop in velocity does not necessarily need the presence of an actual reflected shock wave, as the simple reflection of a large amount of particles travelling at sub-alvenic speeds could also explain it. Figure 6.21 is a zoom on figure 6.16 on which we added the hypothetical trajectory of a particle that would be reflected at the magnetopause and reach back the bow shock to participate in the reversal of its motion. The velocity required for this trajectory is:

$$\frac{\text{x\_bow\_shock} - \text{x\_magnetopause}}{\text{time\_bow\_shock} - \text{time\_magnetopause}} = \frac{39 - 32\ d_i}{228 - 219\ \Omega_{\mathrm{ci}}^{-1}} \simeq 0.8\ V_A^{\mathrm{SW}} \tag{6.4}$$

In the last equation V_A^{SW} represents the Alfvén speed in the solar wind. The Alfvén speed is simply $1\ d_i \times 1\Omega_{ci}$, which we can estimate with the solar wind parameters at the beginning of

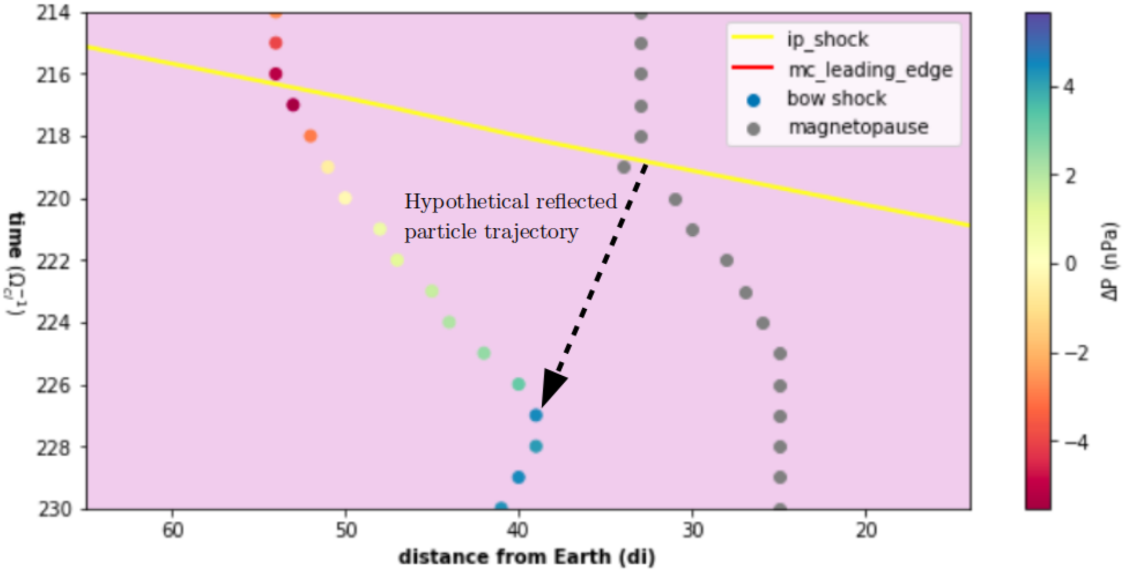

Figure 6.21: *Zoom on figure 6.16: Temporal evolution of the positions along the Sun-Earth line of the bow shock (multicolored dots) and magnetopause (grey dots), as they are impacted by the arrival of the interplanetary shock (gold line). A dashed black arrow has been added to mark the hypothetical trajectory of particle that would be reflected at the magnetopause and reach back the bow shock to participate in its expansion.*

the simulation. To know whether or not counter-streaming particles following the dashed-line trajectory drawn on figure 6.21 are subalfvénic, we need an estimate of the Alfvén speed inside the magnetosheath V_A^{MS} at the time of their counter-propagation. Let us use time $t = 222\ \Omega_{\mathrm{ci}}^{-1}$: with $B \sim 70$ nT and $n \sim 40\mathrm{cm}^{-3}$, we obtain $V_A^{\mathrm{MS}} \sim 2.7 V_A^{\mathrm{SW}}$. This explains why we do not see a reverse shock on the subsolar line. Particles counter propagating from the magnetopause would travel at a subalfvénic speed ($v^{\text{counter-stream}}$):

$$v^{\text{counter-stream}} \simeq 0.3\ V_A^{\mathrm{MS}} \tag{6.5}$$

Our results therefore partially agree with Samsonov et al. (2006) and Pallocchia et al. (2010): some reflection happens at the magnetopause, which then can participate in the reversal of the bow shock's motion. While both authors simulated the magnetopause as a solid, fixed boundary and observed a reversed fast shock, our magnetopause is self-consistently simulated and we do not observe a reverse fast shock but suggest the reflection of particles which travel at a subalfvénic speed. Moreover, we agree with Šafránková et al. (2007) in stating that the change of plasma conditions (in particular the mounting pressure) inside the magnetosheath is also responsible for the reversal of the bow shock motion, rather than making the reflected particles the only sufficient explanation.

6.4.4 What about a reflection beyond the magnetopause?

Samsonov et al. (2007) showed that the receding motion of the magnetopause and the bow shock could be both interrupted by a reflection of the interplanetary shock beyond the magnetopause on the numerical boundary of their model. They then precised that in reality, a first partial reflection would

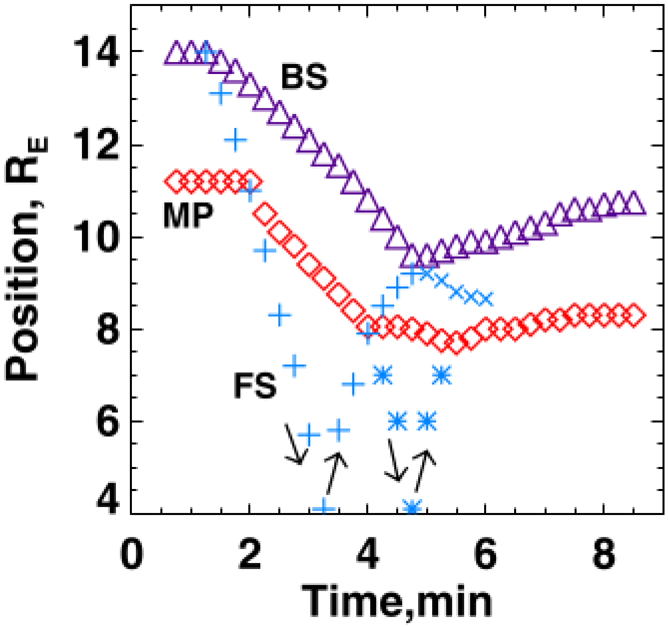

Figure 6.22: ***Figure from Samsonov et al. (2007).*** *The positions of the bow shock (BS) and magnetopause (MP) are respectively represented by purple triangles and red squares. The position of the interplanetary shock is represented with blue crosses. The x-axis shows the time (in minutes) and the y-axis shows the position (in R_E). A reflection of the interplanetary shock takes place at the numerical boundary, at $4R_E$.*

take place at the plasmapause, followed by another reflection on the dayside ionosphere. Since figure 6.22 from Samsonov et al. (2007) closely resembles our simulation results, it is worth exploring their interpretation.

On figure 6.23, made from our simulation results, we represented two hypothetical trajectories for reflected particles. Trajectory **A** (black dashed line) assumes particles are reflected back from the magnetopause and reach the bow shock at the time of the reversal of its motion. Trajectory **B** (red dashed line) assumes particles are reflected back beyond the magnetopause. Only the $\mathbf{B}_2$ part of the trajectory is really relevant for the current argument: it links the points where the magnetopause and bow shock motions change. The $\mathbf{B}_1$ part is just an example of where the particles could reflect: here, they would be reflecting on the absorbing surface of the obstacle used in our simulation. In practice, in our simulation we lose track of the interplanetary shock once it crosses the magnetopause, so we do not actually know where a hypothetical reflection would take place. The $\mathbf{B}_2$ part, however, simply corresponds to Samsonov et al. (2007)'s conclusions. As mentioned earlier, if a number of particles are reflected back, we should see a change in the averaged velocity in the "nose" box obtained with the box method: as counter streaming particles reach the box, the velocity u^{nose} should start decreasing. This gives us an easy way to decide between trajectories **A** and **B**: if the change of u^{nose} takes place around $t = 222-223\ \Omega_{\text{ci}}^{-1}$, trajectory **A** is favoured, while if the change takes place around $t = 225-226\ \Omega_{\text{ci}}^{-1}$, then **B** is favoured. A quick glance at the blue scattered dots representing u^{nose} on figure 6.24 allows us to conclude in favour of hypothesis **A** and disagree with Samsonov et al. (2007).

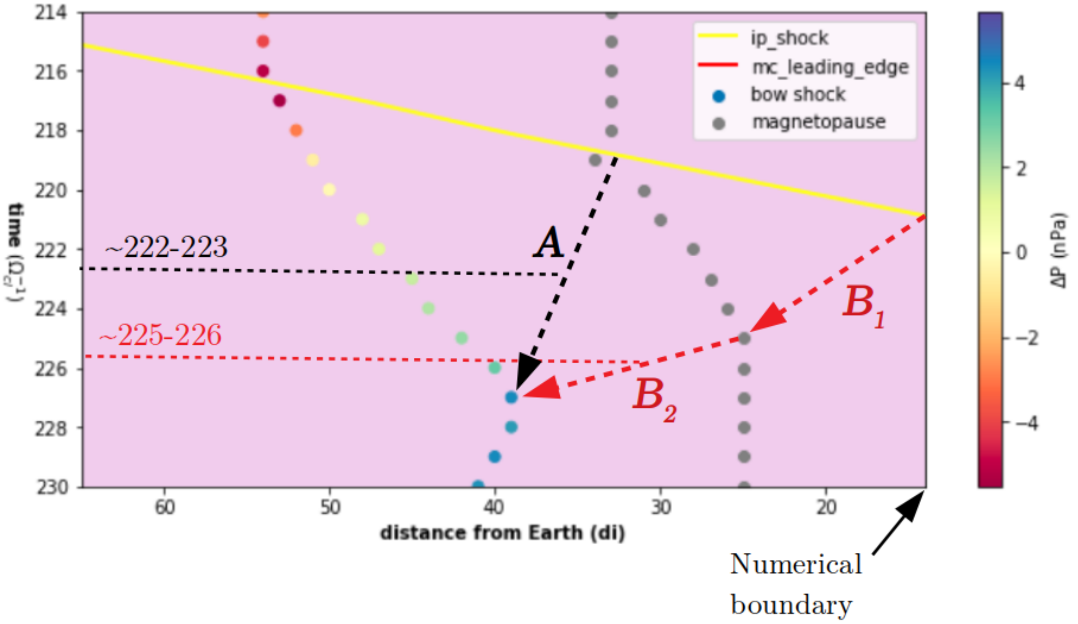

Figure 6.23: *Zoom on figure 6.16. Two different hypothetical trajectories have been marked on the figure: trajectory **A** (black dashed line) assumes particles are reflected back from the magnetopause and reach the bow shock at the time of its expansion. Trajectory **B** (red dashed line) assumes particles are reflected back beyond the magnetopause. Corresponding horizontal dashed lines show the estimated times at which we these hypothesis would lead to a change in the evolution of the velocity in the "nose", as computed with the "boxes method".*

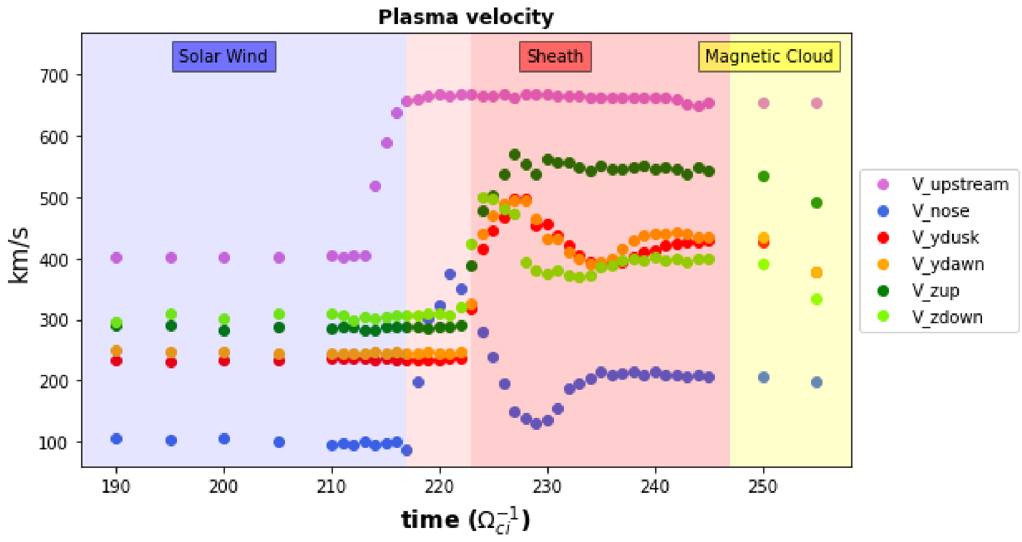

Figure 6.24: *Evolution of the plasma velocity at different locations in the magnetosheath.*

In conclusion, we offer the following explanation for the bow shock's motion reversal: Two concomitant processes explain this reversal. On the one hand, there is a build-up of thermal and magnetic pressure inside of the magnetosheath due to the mixing of the plasma from the magnetosheath and interplanetary sheath. On the other hand, a significant amount of particles are reflected on the magnetopause and travel back towards the bow shock, thus diminishing the total dynamic pressure differential between the two sides of the bow shock. Together, these two processes lead to a reversal of the bow shock's motion, without the need for any change in the upstream conditions. We are currently investigating the question of which process dominates and should address it in an upcoming paper.

> **Note:** If we look more closely at figures 6.18 and 6.19, we see an acceleration of the increase of magnetic and thermal pressure right around the peak of average velocity. This could be interpreted as an effect of the counter streaming flow of particles, which could be the source of an instability – *e.g.* two-stream instability (Farley (1963)) or counter filamentation (Dieckmann et al. (2009)) – which could reinforce the build-up of magnetic and thermal pressure in the magnetosheath. This warrants a closer investigation in the near future.

6.4.5 Flanks of the magnetopause

Figure 6.25 depicts the evolution of the position of the bow shock (top four scatter-lines) and the position of the magnetopause (bottom four scatter-lines). The dark green line represents the northern boundaries' locations: for $x = y = 0$ and for $z > 0$ (above the nothern pole). The light green represents the southern boundaries' locations: for $x = y = 0$ and for $z < 0$ (below the southern pole). Similarly, the red and orange lines depict the duskward ($y > 0$) and dawnward ($y < 0$) locations of the bow shock and magnetopause in the ecliptic plane ($x = z = 0$) .

At first glance, the story appears to be quite similar to what it was along the Sun-Earth line. Both the bow shock and magnetopause are compressed by the arrival of the interplanetary shock. Shortly after, the bow shock starts expanding into the solar wind before the upstream pressure conditions have changed (before the arrival of the magnetic cloud), and the magnetopause stops receding.

However, at least three notable differences can be listed:

First, the bow shock locations do not start expanding at the same time for different locations: the southern (z_down) bow shock location starts expanding at $t = 231\ \Omega_{\text{ci}}^{-1}$, before the y_dawn bow shock location at $t = 233\ \Omega_{\text{ci}}^{-1}$, then the z_up location, at $t = 234\ \Omega_{\text{ci}}^{-1}$ and eventually, the y_dusk location, at $t = 235\ \Omega_{\text{ci}}^{-1}$. The fact that the expansion along the y direction falls behind the expansion along the z direction can be understood from the end of the previous section: 6.2.2. Indeed, if looking at figure 6.6 on page 135, we can see that the bow shock propagates faster in the (xz) plane than in the (xy) plane, leading to earlier changes in the (xz) compared to the (xy) plane. The z_up location, however, does not quite seem to follow this explanation.

This leads us to the second remarkable result on this figure: the peculiar behaviour of z_bow_shock_up/down. The bow shock position in the south recedes much more than its northern counterpart, which does not move much under the impact of the sheath. A strong asymmetry seems to develop in the (xz) plane. We will discuss this further in section 6.5.

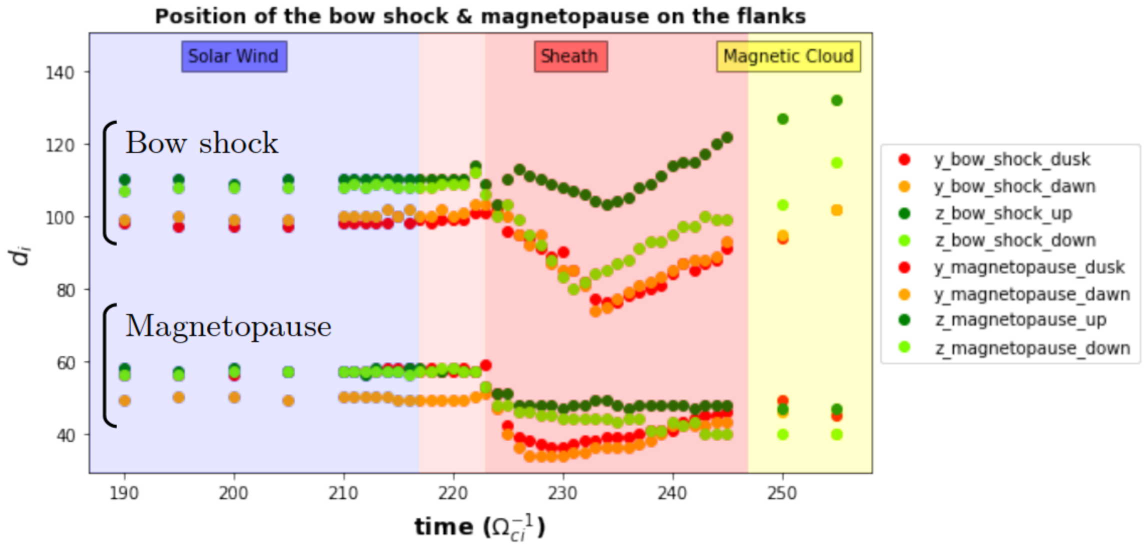

Figure 6.25: *Evolution of the bow shock and magnetopause positions: during pristine solar wind conditions (blue span), then sheath (red span), then magnetic cloud (yellow span). The passage of the sheath has been divided in two different colors to represent its progressive crossing of the magnetosheath. The first transition (from blue to pale red) represents the arrival of the interplanetary shock at the nose of the bow shock. The second transition (from pale red to red) represents the arrival of the interplanetary shock at* $x = 0$*. The colors of the dots represent different boundaries: y_bow_shock_dusk is the position of the bow shock at* $x = z = 0$ *and y positive, y_bow_shock_dawn is for y negative. z_bow_shock_up/down are the positions of the bow shock for* $x = y = 0$ *and z positive/negative. The same terminology is used for the magnetopause positions.*

Finally, contrarily to the magnetopause motion along the Sun-Earth line, the magnetopause location in the ecliptic plane seems to go back and forth: first it recedes under the pressure of the interplanetary sheath, then it expands back out. This is not the case in the (xz) plane.

6.5 Asymmetries in the (xz) plane

We have noted in a few figures, such as 6.25 on page 154; or 6.10 on page 139, that a strong asymmetry seems to form in the noon-midnight meridian (xz) plane: the southern part of the magnetosheath is more compressed than its northern part during the interaction with the sheath. This, as far as we know, is unheard of, and will need experimental confirmation. This section presents our interpretation of this phenomenon:

6.5.1 An effect of a change of velocity direction

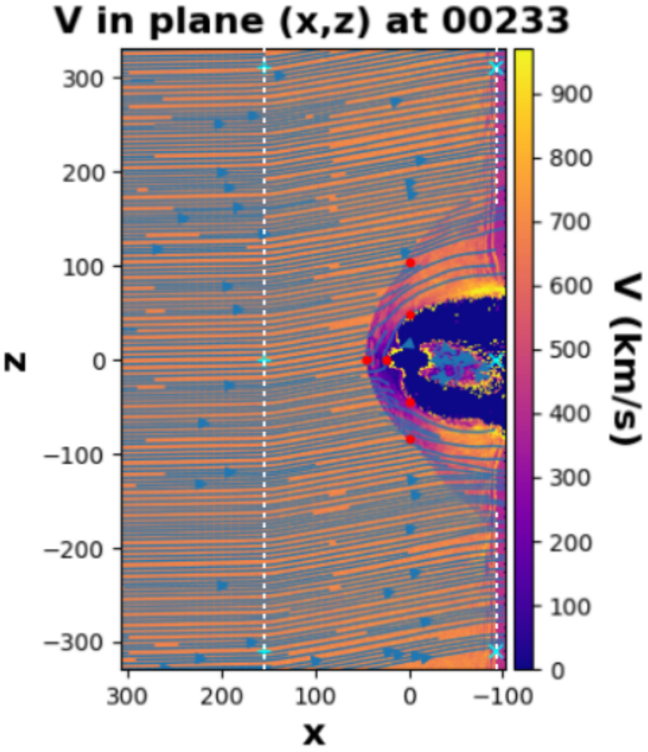

Figure 6.26: *2D representation of the velocity in the noon-midnight meridian (xz) plane. Flow lines are represented in blue. The white dashed line around* $x = 150\ d_i$ *marks the leading edge of the magnetic cloud, while broken white dashed line at the far right end of the figure marks the location of the interplanetary shock outside of the magnetosheath. Most of the simulated magnetosheath is interacting with the interplanetary sheath on this time dump.*

Figure 6.26 represents the velocity in the noon-midnight meridian (xz) plane. It is made at time $t = 233\ \Omega_{\mathrm{ci}}^{-1}$, when the interplanetary sheath (delimited on each side by a white dashed line representing respectively the leading edge of the magnetic cloud and the shock front) has penetrated deeply through the magnetosheath. We can see the asymmetry quite clearly: the southern half of the magnetosheath is much smaller than the northern half. From the drawing of the flow lines of the velocity (in blue), it appears that the asymmetry comes from the direction of the plasma flow inside the interplanetary sheath. From the solar wind to the sheath, the plasma changes direction (from solely x to mostly x and a non-negligible z component), and the magnetosheath adapts to this change.

6.5.2 On the origin of the change of velocity direction

Figure 6.27 is a zoom on figure 5.11, centred on the sheath. From top to bottom we see the magnetic field components, the electric field components, the velocity components and the density. The velocity clearly changes direction from the solar wind to the sheath, with the apparition of a u_z component of roughly 120 km/s. It is consistent with the apparition of a non zero E_x component of the electric field; since most of the magnetic field consists of its B_y component.

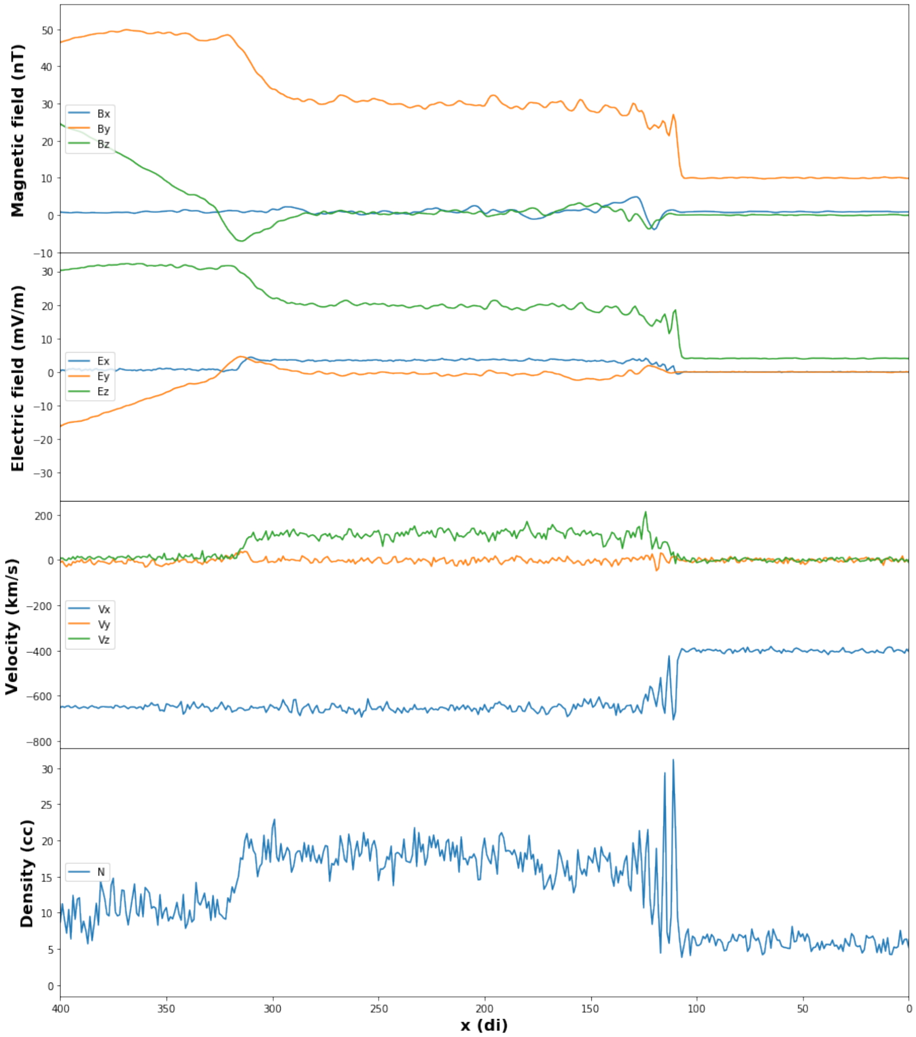

Figure 6.27: *1D representation of the LatHyS-simulated sheath. From top to bottom: magnetic field components, electric field components, velocity components, and ion density.*

The surprise comes from the fact that Rankine-Hugoniot equations, applied between the solar wind and the sheath, would predict a null velocity along the z direction, and yet we obtain $u_z \sim 120$ km / s. Indeed, the Rankine-Hugoniot equation that derives from Maxwell-Faraday, and ultimately, from Ohm's law ($\boldsymbol{E} = -\boldsymbol{u} \times \boldsymbol{B}$): $[u_x B_z - u_z B_x] = 0$, indicates that if $B_z = 0$ and $u_z = 0$ in the solar wind, and $B_z = 0$ and $B_x \neq 0$ in the sheath, we should expect $u_z = 0$ in the sheath:

$$
\begin{aligned}
u_z^{\mathrm{SH}} &= \frac{1}{\underbrace{B_x}_{\neq 0}} \left(\left(u_x \overbrace{B_z}^{=0} + \overbrace{u_z}^{=0} B_x \right)^{\mathrm{SW}} - \left(u_x \overbrace{B_z}^{=0} \right)^{\mathrm{SH}} \right) \\
&\implies \underline{u_z^{\mathrm{SH}} = 0}
\end{aligned}
\tag{6.6}
$$

Equation (6.6), based on ideal MHD, almost reads: $0 = 0$. Therefore, terms that are usually neglected (non-MHD) can become important, and may explain why our simulation returns $u_z^{\mathrm{SH}} \neq 0$.

In order to explain this velocity along z we need look at the non-MHD terms in Ohm's law (see equation (5.4)). If we can explain the appearance of the x component of the electric field at the shock, then through the drift velocity $\boldsymbol{u} = \frac{\boldsymbol{E} \times \boldsymbol{B}}{B^2}$, since $\boldsymbol{B}$ is mostly along $\boldsymbol{e}_y$, we could explain the appearance of the u_z component. Indeed, once particles are set in motion in the z direction, since they evolve without collisions, there is no reason why the would not continue their course along z. Let us therefore focus on the creation of E_x within the shock[1].

The first term we shall look at to create E_x is the pressure term: $\frac{\boldsymbol{\nabla} n_e k_B T_e}{e n_e}$. In LatHyS, n_e is equal to the ionic density n_i (plasma neutrality) and T_e is computed from n_e with a polytropic coefficient of 2, which leads to $n_e / T_e = Constant$. Figure 6.27 shows a strong increase of plasma density from solar wind to sheath, by a factor of roughly 3. The electronic temperature is therefore also multiplied by 3, which leads to the multiplication of the pressure by a factor of roughly nine. The electronic temperature in the solar wind is of approximately 150 kK. The thickness of the shock is of a couple d_i, which each represent 93 km. This is also roughly the thickness expected for the interplanetary shock, given that $\beta = 0.5$ (Pinter (1980)). In order of magnitude, we therefore have:

$$
\frac{\boldsymbol{\nabla} n_e k_B T_e}{e n_e} \sim \frac{8 \times k_B T_e^{\mathrm{SW}}}{2 d_i e} \sim \frac{8 \times 1.4 \cdot 10^{-23} \times 1.5 \cdot 10^5}{2 \times 9.3 \cdot 10^4 \times 1.6 \cdot 10^{-19}} \sim 0.5 \text{ mV} \tag{6.7}
$$

An E_x of 0.5 mV, together with a B_y of 20 nT should give rise to velocity along u_z of:

$$
u_z \sim \frac{E_x B_y}{B_y^2} \sim \frac{0.5 \cdot 10^{-}3}{20 \cdot 10^{-9}} \sim 25 \text{ km/s} \tag{6.8}
$$

The second term we want to look at is the contribution of the Hall term:

$$
\frac{(\boldsymbol{\nabla} \times \boldsymbol{B}) \times \boldsymbol{B}}{e n_e \mu_0} \sim \frac{B_y^2}{2 d_i e n_e \mu_0} \sim \frac{(20 \cdot 10^{-9})^2}{2 \times 9.2 \cdot 10^4 \times 1.6 \cdot 10^{-19} \times 6 \cdot 10^6 \times 4\pi \cdot 10^{-7}} \sim 1.8 \text{ mV} \tag{6.9}
$$

This would correspond to:

$$
u_z \sim \frac{E_x B_y}{B_y^2} \sim \frac{1.8 \cdot 10^{-3}}{20 \cdot 10^{-9}} \sim 90 \text{ km/s} \tag{6.10}
$$

The addition of these two terms would give a u_z of a little over 100 km/s, which is indeed what we see on figure 6.27.

---

[1] In the remainder of the sheath, it is the old "chicken or egg" paradox: E_x, u_z and B_y coexist, but it is impossible to say which causes which.

6.6 Summary

In this chapter, we have used a 3D global PIC-hybrid simulation to study the interaction of a magnetic cloud – driven sheath with the geomagnetic environment. This is the first time that a numerical simulation included both a self-consistent treatment of the magnetopause (and bow shock) as well a self-consistent creation and propagation of the interplanetary shock. It is also the first time that a sheath has been included in numerical simulations. The magnetic cloud was set-up with a strong (50 nT) northward magnetic field, and travelled at a velocity of ~ 675 km/s. The solar wind with which the cloud interacts was given a magnetic field of 10 nT, mostly in the y direction in the ecliptic plane (85° from the x direction). The solar wind's velocity was chosen to be a standard 400 km/s, with a density of 6 ions/cm^3. These parameters give the bow shock an Alfvén Mach number of $M_A^{\text{bow shock}} = 4.5$, and the magnetic cloud – driven shock a $M_A^{\text{IP shock}} = 3.1$. Having chosen these two shocks a similar strength insures that they affect each other significantly.

First, we have seen how the geomagnetic environment impacts the interplanetary shock. Section 6.2 confirms some earlier conclusions by Koval et al. (2005), Koval et al. (2006a), Samsonov et al. (2006), Samsonov et al. (2007) and Pallocchia et al. (2010): the interplanetary shock is curved in the magnetosheath, as a result of its braking. Along the Sun-Earth line, the interplanetary shock's velocity inside of the magnetosheath is 0.8 times what it was in the solar wind prior to its encounter with the bow shock. Our simulation also also contains a novel result: the part of the shock that slides along the magnetopause in the plane perpendicular to the interplanetary magnetic field can actually be accelerated at a larger velocity than in the solar wind: in the conditions of our simulation, a satellite placed at 17 Earth radii downstream of Earth and near the magnetopause in the magnetosheath would encounter the shock with an advance of 16 seconds compared to the scenario where the interplanetary shock would have kept its initial velocity.

Second, we have seen in sections 6.3, 6.4 and 6.5 how the interplanetary shock/sheath impacts the geomagnetic environment:

In section 6.3, we gave a view of the evolution of different plasma values in the magnetosheath. We noted, for example, a fourfold increase in the magnetosheath density in the nose of the magnetosheath while in the flanks, the density was multiplied by two. We also explored energy exchanges between fields and particles and noted, in chronological order: a strong braking in the nose of the magnetosheath; with $\boldsymbol{j}\cdot\boldsymbol{E}$ ranging from -20 pW/m^3 during quiet solar wind conditions down to an average of -200 pW/m^3 during the passage of the interplanetary sheath. On the flanks, we found that particles were loosing energy to the fields in the ecliptic plane (during the sheath passage, $\langle \boldsymbol{j}\cdot\boldsymbol{E}\rangle \sim -24$ pW/m^3) but gaining energy in the noon-midnight meridian plane $\langle \boldsymbol{j}\cdot\boldsymbol{E}\rangle \sim 71$ pW/m^3.

Section 6.4 explored the same question as Samsonov et al. (2007): how do the geomagnetic boundaries along the Sun-Earth line react to the passage of an interplanetary shock. We have found a different answer from Samsonov et al. (2007): while the authors of this study found that the interplanetary shock was reflected inside the magnetosphere, propagated Sunward and then only caused a reversal of the bow shock's motion; we have found that particles from the sheath were reflected on the magnetopause without causing a shock, and helped the reversal, without being its only cause. Our results are therefore more in line with Samsonov et al. (2006) and Pallocchia et al. (2010) albeit a bit different: while these authors observed a reverse fast shock after the reflection of the interplanetary shock on the magnetopause, we only seem to observe a subalfvénic ($M_A \sim 0.3$) counter-streaming flow. Our 3D simulation allowed us to also look at the motions of the bow shock in ecliptic and noon-midnight meridian plane. While we did not go into as much details as for the Sun-Earth line, we observed a couple of asymmetries: the most obvious one was the very different behaviour between the southern and northern hemispheres, the cause of which we explored in section 6.5. A less obvious but surprising one is an asymmetry between the (xy) and (xz) plane: the magnetopause in the ecliptic plane exhibits a back and forth motion not seen in the noon-midnight meridian plane.

Finally, section 6.5 introduced and explained a phenomena that, to our knowledge, had not been previously reported: at high angles ($\sim 85^\circ$) between the shock normal and the interplanetary magnetic field, we see a non-negligible velocity component ($u_z \simeq 120$ km/s) appear behind the shock in the direction perpendicular to the plane of the interplanetary magnetic field and the shock normal. This velocity component has important consequences on the geomagnetic environment, by preferentially compressing one side of the magnetosheath. We offered the following causes for the arising of this component: the principal cause – with a contribution of ~ 90 km/s – is the Hall term in Ohm's law; the secondary cause - with a contribution of ~ 25 km/s – is the electron pressure gradient term in Ohm's law.

In a few words

We ran the first 3D PIC-hybrid of an interaction between an interplanetary shock/sheath and a global magnetopause/bow shock structure. It is also the first simulation of any kind to include a sheath, created by a self-consistent interplanetary shock. The bow shock and magnetopause were also self-consistently simulated.

At the beginning of its interaction with the magnetosheath, the interplanetary shock slows down noticeably (to 80 % of its initial speed). Then, on the flanks of the magnetopause, the interplanetary shock slows down in the plane of the interplanetary magnetic field (to $\sim 80\%$ of what an unperturbed propagation would be), but accelerates in the plane perpendicular to the interplanetary magnetic field (up to $\sim 120\%$ of its initial speed).

When the shock and the sheath penetrate into the magnetosheath, they heavily compress it, leading to a strong rise in density ($\sim 4\times$) and fostering strong energy exchanges between fields and particles (average $\boldsymbol{j} \cdot \boldsymbol{E}$ of -200 pW/m^3, which is $\sim 10\times$ more than during quiet upstream conditions).

During the passage of the interplanetary sheath, the magnetosheath gets compressed down to 67% of its initial size, then expands back to 123% of its initial size before the arrival of the magnetic cloud. We explain this by two complementary causes: on the one hand, the rise of total pressure in the magnetosheath as it reacts to the elevated upstream pressure and mixes with the interplanetary sheath; and on the other hand, the apparition of a counter-streaming subalfvénic flow after the interplanetary shock reaches the magnetopause. The bow shock has a similar behaviour on the flanks of the magnetopause. The magnetopause motion is different from place to place: while at the nose and in the noon-midnight meridian plane it recedes then finds a new place of equilibrium, in the ecliptic plane the magnetopause has a back and forth motion.

Additionally, in the sheath, non-MHD terms in the Ohm's law give rise to an important velocity component (~ 120 km/s) in the plane perpendicular to the interplanetary magnetic field, leading to a strong asymmetry in the magnetosheath's compression.

7. Conclusions

Note: This last chapter is divided in two main parts. First, in section 7.1, we give a brief overview of the argument developed in this thesis as well as a summary of our main results. Finally, in sections 7.2 and 7.3 we present some thoughts on how some of our methods could be developed, and some of our results built upon. When applicable, we presented some preliminary results.

Contents

7.1 Overview

7.1.1 Context

It is well-known that magnetic clouds are the most geoeffective structures in the heliosphere. While not entirely sufficient, the most common and robust explanation for this fact is the likelihood that magnetic clouds present few hours-long stretches of strong southward interplanetary magnetic field (see Tsurutani et al. (2020) and references therein). Magnetic clouds, however, are not the only drivers of geomagnetic activity. Shocks and their associated sheaths preceding the clouds also account for a large fraction of geomagnetic storms (Huttunen and Koskinen (2004); Yermolaev et al. (2010)). While their geoeffectiveness can often be understood in terms of the presence of strong southward interplanetary B_z (Lugaz et al. (2016)), geomagnetic activity driven by sheaths cannot solely be explained by this, as it is different from geomagnetic activity driven by magnetic clouds (*e.g.* Kilpua et al. (2017a) and references therein). The main candidates to explain these differences are sheaths' high dynamic pressure and levels of turbulence.

7.1.2 Spectral analysis of space data

Sheaths themselves are not very well-known yet, and one of the main aspects that needs advancement in knowledge is the wave content of sheaths. Recently, there has been a push to know more about this (*e.g.* Kilpua et al. (2017b); Ala-Lahti et al. (2018); Good et al. (2020); Kilpua et al. (2020)). The first half of the work presented in this thesis (chapters 3 and 4) is a part of this line of investigation.

In chapter 4 we found that, in sheaths driven by magnetic clouds, the power of magnetic fluctuations was generally an order of magnitude above fluctuations in the solar wind ($P_{sh} = 9.3 \pm 10.8 > 0.8 \pm 1.0 = P_{sw}$), and that they were less anisotropic/more compressible ($A_{sh} = 5 \pm 3 < 10 \pm 6 = A_{sw}$, $C_{Sh} = 0.15 \pm 0.08 > 0.07 \pm 0.04 = C_{SW}$). Looking at the relationship between these features (power P_{sh} and anisotropy A_{sh}) and the environment of the sheaths, we found that sheaths with powerful, quite isotropic magnetic fluctuations were most likely to be driven by fast magnetic clouds with typical velocities larger than 750 km/s, interacting with an already turbulent solar wind with a magnetic fluctuation power typically larger than 1 nT^2, and with a high shock Alfvén Mach number (typically above 4). The relations with the shock angle and β upstream are a little more complex. Downstream of quasi-perpendicular shocks and high-beta ($\beta > 1.1$) solar wind, the observed sheaths show a trend toward isotropy but also a weak fluctuation power, while downstream of quasi-perpendicular shocks and low-beta ($\beta < 1.1$) solar wind, both fluctuation power and anisotropy cover a wide range of values.

While it is still not clear how important it is, many authors believe that fluctuations in the interplanetary medium can play a role in geomagnetic activity (Borovsky (2003); D'Amicis et al. (2007); Jankovičová et al. (2008); Yermolaev et al. (2018); Bonde et al. (2018)). Our results, showing the level and type of fluctuations in sheaths, are a first step to answering both the questions of the peculiarity of sheaths' impact on the geomagnetic environment and of the role of fluctuations in this impact.

7.1.3 Global numerical simulations

The interaction of sheaths with the geomagnetic environment is not very well-known either. Recently, observational studies have come up to study this interaction (*e.g.* Kilpua et al. (2017a) and references therein, or Kilpua et al. (2019); Kalliokoski et al. (2020)). While there are a few global MHD simulations of the interaction of an (artificially injected) interplanetary shock with the geomagnetic environment (Koval et al. (2005, 2006b); Samsonov et al. (2006, 2007); Šafránková et al. (2007); Pallocchia et al. (2010)), so far there have been no global hybrid simulations of the interaction of a shock with the geomagnetic environment, and much less global hybrid simulations also including a sheath (as a consequence of a self-consistently formed shock). The second half (chapters 5 and 6 of the work presented in this thesis aimed to bridge this gap, as we performed the first global hybrid-PIC simulation including an self-consistently generated interplanetary shock and its sheath.

In chapter 6, we explored the propagation of an interplanetary shock inside the magnetosheath, and the consequences these two structures had on each other. Similarly to Koval et al. (2005); Samsonov et al. (2006) and Pallocchia et al. (2010), we found that the interplanetary shock travelling in the magnetosheath slows down to 80% of its speed in the solar wind, which is not as much as was previously estimated by Villante et al. (2004), which concluded with a velocity in the magnetosheath of 25-33% of the velocity in the solar wind. While already reported, this result is quite counter-intuitive: the shock barely slows down, while the solar wind ions almost stop. This slowing down leads to a small but noticeable curvature of the transmitted interplanetary shock in the magnetosheath. Further along the propagation of the transmitted interplanetary shock, we found that the shock front could be accelerated, close to the magnetopause, in the plane perpendicular to the interplanetary magnetic field (Placed inside of the magnetosheath next to the magnetopause at 17 Earth radii downstream of Earth we would encounter the interplanetary shock with an advance of 16 seconds compared to if we were placed outside of the magnetosheath altogether). We qualitatively attributed this acceleration to the so-called “slingshot” effect (Chen et al. (1993), Lavraud et al. (2013) and Turc et al. (2015)). This is a new result, that was not seen in previous MHD simulations of interplanetary shocks propagating in the magnetosheath; for example, Šafránková et al. (2007) explicitly reported that in their MHD simulations, the interplanetary shock was slowed down in both the plane of the interplanetary magnetic field and in the plane perpendicular to it. This is actually quite surprising, because the “slingshot” effect is an MHD effect.

Along the Sun-Earth line, we explored the inward motion of the bow shock (the magnetosheath contracts to 67% of its initial thickness), followed by an outward motion. Šafránková et al. (2007) reported that the bow shock’s outward motion was due to modifications of the magnetosheath’s parameters, while Samsonov et al. (2006) and Pallocchia et al. (2010) attributed this outward motion to a reflection of the interplanetary shock (either as a reverse fast shock or as rarefaction wave) on the inner boundary of their numerical model. Samsonov et al. (2007) went further in the analysis and showed that the fast shock would actually travel through the magnetosphere, with a first partial reflection/transmission at the plasmapause then reach the ionosphere where the rest of the shock’s energy could be reflected as well. In our simulation, we found that both explanations (the variation of the magnetosheath parameters along with a reflection of the interplanetary shock) concurred to explain the outward motion of the bow shock. However, we clearly showed that the reflection of the interplanetary particles on the magnetopause was sufficient to explain the outward motion, as there was no reflection further inside the magnetosphere. We did not observe the presence of a reverse fast shock, which points towards the reflection of particles counter-streaming at subalfvénic speeds. Taking advantage of our 3D simulations, we also observed a similar behaviour of the bow shock on the flanks of the magnetopause. The motion of the magnetopause appeared different from place to place: while at the nose and in the noon-midnight meridian plane it recedes then finds a new place of equilibrium, in the ecliptic plane the magnetopause has a back and forth motion. We also estimated a lower contraction of the magnetosheath on the flanks than on the nose: on the flanks, the magnetosheath contracts on average to 84% of its initial thickness.

Finally, we found that, in the sheath, non-MHD terms in the Ohm's law gave rise to a substantial electric field along the x direction ($E_x \simeq 2.3$ mV), which together with the interplanetary magnetic field gave rise to a non-negligible velocity component in the plane perpendicular to the interplanetary magnetic field. This component was mostly due to the Hall term (78% of the non-MHD E_x), and secondarily, to the electron pressure term (22% of the non-MHD E_x). The marked change of direction of the flow in the sheath led to a strong asymmetry in the magnetosheath's compression.

Table 7.1 summarises which of the results obtained through our simulations have been previously obtained with MHD simulations, and which demanded an hybrid PIC code. More subtle is the case of the acceleration/braking of the interplanetary shock, which; if it corresponds indeed to the "slingshot" effect, should be observable in MHD simulations, but has not yet – to our knowledge – been reported. Note that the assymetry brought about by non-ideal terms in Ohm's law could in theory appear in Hall-MHD simulations of an interplanetary shock/sheath. This has never – to our knowledge – been reported.

	MHD	Hybrid PIC
Braking/acceleration of IP shock in MSH	?	✓
Compression of MSH, calculation of $\boldsymbol{j} \cdot \boldsymbol{E}$	✓	✓
Compression / Expansion of MSH	✓	✓
Counter-streaming subalfvénic ion population	✗	✓
Assymetry appearing in non-ideal Ohm's law	✗	✓
Foreshock & interaction with IP shock/sheath (in progress)	✗	✓

Table 7.1: *Our Hybrid PIC results versus MHD results from the litterature*

7.2 Spectral analysis of space data: Perspectives

7.2.1 Other fluctuations in the sheaths

In chapters 3 and 4 we focused on the fluctuations of the magnetic field. This is mostly because on the ACE mission, the magnetic data is far superior to the particles data in at least three different aspects: There are much less data gaps, the temporal resolution is much better (1 s for the magnetic field, and about 1 min for particles data), and the time interval between two measurements is constant.

There is however, no theoretical reason why the fluctuations of the magnetic field should be given more attention than the fluctuations of the other quantities. With the better quality of measurements offered by new generation missions such as MMS, there is much to learn by directing our attention to other types of fluctuations.

When thinking about the role of fluctuations in geomagnetic activity, magnetic and dynamic pressure fluctuations may play a different role: while magnetic fluctuations could increase the probability of magnetic reconnection, the fluctuations of dynamic pressure could send pressure pulses directly in the magnetosphere through the magnetopause without any need for plasma exchange at the frontier. We do not yet know well the fluctuations inside sheaths, however. In Kilpua et al. (2013), the authors performed a wavelet analysis of both the magnetic fluctuations and the fluctuations of the dynamic pressure inside sheaths. In order to improve upon this first study and compare the power in these two types of fluctuations, we believe that one should arrange the analysis so that the results have the same units.

We based our way to do this on what is usually done in solar wind turbulence studies: comparing the local Alfvén speed ($\frac{B}{\sqrt{\mu_0 \rho}}$) to the local velocity. We found it more natural, however, to multiply these two quantities by $\sqrt{\rho \mu_0}$ so that they could both be expressed in nanoteslas (nT). This, in turn, allows the result of a wavelets analysis (as presented in chapter 3) to be expressed in nT^2. Since the unit of our wavelets analysis of a signal f is the square of the original signal's unit ($[\mathscr{W}(f)] = [f]^2$), and $(\sqrt{\rho}u)^2 = P_{dyn}$ it is not unreasonable to call the fluctuations of $\sqrt{\rho}u$ the fluctuations of the dynamic pressure.

We mentioned that the particles data were only available with a rate of ~ 60 seconds. In order to make comparisons possible between magnetic fluctuations and fluctuations of dynamic pressure, we had to degrade the magnetic data by interpolating them to the particles data.

In figure 7.1, we have plotted, for the 14-12-2006 event, the quantity: $P(t) = \int_{f_{min}}^{f_{max}} \mathscr{W}(f,t)(x)df$, where $\mathscr{W}$ is the result of the wavelets analysis used in chapter 4 and f_{min} and f_{max} correspond to the limits set by the data resolution and the spin of the satellite. $P(t)$ can therefore be seen as the instantaneous energy per unit volume contained in the fluctuations between the frequencies f_{min} and f_{max}. From top to bottom, the figure shows the fluctuations of the magnetic field, the fluctuations of the dynamic pressure, and the temperature. At first sight, then, we find similar results to Kilpua et al. (2013), both types of fluctuations have elevated power just after the shock front, and next to the magnetic cloud's leading edge. Contrary to Kilpua et al. (2013), we also have the ability to quantitatively compare the energy in both types of fluctuations: in this particular case, magnetic fluctuations seem stronger than dynamic pressure fluctuations by a factor of roughly 5. The evolution of the temperature inside the sheath is also valuable information, as it indicates where the dissipation

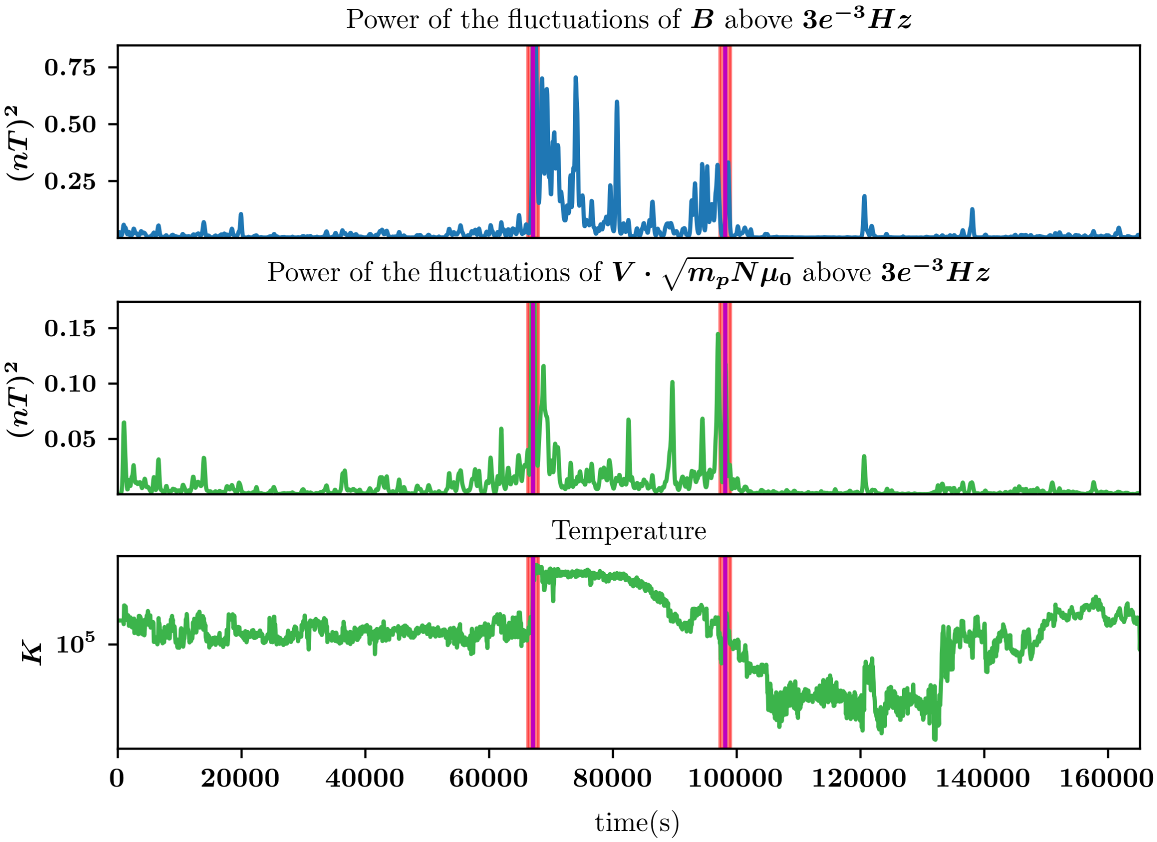

Figure 7.1: $P(t) = \int_{f_{min}}^{f_{max}} \mathscr{W}(f,t)(x)df$. *Comparison between the energy contained in the magnetic fluctuations and the fluctuations of the dynamic pressure inside the 14-12-2006 sheath.*

to lower scales happens. In this case, it seems strong in the first half of the sheath before taking a sharp drop. Next to the magnetic cloud's leading edge, however, a small rebound of the temperature seems to be consistent with the elevated levels of magnetic and pressure fluctuations.

As more and more particle data of good quality (good resolution, few gaps) are recorded by MMS, this type of analysis should yield interesting results in the future.

7.3 Global numerical simulations: Perspectives

7.3.1 Pushing the macroscopic analysis further

The simulation we presented in chapter 6 still has lots to teach us, and we plan to continue working on it. Let us give an example of the type of information we are still hoping to obtain:

It would be interesting to explore the transfers of energy between the particles and the fields. To learn more about this, the tools we have already developed could help. Figure 7.2, for example, compares the Lorentz force in the (xy) plane and the (xz) plane. It is visible that the Lorentz force acts as a brake along the magnetopause in the (xy) plane: it has positive values, represented in red. The behaviour in the (xz) plane is more difficult to read, as it is heavily unhomogeneous. We plan to learn more about the causes an effects of the interplanetary shock's deformation by splitting the Lorentz force into its two components (magnetic pressure and tension), and analysing its evolution over time.

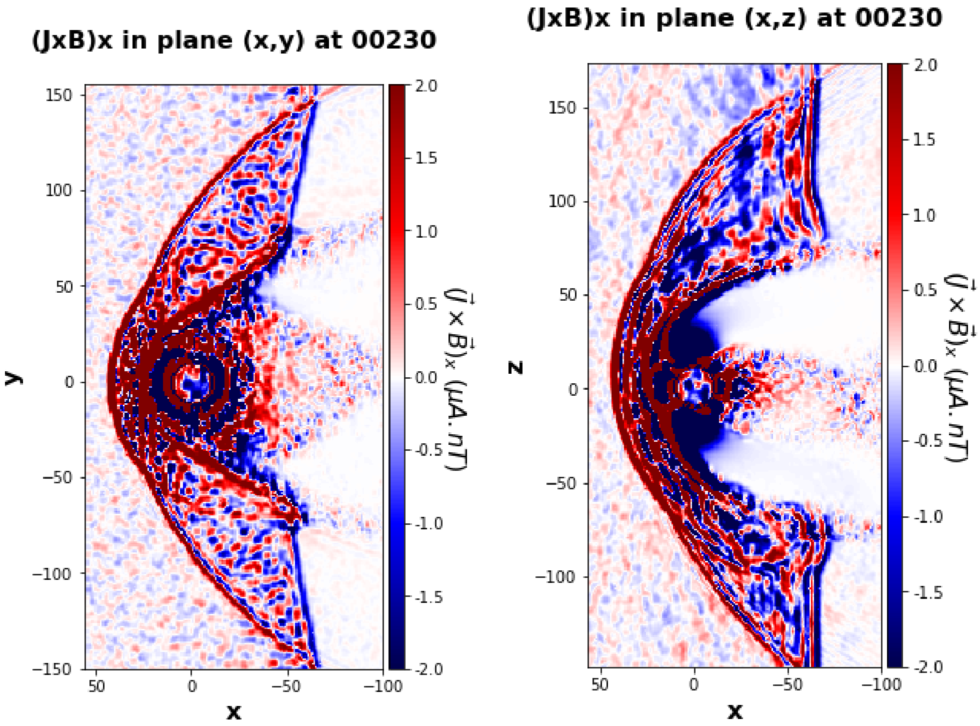

Figure 7.2: *Lorentz force along x* $(\boldsymbol{J}\times\boldsymbol{B})\cdot\boldsymbol{e}_x$ *in the ecliptic plane (left panel) and noon-midnight meridian plane (right panel)*

LatHyS also allows the user to save the particles' information, at some extra cost in computing time and memory. We could learn more about the energisation processes from a study of the phase space, as well as study more precisely the population of reflected subalfvénic particles that our results hinted at in chapter 6.

7.3.2 Fluctuations in the magnetosheath

Sheaths have two main characteristics that make them differ greatly from magnetic clouds: their high dynamic pressure, and their high levels of fluctuations. In the previous chapter 6, we have studied effects that are mostly a consequence of the sheath's dynamic pressure. However, it is believed that the fluctuations contained in sheaths may also play a role in their geomagnetic impact.

In this section, we present some early results pertaining to the crossing of the bow shock by the fluctuations contained in the sheath: First, we use the "boxes method" to study the general trends of the evolution of turbulence over time inside the magnetosheath, as it interacts with the shock, sheath and magnetic cloud. Then, we use observational analysis methods on the LatHyS data to compare the fluctuations inside of the interplanetary sheath as simulated in LatHyS to the fluctuations found in observations using the ACE satellite (see chapter 4). Finally, we look at the magnetic field recorded by virtual satellites at different places in the magnetosheath, and use Morlet wavelets to analyse the magnetic fluctuations.

Evolution of the turbulence: general trends

In order to have an idea of the general trends of the evolution of turbulence during the passage of the interplantary sheath through the magnetosheath, we plot (figure 7.3) the root mean square of the magnetic field.

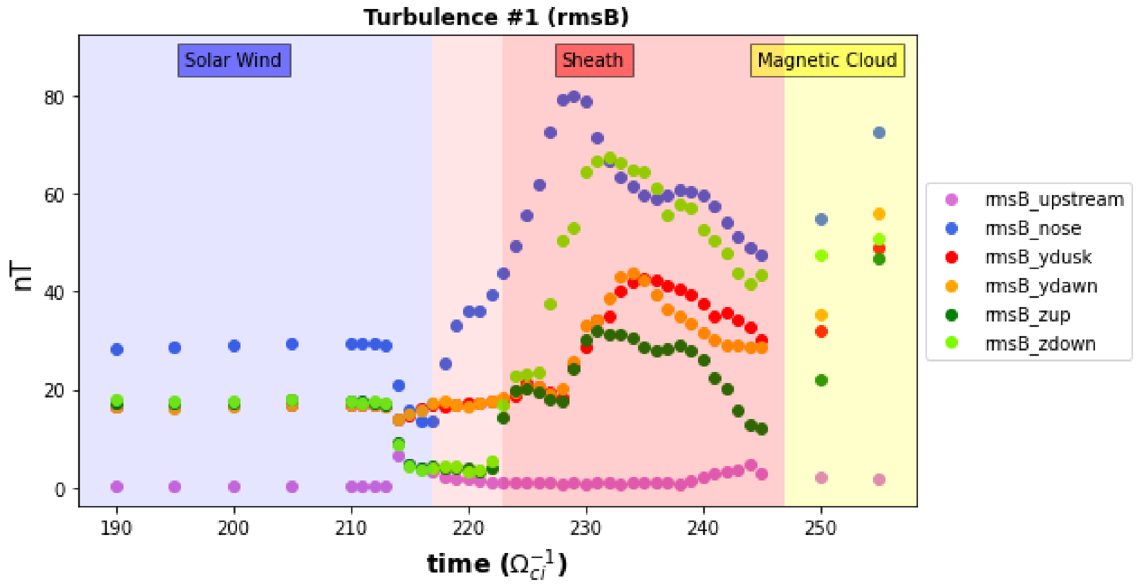

Figure 7.3: *Evolution of the root mean square of the magnetic field (rms(B)) at different locations.*

For each component j of the magnetic field, we compute the root mean square of the field in the "boxes", $rmsB_j$:

$$rms(B_j) = \sqrt{\langle\, (B_j(\mathbf{r}) - \langle B_j(\mathbf{r})\rangle)^2\, \rangle} \tag{7.1}$$

In this equation, $\boldsymbol{r}$ goes through all the cells in each of the “boxes”.

The quantity $rms(\boldsymbol{B})$ is then defined as:

$$rms(\boldsymbol{B}) = \sqrt{\sum_{j=[x,y,z]} rms(B_j)^2} \tag{7.2}$$

Figure 7.3 tells us that as the sheath goes through the magnetosheath, the level of turbulence increases strongly. It starts dropping as the bow shock starts moving sunward (from 229 $\Omega_{\mathrm{ci}}^{-1}$ in the “nose”, and slightly later for the other “boxes”). For now, we do not know why there is a drop in $rms(\boldsymbol{B})$ just prior to the shock-shock interaction. This will be investigated.

Another interesting quantity for turbulence studies is the normalised rms, or $rms(\boldsymbol{B})/\langle|\boldsymbol{B}|\rangle$, often noted rmsBoB.

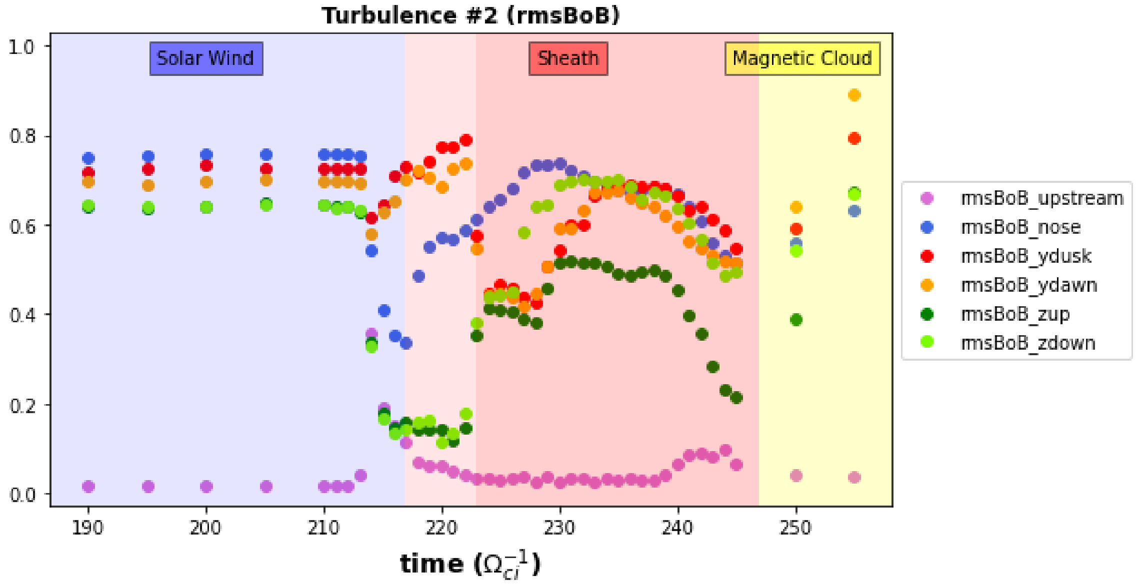

Figure 7.4: *Evolution of the normalised root mean square ($rms(B)/\langle B\rangle$) of the magnetic field at different locations.*

Figure 7.4, which shows rmsBoB, tells us that the turbulence regime in the magnetosheath is actually stronger prior to the interaction with the interplanetary sheath, which is surprising and could be, if proven to be correct, really interesting.

The definition of rmsB and rmsBoB in our boxes however, raises an important question: since the *rms* is computed spatially on dynamic data, it can be quite flawed. As sketched on figure 7.5, while the definition of the fluctuations δB seem perfectly natural in the situation represented on the left panel, the steady rise of magnetic field sketched on the right panel, which would not generally be considered as turbulent, would be interpreted by the *rms* calculations as heavily turbulent. A direct consequence of this definition problem is visible on figure 7.3: the magnetic cloud is depicted by

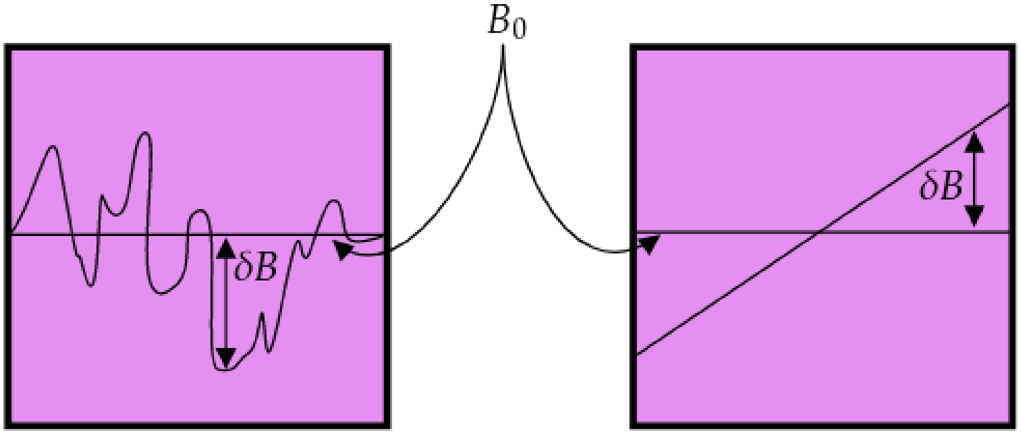

Figure 7.5: *The purple square represent a "box" from the "boxes method". The black line crossing it represents the magnetic field. Two situations are represented: fluctuations as we expect them, and a problematic situation. Both panels would lead to high values of the rmsB and rmsBoB.*

the rmsB as highly turbulent. What is happening, however, is simply that the magnetic field varies slowly and steadily, which leads to large difference, on average, between the mean magnetic field in the "box" and the local magnetic field at each grid cell. More work is planned to find a more correct way of describing the general evolution of turbulence in the magnetosheath.

Comparison of the simulated sheath with ACE data

Figure 7.6 shows the data from a virtual satellite placed at $x = 0$, and as far away as possible from the geomagnetic environment ($y = 300$, $z = 0$). This means that the virtual satellite observes the passage of the sheath and magnetic cloud unchanged by any interaction with the magnetosheath. This figure can therefore serve as a reference for the amount of fluctuations in the pristine solar wind, the interplanetary sheath, and the magnetic cloud.

The upper panel of figure 7.6 is a representation of the magnetic field amplitude over time, along with its components (B_x in blue, B_y in orange, and B_z in green). Superimposed on this upper plot are three coloured spans: blue in the solar wind, red in the sheath, and yellow in the magnetic cloud. These spans mark three relatively homogeneous regions for each of which we drew a spectrum obtained from a Morlet wavelet transform. Inside of each span, a smooth line of the same colour as the span is superimposed on the signal. This line represents the mean value of the signal, which is necessary to compute the wavelets. In the solar wind and sheath, this mean value has been computed as a linear fit of each magnetic field components, while in the magnetic cloud, it has been computed with a sliding window of 11 points large, in order to not mathematically mistake the natural slow variation of the magnetic field with fluctuations.

The three corresponding spectra are represented on the lower panel of figure 7.6. Similarly to what was done in chapter 4, the spectrum of the fluctuations perpendicular and parallel to the mean

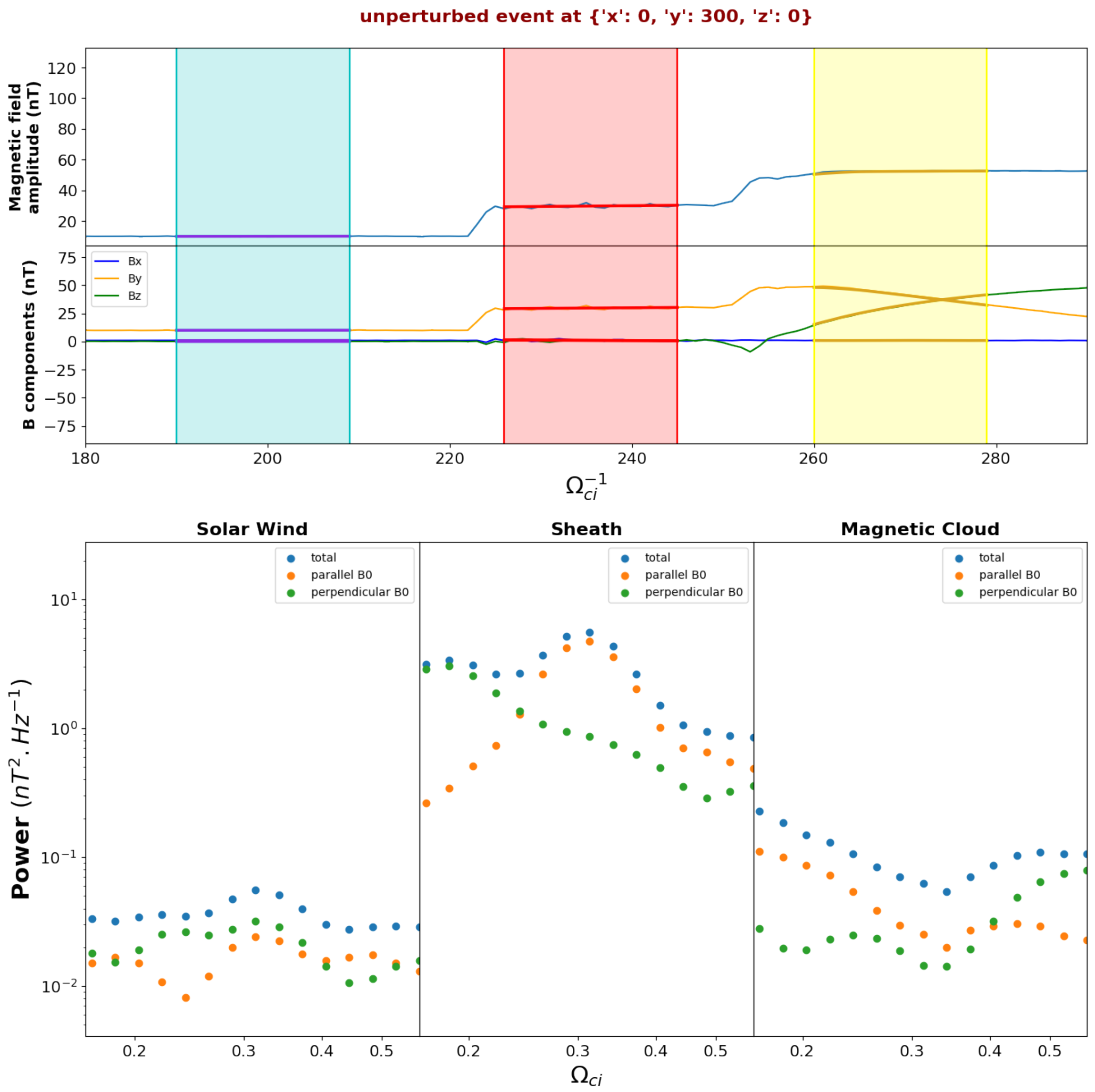

Figure 7.6: *(LatHyS results.) Upper two plots (upper panel): Magnetic field amplitude against time. Components of the magnetic field against time. The three coloured spans represent homogeneous regions on which we perform a spectral analysis. Blue span: solar wind, red span: sheath, yellow span: magnetic cloud. Bottom three plots (bottom panel): Spectra of the magnetic fluctuations in the solar wind region, sheath, and magnetic cloud. The total is represented in blue, the power in the parallel component of the fluctuations is represented in orange, and the power in the perpendicular component of the fluctuations is represented in green.*

magnetic field were computed and represented separately. The parallel fluctuations are represented in orange, and the perpendicular fluctuations in green. Their sum is represented in blue. The frequency range is chosen as follows (the reasoning is the same as explained on page 64, in chapter

4): the smallest frequency corresponds to twice the inverse of the averaging window, and the largest frequency is half the inverse of the maximum resolution.

It is instructive to compare the bottom three plots of 7.6 to the three plots of figure 4.3, on page 65. Useful to remember, and making conversions easy, is that in our simulations, $\Omega_{\mathrm{ci}} \simeq 1\mathrm{Hz}$. The range of frequencies studied in this simulated sheath and in the earlier observational analysis are not the same, as in LatHyS we are looking at frequencies roughly ten times higher than those we had using ACE data. This is simply because the simulation box is at a reduced scale from reality, therefore we have to probe smaller areas and faster variations. Since the power of the magnetic fluctuations decreases with frequency, the power of the fluctuations in the range of frequency displayed for the simulated sheath (figure 7.6) should be lower than in the range of frequency displayed for the real sheath (figure 4.3). Actually, if we were to prolong the spectra on figure 4.3 to reach $f = 0.4$ Hz (assuming no change of slope, since it is the inertial range), we would find: $PSD_{\mathrm{SW}} \simeq 1 \cdot 10^{-1}$ nT/Hz, $PSD_{\mathrm{Sh}} \simeq 3 \cdot 10^{0}$ nT/Hz, and $PSD_{\mathrm{MC}} \simeq 5 \cdot 10^{-2}$ nT/Hz. These are the same order of magnitude as what we obtain in LatHyS, albeit twice to three times larger. On figure 7.6, we can note that the variation of the power in the fluctuations from region to region follows the same pattern as the one reported in chapter 4: the power in the sheath is roughly an order of magnitude above the power in the magnetic cloud and solar wind, which resemble each other. In terms of power, then, our simulated sheath seems to behave realistically. In terms of anisotropy and slope, however, the fluctuations in LatHyS are very different from the observations. Indeed, on our results from LatHyS, the magnetic fluctuations barely present any slope, and the behaviour of the power of the parallel and perpendicular components of the magnetic field are very different from what they are observational data. Worthy of note, however, is the fact that just like in the observations, the parallel power (orange dots in figure 7.6) seems to dominate in the sheath, whereas it is not the case in the solar wind and magnetic cloud. This indicates the presence of more compressible waves in the sheath than in the rest of the simulation box.

In the remainder of this subsection, we will put aside the fact that the fluctuations in the unperturbed simulated sheath only superficially fit with observations, and simply think about them as a reference for the fluctuations outside of the magnetosheath. Seen as an input, we will investigate what these fluctuations become once they interact with the magnetosheath.

Spectra from virtual satellites

Here, we use the data from the restricted fleet of satellites presented in figure 5.14 (page 115). They were chosen to be as close as possible to the centre of the boxes presented in figure 5.23 (page 125). Of course, since the shape of the magnetosheath changes overtime, so too do the positions of the boxes. This means that the virtual satellites, which stay at fixed locations, cannot strictly stay in the centre of the boxes and the corresponding magnetosheath regions. The virtual satellites therefore explore slightly different parts of the magnetosheath as the data evolve. This is exactly the situation we face when using data from real satellites.

Magnetic fluctuations in the nose of the magnetosheath

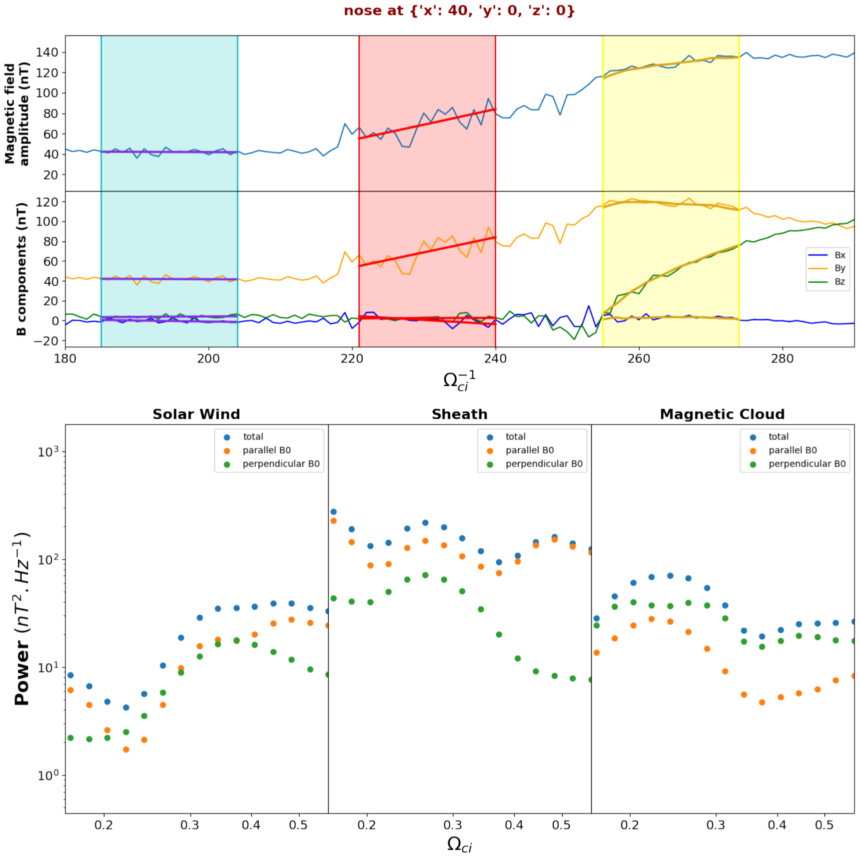

Figure 7.7: *This figure is constructed in the same way as figure 7.6: the upper two plots represent the magnetic field as measured by a virtual satellite placed in the "nose" of the magnetosheath, and the three lower plots are the power spectrum density of the magnetic field computed in the three different regions (solar wind, sheath, magnetic cloud).*

Figure 7.7 shows an analysis of the magnetic data measured by a virtual satellite placed in the nose of the magnetosheath. We can compare figure 7.7 with figure 7.6, which serves as a reference. In the solar wind, the power of the magnetic fluctuations is $PSD_{SW}^{unperturbed} \sim 3 \cdot 10^{-1}\ \mathrm{nT}^2/\mathrm{Hz}$, whereas in the nose of the magnetosheath during the solar wind upstream conditions, we obtain

$PSD_{SW}^{nose} \sim 2 \cdot 10^1$ nT^2/Hz. The fluctuations gain almost two orders of magnitude from the solar wind to the magnetosheath during pristine solar wind upstream conditions. In the unperturbed sheath, we have $PSD_{Sh}^{unperturbed} \sim 3$ nT^2/Hz, whereas in the nose of the magnetosheath during the sheath upstream conditions, we obtain $PSD_{SW}^{nose} \sim 1 \cdot 10^2$ nT^2/Hz. The ratio between the level of fluctuations in the magnetosheath and upstream of it is now closer to a few dozens. This is interesting: while the sheath upstream conditions lead unquestionably to a large amount of fluctuations in the magnetosheath, the increase between downstream and upstream of the bow shock is less during the sheath interval (multiplication by ~ 30) than during the solar wind interval (multiplication by ~ 70). Our simple interpretation is that it may be harder to compress fluctuations that are already quite compressed.

Magnetic fluctuations on the flanks of the magnetosheath

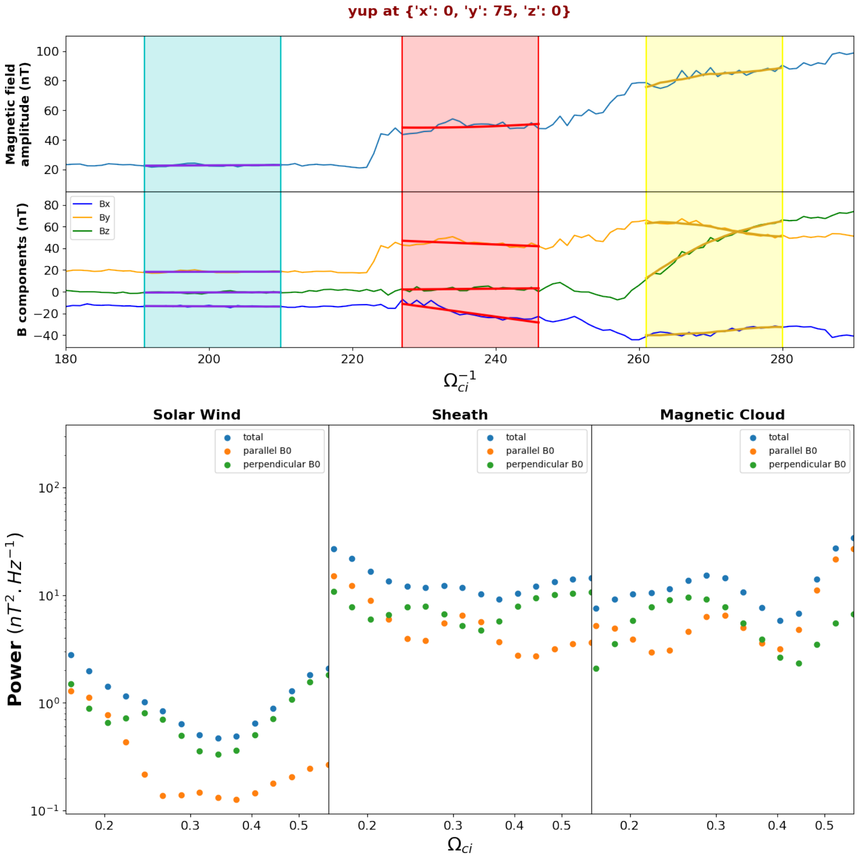

Figure 7.8: *This figure is constructed in the same way as figure 7.6: the upper two plots represent the magnetic field as measured by a virtual satellite placed in the "ydusk" region of the magnetosheath, and the three lower plots are the power spectrum density of the magnetic field computed in the three different regions (solar wind, sheath, magnetic cloud).*

The same analysis can be performed at the other virtual satellites' positions in the magnetosheath ("ydusk", "ydawn", "zup" and "zdown"). Figure 7.8 shows the analysis for the "ydusk" satellite. The power is generally an order of magnitude less than in the "nose", but interestingly, the magnetic cloud interval seems to raise the level of fluctuations in the magnetosheath (“ydusk”) to levels almost as high as the sheath interval does. We find similar responses at the other locations. Could this mean that a magnetic cloud crossing the magnetosheath leads to high fluctuation levels on the flanks? This is definitely an interesting question for future work.

7.3.3 Implementing realistic fluctuations in LatHyS

We noted earlier that the level of fluctuations observed in the simulation’s results is not as high as it would be in reality, even if we take into account the fact that we are analysing fluctuations at a relatively high frequency, compared to what we did in chapter 4. We have also shown that apart from their power, the characteristics of the fluctuations were not consistent with observations: their anisotropy and slope did not look like what we find in observations.

The reason for these limitations is quite simple: the only fluctuations explicitly included in LatHyS are thermal fluctuations and some new fluctuations are generated self-consistently by the interplanetary shock. In reality, in the solar wind, a vast amount of fluctuations are not created locally but transported from their place of creation, which may be other discontinuities, or directly the solar corona. For obvious reasons, neither the Sun nor other discontinuities are present in our simulation, therefore lessening the amount of fluctuations present in our simulated solar wind.

In order to address these limitations, we want to include a spectrum of Alfvén-like fluctuations in LatHyS, entering the simulation box with the solar wind. So far, we have developed a module to inject a monochromatic Alfvén wave in the simulation, which is compatible with our injection of a magnetic cloud. Figure 7.9 shows an example of a monochromatic wave modeled in LatHyS. The z components of the magnetic field and the plasma velocity oscillate with a 180° phase shift.

We also have developed a simple model, coded in Fortran but not yet included in LatHyS, of a signal which exhibits a Kolmogorov-like spectrum. In figure 7.10, the signal B drawn on the top panel is built using the following formula:

$$B(t)=\sum_{j=1}^{n}\left(\frac{j}{n}\right)^{5/3}\cos\left(2\pi\frac{t}{t_{max}}\frac{j}{n}+\phi(j)\right) \tag{7.3}$$

In this formula, j is the mode, n is highest mode. On figure 7.10 we can see towards the highest frequencies that n has been chosen to be smaller than the total number of points. This is to avoid aliasing by forcing the description of sub-grid sized modes. t is the time, t_{max} is the duration of the simulation, and $\phi(j)$ is a random phase for the mode j. This random phase avoids unnatural wave interference between the different modes.

Once we include formula (7.3) into the module that generates figure 7.9, the solar wind in LatHyS will be injected with a turbulence spectrum resembling what we observe in the solar wind. We then expect the fluctuations in LatHyS to be more realistic, not only in the solar wind, but also in the sheath and magnetosheath. This will allow two types of studies:

The first one is that it will allow us to explore with relatively small simulations the processes of the creation of waves in the sheath. We do not need to simulate the geomagnetic environment, and can simply use a relatively long box (*e.g.* $N_x=1500, N_y=N_z=32$) and try and reproduce

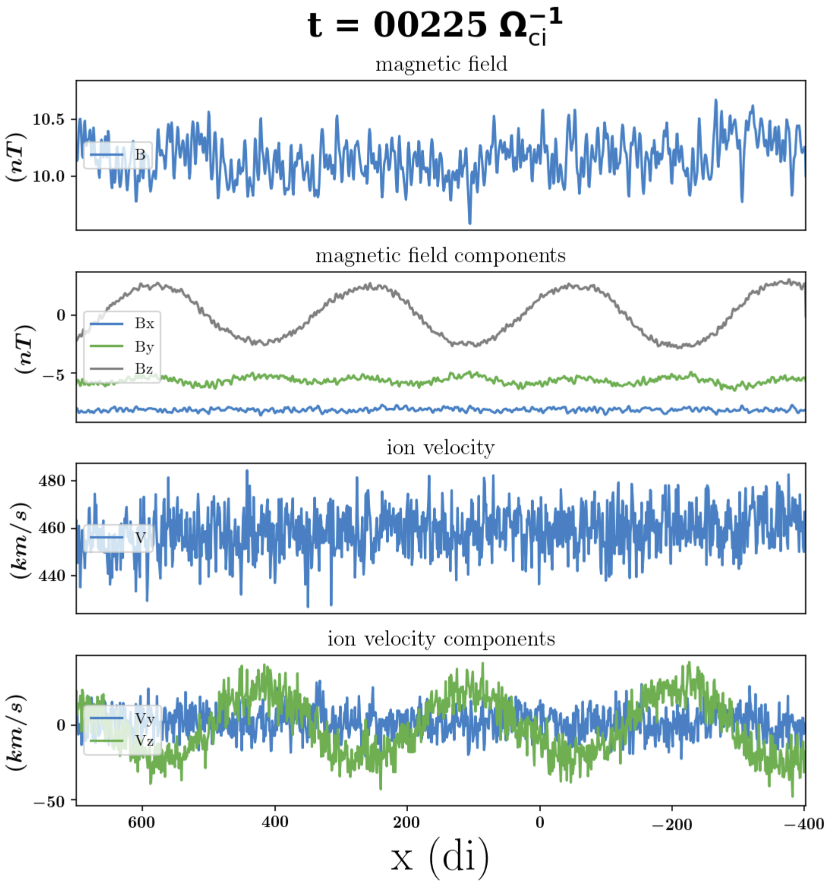

Figure 7.9: *A monochromatic Alfvén wave in LatHyS.*

with numerical simulations the results obtained in chapter 4. For example: how does the level of fluctuations in the sheath react to the level of fluctuations in the preceding solar wind? To the magnetic cloud's velocity? *etc.*

The second will be a more realistic study of the transfer of fluctuations from upstream of the bow shock to the magnetosheath. Essentially, we want to push further the preliminary study shown in subsection 7.3.2, but with fluctuations that more closely mirror those found in the observational data of solar wind intervals and sheaths.

7.3.4 Quasi-parallel case

Another way that fluctuations can be generated upstream of the bow shock is the presence of a foreshock. An ionic foreshock can be obtained in LatHyS simply by changing the orientation of the interplanetary magnetic field so that some part of the bow shock becomes a quasi-parallel shock. A question that our simulations could answer is the question of the interaction between an interplanetary shock and the foreshock: would it lead to more fluctuations in the sheath? Would this in turn lead to a different, maybe stronger, geomagnetic impact?
These questions will not be easy to answer, as changing the interplanetary magnetic field's direction

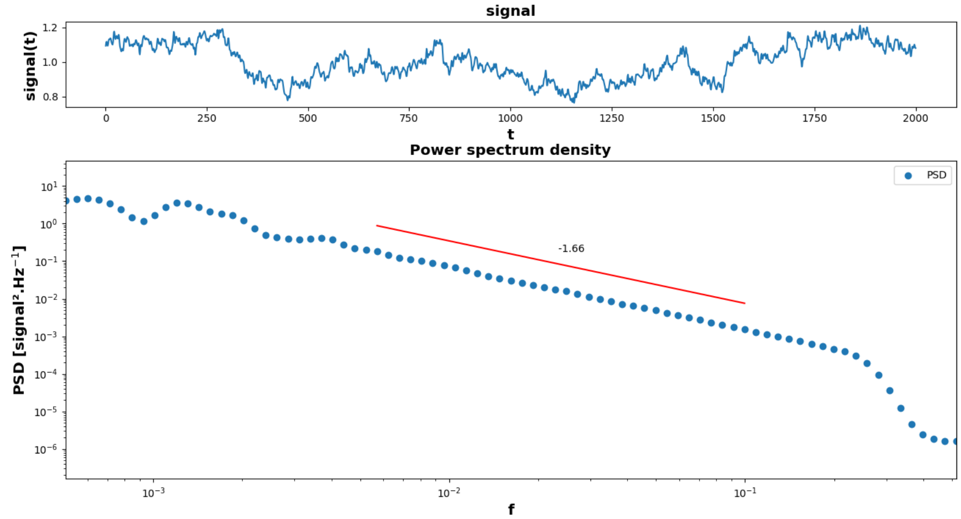

Figure 7.10: *Top panel: signal hand-built to contain fluctuations resembling a Kolmogorov-like spectrum. Bottom panel: PSD of the above signal.*

has a strong impact on both the magnetosheath and the interplanetary sheath; but for the same reason, trying to answer them should prove rewarding.

We have started running these types of simulations. Figure 7.11 shows a couple of the last snapshots we obtained from a quasi-parallel simulation. We hope to be able to resume it in the near future.

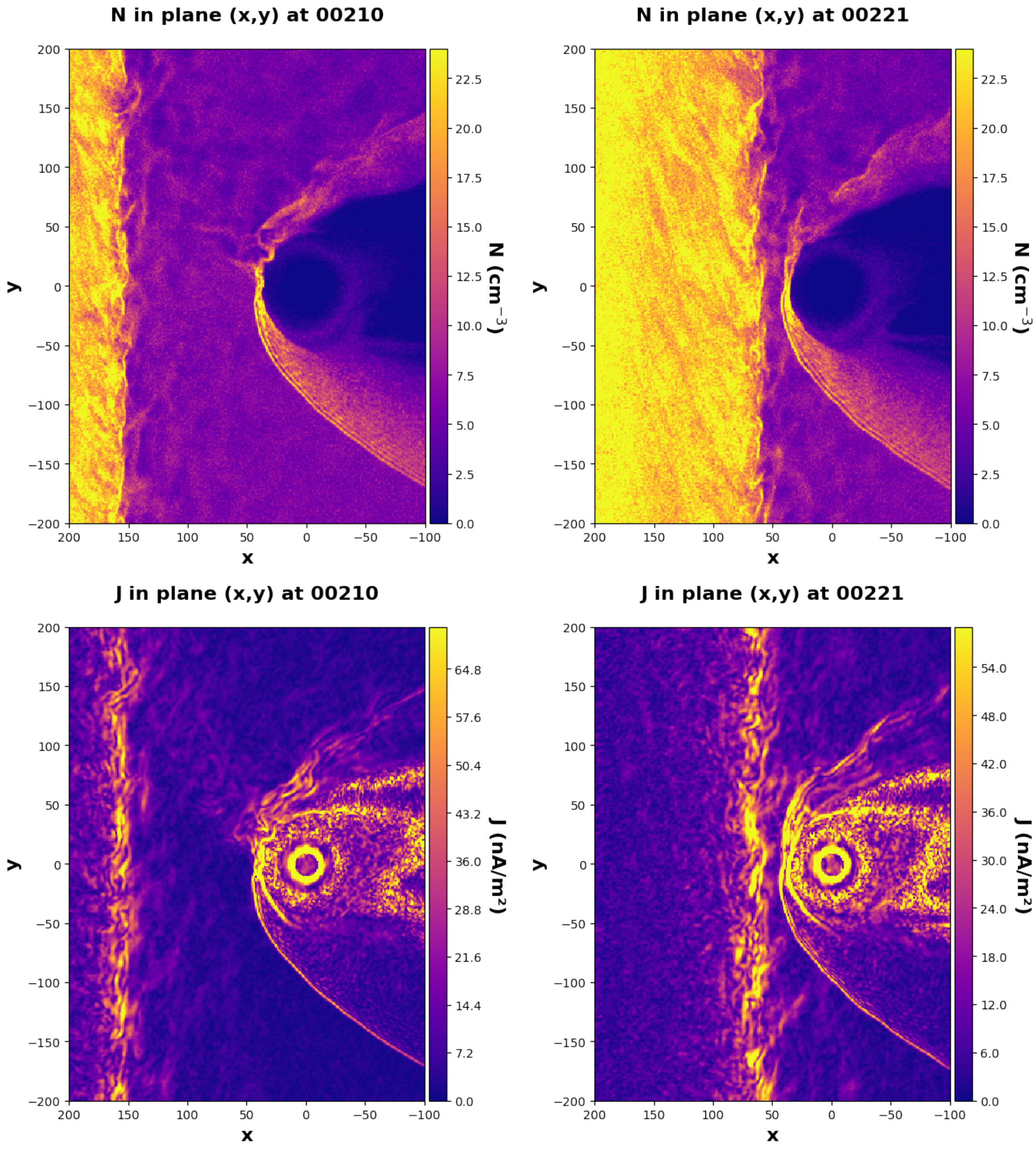

Figure 7.11: *Simulation of the collision between two quasi-parallel shocks. Top panels display the density in the (xy) plane. Bottom panels display the current density in the (xz) plane. Left panels: time 210, Right panels: time 221, just prior to the shock-shock collision.*

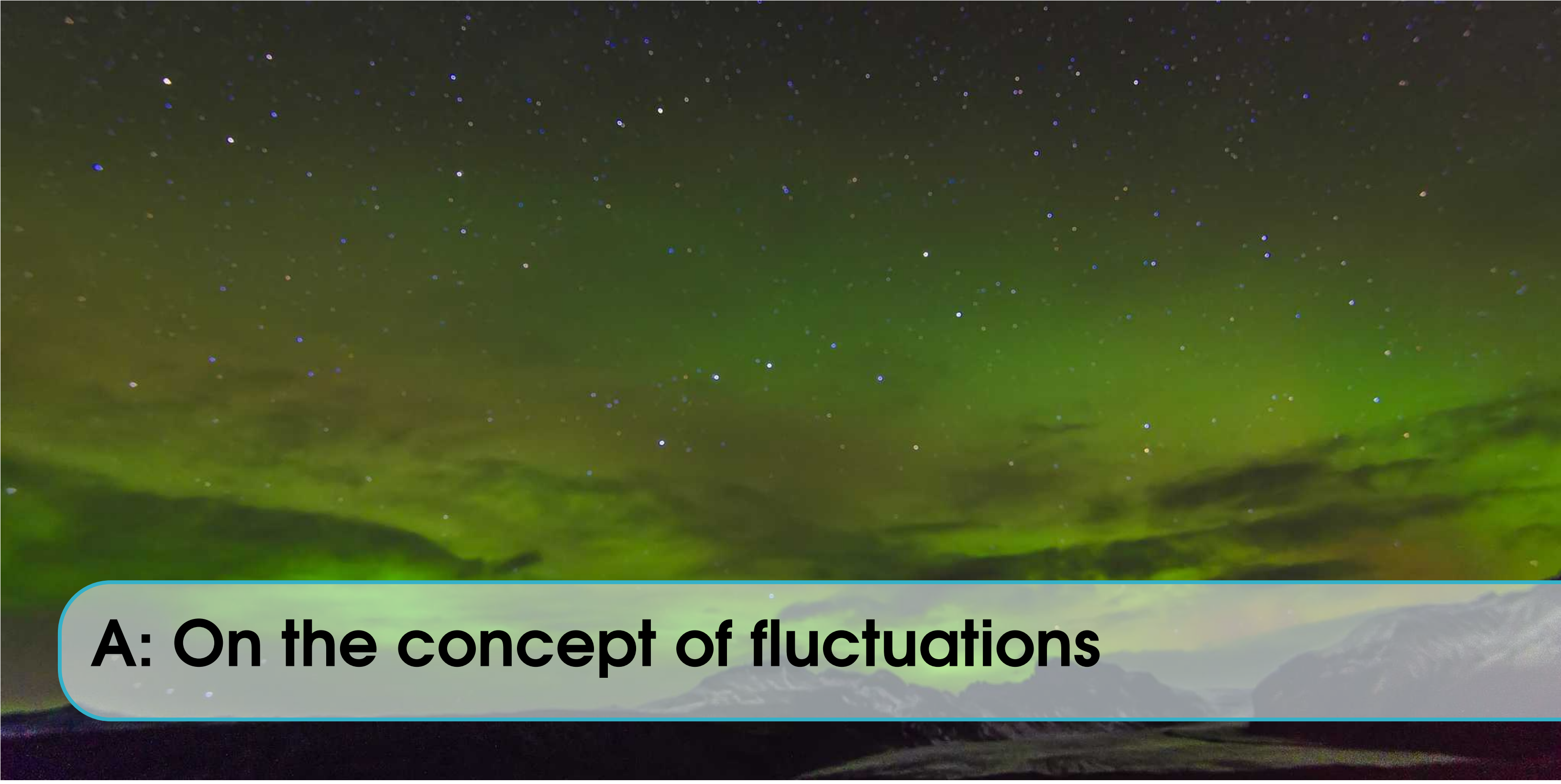

A: On the concept of fluctuations

> Mystery. You're always surrounded by them. But if you tried to solve them all, you'd never get the machine fixed. - Zen and the art of motorcycle maintenance - Robert M. Pirsig, 1974

Limits of this definition

The concept of fluctuations implies, in itself, an arbitrary point of view on the physics at play: talking about the fluctuations of, for example, $\boldsymbol{B}$ means dividing this quantity in two different parts: the mean, and the fluctuations. This is called the Reynolds decomposition, in which we write $\boldsymbol{B} = \boldsymbol{B}_0 + \delta\boldsymbol{B}$. This allows us to talk about how the physics is different parallel to the mean magnetic field $\boldsymbol{B}_0$, or perpendicular to it. It also allows one to make mathematical developments, by assuming, for example, that $|\delta\boldsymbol{B} \ll |\boldsymbol{B}|$. This conceptual separation between mean and fluctuations is based on the underlying hypothesis that there is a mean magnetic field, that there are fluctuations, and that the physics of these two quantities is different. This hypothesis seems natural nowadays, and that is probably because it is extremely productive.

It may seem natural to define the magnetic fluctuations in this way, and it is indeed a very common way to do so, but it came to our attention during this work that this approach is limited in some aspects. This paragraph intends to show some of the problems created by this definition.

What is the mean magnetic field? What are the magnetic fluctuations?

When writing $\boldsymbol{B} = \boldsymbol{B}_0 + \delta\boldsymbol{B}$, the divide between fluctuations and mean magnetic field is arbitrary. If we look at the magnetic spectrum on figure 12, we see that defining the magnetic fluctuations as anything happening above a certain frequency, and of the mean magnetic field as anything happening below the said frequency does not seem very natural after all. Yet, the definition of this frequency is extremely important, for something so arbitrary.

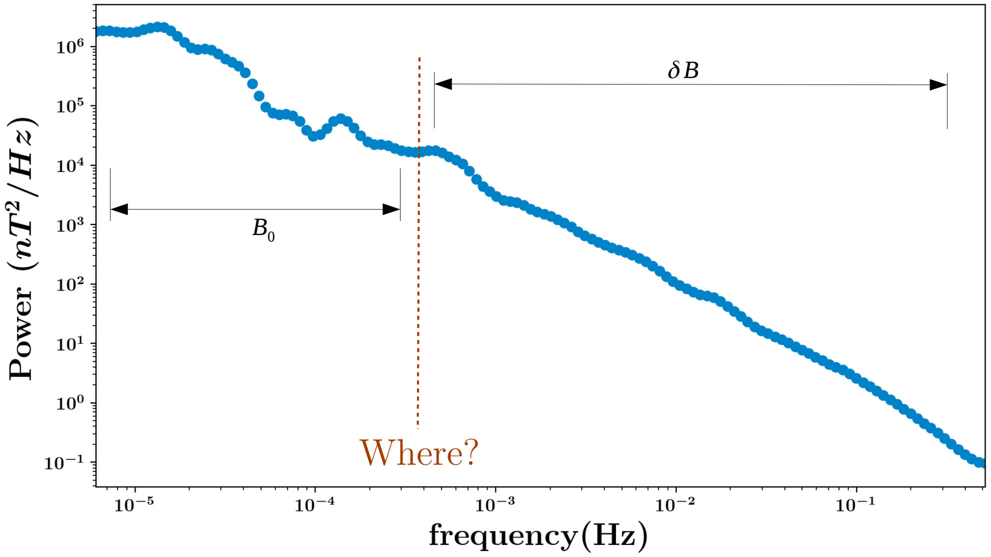

Figure 12: *Power spectrum density of the magnetic field on the 14 December 2006. Marked on the plot is one of the infinite possibilities for the choice of the frequency under which the field is called the "mean field" and above which the "fluctuations" are defined.*

The problem with a rectangle window

In order to define the mean magnetic field, it is then usual to use a sliding rectangular window, *i.e.*:

$$\langle B_{x,y,z} \rangle (t) = \frac{1}{T} \int_t^{t+T} B_{x,y,z}(\tau) d\tau$$

This, however, is quite a poor low-pass filter. To show this, let us take, for example, the rectangular window – type average of $\cos(\omega t)$, ω being an arbitrary pulsation:

$$\begin{aligned}
\langle \cos(\omega t) \rangle_T &= \frac{1}{T} \int_t^{t+T} \cos(\omega\tau) d\tau \\
&= \frac{1}{\omega T} \left[\sin(\omega\tau)\right]_t^{t+T} \\
&= \frac{1}{\omega T} \left(\sin(\omega(t+T)) - \sin(\omega t)\right) \\
\langle \cos(\omega t) \rangle_T &= \frac{1}{\omega T} \left((\cos(\omega T) - 1)\sin(\omega t) + \cos(\omega t)\sin(\omega T)\right)
\end{aligned}$$

This expression generally behaves as one would expect from a low-pass filter:

At low frequencies ($\omega T \ll 1$):

$$\begin{aligned}
\cos(\omega T) &\to 1 \\
\sin(\omega T) &\to \omega T \\
&\implies \langle \cos(\omega t) \rangle_T \to \cos(\omega t)
\end{aligned}$$

At high frequencies ($\omega T \gg 1$):

$$\frac{1}{\omega T} \to 0$$
$$\Longrightarrow \langle \cos(\omega t) \rangle_T \to 0$$

For intermediate frequencies, however, the average produced with a moving rectangular window associates the signal to a relatively complicated function:

$$\langle \cos(\omega t) \rangle_T = \frac{1}{\omega T} \left(\sin(\omega(t+T)) - \sin(\omega t) \right)$$

A complex, "real-world" signal containing a mix of components at all frequencies is therefore transformed in a relatively peculiar way by a rectangle window.

Some concerns about the use of a moving frame

Another concern is to do calculations of fluctuations from a rotating frame.
A very simple example shows how that might be a problem. Let us study an idealised magnetic field of constant magnitude, rotating around the z-axis:

$$B = B_0(\cos(\omega t)\boldsymbol{e}_x + \sin(\omega t)\boldsymbol{e}_y)$$

In the ($\boldsymbol{e}_x$, $\boldsymbol{e}_y$) frame, this magnetic field is rotating. Therefore a spectral analysis would show a component for the pulsation ω. In the rotating frame ($\boldsymbol{e}_B = \boldsymbol{B}/B_0$, $\boldsymbol{e}_\theta = \boldsymbol{e}_B \times \boldsymbol{e}_z$), the field is constant. Therefore a spectral analysis would show nothing.

Another way to think about what this is in terms of energy. Indeed, seeing some components at a certain frequency after a spectral analysis means that the fluctuations of the magnetic field contain some energy. If we do the same analysis in a rotating frame, the frame itself carries a part of this energy, and therefore the spectral analysis returns no component at the frame's rotating frequency. This means that the *PSD* in the moving frame should therefore be lower than the *PSD* in the fixed frame, which can be seen in figure 13.

In practice, this concern has a very simple solution: we should only do the spectral analysis on frequencies quite far above the "frequency" of rotation of the moving frame that follows the mean magnetic field. As can be seen in figure 13, for example, the *PSD* in the rotating frame and in the cartesian frame are essentially equal to each other at high frequencies.

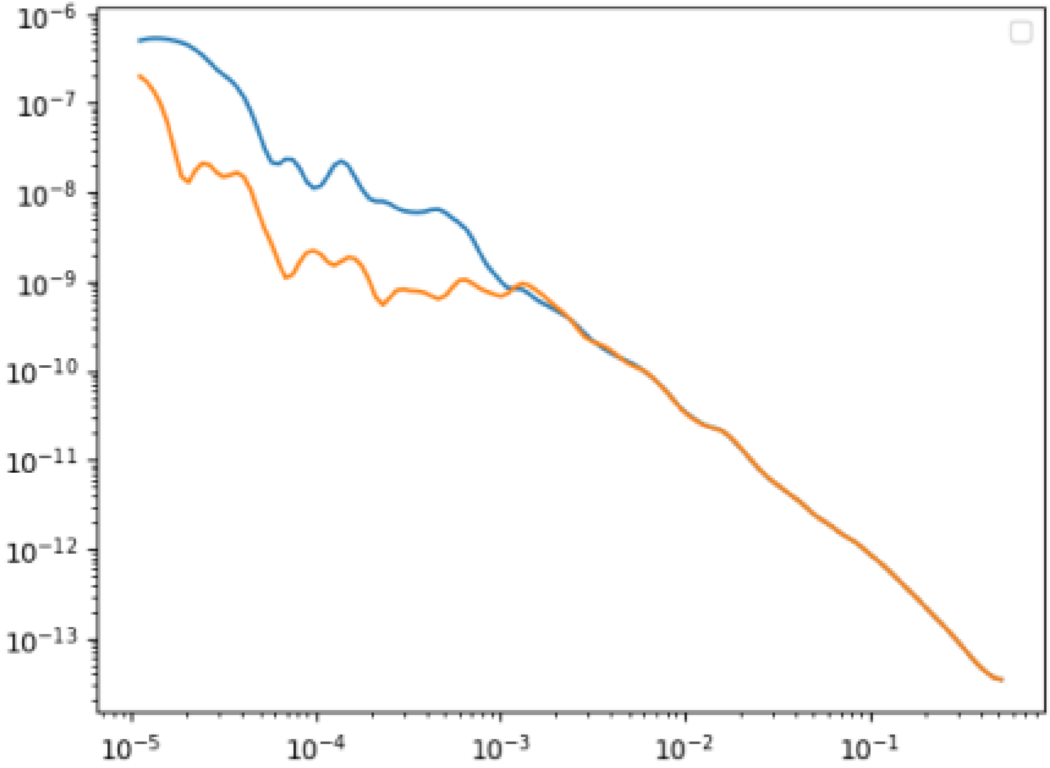

Figure 13: *The PSD shown were created from the spectral analysis of the whole of the 14-12-2006 event. In blue:* $PSD(B_x)+PSD(B_y)+PSD(B_z)$*. In orange:* $PSD(\boldsymbol{B}\cdot\boldsymbol{b}_0)+PSD(\boldsymbol{B}\cdot\boldsymbol{b}_1)+PSD(\boldsymbol{B}\cdot\boldsymbol{b}_2)$ *where the* $\boldsymbol{b}_j$ *vectors are those defined in equation* (4.2)

Toward a more rigorous definition?

There are probably many avenues to make these definitions "cleaner". I did not yet figure out a way to avoid the definition of a mean magnetic field, but the projection on said $\boldsymbol{B}_0$ can be avoided. This should eliminate the concern of the rotating frame. I present this idea for the sake of discussion, but because it involves some hypotheses on the physics, I would not necessarily recommend to use it as is.

Statement:

We could define the anisotropy as:

$$A=\frac{power(|\delta\boldsymbol{B}|)}{2\cdot power(\delta|\boldsymbol{B}|)} \tag{4}$$

Explanation:

- $\underline{power(|\delta \boldsymbol{B}|) \simeq power(\delta B_\perp)}$

In the solar wind, it is generally the case – as made clear by figure 4.3: the perpendicular power (grey line) is almost equal to the total power (blue line)), and 4.4: our previous way of defining the anisotropy shows that the parallel fluctuations are generally much smaller than the perpendicular fluctuations – that the power in the perpendicular fluctuations represents most of the power.

- $\underline{\delta|\boldsymbol{B}| \simeq \delta B_{||}}$

$$\begin{aligned}
|\boldsymbol{B}| &= |(B_0+\delta B_{||})\boldsymbol{e}_{||} + \delta B_\perp \boldsymbol{e}_\perp| \\
&= \sqrt{(B_0+\delta B_{||})^2+\delta B_\perp^2} \\
&= (B_0+\delta B_{||})\sqrt{1+\frac{\delta B_\perp^2}{(B_0+\delta B_{||})^2}} \\
&\simeq B_0+\delta B_{||} \quad \text{if } B_0 \gg \delta B_\perp
\end{aligned} \tag{5}$$

From this, we have:

$$\delta|\boldsymbol{B}| = |\boldsymbol{B}| - B_0 \simeq \delta B_{||} \tag{6}$$

B: Moissard et al. 2019

Note: Here, we reproduce Moissard et al. (2019) as published in JGR Space Physics.

JGR Space Physics

RESEARCH ARTICLE
10.1029/2019JA026952

A Study of Fluctuations in Magnetic Cloud-Driven Sheaths

C. Moissard[1], D. Fontaine[1], and P. Savoini[1]

[1]LPP, CNRS, Ecole Polytechnique, Sorbonne Université, Université Paris Sud, Observatoire de Paris, Université Paris-Saclay, PSL Research University, Palaiseau, France

Key Points:
- The fluctuations in sheaths have increased power (~10 times) and compressibility (~2 times) compared to the solar wind's
- Those characteristics depend on magnetic clouds' speed, preexisting fluctuations in the solar wind, and shock's parameters

Correspondence to:
C. Moissard,
clement.moissard@lpp.polytechnique.fr

Citation:
Moissard, C., Fontaine, D., & Savoini, P. (2019). A study of fluctuations in magnetic cloud-driven sheaths. *Journal of Geophysical Research: Space Physics*, *124*, 8208–8226. https://doi.org/10.1029/2019JA026952

Received 16 MAY 2019
Accepted 2 SEP 2019
Accepted article online 16 OCT 2019
Published online 7 NOV 2019

Abstract Interplanetary coronal mass ejections are at the center of the research on geomagnetic activity. Sheaths, highly fluctuating structures, which can be found in front of fast interplanetary coronal mass ejections, are some of the least known geoeffective solar transients. Using Morlet transforms, we analyzed the magnetic fluctuations in a list of 42 well-identified and isolated magnetic clouds driving a sheath and shock (Masías-Meza et al., 2016, https://doi.org/10.1051/0004-6361/201628571. We studied the fluctuations inside sheaths by defining two quantities: the power and the anisotropy. With a simple statistical approach we found that sheaths, in particular, those driven by a fast magnetic cloud, encountering a highly turbulent solar wind, and forming a high Alfvén Mach number shock have high levels of turbulent energy (~10 times compared with the solar wind) as well as a low anisotropy (approximately halved compared with the solar wind) of their fluctuations. On the other hand, the effect of the shock angle and plasma beta in the solar wind are less straightforward: If the shock is quasi-parallel or the beta in the solar wind is high, both the turbulent energy in the sheaths and the anisotropy of the fluctuations are reduced; but for quasi-perpendicular shocks or low beta solar wind the turbulent energy and anisotropy can take any value.

Plain Language Summary Solar flares are sometimes linked with the emission of interplanetary structures, which may collide with Earth. When this happens, it can lead to temporary changes in the magnetic field of Earth and possibly affect human technology. These effects are a subset of what is known as *geoeffectiveness*. We do have an idea of which types of structures may or may not have consequences on Earth, and, for example, *magnetic clouds* are quite well known for their large impact on the Earth magnetic field; however, we still struggle to understand the consequences of some puzzling interplanetary structures called *sheaths*. These can often be found preceding a magnetic cloud when the latter is fast enough to generate a shock wave. We think that one of the reasons these sheaths keep having surprising effects on the Earth's magnetic field is because they, themselves, are not yet very well known. The present paper aims at characterizing one of the key properties of sheaths: their *magnetic fluctuations*, that is, the rapid temporal variation of the magnetic field. We found that those *fluctuations* are indeed quite particular in sheaths: They have markedly more energy than in the usual solar wind (about 10 times more) and tend to change direction all the time. Conversely, in the solar wind, some directions seem to be privileged and the energy is relatively low. In this paper, we also show that these particular properties of the magnetic fluctuations are all the more pronounced when the magnetic cloud driving the sheath is moving faster and when the solar wind in front of the sheath already has strong fluctuations and magnetic pressure. This work gives us a better insight into the dynamics of the sheath, which may eventually improve our understanding of their geoeffectiveness.

1. Introduction

It has been extensively shown in the literature that magnetic clouds are the most geoeffective transient structures found in the solar wind (Kilpua et al., 2017; Wilson, 1987; Yermolaev et al., 2012; G. Zhang & Burlaga, 1988). This stems from the high probability of a magnetic cloud to present a long-lasting negative B_z component (Burlaga, 1991), which is a well-documented cause of geomagnetic storms (Dungey, 1961; Gonzalez & Tsurutani, 1987; Gonzalez et al., 1994; Kilpua et al., 2012; Russell et al., 1974; Tsurutani et al., 1992; Zhang & Moldwin, 2014), the explanation being that it favors magnetic reconnection at the nose of the magnetopause (Dungey, 1961; Gonzalez et al., 1989; Turc et al., 2014). However, this is not enough, as

©2019. American Geophysical Union. All Rights Reserved.

magnetic storms on Earth are not all caused by magnetic clouds, and not all magnetic clouds cause magnetic storms.

When a magnetic cloud has a velocity higher than the characteristic speeds (sound speed or Alfvén speed) of the solar wind in which it is traveling, its interaction with the solar wind is likely to form a shock wave propagating away from the Sun. Between the shock front and the leading edge of the cloud we find a sheath, which is a highly turbulent region (Kilpua et al., 2017). Huttunen and Koskinen (2004) have shown that, between 1997 and 2002, 45% of the 53 intense (as defined by the geomagnetic index $Dst < -100$ nT) magnetic storms observed on Earth were caused by a turbulent sheath region or postshock stream, thus exposing in a particularly convincing way the important role played by interplanetary coronal mass ejection (ICME) sheaths but pointing out the fact that it is not always possible to separate their effect from the ICMEs following them, when there is one. More than half of the magnetic clouds are accompanied by a sheath (Chi et al., 2016), and the role of these sheaths is increasingly regarded as important (Echer et al., 2008; Kilpua et al., 2017; Tsurutani et al., 1988). For example, out of the 73 solar storms (defined by $Dst < -50$ nT) of Solar Cycle 23 (1997 to 2005), Huttunen et al. (2005) identified eight events—composed of both a magnetic cloud and a sheath—where the magnetic storm was clearly caused by the sheath and not the magnetic cloud. Gonzalez et al. (2007) found similar results studying Solar Cycle 23: Sheaths were responsible for the generation of 24% of the intense storms ($Dst < -100$ nT) during the cycle, and magnetic clouds accompanied by a sheath for 14%.

The reasons that may lead to the geoeffectiveness of sheaths are still unclear. Tsurutani et al. (1990) emphasized the high probability of a sheath to include southward magnetic field due to the numerous large-amplitude turnings of the magnetic field. The geoeffectiveness of sheaths has also been suggested to be linked to their most obvious traits: high density, high dynamic pressure, high magnetic field, high variability of the magnetic field (Yermolaev et al., 2012), or high Alfvén Mach number (Guo et al., 2011; Kilpua et al., 2017; Myllys et al., 2016). These traits, especially the high dynamic pressure, high level of fluctuations of the magnetic field, and high Alfvén Mach number, are known to increase solar wind-magnetosphere coupling (Kilpua et al., 2017).

Another visible trait of sheaths is their turbulence. Their internal structure, however, is still mostly unknown, and the role it plays in their geoeffectiveness could be underestimated. Indeed, it is known that the turbulence in the solar wind plays a role in the efficiency of its coupling with the magnetosphere: For example, Tsurutani et al. (1988) noted that, surprisingly, some major storms seem to be caused by something else than a long-lasting southward magnetic field and pointed at turbulence, waves, and discontinuities as drivers of geomagnetic activity; Borovsky (2003) showed correlations between the amplitude of turbulence in the solar wind and different geomagnetic activity indices; Jankovičvá et al. (2008) did a similar study with similar conclusions and introduced the anisotropy of the fluctuations in the discussion; Osmane et al. (2015) compared the ultralow frequency (ULF) fluctuations of the interplanetary magnetic field and the AL index (amplitude lower for the auroral electrojet index) and concluded that, by enhancing viscous interaction between the solar wind and the magnetosphere, fluctuations can drive geomagnetic activity. Those studies, which strongly link the level of turbulence in the solar wind in general with geoeffectiveness, suggest that the turbulence in sheaths may play a major part in geoeffectiveness.

Before even considering geoeffectiveness, more information is needed to uncover as much as possible about the waves and fluctuations in sheaths. Only a few studies have been performed on the subject. For example, Kataoka et al. (2005) evidenced the importance of the shock parameters in influencing the structure of the sheaths of ICMEs. Kilpua et al. (2013) showed that the power of the ULF waves evolved within sheaths with respect to the distance with the shock and the leading edge of the magnetic cloud. Shaikh et al. (2017) found in two cases that sheaths were home not only to turbulence but also to ordered local structures such as magnetic islands, which are strong candidates to explain multisteps Forbush decreases (a rapid decrease of the detected galactic cosmic rays). And recently, a statistical study by Ala-Lahti et al. (2018) suggested that, in sheaths, mirror modes could stem from the shock compression, making the Alfvénic Mach number the key parameter governing the structure of sheaths.

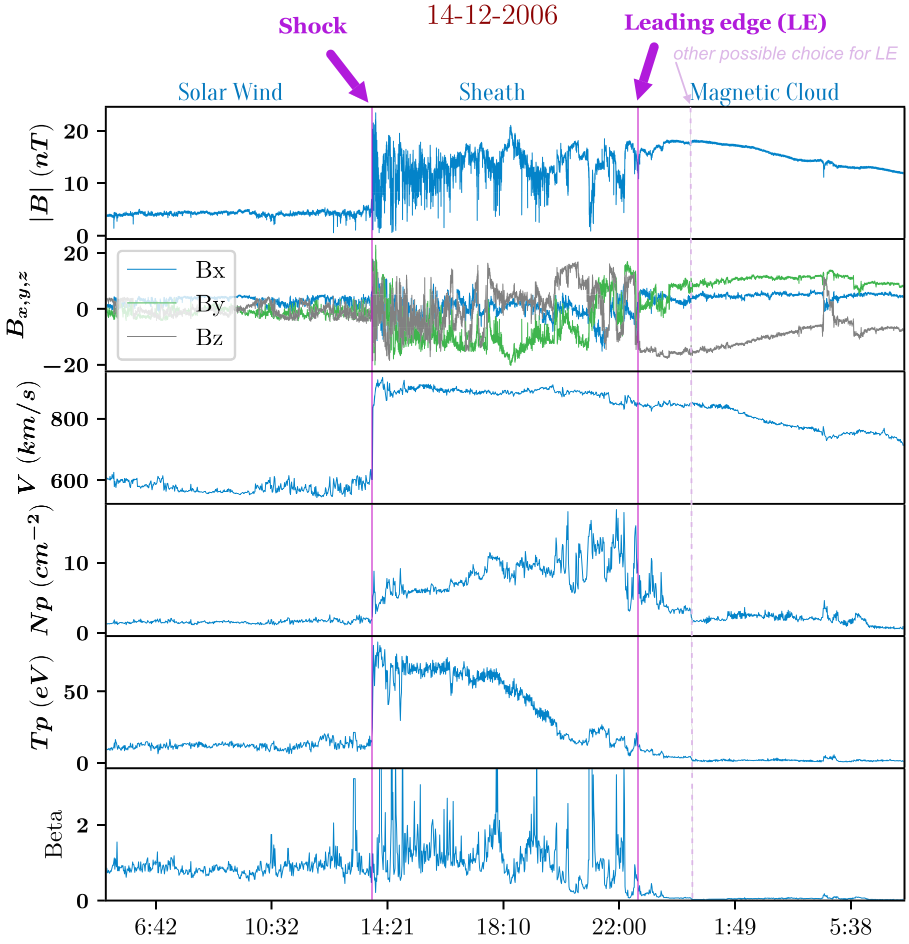

Figure 1. Observation from ACE spacecraft of a typical magnetic cloud event, centered on the sheath. From top to bottom are $|B|$ the amplitude of the magnetic field, $B_{x,y,z}$ its components, V the bulk flow velocity, N_p the proton density, T_p the proton temperature, and the plasma Beta. On this plot, and for all subsequent analysis of this event: the solar wind region spans from 14 December 2006 5:04 UT to 14 December 2006 14:14 UT, the sheath region spans from 14 December 2006 14:14 UT to 22:52 UT and the magnetic cloud region spans from 14 December 2006 22:52 UT to 15 December 2006 7:25 UT. Vertical purple bars separate the three different regions of the event, from left to right: the solar wind, the sheath, and the magnetic cloud. The dashed vertical bar shows another possible choice for the leading edge.

In the present paper we aim at characterizing the turbulence in the sheaths of magnetic clouds by considering the following questions:

- How does the spectral content of sheaths differ from the ones of the solar wind and magnetic clouds?
- What are the main parameters influencing the fluctuations in sheaths?

The following paper is organized as follows: In section 2, we present the list of events used as well as the means to retrieve the corresponding data. In section 3, we present a method to characterize the turbulence in sheaths, before showing in section 4 how the fluctuations in sheaths differ from those in their surrounding media. Section 5 draws a picture of what the fluctuations depend on and we conclude with section 6.

2. Data Description

In order to avoid mistaking phenomena arising from the sheaths themselves for phenomena arising from its interaction with another preceding event, it is important to study well-identified and isolated (far from any other event) magnetic cloud-driven sheaths. Masías-Meza et al. (2016) built a list containing 44 such events that we used for the present study. We used the data from the ACE spacecraft and in particular from the Magnetic Field Experiment with a 1-s resolution measurement of the magnetic field components and from the Solar Wind Electron Proton Alpha Monitor (SWEPAM), with a 64-s resolution measurement of the velocity, density, and temperature (Stone et al., 1998). Both can be downloaded from the website (https://cdaweb.sci.gsfc.nasa.gov/index.html/). Two of the events ("18 March 2002" and "23 March 2002") from Table A.1 of Masías-Meza et al. (2016) do not have available data at 1-s resolution and have therefore been excluded from the present study.

Figure 1 shows an example of a typical event in the list. After a period of quiet solar wind the satellite encounters a shock, which marks the beginning of a highly turbulent sheath with high magnetic field amplitude, high velocity, high density, and high temperature. The time of the shock is easily identifiable by the simultaneous jumps of several quantities: We used the date and time given by the IPshock Database (http://ipshocks.fi/) when the shock is referenced there, and we defined it manually when not. The sheath itself is followed by a smoothly rotating magnetic field at a low plasma beta: the magnetic cloud. The transition between the sheath and magnetic cloud is called the leading edge of the magnetic cloud. The time of the leading edge of the magnetic cloud is somewhat more difficult to define, possibly controversial. It depends on criteria such as drop of the ratio of the plasma pressure to the magnetic pressure β, drop of the proton temperature T_p, beginning of a smooth rotation of the magnetic field B, and drop of the proton density N_p. Ambiguities arise when some of these criteria are not satisfied at the same moment. In these cases, we decided on a time and date for the leading edge ourselves. Because, as illustrated in Figure 1, the area surrounding the leading edge is not always clearly belonging to either the sheath or the magnetic cloud, we excluded ambiguous areas and focused only on zones unambiguously belonging to one or the other.

This led, for every event, to the definition of three *regions*: solar wind (SW), sheath (Sh) between the two solid lines, and magnetic cloud (MC) after the dashed line as illustrated in Figure 1.

As can be seen in Figure 1, we arbitrarily decided to analyze the data on a duration that depends on the length of the sheath: If T_{Sh} is the duration of the sheath, we analyzed the data for a total time of $3 \times T_{\mathrm{Sh}}$, with the solar wind in the first third, the sheath being placed in the middle, and the magnetic cloud in the last third. The same choice was made for every event.

3. Method: Analysis of a Single Event

3.1. Definition of the Fluctuations

We defined the fluctuations of the magnetic field as the variation around quantities averaged with the help of a sliding window (similarly to Tao et al., 2015) of $T_W = 15$-min length. The duration of the window has been chosen to follow the slower variations of the magnetic field while not filtering the faster ones:

$$\begin{aligned} \langle B_{x,y,z}\rangle(t) &= \frac{1}{T_W}\int_{t-T_W/2}^{t+T_W/2} B_{x,y,z}(\tau)\mathrm{d}\tau \\ \delta B_{x,y,z}(t) &= B_{x,y,z}(t) - \langle B_{x,y,z}\rangle(t) \end{aligned} \tag{1}$$

A good indicator of the nature of the fluctuations is the difference of behavior between fluctuations of the component of B, which is aligned with the average magnetic field $B_0 =< B >$, hereafter $\delta B_{||}$, and the fluctuations of the components that are perpendicular to B_0, hereafter $\delta B_{\perp}$.

In order to define those two quantities, we produced a moving orthonormal frame as described in equation 2:

$$\begin{aligned} \boldsymbol{b}_0 &= \frac{\boldsymbol{B}_0}{|\boldsymbol{B}_0|} \\ \boldsymbol{b}_1 &= \frac{\boldsymbol{e}_j \times \boldsymbol{B}_0}{|\boldsymbol{e}_j \times \boldsymbol{B}_0|} \\ \boldsymbol{b}_2 &= \frac{\boldsymbol{B}_0 \times (\boldsymbol{e}_j \times \boldsymbol{B}_0)}{|\boldsymbol{B}_0 \times (\boldsymbol{e}_j \times \boldsymbol{B}_0)|} \end{aligned} \tag{2}$$

In equation (2), for every region, e_j is automatically chosen from $[e_x, e_y, e_z]$ to maximize the quantity $||e_j \times B_0||$. Indeed, if the angle between e_j and B_0 is too small, the definition of the frame may be prone to error or high variability from a time step to the next (Duff et al., 2017). e_j itself is not perpendicular to B_0.

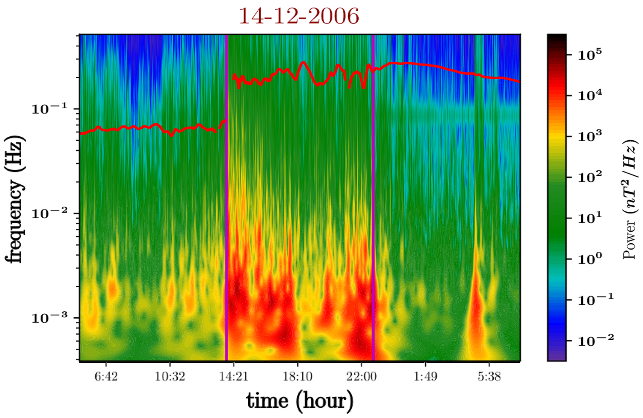

Figure 2. Morlet wavelets of the 14 December 2006 event. The vertical axis represents the frequency of waves. The horizontal axis represents the time. The color palette represents the amount of energy per unit volume and per unit frequency of the magnetic field: blue and green represent "low" energy content, while yellow and shades of red represent "high" energy content. Toward the top of the figure, the red line represents the gyrofrequency of protons $f_c = \omega_c/2\pi$ based on the value of B_0.

This comoving frame allowed us to define the parallel and perpendicular fluctuations by simple projections of δB on its axes:

$$\begin{aligned} \delta B_{||} &= (\boldsymbol{B} - \boldsymbol{B}_0) \cdot \boldsymbol{b}_0 \\ \delta B_{\perp 1} &= (\boldsymbol{B} - \boldsymbol{B}_0) \cdot \boldsymbol{b}_1 \\ \delta B_{\perp 2} &= (\boldsymbol{B} - \boldsymbol{B}_0) \cdot \boldsymbol{b}_2 \end{aligned} \tag{3}$$

3.2. Spectra

We applied the previous steps to the "14 December 2006" event shown in Figure 1 and used it to define the tools used in our statistical study.

Following the idea presented in de Wit et al. (2013), we used a Morlet wavelet transform (Torrence & Compo, 1998) to produce the spectra of $\delta B_{||}$, $\delta B_{\perp 1}$, and $\delta B_{\perp 2}$, respectively noted $\mathcal{W}(\delta B_{||})$, $\mathcal{W}(\delta B_{\perp 1})$ and $\mathcal{W}(\delta B_{\perp 2})$. We then defined $\mathcal{W}_{||} = \mathcal{W}(\delta B_{||})$, and $\mathcal{W}_{\perp} = \mathcal{W}(\delta B_{\perp 1}) + \mathcal{W}(\delta B_{\perp 2})$ as well as $\mathcal{W} = \mathcal{W}_{||} + \mathcal{W}_{\perp}$, which represents the total energy per unit volume and unit frequency of the fluctuations of B.

Figure 2 represents the temporal evolution of $\mathcal{W}(f, t)$ for the same event as in Figure 1 ("14 December 2006"): The horizontal axis represents the time, the vertical axis represents the frequency, and the colors represent the intensity $\mathcal{W}$ of the fluctuations, (J·m^{-3} ·Hz^{-1}). We can see that the sheath region corresponds with a rise of $\mathcal{W}$. The green horizontal bar near 10^{-1} Hz is due to the satellite spin (Stone et al., 1998). As we averaged out the low frequencies through equation (1), we can see that the fluctuation spectra contains low power under 10^{-3} Hz. Then, there are two natural limits for the frequencies:

- A maximal limit to exclude the spin of the satellite $f_{\text{max}} = 5 \cdot 10^{-2}$ Hz $< f_{\text{spin}}$.
- And a lower limit which comes from the definition of the mean field B_0: $f_{\text{min}} = 2/(15\text{min.}) = 3 \cdot 10^{-3}$ Hz $> 2/T_W$. The factor 2 here was arbitrarily chosen to keep the analysis away from mathematical artifacts due to the edges of the sliding window, which arise below and around $1/T_W$.

Outside of these limits, the spectrum was not considered. Those limits also correspond to what is usually called the ULF bandwidth, which is relevant to interplanetary shocks (Kajdič et al., 2012), to the study of sheaths (Kilpua et al., 2013), and to the interaction of the solar wind with the terrestrial magnetosphere (Alimaganbetov & Streltsov, 2018; Kepko et al., 2002; Osmane et al., 2015). One can also see, at the shock, approximately at 14:21, that every frequency presents a heightened $\mathcal{W}$. The same thing can be seen around 5:38 when a small structure is encountered in the magnetic cloud. One problem with our definition of fluctuations (equation (1)) is that it does not apply well to jumps, such as shocks, large discontinuities, or small-scale structures. The Morlet transform is also particularly susceptible to these sudden changes and they should therefore be avoided in the analysis.

Figure 3 represents the power spectrum density ($\mathcal{PSD}$) of the magnetic fluctuations and their components, by integration on time of $\mathcal{W}(f, t)$ over time in each different region (solar wind, sheath, magnetic cloud), excluding the immediate surroundings of the shock and the leading edge. The power spectrum density of the parallel fluctuations $\mathcal{PSD}_{||}$ is represented in green, of the perpendicular fluctuations $\mathcal{PSD}_{\perp}$ in gray and the total in blue.

$$\mathcal{PSD}_{\perp,||}(f) = \frac{1}{T_{\text{region}}} \int_{T_{\text{region}}} \mathcal{W}_{\perp,||}(t, f)\,\mathrm{d}t \tag{4}$$

In Figure 3, we can see two clear trends. First, the fluctuation spectrum has much more power in the sheath than in the other regions investigated. We also note that the fluctuations in the solar wind preceding the sheath and in the following magnetic cloud have, on average, a similar power. And second, the gap between the green and the gray dotted lines is smaller in the middle panel than in the first one, which suggests more isotropic (or compressible) fluctuations in the sheath. On the other hand, the gap is very large in the right panel, the parallel power being so low that the total power is almost equal to the perpendicular power: The fluctuations in the magnetic cloud are very anisotropic (or almost incompressible).

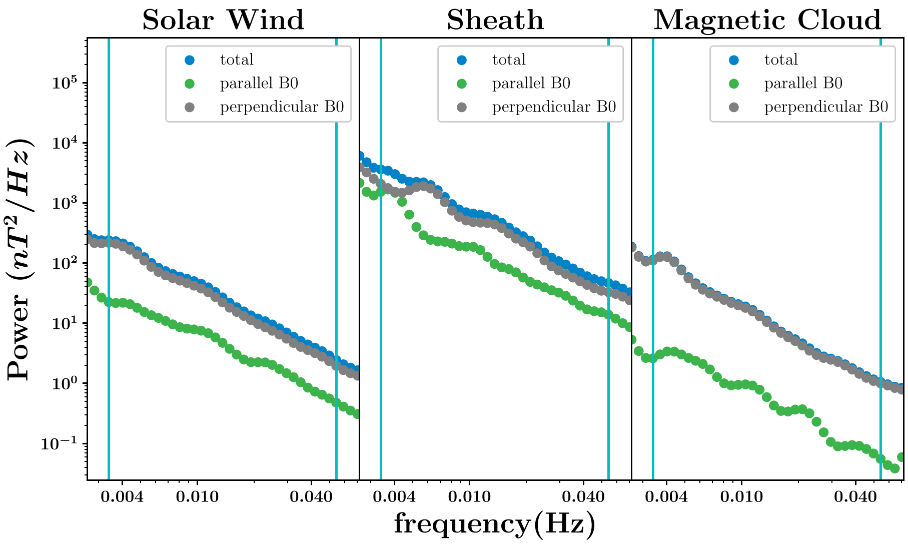

Figure 3. Spectrum of the fluctuations of the magnetic field (or power spectrum density) on each region of the 14 December 2006 event. The vertical axis represents the energy per unit volume and per unit frequency, and the horizontal axis represents the frequency. In blue is the total energy $\mathcal{PSD}$, in gray the energy of the fluctuations perpendicular to the mean magnetic field $\mathcal{PSD}_\perp$, and in green is the energy of the fluctuations parallel to the mean magnetic field $\mathcal{PSD}_{||}$. The cyan vertical bars mark the frequency limits inside of which the analysis was performed. A blue dashed line represents a linear fit of the spectrum between the frequency limits; the corresponding slope is reported in the upper-right corner.

3.3. Definition of Relevant Zones

As seen in the previous section 3.2, the Morlet transform, along with our definition of the fluctuations, does not apply well to jumps. The first consequence is that we did not analyze the data directly close to the shock or the leading edge of the magnetic cloud. Sheaths are made of a mixture of waves and small-scale structures, which occasionally form strong jumps. The second consequence, therefore, is that the best we could do was to avoid any visible and rapid jumps. For example, we show in Figure 4a possible selection of zones avoiding such jumps in the sheath of the “14 December 2006” event. The first zone, in red, starts slightly away from the shock and stops just before a rapid drop of B_z. The second zone, in pale blue, starts after this drop and stops before a large rise of both B_y and B_z. The third zone, in yellow, stops just before a small area where the amplitude of the mean magnetic field $|B_0|$ (in orange) does not follow the rapidly varying magnetic field $|B|$ (in blue). Lastly, the fourth zone, in blue, stops before a series of large variations of all the components of B. This choice allowed for a better analysis of the fluctuations without the inclusion of drastic changes.

Also, another type of problem is that some events include some unusual features: For example, there can be more organized structures within the sheath, some of them resembling flux ropes. The source for this is currently not understood. Likewise, short, highly turbulent zones can sometimes be found in a magnetic cloud, or a small area in the solar wind may occasionally be heavily perturbed by the shock. The definition of zones allowed us to exclude such unusual features from our analysis. No solution has been found yet to automate this choice of zones, which had to be made manually for every region of every considered event.

It is also possible to perform the analysis without introducing zones and therefore including every discontinuities and unusual features in the calculations. Tests show that this does not affect the general trends for the power and anisotropy but that the selection of zones enables a better separation of the different regions, which in turn improves their characterization. For example, without the selection of zones, the analysis of a magnetic cloud containing a short but strong discontinuity would yield values intermediate between a magnetic cloud and a sheath, and the same goes for a sheath including a small flux rope.

3.4. Definition of the Power and the Anisotropy of the Fluctuations

We used the wavelets analysis described in the section 3.2 on every zone, and, from it, we computed two quantities: The power P_{zone} and the anisotropy A_{zone}. The power P_{zone} represents the average quantity of

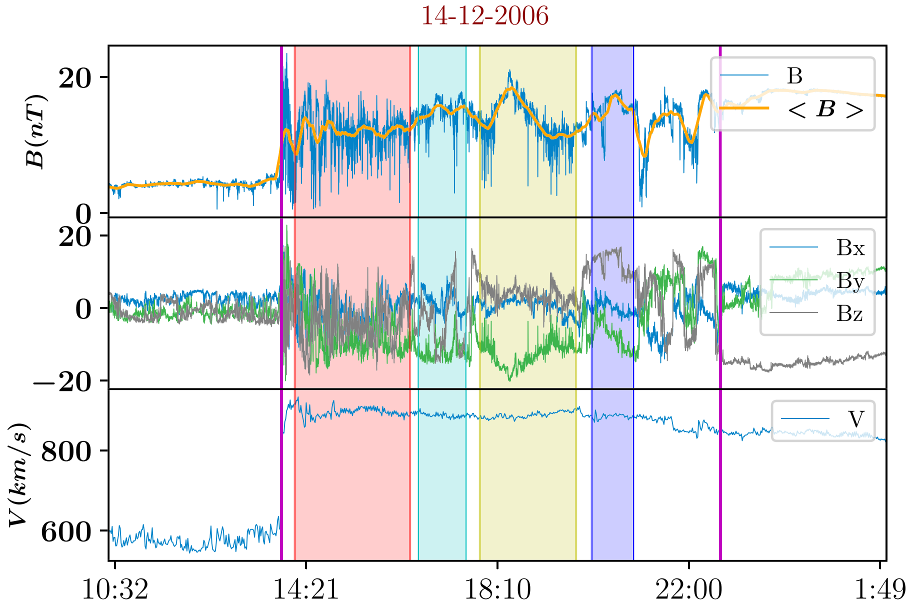

Figure 4. Here is a zoom on the sheath of the 14 December 2006 event, the sheath is delimited by the two purple vertical bars. Four different zones (in red, blue, yellow, and purple) were chosen manually to avoid jumps in the data.

energy per unit volume found in a zone between frequencies f_{min} and f_{max} and is defined as follows:

$$P_{\text{zone}\quad(\perp,||)} = \frac{1}{T_{\text{zone}}} \int_{T_{\text{zone}}} \int_{f_{\min}}^{f_{\max}} \mathcal{W}_{(\perp,||)}(t,f)\,\mathrm{d}f\,\mathrm{d}t \tag{5}$$

The anisotropy A measures the amount by which the measurements differ from the isotropic case:

$$A_{\text{zone}} = \frac{P_{\text{zone}\perp}}{2 \cdot P_{\text{zone}||}} \tag{6}$$

The factor 2 at the denominator allows $A = 1$ to represent the isotropic case, and $A > 1$ to represent stronger perpendicular fluctuations than parallel fluctuations.

Each region contains a few zones, and each of these are henceforth characterized by two scalar quantities: P_{zone} and A_{zone}. For each region we defined P_{region} and A_{region} as an average on the zones in that region:

$$\begin{aligned} P_{\text{region}} &= \frac{\sum_{[\text{zone}\in\text{region}]}(T_{\text{zone}} \cdot P_{\text{zone}})}{\sum_{[\text{zone}\in\text{region}]} T_{\text{zone}}} \\ A_{\text{region}} &= \frac{\sum_{[\text{zone}\in\text{region}]}(T_{\text{zone}} \cdot A_{\text{zone}})}{\sum_{[\text{zone}\in\text{region}]} T_{\text{zone}}} \end{aligned} \tag{7}$$

These quantities, defined for each region, are noted accordingly (P_{SW}, P_{Sh}, P_{MC}, A_{SW}, A_{Sh}, and A_{MC}). The results of this analysis for the "14 December 2006" event are given in Table 1.

Table 1 is a concise and more quantitative way of representing the already mentioned properties of the fluctuations in the "14 December 2006" event: Compared to the solar wind, there is an augmentation of the

Table 1
Power and Anisotropy of the Different Regions of the "14 December 2006" Event

P_{SW}	P_{Sh}	P_{MC}	
0.7	1.1	0.1	(nT^2)
A_{SW}	A_{Sh}	A_{MC}	
5.1	1.5	85.3	

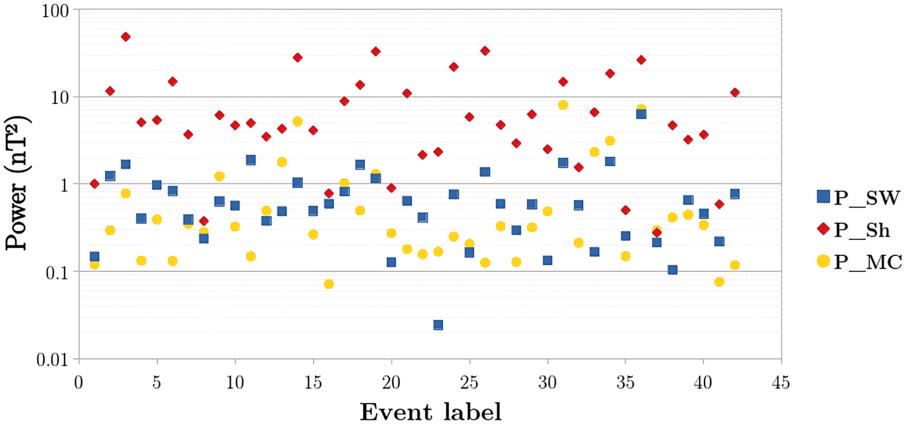

Figure 5. Every event is labeled by a number from 1 to 42 represented on the horizontal axis. The vertical axis is the value of the power P, which is the average quantity of energy per unit volume for a region of the event. The values of P vary between 0.01 and 100 nT^2. The power of the fluctuations P_{SW} in the solar wind preceding the sheath is represented in blue, P_{Sh} in the sheath in red, and P_{MC} in the magnetic cloud in yellow.

power in the sheath ($P_{\mathrm{SW}} < P_{\mathrm{Sh}}$) as well as a decrease of the anisotropy ($A_{\mathrm{SW}} > A_{\mathrm{Sh}}$). The fluctuations have a totally opposite behavior in the magnetic cloud, where their power drops ($P_{\mathrm{MC}} < P_{\mathrm{Sh}}$), and their anisotropy increases dramatically ($A_{\mathrm{MC}} \gg A_{\mathrm{Sh}}, A_{\mathrm{SW}}$).

4. Power and Anisotropy in the 42 Events of Masías-Meza Et Al. (2016)

4.1. Power

Figure 5 presents, on the vertical axis, the values of P_{SW} (blue squares), P_{Sh} (red diamonds), and P_{MC} (yellow dots) for every event, labeled from 1 to 42 on the horizontal axis. We can observe that the values for the magnetic clouds (P_{MC}) and the solar wind (P_{SW}) are spread over approximately 1 order of magnitude, while they approximately span 2 orders of magnitude in the sheaths (P_{Sh}). We see a clear trend that the power of the fluctuations in the sheaths is higher by approximately an order of magnitude than in the other parts of the events. The average and standard deviation of the results are provided in Table 2.

In Table 2 we see that the distributions are quite spread, but there is a very clear trend that the sheaths contain about an order of magnitude more power in their fluctuations than the other regions. Solar wind and magnetic clouds seem to contain a similar range of power, which may seem quite surprising. We have no clear explanation but one possibility could be the following: when looking at Figure 1, we see indeed less fluctuations in the magnetic cloud compared with the solar wind, but this is mostly due to the high value of the mean magnetic field in the cloud, which may let us think that the fluctuations are smaller, by visual comparison. Also, it is quite common to plot or talk about the relative strength of fluctuations $\mathrm{d}B/B_0$, which is indeed lower in magnetic clouds.

4.2. Anisotropy

Figure 6 presents, on the vertical axis, the values of A_{SW} (blue squares), A_{Sh} (red diamonds), and A_{MC} (yellow dots) for every event, labeled from 1 to 42 on the horizontal axis. Values of the anisotropy, range from 1 (*isotropic case*) to almost 91 (*very anisotropic case*). The values for each region (solar wind, sheath, or magnetic cloud) roughly spread over an order of magnitude. We can see that the sheaths tend to have a lower anisotropy (red diamonds), ranging from ~1 to 13, than the solar wind preceding them (blue squares), ranging from ~4 to 20. The magnetic clouds (yellow dots) tend to have a much higher anisotropy, with A_{MC} starting from 8 and reaching up to 91. Interestingly, some of the intervals of the solar wind (cyan stars) with higher values of A actually contain, upon close inspection, flux ropes. Most of these flux ropes are quite

Table 2
Average Power of the Magnetic Field Fluctuations and Its Standard Deviation in the Different Parts of the 42 Events in Square Nanoteslas

P_{SW}	P_{Sh}	P_{MC}	Unit
0.8 ± 1.0	9.3 ± 10.8	1.0 ± 1.8	(nT^2)

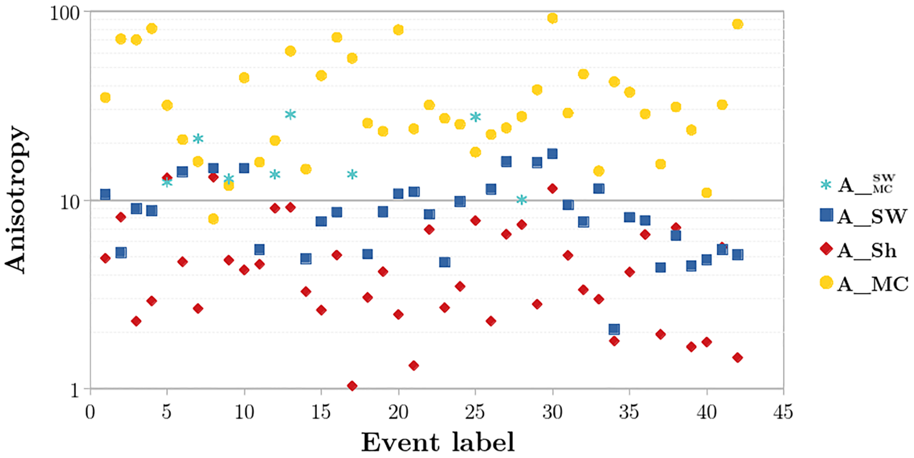

Figure 6. Every event is labeled by a number from 1 to 42 represented on the horizontal axis. The vertical axis is the value of A, the anisotropy of the fluctuations of the magnetic field. In blue we represent A in the solar wind preceding the sheath, in red we represent the value of A in the sheath, and in yellow we represent A in the magnetic cloud. In light blue, we represented the cases where the solar wind preceding the sheath was, in fact, a flux rope.

small and were understandably not identified as magnetic clouds, and one of them was an actual magnetic cloud (Case 30, in Masías-Meza et al.'s, 2016, list).

The results are summarized in Table 3, which shows that despite quite spread distributions, there is a very clear trend that the fluctuations in the sheath are much more isotropic than in the solar wind, whereas the fluctuations in the magnetic cloud are much more anisotropic than in any other region. We also provide the values of the compressibility, defined as the ratio of the power of the parallel fluctuations over the total power $C = \frac{P_{||}}{P}$, and computed using the same method as the power and anisotropy. The compressibility is a commonly used quantity that represents the same physics as the anisotropy. Indeed, because almost all the power of the fluctuations is contained in the perpendicular fluctuations, the compressibility and anisotropy have almost inverse behaviors. Therefore, the last results show that the plasma in sheaths is much more compressible than in the preceding solar wind and even more so than in the following magnetic cloud.

Our results for the solar wind and magnetic clouds match those of Leamon et al. (1998), who studied the power and the anisotropy of the fluctuations of a single event, but differ for the sheath. The differences noted for the sheath are easy to understand: First, Leamon et al. (1998) studied a single event, which may well have been a sheath with a relatively high anisotropy but still contained within the standard deviation given in Table 3. Second, they were not particularly interested in the sheath and used only a few fixed 1-hr-long windows to describe it: As seen in section 3.3 of the present paper, this is likely to be insufficient to study the highly complex fluctuations of the sheath. Another paper (Hu et al., 2013) reported variations from upstream to downstream of interplanetary shocks that are very similar to ours: Lower anisotropy and increased fluctuation power after the shock were found.

5. Correlations Between Sheaths' Fluctuations and Events' Main Parameters

So far in this paper, we chose two main parameters to characterize the fluctuations: the anisotropy and power, A and P. In Figure 7, every event is represented by a red dot in the (A_{Sh}, P_{Sh}) plane. We can see that

Table 3
Anisotropy and Compressibility: Average Value and Standard Deviation in the Different Parts of the Events

A_{SW}	A_{Sh}	A_{MC}
10 ± 6	5 ± 3	36 ± 23
C_{SW}	C_{Sh}	C_{MC}
0.07 ± 0.04	0.15 ± 0.08	0.02 ± 0.01

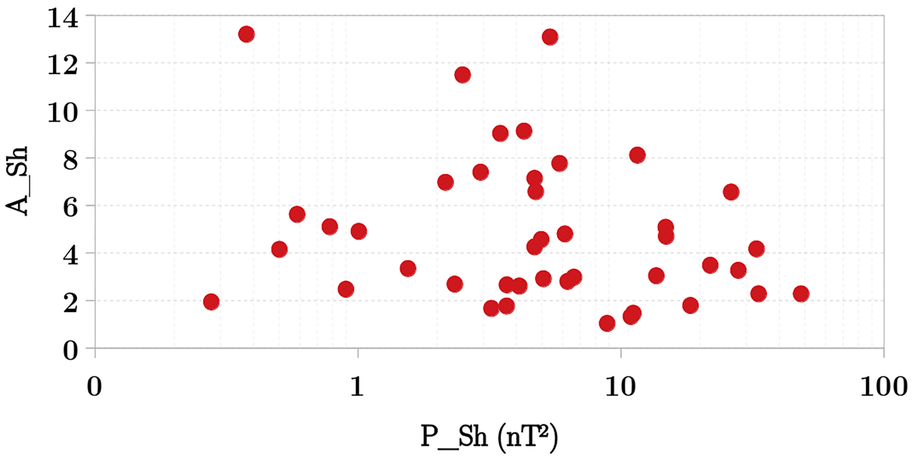

Figure 7. For every event, a red dot is placed on the diagram shown above with, on the vertical axis the anisotropy in the sheath and on the horizontal axis the power in the sheath.

the cloud of red dots is not forming any clear pattern: The values of A_{Sh} vary apparently randomly between 1 and 13 regardless of the value of P_{Sh}. In other words, the anisotropy does not depend on the power and therefore is not caused by a strong P. This test is important because it proves the nonredundancy of the chosen parameters P and A to characterize the fluctuations.

In the previous section, we have evidenced two main characteristics of the fluctuations in sheaths: high power P_{Sh} and low anisotropy A_{Sh}. We now analyze the dependency of the sheath's fluctuations (as represented by their power P_{Sh} and anisotropy A_{Sh}) on the surrounding media. Proxies for the surrounding media of the sheaths are (see definitions in Appendix A):

- parameters characterizing the solar wind: plasma density N_{SW}, magnetic field magnitude B_{SW}, ion velocity V_{SW}, Mach number in the solar wind M_A^{SW}, dynamic pressure in the solar wind $P_{\text{dyn}}^{\text{SW}}$, state of the fluctuations described by $\{P_{\text{SW}}, A_{\text{SW}}\}$
- parameters characterizing the shock: Mach number M_A, the ratio of thermal and magnetic pressure in the solar wind β_{up}, and the angle between the magnetic field in the solar wind and the shock's normal θ_{Bn}
- parameters characterizing the magnetic cloud: N_{MC}, B_{MC}, V_{MC}, M_A^{MC}, $P_{\text{dyn}}^{\text{MC}}$, $\{P_{\text{MC}}, A_{\text{MC}}\}$

Note that P_{SW}, A_{SW}, P_{MC}, and A_{MC} were computed on the solar wind and magnetic cloud regions, while all the other “SW” and “MC” parameters were computed on the “up” and “leading edge” interval as defined in Appendix A.

Among the different combinations that we tested, we show only the correlations which we deemed interesting. No clear conclusion could be extracted from the others.

In Figure 8 we compare the fluctuations in the sheaths with the fluctuations in the solar wind that precedes them, using A_{SW} and P_{SW} as proxies for the state of the fluctuations in the solar wind. We can see that the anisotropy in the sheath does not depend on the fluctuations already present in the solar wind: Indeed, in panels (a) and (c), we can see that both solar wind anisotropy and power can correspond to any value of the anisotropy in the sheath. This is also the case for the power in the sheath, which mostly does not seem to depend on A_{SW}. Indeed, panel (b) shows that high values of P_{Sh} are not reached when A_{SW} is high but only for a hardly significant number of cases, whereas values of P_{Sh} span the whole range when A_{SW} is low. The correlation between P_{Sh} and P_{SW}, in panel (d) is, on the other hand, stronger. Indeed, a linear fit roughly indicates a significant link between P_{Sh} and P_{SW}, while also making clear that P_{SW} is not the only factor at play (regression coefficient $R^2 = 0.42$). This may indicate that the power of the fluctuations in the solar wind has an effect on the fluctuations in the sheath. It is therefore suggested that highly turbulent sheaths are preceded by highly turbulent solar wind.

We now concentrate on the effect of the shock's parameters on the sheath's fluctuations. Indeed, the shock, by dissipating energy, is a priori the main reason for the existence of the turbulent sheath (Kataoka et al., 2005). We now analyze (Figure 9) the sheath anisotropy and power as a function of the shock's main

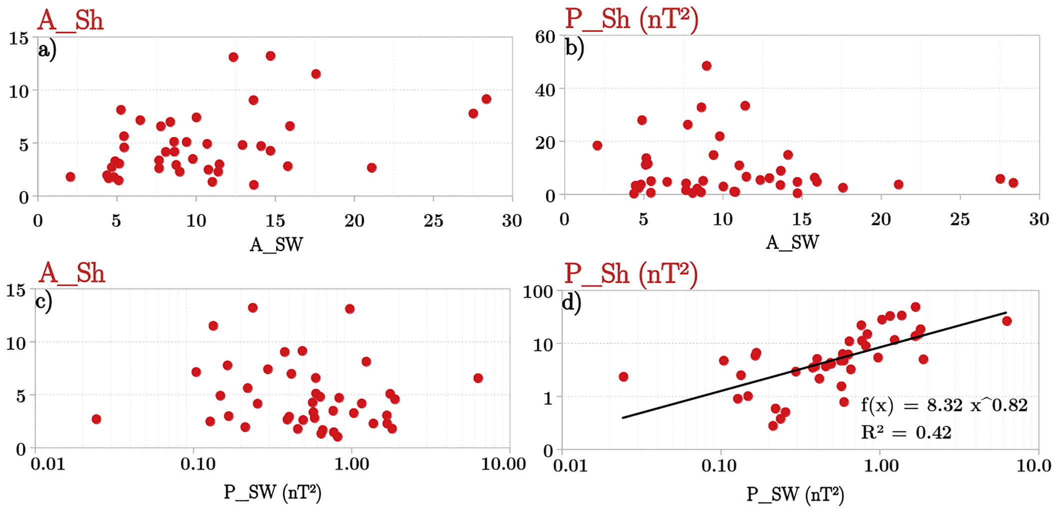

Figure 8. The four panels represent the state of the fluctuations in the sheath ($P_{\mathrm{Sh}}, A_{\mathrm{Sh}}$) versus the state the fluctuations in the solar wind ($P_{\mathrm{SW}}, A_{\mathrm{SW}}$) for every event. (a) A_{Sh} versus A_{SW}. (b) P_{Sh} versus A_{SW}. (c) A_{Sh} versus P_{SW}. (d) P_{Sh} versus P_{SW}, a linear regression is made (black line).

parameters M_A, β_{up}, and θ_{Bn} (see appendix for definitions). In Figure 9a we observe that for low values of the Alfvén Mach number ($M_A < 4$ or so) A_{Sh} can take on any value. The values of A_{Sh} seem to be more constrained at higher values of M_A. In panel (b), we see that for $M_A < 4$ or so, most P_{Sh} do not reach higher values that 10 nT^2. At higher values of M_A, the power tends to be high, which is expected due to the energy

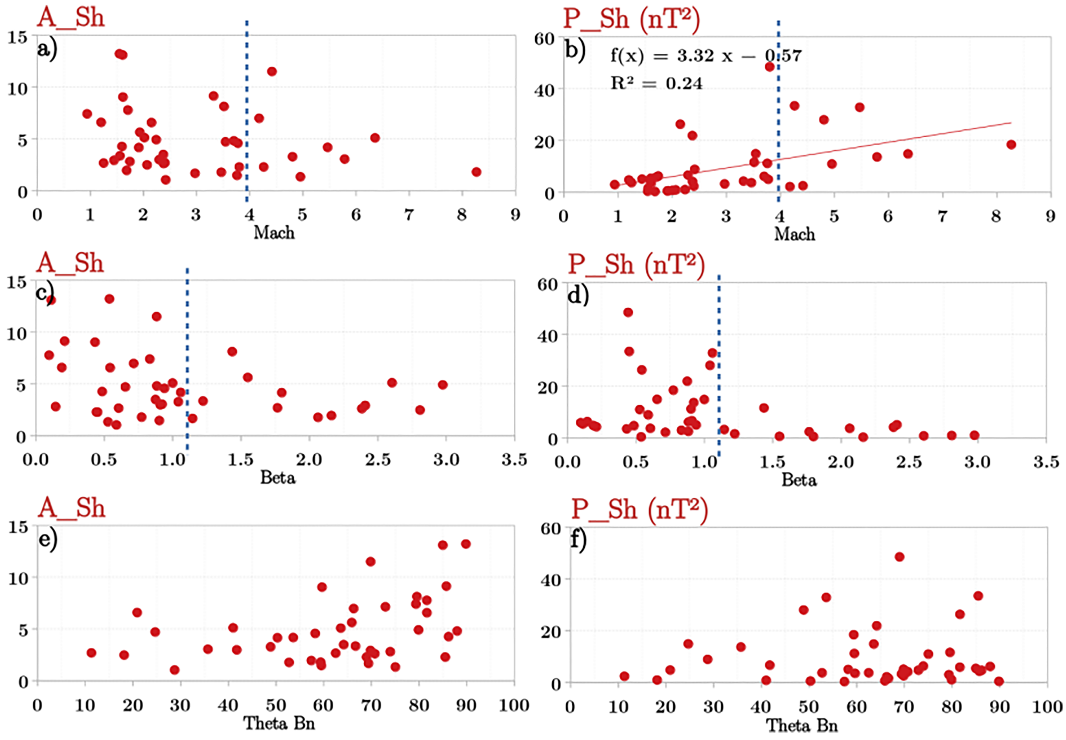

Figure 9. The two upper panels (a, b) represent the state of the fluctuations in the sheath against the shock's Mach number with a linear fit in panel (b), the two middle panels (c, d) represent the fluctuations in the sheath against the Beta upstream of the shock, and the two panels on the bottom (e, f) represent the fluctuations against the θ_{Bn}. Blue dashed vertical bars are visual aids showing a rough threshold of M_A and β.

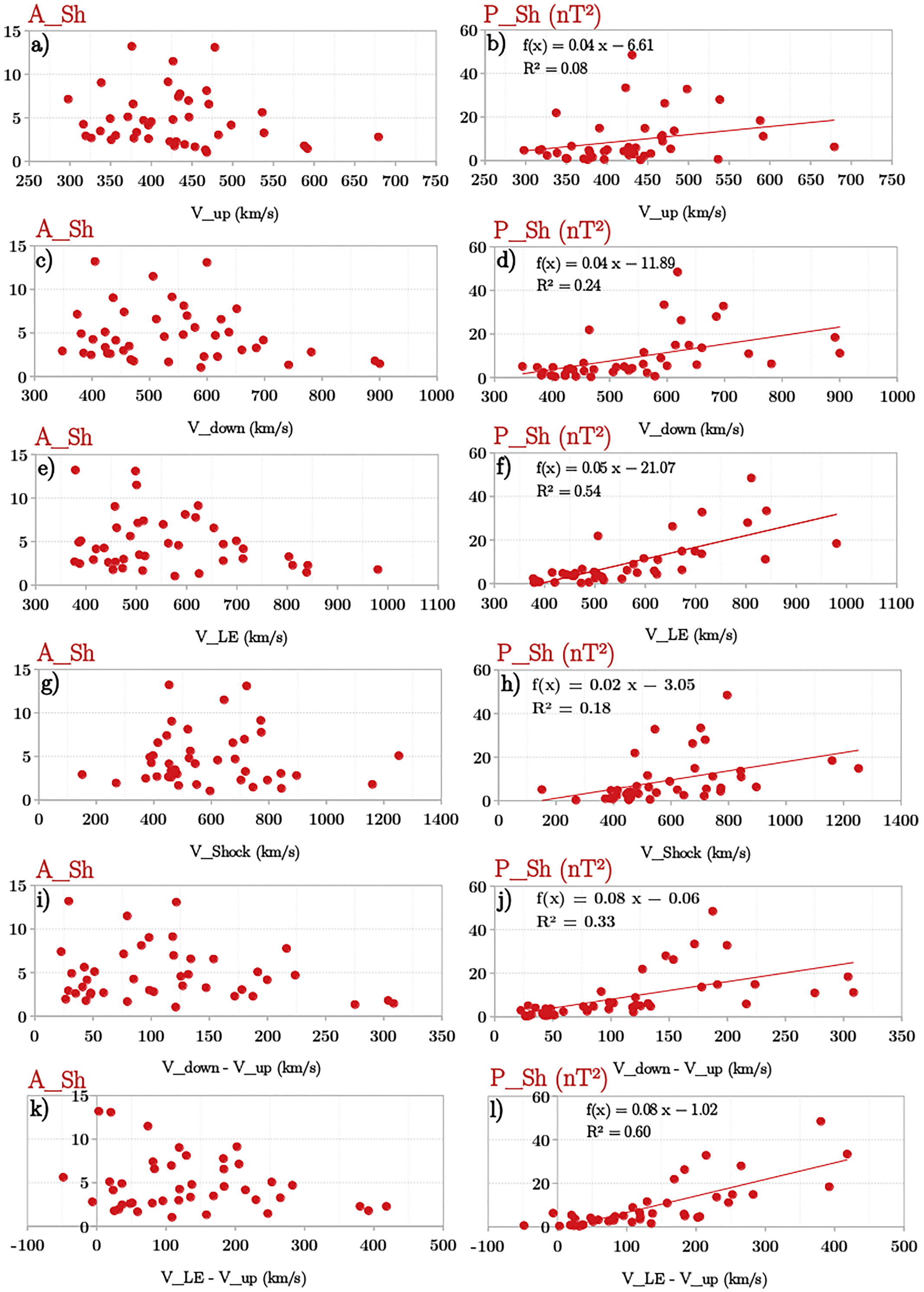

Figure 10. (a–l) The 12 panels represent the anistropy A_{Sh} and the power P_{Sh} of the fluctuations in the sheath plotted against different velocities. From top to bottom, those velocities are the velocity upstream of the shock, the velocity just downstream of the shock, the velocity of the leading edge of the magnetic cloud, the velocity of the shock, the difference between the velocities downstream and upstream of the shock, and the difference between the velocity of the leading edge and the velocity upstream of the shock.

dissipated by the shock, and the anisotropy tends to be low. We can see, though, that the regression coefficient of the linear fit in panel (b) is—maybe surprisingly—quite low, indicating that the shock's Mach number is not the main factor in producing the magnetic fluctuations in the sheath. Rather, it seems that the value $M_A \sim 4$ serves as a threshold for the state of the fluctuations downstream of the shock. Looking at panels (c) and (d), one can see that for $\beta_{\mathrm{up}} > 1.1$ or so are associated with a smaller range of values for both A_{Sh} and P_{Sh}, whereas almost any type of fluctuations can be found at $\beta_{\mathrm{up}} < 1.1$ or so. A possible interpretation is that high β_{up} events are plasmas dominated by the physics of thermal agitation, which is isotropic and potentially containing only weak magnetic fields, whereas low β_{up} events are dominated by the magnetic field, with potentially opposite consequences. Similarly, the range of values accessible to A_{Sh} and P_{Sh} seems to be constrained by θ_{Bn}. For $\theta_{Bn} < 45°$ (indicative of quasi-parallel shocks) there is a limited number of events but the trend shows that $A_{\mathrm{Sh}} < 7$ and $P_{\mathrm{Sh}} < 15$ nT^2. Whereas for higher values of θ_{Bn} (indicative of quasi-perpendicular shocks), A_{Sh} and P_{Sh} explore the whole range of values. The fact that quasi-parallel shocks show a relatively low level of turbulence in the sheath is rather surprising (Treumann, 2009) but may be understood by a low compression by the shock of the magnetic field present in the solar wind due to the geometry.

We analyze in Figure 10 the dependency of the sheath fluctuations on different velocities relevant to the events' description (see the appendix). Indeed, the velocity of the event admits several definitions: the velocity of the solar wind upstream of the shock V_{up}, the velocity in the sheath downstream of the shock V_{down}, the velocity in the beginning of the magnetic cloud V_{LE}, and some combinations of the previous velocities: V_{shock}, $V_{\mathrm{down}} - V_{\mathrm{up}}$, $V_{\mathrm{LE}} - V_{\mathrm{up}}$. On all of the panels we can see a similar pattern: As the velocity increases, A_{Sh} can take on a smaller range of value, while P_{Sh} tends to increase. This pattern is similar to the one observed in Figure 9 with M_A, which is not surprising: The velocities can serve as a proxy for the energy to be dissipated by the shock. The only case where this trend is not observed is in panel g), where A_{Sh} seems to not be constrained by the value of V_{Shock}. It is quite clear on the two bottom panels (k) and (l) that $V_{\mathrm{LE}} - V_{\mathrm{up}}$ presents the best correlations with the anisotropy and power in the sheath. It is also worthy of note that the magnetic cloud's leading edge velocity V_{LE} (panels e and f) shows to be also quite a good predictor of the characteristics of the fluctuations.

6. Discussion and Conclusions

In this paper we focused on characterizing the magnetic fluctuations in magnetic clouds' sheaths, which are presently largely unknown. We started from a catalog of 44 isolated magnetic clouds, which are not disturbed by preceding and following events and identified by Masías-Meza et al. (2016). We mainly used 1-s magnetic field data from ACE near L1. We applied the Morlet wavelets transform on zones carefully defined in order to avoid jumps and unusual features in order to estimate the proper power spectral density of components parallel and perpendicular to the mean magnetic field. Two quantities were computed to characterize the fluctuations: The total power P and the anisotropy $A = \frac{P_\perp}{2P_{||}}$ (section 3). It was found that P reaches an average value of about 10 nT^2 in the sheaths, significantly exceeding, by a factor of about 10, the corresponding power in the preceding solar wind and the following magnetic cloud. Conversely, the anisotropy A takes its smallest values in sheaths, 5 on average and sometimes close to the isotropy level ($A = 1$), while it ranges around 10 in the preceding solar wind and reaches the largest values in magnetic clouds, 36 on average and sometimes almost 100 (section 4). In terms of the compressibility defined as $C = \frac{P_{||}}{P}$, the plasma in sheaths (~ 0.15 on average) is more compressible than in the preceding solar wind (~ 0.07) and much more than in almost incompressible magnetic clouds (~ 0.02). Section 5 reveals that there is no correlation between power and anisotropy in sheaths. Therefore, isotropy is not necessarily a consequence of powerful fluctuations. P and A can be regarded as independent quantities, which justifies the use of both to describe the characteristics of the fluctuations of sheaths.

We then estimated the role of the surrounding media on the characteristics of the fluctuations in sheaths. In line with Kilpua et al. (2013), our results show that one of the most significant parameters is the speed of the magnetic clouds: Larger powers are found in sheaths driven by faster magnetic clouds ($V_{\mathrm{LE}} > 750$ km/s), their velocity V_{LE} being estimated at their leading edge. The anisotropy in sheaths also reacts to the cloud velocity: It can take any value within a wide range from 1 to 14 in sheaths related to slow clouds, but it is confined in the range 1–5, that is, closer to isotropy when the sheaths are associated with fast clouds.

Conversely, we found no correlation of sheath characteristics with the amplitude of the cloud magnetic field. Finally, we can give the following interpretation of the increased power: The enhanced kinetic energy carried by fast magnetic clouds is dissipated in the sheath, giving rise through turbulent processes to small-scale structures, such as these powerful magnetic fluctuations observed in the sheaths.

Another significant parameter for the sheath fluctuations is the turbulence of the pristine solar wind upstream the shock. The magnetic fluctuation power in the sheaths increases with that of the solar wind, with the most powerful sheaths (typically above 10 nT^2) observed after intervals of highly turbulent solar wind (typically above 1 nT^2). Conversely, the sheath anisotropy does not seem to be affected by the solar wind power or anisotropy. Also parameters such as the solar wind density or dynamic pressure do not seem to play a role for sheath fluctuations. Therefore, it seems that a high level of magnetic fluctuations preexisting in the solar wind likely represents a good seed for turbulence in the sheath downstream of the shock.

We estimated the influence of the parameter β computed in the solar wind just upstream of the shock. Below a threshold value of about 1.1, the fluctuation power and anisotropy in the sheath cover a wide range of values without any obvious correlation. Above this threshold value of 1.1, both the sheath power and anisotropy reduce to weak values. In this case, the thermal energy exceeds the magnetic energy and therefore the magnetic fluctuations might become a secondary effect, possibly less powerful and guided than in presence of a strong magnetic field.

We also analyzed the dependency of the sheath's characteristics on the parameters of the shock. We found that both sheath power and anisotropy correlate only poorly with the shock velocity unlike the cloud velocity. The shock Mach number appears to be a more relevant parameter separating the events in two groups apart a threshold value around 4. Below it, the fluctuation power is low and the anisotropy varies over a wide range, while above it, the sheath fluctuations become more powerful and isotropic. Indeed, the shock's Alfvén Mach number acts as a proxy for the energy dissipation at the shock and plays, in this regard, a similar role to the cloud velocity. The shock angle also seems to play a role. Downstream of a quasi-perpendicular shock ($\theta_{Bn} > 45°$), both the fluctuation power and anisotropy in the sheaths cover a wide range of values. Downstream of quasi-parallel shocks ($\theta_{Bn} < 45°$), there is a trend toward more isotropy, which is expected. However, the fluctuation power goes down to low values, which is the opposite of what we find behind the terrestrial bow shock (Blanco-Cano et al., 2006; Du et al., 2008; Narita et al., 2006). The low number of quasi-parallel shocks in our set of data does not allow us to make any conclusion. The latter effect (low power) might be linked to a weaker compression of the interplanetary magnetic field in quasi-parallel than in quasi-perpendicular configurations, leading to weaker magnetic fields in the sheath and maybe to weaker fluctuations. Such an effect would require to be more deeply investigated.

In summary, in clouds' sheaths, the magnetic fluctuations which are the most powerful and the closest to isotropy are likely to be driven by fast magnetic clouds with typical velocities larger than 750 km/s as estimated at their leading edge, interacting with an already turbulent solar wind with a magnetic fluctuation power typically larger than 1 nT^2, and with a high Alfvén Mach number at shock (typically above 4). The relations with the shock angle and β upstream are a little more complex. Downstream of quasi-perpendicular shocks and high-β solar wind, the observed sheaths show a trend toward isotropy but also a weak fluctuation power, while downstream of quasi-perpendicular shocks and low-β solar wind, both fluctuation power and anisotropy cover a wide range of values.

Interestingly, Leamon et al. (1998) studied an ICME encountering an undisturbed, slow solar wind. The magnetic cloud in that paper has quite a low speed and a high beta prior to the sheath. Therefore, the sheath in Leamon et al. (1998) has all the ingredients to present a high anisotropy, and a low power, which is what the authors found.

In the case of the solar wind, it has been shown that fluctuations with large-amplitude and low anisotropy imply a good coupling of the solar wind with the magnetosphere (Jankovičvá et al., 2008). Our results suggest that turbulent sheaths preceding magnetic cloud present a high energy content of their fluctuations, as well as a low anisotropy, which may favor their geoeffectiveness.

Future observational work will be needed in order to further investigate the evolution of fluctuations inside the sheaths themselves. Indeed, it will be interesting to compare the evolution of the fluctuations of the

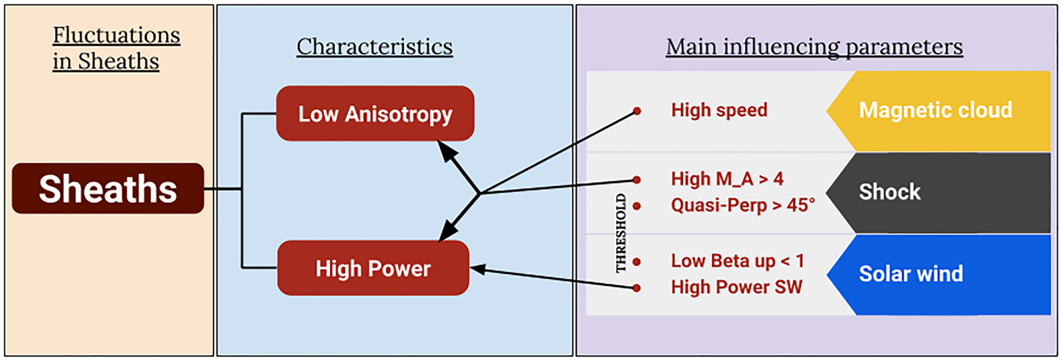

Figure 11. Characterizing the fluctuations in sheaths by two numbers (power and anisotropy), we find that, compared with the solar wind, sheaths have high power and low anisotropy. This is further enhanced when certain parameters are found in the magnetic cloud, shock and solar wind surrounding the sheaths.

magnetic field with other fluctuations such as the velocity or dynamic pressure fluctuations. It is also of importance for geoeffectiveness to estimate the fluctuation characteristics between the different sheath regions from the shock to the cloud's leading edge (as suggested by Kilpua et al., 2013).

7. Summary

From a list of 42 isolated events (Masías-Meza et al., 2016), we characterized the fluctuations in the three regions (solar wind, sheath, and magnetic cloud) based on their power and anistotropy, which appear as two independent parameters. Figure 11 gives a brief summary of the results.

- The fluctuations have much more power in the sheath (P_{Sh} ~9 nT^2) than in the preceding solar wind and following magnetic cloud ($P_{SW} \simeq P_{MC} \sim 0.9$ nT^2), by an order of magnitude.
- The fluctuations seem to be more isotropic (and thus more compressible) in the sheath ($A_{Sh} \sim 5$, or correspondingly $C_{Sh} \sim 0.15$) than in the solar wind ($A_{SW} \sim 10$, or $C_{SW} \sim 0.07$), and are much more anisotropic (and thus more incompressible) in the magnetic cloud ($A_{MC} \sim 36$, or $C_{MC} \sim 0.02$)

The parameters that have the strongest influence on the power and anisotropy of the fluctuations in the sheaths of these events, are mainly the following:

(i) the speed of the magnetic cloud,
(ii) the Alfvén Mach number of the shock, as those parameters increase, the power and isotropy of the fluctuations in the sheath increase.
(iii) the preexisting fluctuation power in the solar wind to which the power in the sheath is roughly proportional but not the anisotropy.
(iv) the angle between the shock's normal and the magnetic field upstream of the shock,
(v) the beta of the solar wind,

which have a somewhat more subtle role. $\beta \sim 1$ in the solar wind serves as a threshold above which both the power and the anisotropy of the fluctuations in sheaths drop significantly. Similarly, quasi-parallel shocks have both low power and anisotropy whereas any values of P_{Sh} and A_{Sh} can be found next to quasi-perpendicular shocks.

Appendix A: Definition of the Events' Main Parameters

We define in this sections the parameters against which the power and anisotropy of sheath are plotted in section 5. Some of these parameters depend on upstream and downstream (to the shock) values. We define the interval of time upstream as $\Delta t_{up} = [t_{shock} - 30\text{min}, t_{shock} - 15\text{min}]$ and the interval of time downstream as $\Delta t_{down} = [t_{shock} + 15\text{min}, t_{shock} + 30\text{min}]$. These intervals are defined as such in order to be the same length as the sliding window we use for all our averages and away from the transition layers by the same length. Any quantity Q computed on the interval Δt_{up} or Δt_{down} is respectively noted Q_{up} or Q_{down}.

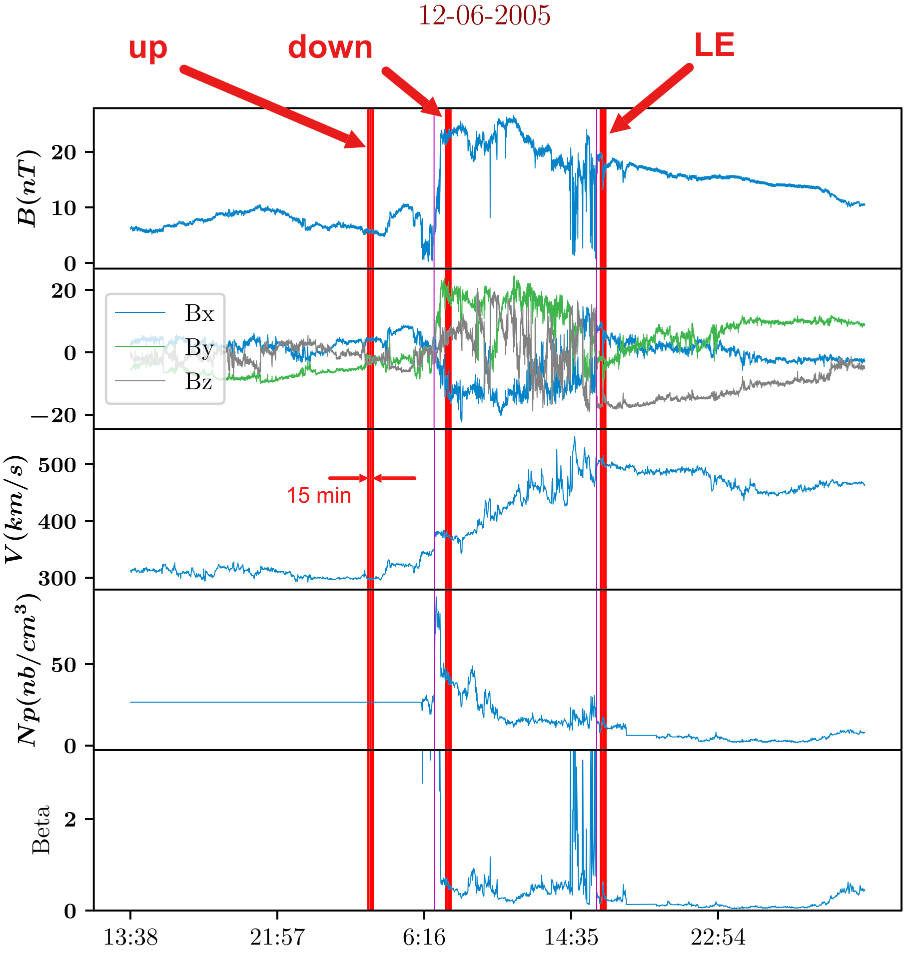

Figure A1. The three red vertical bands marked “up,” “down,” and “LE” represent the small areas of 15-min length used to compute most of the event's main parameters. For this particular event “upstream” is defined, manually, away from the shock to avoid a zone that is not representative of the pristine solar wind ahead of the event.

For a dozen of cases, taking data just upstream and downstream of the shock seemed flawed because of, for example, the presence of a structure just in front of the shock. In those cases, we defined manually upstream in the “pristine” solar wind. Any quantity used to describe the solar wind is then computed on the interval of time Δt_{up}.

Another area of interest is just after the leading edge of the magnetic cloud: $\Delta t_{\mathrm{LE}} = [t_{\text{leading edge}} + 15\text{min}, t_{\text{leading edge}} + 30\text{min}]$. Quantities representative of the magnetic clouds are computed in the interval of time Δt_{LE}. Any quantity Q computed on the interval Δt_{LE} is noted Q_{LE}.

Those areas are represented in Figure A1

Parameters describing the solar wind, defined on Δt_{up}.

$$\begin{aligned}
N_{\mathrm{SW}} &= \langle N \rangle_{\mathrm{up}} \\
B_{\mathrm{SW}} &= \langle |\boldsymbol{B}| \rangle_{\mathrm{up}} \\
V_{\mathrm{SW}} &= V_{\mathrm{up}} = \langle |\boldsymbol{V}| \rangle_{\mathrm{up}} \\
V_A^{\mathrm{up}} &= \langle v_A \rangle_{\mathrm{up}} = \left\langle \frac{B}{\sqrt{\mu_0 N_p m_p}} \right\rangle_{\mathrm{up}} \\
M_A^{\mathrm{up}} &= \frac{V_{\mathrm{up}}}{V_A^{\mathrm{up}}}
\end{aligned} \tag{A1}$$

P_{SW} and A_{SW} are the ones defined in section 3.4

Parameters describing the magnetic cloud, defined on Δt_{LE}.

$$\begin{aligned}
N_{\mathrm{MC}} &= \langle N \rangle_{\mathrm{LE}} \\
B_{\mathrm{MC}} &= \langle |\boldsymbol{B}| \rangle_{\mathrm{LE}} \\
V_{\mathrm{MC}} &= V_{\mathrm{LE}} = \langle |\boldsymbol{V}| \rangle_{\mathrm{LE}} \\
V_A^{\mathrm{LE}} &= \langle v_A \rangle_{\mathrm{LE}} = \left\langle \frac{B}{\sqrt{\mu_0 N_p m_p}} \right\rangle_{\mathrm{LE}} \\
M_A^{\mathrm{LE}} &= \frac{V_{\mathrm{LE}}}{V_A^{\mathrm{LE}}}
\end{aligned} \tag{A2}$$

P_{MC} and A_{MC} are the ones defined in section 3.4.

Parameters describing the shock. We use the definitions given at https://ipshocks.fi/documentation to define the main shocks' parameters: Alfvén Mach (M_A), plasma beta upstream of the shock (β), the angle between the normal of the shock, and the magnetic field upstream of the shock (θ_{Bn}).

shock normal

$$\hat{\boldsymbol{n}} = \frac{(\boldsymbol{B}_{\mathrm{down}} - \boldsymbol{B}_{\mathrm{up}}) \times ((\boldsymbol{B}_{\mathrm{down}} - \boldsymbol{B}_{\mathrm{up}}) \times (\boldsymbol{V}_{\mathrm{down}} - \boldsymbol{V}_{\mathrm{up}}))}{|(\boldsymbol{B}_{\mathrm{down}} - \boldsymbol{B}_{\mathrm{up}}) \times ((\boldsymbol{B}_{\mathrm{down}} - \boldsymbol{B}_{\mathrm{up}}) \times (\boldsymbol{V}_{\mathrm{down}} - \boldsymbol{V}_{\mathrm{up}}))|} \tag{A3}$$

shock speed

$$V_{\mathrm{shock}} = \left| \frac{N_p^{\mathrm{down}} \boldsymbol{V}_{\mathrm{down}} - N_p^{\mathrm{up}} \boldsymbol{V}_{\mathrm{up}}}{N_p^{\mathrm{down}} - N_p^{\mathrm{up}}} \cdot \hat{\boldsymbol{n}} \right| \tag{A4}$$

Alfvén Mach number

$$M_A = \frac{|\boldsymbol{V}_{\mathrm{up}} \cdot \hat{\boldsymbol{n}} - V_{\mathrm{shock}}|}{V_A^{\mathrm{up}}} \tag{A5}$$

Upstream plasma beta

$$\beta^{\mathrm{up}} = \langle \beta \rangle_{\mathrm{up}} = \left\langle \frac{2\mu_0 k_B N_p (T_p + T_e)}{B^2} \right\rangle_{\mathrm{up}} \tag{A6}$$

shock theta

$$\theta_{Bn} = \frac{180°}{\pi} \arccos\left(\frac{|\boldsymbol{B}_{\mathrm{up}} \cdot \hat{\boldsymbol{n}}|}{|\boldsymbol{B}_{\mathrm{up}}| \quad |\hat{\boldsymbol{n}}|} \right) \tag{A7}$$

A few more definitions

Velocities

$$\begin{aligned}
V_{\mathrm{down}} &= \langle |\boldsymbol{V}| \rangle_{\mathrm{down}} \\
V_{\mathrm{down}} - V_{\mathrm{up}} &= \langle |\boldsymbol{V}| \rangle_{\mathrm{down}} - \langle |\boldsymbol{V}| \rangle_{\mathrm{up}} \\
V_{\mathrm{LE}} - V_{\mathrm{up}} &= \langle |\boldsymbol{V}| \rangle_{\mathrm{LE}} - \langle |\boldsymbol{V}| \rangle_{\mathrm{up}}
\end{aligned} \tag{A8}$$

Acknowledgments

We are thankful to Gautier Nguyen for a part of the code used to easily retrieve ACE data and to Roland Grappin for enlightening discussions. This work received financial support by the program "Investissements d avenir" under the Reference ANR-11-IDEX-0004-02 (Plas@Par). We are indebted to ANR for the project TEMPETE (ANR-17-CE31-0016). Numerical simulations which were useful to interpret the results described in this paper were performed on the supercomputer center "IDRIS" institute of the Centre National de la Recherche Scientifique (CNRS) (http://www.idris.fr). We are also thankful to the two anonymous reviewers of this article, who helped in making it better organized and easier to read. All relevant data can be accessed from the website (https://cdaweb.sci.gsfc.nasa.gov/index.html/).

References

Ala-Lahti, M. M., Kilpua, E. K. J., Dimmock, A. P., Osmane, A., Pulkkinen, T. I., & Soućek, J. (2018). Statistical analysis of mirror mode waves in sheath regions driven by interplanetary coronal mass ejection. *Annales Geophysicae*, *36*(3), 793–808. https://doi.org/10.5194/angeo-36-793-2018

Alimaganbetov, M., & Streltsov, A. V. (2018). ULF waves observed during substorms in the solar wind and on the ground. *Journal of Atmospheric and Solar-Terrestrial Physics*, *181*, 10–18. https://doi.org/10.1016/j.jastp.2018.10.007

Blanco-Cano, X., Omidi, N., & Russell, C. T. (2006). Macrostructure of collisionless bow shocks: 2. ULF waves in the foreshock and magnetosheath. *Journal of Geophysical Research*, *111*, A10205. https://doi.org/10.1029/2005JA011421

Borovsky, J. E. (2003). Role of solar wind turbulence in the coupling of the solar wind to the Earth's magnetosphere. *Journal of Geophysical Research*, *108*(A6), 1246. https://doi.org/10.1029/2002JA009601

Burlaga, L. F. E. (1991). Physics of the inner heliosphere II: Particles, waves and turbulence (pp. 1–22). https://doi.org/10.1007/978-3-642-75364-0_1

Chi, Y., Shen, C., Wang, Y., Xu, M., Ye, P., & Wang, S. (2016). Statistical study of the interplanetary coronal mass ejections from 1995 to 2015. *Solar Physics*, *291*(8), 2419–2439. https://doi.org/10.1007/s11207-016-0971-5

de Wit, T. D., Alexandrova, O., Furno, I., Sorriso-Valvo, L., & Zimbardo, G. (2013). Methods for characterising microphysical processes in plasmas. *Space Science Reviews*, *178*(2-4), 665–693. (arXiv: 1306.5303)https://doi.org/10.1007/s11214-013-9974-9

Du, J., Wang, C., Song, P., & Zhang, T. (2008). Low-frequency fluctuations in the magnetosheath: Double Star TC-1 and Cluster observations. *Science in China Series E Technological Sciences*, *51*(10), 1626–1638. https://doi.org/10.1007/s11431-008-0250-2

Duff, T., Burgess, J., Christensen, P., Hery, C., Kensler, A., Liani, M., & Villemin, R. (2017). Building an orthonormal basis, Revisited. *Journal of Computer Graphics Techniques*, *6*(1), 8.

Dungey, J. W. (1961). Interplanetary magnetic field and the auroral zones. *Physical Review Letters*, *6*(2), 47–48. https://doi.org/10.1103/PhysRevLett.6.47

Echer, E., Gonzalez, W. D., & Tsurutani, B. T. (2008). Interplanetary conditions leading to superintense geomagnetic storms (Dst $\leq$- 250 nT) during solar cycle 23. *Geophysical Research Letters*, *35*, L06S03. https://doi.org/10.1029/2007GL031755

Gonzalez, W. D., Echer, E., Clua-Gonzalez, A. L., & Tsurutani, B. T. (2007). Interplanetary origin of intense geomagnetic storms (Dst $<$ 100 nT) during solar cycle 23. *Geophysical Research Letters*, *34*, L06101. https://doi.org/10.1029/2006GL028879

Gonzalez, W. D., Joselyn, J. A., Kamide, Y., Kroehl, H. W., Rostoker, G., Tsurutani, B. T., & Vasyliunas, V. M. (1994). What is a geomagnetic storm? *Journal of Geophysical Research*, *99*(A4), 5771–5792. https://doi.org/10.1029/93JA02867

Gonzalez, W. D., & Tsurutani, B. T. (1987). Criteria of interplanetary parameters causing intense magnetic storms (Dst of less than -100 nT). *Planetary and Space Science*, *35*, 1101–1109. https://doi.org/10.1016/0032-0633(87)90015-8

Gonzalez, W. D., Tsurutani, B. T., Gonzalez, A. L. C., Smith, E. J., Tang, F., & Akasofu, S. I. (1989). Solar wind-magnetosphere coupling during intense magnetic storms (1978–1979). *Journal of Geophysical Research*, *94*(A7), 8835–8851. https://doi.org/10.1029/JA094iA07p08835

Guo, J., Feng, X., Emery, B. A., Zhang, J., Xiang, C., Shen, F., & Song, W. (2011). Energy transfer during intense geomagnetic storms driven by interplanetary coronal mass ejections and their sheath regions: Energy transfer. *Journal of Geophysical Research*, *116*, A05106. https://doi.org/10.1029/2011JA016490

Hu, Q., Zank, G. P., Li, G., & Ao, X. (2013). A power spectral analysis of turbulence associated with interplanetary shock waves. *Solar Wind 13*, *1539*, 175–178. https://doi.org/10.1063/1.4811016

Huttunen, K. E. J., & Koskinen, H. E. J. (2004). Importance of post-shock streams and sheath region as drivers of intense magnetospheric storms and high-latitude activity, *Annales Geophysicae* (Vol. 22, pp. 1729–1738). https://doi.org/10.5194/angeo-22-1729-2004

Huttunen, K. E. J., Schwenn, R., Bothmer, V., & Koskinen, H. E. J. (2005). Properties and geoeffectiveness of magnetic clouds in the rising, maximum and early declining phases of solar cycle 23, *Annales Geophysicae* (Vol. 23, pp. 625–641). https://doi.org/10.5194/angeo-23-625-2005

Jankovičvá, D., Vörös, Z., & Šimkanin, J. (2008). The effect of upstream turbulence and its anisotropy on the efficiency of solar wind-magnetosphere coupling. *Nonlinear Processes in Geophysics*, *15*(4), 523–529. https://doi.org/10.5194/npg-15-523-2008

Kajdič, P., Blanco-Cano, X., Aguilar-Rodriguez, E., Russell, C. T., Jian, L. K., & Luhmann, J. G. (2012). Waves upstream and downstream of interplanetary shocks driven by coronal mass ejections: Waves associated with IP shocks. *Journal of Geophysical Research*, *117*, A06103. https://doi.org/10.1029/2011JA017381

Kataoka, R., Watari, S., Shimada, N., Shimazu, H., & Marubashi, K. (2005). Downstream structures of interplanetary fast shocks associated with coronal mass ejections. *Geophysical Research Letters*, *32*, L12103. https://doi.org/10.1029/2005GL022777

Kepko, L., Spence, H. E., & Singer, H. J. (2002). ULF waves in the solar wind as direct drivers of magnetospheric pulsations. *Geophysical Research Letters*, *29*(8), 1197. https://doi.org/10.1029/2001GL014405

Kilpua, E. K. J., Balogh, A., von Steiger, R., & Liu, Y. D. (2017). Geoeffective properties of solar transients and stream interaction regions. *Space Science Reviews*, *212*(3-4), 1271–1314. https://doi.org/10.1007/s11214-017-0411-3

Kilpua, E. K. J., Hietala, H., Koskinen, H. E. J., Fontaine, D., & Turc, L. (2013). Magnetic field and dynamic pressure ULF fluctuations in coronal-mass-ejection-driven sheath regions. *Annales Geophysicae*, *31*(9), 1559–1567. https://doi.org/10.5194/angeo-31-1559-2013

Kilpua, E. K. J., Koskinen, H. E. J., & Pulkkinen, T. I. (2017). Coronal mass ejections and their sheath regions in interplanetary space. *Living Reviews in Solar Physics*, *14*, 5. https://doi.org/10.1007/s41116-017-0009-6

Kilpua, E. K. J., Li, Y., Luhmann, J. G., Jian, L. K., & Russell, C. T. (2012). On the relationship between magnetic cloud field polarity and geoeffectiveness. *Annales Geophysicae*, *30*(7), 1037–1050. https://doi.org/10.5194/angeo-30-1037-2012

Leamon, R. J., Smith, C. W., & Ness, N. F. (1998). Characteristics of magnetic fluctuations within coronal mass ejections: The January 1997 event. *Geophysical Research Letters*, *25*(14), 2505–2508. https://doi.org/10.1029/98GL00305

Masías-Meza, J. J., Dasso, S., Démoulin, P., Rodriguez, L., & Janvier, M. (2016). Superposed epoch study of ICME sub-structures near Earth and their effects on galactic cosmic rays. *Astronomy & Astrophysics*, *592*, A118. https://doi.org/10.1051/0004-6361/201628571

Myllys, M., Kilpua, E. K. J., Lavraud, B., & Pulkkinen, T. I. (2016). Solar wind-magnetosphere coupling efficiency during ejecta and sheath-driven geomagnetic storms. *Journal of Geophysical Research: Space Physics*, *121*, 4378–4396. https://doi.org/10.1002/2016JA022407

Narita, Y., Glassmeier, K. H., Fornaçon, K. H., Richter, I., Schäfer, S., Motschmann, U., & Georgescu, E. (2006). Low-frequency wave characteristics in the upstream and downstream regime of the terrestrial bow shock. *Journal of Geophysical Research*, *111*, A1. https://doi.org/10.1029/2005JA011231

Osmane, A., Dimmock, A. P., Naderpour, R., Pulkkinen, T. I., & Nykyri, K. (2015). The impact of solar wind ULF Bz fluctuations on geomagnetic activity for viscous timescales during strongly northward and southward IMF. *Journal of Geophysical Research: Space Physics*, *120*, 9307–9322. https://doi.org/10.1002/2015JA021505

Russell, C. T., McPherron, R. L., & Burton, R. K. (1974). On the cause of geomagnetic storms. *Journal of Geophysical Research*, *79*(7), 1105–1109. https://doi.org/10.1029/JA079i007p01105

Shaikh, Z., Raghav, A., & Bhaskar, A. (2017). The presence of turbulent and ordered local structure within the ICME shock-sheath and its contribution to Forbush decrease. *The Astrophysical Journal*, *844*(2), 121. https://doi.org/10.3847/1538-4357/aa729f

Stone, E. C., Frandsen, A. M., Mewaldt, R. A., Christian, E. R., Margolies, D., Ormes, J. F., & Snow, F. (1998). The Advanced Composition Explorer. *Space Science Reviews*, *86*, 1. https://doi.org/10.1023/A:1005082526237

Tao, C., Sahraoui, F., Fontaine, D., de Patoul, J., Chust, T., Kasahara, S., & Retinó, A. (2015). Properties of Jupiter's magnetospheric turbulence observed by the Galileo spacecraft: Jovian magnetospheric turbulence. *Journal of Geophysical Research: Space Physics*, *120*, 2477–2493. https://doi.org/10.1002/2014JA020749

Torrence, C., & Compo, G. P. (1998). A practical guide to wavelet analysis. *Bulletin of the American Meteorological Society*, *79*(1), 61–78. https://doi.org/10.1175/1520-0477 (1998)079<0061:APGTWA>2.0.CO;2

Treumann, R. A. (2009). Fundamentals of collisionless shocks for astrophysical application, 1. Non-relativistic shocks. *The Astronomy and Astrophysics Review*, *17*(4), 409–535. https://doi.org/10.1007/s00159-009-0024-2

Tsurutani, B. T., Goldstein, B. E., Smith, E. J., Gonzalez, W. D., Tang, F., Akasofu, S. I., & Anderson, R. R. (1990). The interplanetary and solar causes of geomagnetic activity. *Planetary and Space Science*, *38*(1), 109–126. https://doi.org/10.1016/0032-0633(90)90010-N

Tsurutani, B. T., Gonzalez, W. D., Tang, F., Akasofu, S. I., & Smith, E. J. (1988). Origin of interplanetary southward magnetic fields responsible for major magnetic storms near solar maximum (1978–1979). *Journal of Geophysical Research*, *93*(A8), 8519. https://doi.org/10.1029/JA093iA08p08519

Tsurutani, B. T., Gonzalez, W. D., Tang, F., & Lee, Y. T. (1992). Great magnetic storms. *Geophysical Research Letters*, *19*(1), 73–76. https://doi.org/10.1029/91GL02783

Turc, L., Fontaine, D., Savoini, P., & Kilpua, E. K. J. (2014). A model of the magnetosheath magnetic field during magnetic clouds. *Annales Geophysicae*, *32*(2), 157–173. https://doi.org/10.5194/angeo-32-157-2014

Wilson, R. M. (1987). Geomagnetic response to magnetic clouds. *Planetary and Space Science*, *35*(3), 329–335. https://doi.org/10.1016/0032-0633(87)90159-0

Yermolaev, Y. I., Nikolaeva, N. S., Lodkina, I. G., & Yermolaev, M. Y. (2012). Geoeffectiveness and efficiency of CIR, sheath, and ICME in generation of magnetic storms. *Journal of Geophysical Research*, *117*, A00L07. https://doi.org/10.1029/2011JA017139

Zhang, G., & Burlaga, L. F. (1988). Magnetic clouds, geomagnetic disturbances, and cosmic ray decreases. *Journal of Geophysical Research*, *93*(A4), 2511–2518. https://doi.org/10.1029/JA093iA04p02511

Zhang, X. Y., & Moldwin, M. B. (2014). The source, statistical properties, and geoeffectiveness of long-duration southward interplanetary magnetic field intervals. *Journal of Geophysical Research: Space Physics*, *119*, 658–669. https://doi.org/10.1002/2013JA018937

C: List of Publications

- Moissard et al. (2021):

  Collision of collisionless shocks – Part I: Numerical method & deformation of the interplanetary shock
  C. Moissard, P. Savoini, D. Fontaine , R. Modolo
  (in preparation)

- Kilpua et al. (2020):

  Magnetic field fluctuation properties of coronal mass ejection-driven sheath regions in the near-Earth solar wind
  E. Kilpua, D. Fontaine, S. Good, M. Ala-Lahti, A. Osmane, E. Palmerio, E. Yordanova, C. Moissard, L. Hadid, and M. Janvier
  Annales Geophysicae

- Moissard et al. (2019):

  A Study of Fluctuations in Magnetic Cloud-Driven Sheaths
  C. Moissard, D. Fontaine, and P. Savoini
  Journal of Geophysical Research: Space Physics

- Kilpua et al. (2019):

  Solar Wind Properties and Geospace Impact of Coronal Mass Ejection-Driven Sheath Regions: Variation and Driver Dependence
  E. K. J. Kilpua, D. Fontaine, C. Moissard, M. Ala-Lahti, E. Palmerio, E. Yordanova, S. W.Good, M. M. H. Kalliokoski, E. Lumme, A. Osmane, M. Palmroth, and L. Turc
  Space Weather

- Matteucci et al. (2018):

  Biermann-Battery-Mediated Magnetic Reconnection in 3D Colliding Plasmas
  J. Matteucci, W. Fox, A. Bhattacharjee, D. B. Schaeffer, C. Moissard, K. Germaschewski, G. Fiksel, and S. X. Hu
  Physical Review Letters

- Fox et al. (2018):

  Kinetic simulation of magnetic field generation and collisionless shock formationin expanding laboratory plasmas
  W. Fox, J. Matteucci, C. Moissard, D. B. Schaeffer, A. Bhattacharjee, K. Germaschewski, and S. X. Hu
  Physics of Plasmas

Bibliography

Ala-Lahti, M. M., E. K. J. Kilpua, A. P. Dimmock, A. Osmane, T. I. Pulkkinen, and J. Souček
2018. Statistical analysis of mirror mode waves in sheath regions driven by interplanetary coronal mass ejection. *Annales Geophysicae*, 36(3):793–808.

Alfsen, K. H., C. Bonifazi, A. Pedersen, and P.-A. Lindqvist
1984. Interaction between an interplanetary shock and the Earth's magnetosphere on August 27, 1978: ISEE 1 electric field and ISEE 2 plasma observations. *Journal of Geophysical Research: Space Physics*, 89(A10):8863–8871.

Alimaganbetov, M. and A. V. Streltsov
2018. ULF waves observed during substorms in the solar wind and on the ground. *Journal of Atmospheric and Solar-Terrestrial Physics*, 181:10–18.

Anonymous
1859. AURORAL PHENOMENA.; Remarkable Effect of the Aurora Upon the Telegraph Wires. *The New York Times*.

Axford, W. I.
1962. The interaction between the solar wind and the Earth's magnetosphere. *Journal of Geophysical Research (1896-1977)*, 67(10):3791–3796.

Baker, D. N., E. Daly, I. Daglis, J. G. Kappenman, and M. Panasyuk
2004. Effects of Space Weather on Technology Infrastructure. *Space Weather*, 2(2):n/a–n/a.

Bartels, J.
1936. The eccentric dipole approximating the Earth's magnetic field. *Terrestrial Magnetism and Atmospheric Electricity*, 41(3):225–250.

Battarbee, M., U. Ganse, Y. Pfau-Kempf, L. Turc, T. Brito, M. Grandin, T. Koskela, and M. Palmroth
2020. Non-locality of Earth's quasi-parallel bow shock: Injection of thermal protons in a hybrid-Vlasov simulation. *Annales Geophysicae*, 38(3):625–643.

Belmont, G., Rezeau, L, Riconda, C., and Zaslavsky, A.
2018. *Introduction à la physique des plasmas*. ITSE Group.

Biermann, L.
1951. Kometenschweife und solare Korpuskularstrahlung. *Zeitschrift für Astrophysik*, 29.

Billard, L.
2017. Study of Salary Differentials by Gender and Discipline. *Statistics and Public Policy*, 4(1):1–14.

Bittencourt, J. A.
2004. *Fundamentals of Plasma Physics*.

Blackman, R. B. and J. W. Tukey
1958. The Measurement of Power Spectra from the Point of View of Communications Engineering — Part I. *Bell System Technical Journal*, 37(1):185–282.

Blanco-Cano, X., N. Omidi, and C. T. Russell
2006. Macrostructure of collisionless bow shocks: 2. ULF waves in the foreshock and magnetosheath. *Journal of Geophysical Research (Space Physics)*, 111(A10):A10205.

Bonde, R. E. F., R. E. Lopez, and J. Y. Wang
2018. The Effect of IMF Fluctuations on the Subsolar Magnetopause Position: A Study Using a Global MHD Model. *Journal of Geophysical Research: Space Physics*, 123(4):2598–2604.

Borovsky, J. E.
2003. Role of solar wind turbulence in the coupling of the solar wind to the Earth's magnetosphere. *Journal of Geophysical Research*, 108(A6).

Borovsky, J. E.
2020. A Statistical Analysis of the Fluctuations in the Upstream and Downstream Plasmas of 109 Strong-Compression Interplanetary Shocks at 1 AU. *Journal of Geophysical Research: Space Physics*, 125(6):e2019JA027518.

Borovsky, J. E. and S. P. Gary
2009. On shear viscosity and the Reynolds number of magnetohydrodynamic turbulence in collisionless magnetized plasmas: Coulomb collisions, Landau damping, and Bohm diffusion. *Physics of Plasmas*, 16(8):082307.

Borovsky, J. E. and Y. Y. Shprits
2017. Is the Dst Index Sufficient to Define All Geospace Storms? *Journal of Geophysical Research: Space Physics*, 122(11):11,543–11,547.

Boteler, D. H.
2019. A 21st Century View of the March 1989 Magnetic Storm. *Space Weather*, 17(10):1427–1441.

Boyd, T. J. and J. J. Sanderson
2003. *The Physics of Plasmas*. Cambridge University Press.

Bruno, R. and V. Carbone
2013. The Solar Wind as a Turbulence Laboratory. *Living Reviews in Solar Physics*, 10(1):2.

Bruno, R., L. Trenchi, and D. Telloni
2014. SPECTRAL SLOPE VARIATION AT PROTON SCALES FROM FAST TO SLOW SOLAR WIND. *The Astrophysical Journal*, 793(1):L15.

Burlaga, L. F.
1988. Magnetic clouds and force-free fields with constant alpha. *Journal of Geophysical Research*, 93(A7):7217.

Burlaga, L. F. E.
1991. Magnetic Clouds. In *Physics of the Inner Heliosphere II: Particles, Waves and Turbulence*, R. Schwenn and E. Marsch, eds., Physics and Chemistry in Space, Pp. 1–22. Berlin, Heidelberg: Springer Berlin Heidelberg.

Burton, R. K., R. L. McPherron, and C. T. Russell
1975. An empirical relationship between interplanetary conditions and Dst. *Journal of Geophysical Research (1896-1977)*, 80(31):4204–4214.

Carrington, R. C.
1859. Description of a Singular Appearance seen in the Sun on September 1, 1859. *Monthly Notices of the Royal Astronomical Society*, 20(1):13–15.

Chapman, S.
1944. William Gilbert and the Science of his Time*. *Nature*, 154(3900):132–136.

Chapman, S. and H. Zirin
1957. Notes on the Solar Corona and the Terrestrial Ionosphere. *Smithsonian Contributions to Astrophysics*, 2:1.

Charbonneau, P.
2014. Solar Dynamo Theory. *Annual Review of Astronomy and Astrophysics*, 52(1):251–290.

Chen, F. F.
1974. *Introduction to Plasma Physics*. Springer Science & Business Media.

Chen, S.-H., M. G. Kivelson, J. T. Gosling, R. J. Walker, and A. J. Lazarus
1993. Anomalous aspects of magnetosheath flow and of the shape and oscillations of the magnetopause during an interval of strongly northward interplanetary magnetic field. *Journal of Geophysical Research: Space Physics*, 98(A4):5727–5742.

Chi, Y., C. Shen, Y. Wang, M. Xu, P. Ye, and S. Wang
2016. Statistical Study of the Interplanetary Coronal Mass Ejections from 1995 to 2015. *Solar Physics*, 291(8):2419–2439.

Chou, Y.-C. and L.-N. Hau
2012. A statistical study of magnetopause structures: Tangential versus rotational discontinuities. *Journal of Geophysical Research: Space Physics*, 117(A8).

Daglis, I. A., R. M. Thorne, W. Baumjohann, and S. Orsini
1999. The terrestrial ring current: Origin, formation, and decay. *Reviews of Geophysics*, 37(4):407–438.

D'Amicis, R., R. Bruno, and B. Bavassano
2007. Is geomagnetic activity driven by solar wind turbulence? *Geophysical Research Letters*, 34(5).

De Hoffmann, F. and E. Teller
1950. Magneto-Hydrodynamic Shocks. *Physical Review*, 80(4):692–703.

Dessler, A. J. and E. N. Parker
1959. Hydromagnetic theory of geomagnetic storms. *Journal of Geophysical Research (1896-1977)*, 64(12):2239–2252.

Dieckmann, M. E., P. K. Shukla, and L. Stenflo
2009. Simulation study of the filamentation of counter-streaming beams of the electrons and positrons in plasmas. *Plasma Physics and Controlled Fusion*, 51(6):065015.

Dobrowolny, M. and V. Formisano
1973. The structure of the earth's bow shock. *La Rivista del Nuovo Cimento (1971-1977)*, 3(4):419–489.

Domingo, V., B. Fleck, and A. I. Poland
1995. The SOHO mission: An overview. *Solar Physics*, 162(1):1–37.

Du, A. M., B. T. Tsurutani, and W. Sun
2008a. Anomalous geomagnetic storm of 21–22 January 2005: A storm main phase during northward IMFs. *Journal of Geophysical Research: Space Physics*, 113(A10).

Du, J., C. Wang, P. Song, and T. Zhang
2008b. Low-frequency fluctuations in the magnetosheath: Double Star TC-1 and Cluster observations. *Science in China Series E: Technological Sciences*, 51(10):1626–1638.

Duff, T., J. Burgess, P. Christensen, C. Hery, A. Kensler, M. Liani, and R. Villemin
2017. Building an Orthonormal Basis, Revisited. *Journal of Computer Graphics Techniques*, 6(1):8.

Dungey, J. W.
1961. Interplanetary Magnetic Field and the Auroral Zones. *Physical Review Letters*, 6(2):47–48.

Eastwood, J. P., E. Biffis, M. A. Hapgood, L. Green, M. M. Bisi, R. D. Bentley, R. Wicks, L.-A. McKinnell, M. Gibbs, and C. Burnett
2017. The Economic Impact of Space Weather: Where Do We Stand? *Risk Analysis*, 37(2):206–218.

Echer, E., M. Alves, and W. Gonzalez
2004. Geoeffectiveness of interplanetary shocks during solar minimum (1995–1996) and solar maximum (2000). *Solar Physics*, 221(2):361–380.

Echer, E., M. Alves, and W. Gonzalez
2005. A statistical study of magnetic cloud parameters and geoeffectiveness. *Journal of Atmospheric and Solar-Terrestrial Physics*, 67(10):839–852.

Echer, E., B. T. Tsurutani, and W. D. Gonzalez
2013. Interplanetary origins of moderate (-100 nT $<$ Dst ≤ -50 nT) geomagnetic storms during solar cycle 23 (1996–2008). *Journal of Geophysical Research: Space Physics*, 118(1):385–392.

Egeland, A.
2009. Kristian Birkeland: The first space scientist. *Journal of Atmospheric and Solar-Terrestrial Physics*, 71(17-18):1749–1755.

Egeland, A. and W. J. Burke
2012. The ring current: A short biography. *History of Geo- and Space Sciences*, 3(2):131–142.

Emslie, A. G., H. Kucharek, B. R. Dennis, N. Gopalswamy, G. D. Holman, G. H. Share, A. Vourlidas, T. G. Forbes, P. T. Gallagher, G. M. Mason, T. R. Metcalf, R. A. Mewaldt, R. J. Murphy, R. A. Schwartz, and T. H. Zurbuchen
2004. Energy partition in two solar flare/CME events. *Journal of Geophysical Research: Space Physics*, 109(A10).

Fälthammar, C.-G., S.-I. Akasofu, and H. Alfvén
1978. The significance of magnetospheric research for progress in astrophysics. *Nature*, 275(5677):185–188.

Farley, D. T.
1963. Two-Stream Plasma Instability as a Source of Irregularities in the Ionosphere. *Physical Review Letters*, 10(7):279–282.

Farris, M. H., S. M. Petrinec, and C. T. Russell
1991. The thickness of the magnetosheath: Constraints on the polytropic index. *Geophysical Research Letters*, 18(10):1821–1824.

Fox, W., J. Matteucci, C. Moissard, D. B. Schaeffer, A. Bhattacharjee, K. Germaschewski, and S. X. Hu
2018. Kinetic simulation of magnetic field generation and collisionless shock formation in expanding laboratory plasmas. *Physics of Plasmas*, 25(10):102106.

Galtier, S.
2016. *Introduction to Modern Magnetohydrodynamics*. Cambridge University Press.

Georgoulis, M. K., A. Nindos, and H. Zhang
2019. The source and engine of coronal mass ejections. *Philosophical Transactions of the Royal Society A*.

Goncharov, O., J. Šafránková, Z. Němeček, L. Přech, A. Pitňa, and G. N. Zastenker
2014. Upstream and downstream wave packets associated with low-Mach number interplanetary shocks: GONCHAROV ET AL. *Geophysical Research Letters*, 41(22):8100–8106.

Gonzalez, W. D., E. Echer, B. T. Tsurutani, A. L. Clúa de Gonzalez, and A. Dal Lago
2011. Interplanetary Origin of Intense, Superintense and Extreme Geomagnetic Storms. *Space Science Reviews*, 158(1):69–89.

Good, S. W., M. Ala-Lahti, E. Palmerio, E. K. J. Kilpua, and A. Osmane
2020. Radial Evolution of Magnetic Field Fluctuations in an Interplanetary Coronal Mass Ejection Sheath. *The Astrophysical Journal*, 893(2):110.

Horbury, T. S., P. J. Cargill, E. A. Lucek, A. Balogh, M. W. Dunlop, T. M. Oddy, C. Carr, P. Brown, A. Szabo, and K.-H. Fornaçon
2001. Cluster magnetic field observations of the bowshock: Orientation, motion and structure. *Annales Geophysicae*, 19(10/12):1399–1409.

Hospodarsky, G. B.
2016. Spaced-based search coil magnetometers. *Journal of Geophysical Research: Space Physics*, 121(12):12,068–12,079.

Huba, J. D.
2003. Hall Magnetohydrodynamics - A Tutorial. In *Space Plasma Simulation*, J. Büchner, M. Scholer, and C. T. Dum, eds., Lecture Notes in Physics, Pp. 166–192. Berlin, Heidelberg: Springer.

Hughes, W. J.
1995. The magnetopause, magnetotail, and magnetic reconnection. *Introduction to Space Physics*, Pp. 227–287.

Huttunen, K. E. J. and H. E. J. Koskinen
2004. Importance of post-shock streams and sheath region as drivers of intense magnetospheric storms and high-latitude activity. In *Annales Geophysicae*, volume 22, Pp. 1729–1738.

Huttunen, K. E. J., H. E. J. Koskinen, and R. Schwenn
2002. Variability of magnetospheric storms driven by different solar wind perturbations. *Journal of Geophysical Research (Space Physics)*, 107:1121.

Huttunen, K. E. J., R. Schwenn, V. Bothmer, and H. E. J. Koskinen
2005. Properties and geoeffectiveness of magnetic clouds in the rising, maximum and early declining phases of solar cycle 23. In *Annales Geophysicae*, volume 23, Pp. 625–641.

Hynönen, R., E. I. Tanskanen, and P. Francia
2020. Solar cycle evolution of ULF wave power in solar wind and on ground. *Journal of Space Weather and Space Climate*, 10:43.

Jakosky, B. M., D. Brain, M. Chaffin, S. Curry, J. Deighan, J. Grebowsky, J. Halekas, F. Leblanc, R. Lillis, J. G. Luhmann, L. Andersson, N. Andre, D. Andrews, D. Baird, D. Baker, J. Bell, M. Benna, D. Bhattacharyya, S. Bougher, C. Bowers, P. Chamberlin, J. Y. Chaufray, J. Clarke,

G. Collinson, M. Combi, J. Connerney, K. Connour, J. Correira, K. Crabb, F. Crary, T. Cravens, M. Crismani, G. Delory, R. Dewey, G. DiBraccio, C. Dong, Y. Dong, P. Dunn, H. Egan, M. Elrod, S. England, F. Eparvier, R. Ergun, A. Eriksson, T. Esman, J. Espley, S. Evans, K. Fallows, X. Fang, M. Fillingim, C. Flynn, A. Fogle, C. Fowler, J. Fox, M. Fujimoto, P. Garnier, Z. Girazian, H. Groeller, J. Gruesbeck, O. Hamil, K. G. Hanley, T. Hara, Y. Harada, J. Hermann, M. Holmberg, G. Holsclaw, S. Houston, S. Inui, S. Jain, R. Jolitz, A. Kotova, T. Kuroda, D. Larson, Y. Lee, C. Lee, F. Lefevre, C. Lentz, D. Lo, R. Lugo, Y. J. Ma, P. Mahaffy, M. L. Marquette, Y. Matsumoto, M. Mayyasi, C. Mazelle, W. McClintock, J. McFadden, A. Medvedev, M. Mendillo, K. Meziane, Z. Milby, D. Mitchell, R. Modolo, F. Montmessin, A. Nagy, H. Nakagawa, C. Narvaez, K. Olsen, D. Pawlowski, W. Peterson, A. Rahmati, K. Roeten, N. Romanelli, S. Ruhunusiri, C. Russell, S. Sakai, N. Schneider, K. Seki, R. Sharrar, S. Shaver, D. E. Siskind, M. Slipski, Y. Soobiah, M. Steckiewicz, M. H. Stevens, I. Stewart, A. Stiepen, S. Stone, V. Tenishev, N. Terada, K. Terada, E. Thiemann, R. Tolson, G. Toth, J. Trovato, M. Vogt, T. Weber, P. Withers, S. Xu, R. Yelle, E. Yiğit, and R. Zurek
2018. Loss of the Martian atmosphere to space: Present-day loss rates determined from MAVEN observations and integrated loss through time. *Icarus*, 315:146–157.

Jankovičová, D., Z. Vörös, and J. Šimkanin
2008. The effect of upstream turbulence and its anisotropy on the efficiency of solar wind – magnetosphere coupling. *Nonlinear Processes in Geophysics*, 15(4):523–529.

Janvier, M., R. M. Winslow, S. Good, E. Bonhomme, P. Démoulin, S. Dasso, C. Möstl, N. Lugaz, T. Amerstorfer, E. Soubrié, and P. D. Boakes
2019. Generic Magnetic Field Intensity Profiles of Interplanetary Coronal Mass Ejections at Mercury, Venus, and Earth From Superposed Epoch Analyses. *Journal of Geophysical Research: Space Physics*, 124(2):812–836.

Jonas, S. and E. D. McCarron
2016. White House Releases National Space Weather Strategy and Action Plan. *Space Weather*, 14(2):54–55.

Juckett, D. A.
2007. Correlation of a 140-year global time signature in cancer mortality birth cohorts with galactic cosmic ray variation. *International Journal of Astrobiology*, 6(4):307–319.

Kajdič, P., X. Blanco-Cano, E. Aguilar-Rodriguez, C. T. Russell, L. K. Jian, and J. G. Luhmann
2012. Waves upstream and downstream of interplanetary shocks driven by coronal mass ejections: WAVES ASSOCIATED WITH IP SHOCKS. *Journal of Geophysical Research: Space Physics*, 117(A6):n/a–n/a.

Kalliokoski, M. M. H., E. K. J. Kilpua, A. Osmane, D. L. Turner, A. N. Jaynes, L. Turc, H. George, and M. Palmroth
2020. Outer radiation belt and inner magnetospheric response to sheath regions of coronal mass ejections: A statistical analysis. *Annales Geophysicae*, 38(3):683–701.

Kataoka, R., S. Watari, N. Shimada, H. Shimazu, and K. Marubashi
2005. Downstream structures of interplanetary fast shocks associated with coronal mass ejections. *Geophysical Research Letters*, 32(12).

Kellogg, P. J.
1962. Flow of plasma around the Earth. *Journal of Geophysical Research (1896-1977)*, 67(10):3805–3811.

Kepko, L., H. E. Spence, and H. J. Singer
2002. ULF waves in the solar wind as direct drivers of magnetospheric pulsations. *Geophysical Research Letters*, 29(8):1197.

Kilpua, E. K. J., A. Balogh, R. von Steiger, and Y. D. Liu
2017a. Geoeffective Properties of Solar Transients and Stream Interaction Regions. *Space Science Reviews*, 212(3-4):1271–1314.

Kilpua, E. K. J., D. Fontaine, S. W. Good, M. Ala-Lahti, A. Osmane, E. Palmerio, E. Yordanova, C. Moissard, L. Z. Hadid, and M. Janvier
2020. Magnetic field fluctuation properties of coronal mass ejection-driven sheath regions in the near-Earth solar wind. *Annales Geophysicae*, 38(5):999–1017.

Kilpua, E. K. J., D. Fontaine, C. Moissard, M. Ala-Lahti, E. Palmerio, E. Yordanova, S. W. Good, M. M. H. Kalliokoski, E. Lumme, A. Osmane, M. Palmroth, and L. Turc
2019. Solar Wind Properties and Geospace Impact of Coronal Mass Ejection-Driven Sheath Regions: Variation and Driver Dependence. *Space Weather*, 17(8):1257–1280.

Kilpua, E. K. J., H. Hietala, H. E. J. Koskinen, D. Fontaine, and L. Turc
2013. Magnetic field and dynamic pressure ULF fluctuations in coronal-mass-ejection-driven sheath regions. *Annales Geophysicae*, 31(9):1559–1567.

Kilpua, E. K. J., H. E. J. Koskinen, and T. I. Pulkkinen
2017b. Coronal mass ejections and their sheath regions in interplanetary space. *Living Reviews in Solar Physics*, 14(1).

Kilpua, E. K. J., C. O. Lee, J. G. Luhmann, and Y. Li
2011. Interplanetary coronal mass ejections in the near-Earth solar wind during the minimum periods following solar cycles 22 and 23. *Annales Geophysicae*, 29:1455–1467.

Kolmogorov, A.
1941. The Local Structure of Turbulence in Incompressible Viscous Fluid for Very Large Reynolds' Numbers. *Akademiia Nauk SSSR Doklady*, 30:301–305.

Koval, A., J. Šafránková, Z. Němeček, and L. Přech
2006a. Propagation of interplanetary shocks through the solar wind and magnetosheath. *Advances in Space Research*, 38(3):552–558.

Koval, A., J. Šafránková, Z. Němeček, L. Přech, A. A. Samsonov, and J. D. Richardson
2005. Deformation of interplanetary shock fronts in the magnetosheath. *Geophysical Research Letters*, 32(15).

Koval, A., J. Šafránková, Z. Němeček, A. A. Samsonov, L. Přech, J. D. Richardson, and M. Hayosh
2006b. Interplanetary shock in the magnetosheath: Comparison of experimental data with MHD modeling. *Geophysical Research Letters*, 33:L11102.

Lagrange, Joseph-Louis
1867. *Oeuvres de Lagrange. T. 6 / publiées par les soins de M. J.-A. Serret [et G. Darboux] ; [précédé d'une notice sur la vie et les ouvrages de J.-L. Lagrange, par M. Delambre].*

Lapenta, G.
2012. Particle simulations of space weather. *Journal of Computational Physics*, 231(3):795–821.

Lapenta, G.
2015. Kinetic Plasma Simulation: Particle In Cell Method. In *Proceedings of the XII Carolus Magnus Summer School on Plasma and Fusion Energy Physics*. KU Leuven.

Lavraud, B., E. Larroque, E. Budnik, V. Génot, J. E. Borovsky, M. W. Dunlop, C. Foullon, H. Hasegawa, C. Jacquey, K. Nykyri, A. Ruffenach, M. G. G. T. Taylor, I. Dandouras, and H. Rème
2013. Asymmetry of magnetosheath flows and magnetopause shape during low Alfvén Mach number solar wind. *Journal of Geophysical Research: Space Physics*, 118(3):1089–1100.

Leamon, R. J., C. W. Smith, N. F. Ness, W. H. Matthaeus, and H. K. Wong
1998. Observational constraints on the dynamics of the interplanetary magnetic field dissipation range. *Journal of Geophysical Research: Space Physics*, 103(A3):4775–4787.

Lembège, B. and P. Savoini
2002. Formation of reflected electron bursts by the nonstationarity and nonuniformity of a collisionless shock front. *Journal of Geophysical Research: Space Physics*, 107(A3):SMP X–1–SMP X–18.

Lembège, B., P. Savoini, P. Hellinger, and P. M. Trávníček
2009. Nonstationarity of a two-dimensional perpendicular shock: Competing mechanisms. *Journal of Geophysical Research: Space Physics*, 114(A3).

Lepping, R., D. Berdichevsky, A. Szabo, C. Arqueros, and A. Lazarus
2003. Profile of an Average Magnetic Cloud at 1 au for the Quiet Solar Phase: Wind Observations. *Solar Physics*, 212(2):425–444.

Lepping, R. P., M. H. Acũna, L. F. Burlaga, W. M. Farrell, J. A. Slavin, K. H. Schatten, F. Mariani, N. F. Ness, F. M. Neubauer, Y. C. Whang, J. B. Byrnes, R. S. Kennon, P. V. Panetta, J. Scheifele, and E. M. Worley
1995. The Wind Magnetic Field Investigation. *Space Science Reviews*, 71:207–229.

Lepping, R. P., D. B. Berdichevsky, C.-C. Wu, A. Szabo, T. Narock, F. Mariani, A. J. Lazarus, and A. J. Quivers
2006. A summary of WIND magnetic clouds for years 1995-2003: Model-fitted parameters, associated errors and classifications. *Annales Geophysicae*, 24(1):215–245.

Li, Y., J. G. Luhmann, and B. J. Lynch
2018. Magnetic Clouds: Solar Cycle Dependence, Sources, and Geomagnetic Impacts. *Solar Physics*, 293(10):135.

Lin, A. J., C. Shelden, N. Panagiotacopulos, and B. Ross
2001. Definition of the Neurochemical Patterns of Human Head Injury in 1 H MRS Using Wavelet Analysis. /paper/Definition-of-the-Neurochemical-Patterns-of-Human-1-Lin-Shelden/713c18e7e939218f2414e202af2b683ab3816464.

Lin, N., M. J. Engebretson, R. L. McPherron, M. G. Kivelson, W. Baumjohann, H. Luehr, T. A. Potemra, B. J. Anderson, and L. J. Zanetti
1991. A comparison of ULF fluctuations in the solar wind, magnetosheath, and dayside magnetosphere: 2. Field and plasma conditions in the magnetosheath. *Journal of Geophysical Research: Space Physics*, 96(A3):3455–3464.

Lindemann, F. A.
1919. LXX. Note on the theory of magnetic storms. *The London, Edinburgh, and Dublin Philosophical Magazine and Journal of Science*, 38(228):669–684.

Lucek, E. A., D. Constantinescu, M. L. Goldstein, J. Pickett, J. L. Pinçon, F. Sahraoui, R. A. Treumann, and S. N. Walker
2005. The Magnetosheath. *Space Science Reviews*, 118(1-4):95–152.

Lugaz, N., C. J. Farrugia, R. M. Winslow, N. Al-Haddad, E. K. J. Kilpua, and P. Riley
2016. Factors affecting the geoeffectiveness of shocks and sheaths at 1 AU. *Journal of Geophysical Research: Space Physics*, 121(11):10,861–10,879.

Malin, S. R. C. and D. R. Barraclough
1991. Humboldt and the Earth's Magnetic Field. *Quarterly Journal of the Royal Astronomical Society*, 32:279.

Maltsev, Y.
2004. Points of controversy in the study of magnetic storms. *Space Science Reviews*, 110(3):227–267.

Marsch, E.
1991. MHD Turbulence in the Solar Wind. In *Physics of the Inner Heliosphere II: Particles, Waves and Turbulence*, R. Schwenn and E. Marsch, eds., Physics and Chemistry in Space, Pp. 159–241. Berlin, Heidelberg: Springer.

Masías-Meza, J. J., S. Dasso, P. Démoulin, L. Rodriguez, and M. Janvier
2016. Superposed epoch study of ICME sub-structures near Earth and their effects on Galactic cosmic rays. *Astronomy & Astrophysics*, 592:A118.

Matteucci, J., W. Fox, A. Bhattacharjee, D. B. Schaeffer, C. Moissard, K. Germaschewski, G. Fiksel, and S. X. Hu
2018. Biermann-Battery-Mediated Magnetic Reconnection in 3D Colliding Plasmas. *Physical Review Letters*, 121(9):095001.

Matthews, A. P.
1994. Current Advance Method and Cyclic Leapfrog for 2D Multispecies Hybrid Plasma Simulations. *Journal of Computational Physics*, 112(1):102–116.

Mayaud, P. N.
1980. Derivation, Meaning, and Use of Geomagnetic Indices. *Washington DC American Geophysical Union Geophysical Monograph Series*, 22:607.

McComas, D., S. Bame, P. Barker, W. Feldman, J. Phillips, P. Riley, and J. Griffee
1998. Solar Wind Electron Proton Alpha Monitor (SWEPAM) for the Advanced Composition Explorer. *Space Science Reviews*, 86(1):563–612.

Meng, X., B. T. Tsurutani, and A. J. Mannucci
2019. The Solar and Interplanetary Causes of Superstorms (Minimum Dst $\leq$ -250 nT) During the Space Age. *Journal of Geophysical Research (Space Physics)*, 124(6):3926.

Meyer-Vernet, N.
2007. *Basics of the Solar Wind*, Cambridge Atmospheric and Space Science Series. Cambridge: Cambridge University Press.

Modolo, R.
2004. *Modélisation de l'interaction Du Vent Solaire, Ou Du Plasma Kronien, Avec Les Environnements Neutres de Mars et de Titan*. These de doctorat, Versailles-St Quentin en Yvelines.

Modolo, R., S. Hess, V. Génot, L. Leclercq, F. Leblanc, J. Y. Chaufray, P. Weill, M. Gangloff, A. Fedorov, E. Budnik, M. Bouchemit, M. Steckiewicz, N. André, L. Beigbeder, D. Popescu, J. P. Toniutti, T. Al-Ubaidi, M. Khodachenko, D. Brain, S. Curry, B. Jakosky, and M. Holmström
2018. The LatHyS database for planetary plasma environment investigations: Overview and a case study of data/model comparisons. *Planetary and Space Science*, 150:13–21.

Moissard, C., D. Fontaine, and P. Savoini
2019. A Study of Fluctuations in Magnetic Cloud-Driven Sheaths. *Journal of Geophysical Research: Space Physics*, 124(11):8208–8226.

Mukaka, M.
2012. A guide to appropriate use of Correlation coefficient in medical research. *Malawi Medical Journal : The Journal of Medical Association of Malawi*, 24(3):69–71.

Muller, C.
2014. The Carrington Solar Flares of 1859: Consequences on Life. *Origins of Life and Evolution of the Biosphere*, 44(3):185–195.

Myllys, M., E. K. J. Kipua, and B. Lavraud
2017. Interplay of solar wind parameters and physical mechanisms producing the saturation of the cross polar cap potential: SOLAR WIND CONTROL OF POLAR CAP REGION. *Geophysical Research Letters*, 44(7):3019–3027.

Neugebauer, M. and C. W. Snyder
1962. Solar Plasma Experiment. *Science*, 138:1095–1097.

Nishino, M. N., X.-D. Wang, M. Fujimoto, H. Tsunakawa, Y. Saito, S. Yokota, W. Bian, C.-L. Li, M. Matsushima, H. Shibuya, H. Shimizu, F. Takahashi, and T. Terasawa
2011. Anomalous deformation of the Earth's bow shock in the lunar wake: Joint measurement by Chang'E-1 and SELENE. *Planetary and Space Science*, 59(5):378–386.

Ogilvie, K. W. and M. D. Desch
1997. The WIND spacecraft and its early scientific results. *Advances in Space Research*, 20(4):559–568.

Olson, P. and H. Amit
2006. Changes in earth's dipole. *Naturwissenschaften*, 93(11):519–542.

Omidi, N., X. Blanco-Cano, C. Russell, and H. Karimabadi
2004. Dipolar magnetospheres and their characterization as a function of magnetic moment. *Advances in Space Research*, 33(11):1996–2003.

Osmane, A., A. P. Dimmock, R. Naderpour, T. I. Pulkkinen, and K. Nykyri
2015. The impact of solar wind ULF Bz fluctuations on geomagnetic activity for viscous timescales during strongly northward and southward IMF. *Journal of Geophysical Research: Space Physics*, 120(11):9307–9322.

Pallocchia, G., A. A. Samsonov, M. B. Bavassano Cattaneo, M. F. Marcucci, H. Rème, C. M. Carr, and J. B. Cao
2010. Interplanetary shock transmitted into the Earth's magnetosheath: Cluster and Double Star observations. *Annales Geophysicae*, 28(5):1141–1156.

Palmroth, M., T. I. Pulkkinen, P. Janhunen, D. J. McComas, C. W. Smith, and H. E. J. Koskinen
2004. Role of solar wind dynamic pressure in driving ionospheric Joule heating. *Journal of Geophysical Research: Space Physics*, 109(A11).

Parker, E. N.
1955. The Formation of Sunspots from the Solar Toroidal Field. *The Astrophysical Journal*, 121:491.

Parker, E. N.
1958. Dynamics of the Interplanetary Gas and Magnetic Fields. *The Astrophysical Journal*, 128:664.

Petrinec, S. M.
2002. The location of the Earth's bow shock. *Planetary and Space Science*, 50(5):541–547.

Pinter, S.
1980. The thickness of interplanetary collisionless shock waves. *Bulletin of the Astronomical Institutes of Czechoslovakia*, 31:368–379.

Podesta, J. J., D. A. Roberts, and M. L. Goldstein
2007. Spectral Exponents of Kinetic and Magnetic Energy Spectra in Solar Wind Turbulence. *The Astrophysical Journal*, 664(1):543.

Progressive Management
2015. *21st Century Complete Guide to Space Weather: Solar Storms, Impacts on Human Activity, Flares and Coronal Mass Ejections, Satellite Sun Observation, Forecasting, Carrington Event*.

Pulkkinen, A., E. Bernabeu, A. Thomson, A. Viljanen, R. Pirjola, D. Boteler, J. Eichner, P. J. Cilliers, D. Welling, N. P. Savani, R. S. Weigel, J. J. Love, C. Balch, C. M. Ngwira, G. Crowley, A. Schultz, R. Kataoka, B. Anderson, D. Fugate, J. J. Simpson, and M. MacAlester
2017. Geomagnetically induced currents: Science, engineering, and applications readiness. *Space Weather*, 15(7):828–856.

Ratner, M. I. and J. C. G. Walker
1972. Atmospheric Ozone and the History of Life. *Journal of the Atmospheric Sciences*, 29(5):803–808.

Rax, J.-M.
2005. *Physique des plasmas: Cours et applications*. Dunod.

Regnault, F., M. Janvier, P. Dèmoulin, F. Auchére, A. Strugarek, S. Dasso, and C. Noûs
2020. 20 Years of ACE Data: How Superposed Epoch Analyses Reveal Generic Features in Interplanetary CME Profiles. *Journal of Geophysical Research: Space Physics*, n/a(n/a):e2020JA028150.

Renwick, J. T. and P. E. Babson
1985. Vibration Analysis—A Proven Technique as a Predictive Maintenance Tool. *IEEE Transactions on Industry Applications*, IA-21(2):324–332.

Richardson, I. and H. Cane
2004. The Fraction of Interplanetary Coronal Mass Ejections That Are Magnetic Clouds: Evidence for a Solar Cycle Variation. *Geophysical Research Letters*, 31.

Richardson, I. G. and H. V. Cane
2012. Solar wind drivers of geomagnetic storms during more than four solar cycles. *Journal of Space Weather and Space Climate*, 2:A01.

Šafránková, J., Z. Němeček, L. Přech, A. A. Samsonov, A. Koval, and K. Andréeová
2007. Modification of interplanetary shocks near the bow shock and through the magnetosheath: INTERPLANETARY SHOCKS NEAR THE BOW SHOCK. *Journal of Geophysical Research: Space Physics*, 112(A8):n/a–n/a.

Samsonov, A. A., Z. Němeček, and J. Šafránková
2006. Numerical MHD modeling of propagation of interplanetary shock through the magnetosheath. *Journal of Geophysical Research*, 111(A8).

Samsonov, A. A., D. G. Sibeck, and J. Imber
2007. MHD simulation for the interaction of an interplanetary shock with the Earth's magnetosphere: INTERPLANETARY SHOCK. *Journal of Geophysical Research: Space Physics*, 112(A12):n/a–n/a.

Savoini, P., B. Lembege, and J. Stienlet
2013. On the origin of the quasi-perpendicular ion foreshock: Full-particle simulations: PIC SIMULATION OF ION FORESHOCK. *Journal of Geophysical Research: Space Physics*, 118(3):1132–1145.

Schield, M. A.
1969. Pressure balance between solar wind and magnetosphere. *Journal of Geophysical Research (1896-1977)*, 74(5):1275–1286.

Schrijver, K. and I. Schrijver
2015. *Living with the Stars: How the Human Body Is Connected to the Life Cycles of the Earth, the Planets, and the Stars.* Oxford University Press.

Shue, J.-H., J. K. Chao, H. C. Fu, C. T. Russell, P. Song, K. K. Khurana, and H. J. Singer
1997. A new functional form to study the solar wind control of the magnetopause size and shape. *Journal of Geophysical Research*, 102:9497–9512.

Singh, Y. P. and Badruddin
2012. Study of the influence of magnetic fluctuations and solar plasma density on the solar wind–magnetosphere coupling. *Journal of Atmospheric and Solar-Terrestrial Physics*, 75-76:15–21.

Spreiter, J. R. and S. S. Stahara
1994. Gasdynamic and magnetohydrodynamic modeling of the magnetosheath: A tutorial. *Advances in Space Research*, 14(7):5–19.

Stone, E. C., A. M. Frandsen, R. A. Mewaldt, E. R. Christian, D. Margolies, J. F. Ormes, and F. Snow
1998. The Advanced Composition Explorer. P. 22.

Sugiura, M.
1964. Hourly values of equatorial Dst for the IGY. *Ann. Int. Geophys. Yr.*, Vol: 35.

Szabo, A.
2004. Interplanetary Discontinuities and Shocks in the Earth's Magnetosheath. In *Multiscale Processes in the Earth's Magnetosphere: From Interball to Cluster*, J.-A. Sauvaud and Z. Němeček, eds., NATO Science Series II: Mathematics, Physics and Chemistry, Pp. 57–71, Dordrecht. Springer Netherlands.

Szabo, A., C. W. Smith, and R. M. Skoug
2003. The Transition of Interplanetary Shocks through the Magnetosheath. *AIP Conference Proceedings*, 679(1):782–785.

Tao, C., F. Sahraoui, D. Fontaine, J. de Patoul, T. Chust, S. Kasahara, and A. Retinò
2015. Properties of Jupiter's magnetospheric turbulence observed by the Galileo spacecraft: Jovian magnetospheric turbulence. *Journal of Geophysical Research: Space Physics*, 120(4):2477–2493.

Treumann, R. A.
2009. Fundamentals of collisionless shocks for astrophysical application, 1. Non-relativistic shocks. *The Astronomy and Astrophysics Review*, 17(4):409–535.

Tsurutani, B. T., W. D. Gonzalez, F. Tang, S. I. Akasofu, and E. J. Smith
1988. Origin of interplanetary southward magnetic fields responsible for major magnetic storms near solar maximum (1978–1979). *Journal of Geophysical Research*, 93(A8):8519.

Tsurutani, B. T., G. S. Lakhina, and R. Hajra
2020. The physics of space weather/solar-terrestrial physics (STP): What we know now and what the current and future challenges are. *Nonlinear Processes in Geophysics*, 27(1):75–119.

Tsurutani, B. T., E. J. Smith, and D. E. Jones
1983. Waves observed upstream of interplanetary shocks. *Journal of Geophysical Research: Space Physics*, 88(A7):5645–5656.

Turc, L.
2014. *Interaction des nuages magnétiques éjectés par le Soleil avec l'environnement terrestre*. PhD thesis, Ecole Polytechnique.

Turc, L., D. Fontaine, P. Savoini, and R. Modolo
2015. 3D hybrid simulations of the interaction of a magnetic cloud with a bow shock: SIMULATIONS OF MC/BOW SHOCK INTERACTION. *Journal of Geophysical Research: Space Physics*, 120(8):6133–6151.

Uzdensky, D. A.
2019. Extreme Plasma Astrophysics. https://arxiv.org/abs/1903.05328.

Venzmer, M. S. and V. Bothmer
2018. Solar-wind predictions for the Parker Solar Probe orbit - Near-Sun extrapolations derived from an empirical solar-wind model based on Helios and OMNI observations. *Astronomy & Astrophysics*, 611:A36.

Villante, U., S. Lepidi, P. Francia, and T. Bruno
2004. Some aspects of the interaction of interplanetary shocks with the Earth's magnetosphere: An estimate of the propagation time through the magnetosheath. *Journal of Atmospheric and Solar-Terrestrial Physics*, 66(5):337–341.

Wang, J., C. Huang, Y. S. Ge, A. Du, and X. Feng
2020. Influence of the IMF Bx on the geometry of the bow shock and magnetopause. *Planetary and Space Science*, 182:104844.

Wang, J., Y. Zhao, H. Feng, Q. Liu, Z. Tian, H. Li, A. Zhao, and G. Zhao
2019. Comparison of counterstreaming suprathermal electron signatures of ICMEs with and without magnetic cloud: Are all ICMEs flux ropes? *Astronomy & Astrophysics*, 632:A129.

Webb, D. F. and T. A. Howard
2012. Coronal Mass Ejections: Observations. *Living Reviews in Solar Physics*, 9(1):3.

Wilson, L. B.
2017. Wind 2017 Senior Review Proposal. https://wind.nasa.gov/docs/Wind_SR2017_proposal.pdf.

Wurz, P.
2005. Solarwind Composition. 600:44.1.

Yamada, M., R. Kulsrud, and H. Ji
2010. Magnetic reconnection. *Reviews of Modern Physics*, 82(1):603–664.

Yermolaev, Y. I., I. G. Lodkina, N. S. Nikolaeva, M. Y. Yermolaev, M. O. Riazantseva, and L. S. Rakhmanova
2018. Statistic study of the geoeffectiveness of compression regions CIRs and Sheaths. *Journal of Atmospheric and Solar-Terrestrial Physics*, 180:52–59.

Yermolaev, Y. I., N. S. Nikolaeva, I. G. Lodkina, and M. Y. Yermolaev
2010. Specific interplanetary conditions for CIR-, Sheath-, and ICME-induced geomagnetic storms obtained by double superposed epoch analysis. *Annales Geophysicae*, 28(12):2177–2186.

Zhang, J.
2004. A statistical study of the geoeffectiveness of magnetic clouds during high solar activity years. *Journal of Geophysical Research*, 109(A9).

Zurbuchen, T. H. and I. G. Richardson
2005. In-Situ Solar Wind and Magnetic Field Signatures of Interplanetary Coronal Mass Ejections. *Space Science Reviews*, 123(1):31–43.

Abstract

The Sun often ejects large quantities of magnetic field embedded plasma called magnetic clouds. These can collide with the geomagnetic environment and sometimes perturb it to the point of causing dysfunctions in human technologies. When magnetic clouds travel fast enough, they can generate a shock, itself followed by a turbulent compressed stream named a sheath. Sheaths have recently been recognised as efficient drivers of geomagnetic activity. However, sheaths themselves and their interaction with the geomagnetic environment remain poorly known.

First, by making a statistical study on satellite data of 42 relatively well isolated sheaths, our work is the first to provide values of power and compressibility (which is an indication of the type of fluctuations) in sheaths. We also show the main parameters on which these two quantities depend.

Second, we perform the first ever 3D hybrid PIC simulation to include both an interplanetary shock/sheath self-consistently formed and a model of the geomagnetic environment. From this simulation, we show: the “rebound” of the bow shock’s motion after its interaction with the interplanetary shock (a known phenomenon) can be explained by a counter streaming flow of subalfvénic particles bouncing back on the magnetopause; the interplanetary shock can be accelerated on the flanks of the magnetopause in the plane perpendicular to the interplanetary magnetic field; an important velocity component perpendicular to the interplanetary magnetic field rises in the sheath, leading to a strong asymmetry in the magnetosheath’s compression.

We will conclude by discussing how our observational results could be used to guide efforts in future numerical simulations.

Résumé

Des nuages magnétiques en provenance du soleil peuvent atteindre et perturber l’environnement géomagnétique et endommager certaines technologies. S’ils sont suffisamment rapides, ces nuages peuvent entraîner la formation d’un choc interplanétaire suivi d’une gaine turbulente de plasma compressé. Il a été montré récemment que ces gaines peuvent être très géoeffectives. Pourtant, les gaines, ainsi que leur interaction avec l’environment géomagnétique restent mal connus.

Nous fournissons pour la première fois, grâce à une étude statistique menée sur 42 gaines bien définies et isolées, des valeurs de la puissance des fluctuations magnétiques et de leur compressibilité (une indication sur le type des fluctuations). Les paramètres ayant une influence sur ces valeurs sont également mis en évidence.

Ensuite, nous présentons la première simulation PIC hybride 3D qui inclut à la fois un modèle de l’environnement géomagnétique et une gaine interplanétaire formée de manière auto-cohérente. Cette simulation permet la mise en évidence de plusieurs résultats nouveaux: le rebond du choc d’étrave suite à son interaction avec le choc interplanétaire (un phénomène connu) peut être expliqué par l’apparition d’un flux subalfvénique de particules ayant rebondies sur la magnétopause; le choc interplanétaire, d’abord freiné dans la magnétogaine, peut être accéléré sur les flancs de la magnétopause; enfin le plasma dans la gaine se propage avec une composante de vitesse perpendiculaire au champ magnétique interplanétaire, non présente en aval du choc, ce qui mène à une compression asymétrique de la magnétogaine.

Nous discuterons enfin des pistes que notre étude observationnelle nous donne pour développer plus avant nos simulations numériques.